

Tailoring Intermolecular Interactions for High-Performance Nanocomposites

David L. Inglefield, Jr.

Dissertation submitted to the faculty of the Virginia Polytechnic Institute and State University in partial fulfillment of the requirements for the degree of

Doctor of Philosophy
In
Chemistry

Timothy E. Long, Committee Chair
Harry C. Dorn
Robert B. Moore
Marissa Nichole Rylander

June 12, 2014
Blacksburg, VA

Keywords: polymer nanocomposites, carbon nanomaterials, nanoparticles

Copyright 2014

Tailoring Intermolecular Interactions for High-Performance Nanocomposites

David L. Inglefield, Jr.

ABSTRACT

Acid oxidation of multi-walled carbon nanotubes (MWCNTs) introduced carboxylic acid sites onto the MWCNT surface, which permitted further functionalization. Derivatization of carboxylic acid sites yielded amide-amine and amide-urea functionalized MWCNTs from oxidized precursors. Conventional MWCNT characterization techniques including X-ray photoelectron spectroscopy (XPS), thermogravimetric analysis (TGA), and Raman spectroscopy supported successful MWCNT functionalization. Incorporation of MWCNTs functionalized with hydrogen bonding groups into a segmented polyurethane matrix led to an increase in mechanical properties at optimized MWCNT loadings, in contrast with non-functionalized MWCNTs that resulted in mechanical property decreases across all loadings. Dynamic mechanical analysis (DMA) demonstrated an increase in the polyurethane-MWCNT composite flow temperature with increasing hydrogen bonding MWCNT incorporation, as opposed to non-functionalized MWCNT composites which displayed no significant change in flow temperature. Variable temperature Fourier transform infrared spectroscopy (VT FT-IR) probed temperature-dependent hydrogen bonding in the polyurethane-MWCNT composites and revealed a significant impact on composite hydrogen bonding interactions upon MWCNT incorporation, which was amplified in composites formed using hydrogen bonding functionalized MWCNTs.

Acid oxidation of carbon nanohorns (CNHs) yielded carboxylic acid functionalized CNHs, providing sites for further reaction with histamine to afford histamine-functionalized CNHs (His-CNHs). Raman spectroscopy, XPS and TGA confirmed successful functionalization.

Transmission electron microscopy (TEM) demonstrated that His-CNHs efficiently complex quantum dots (QDs) through imidazole-Zn interactions. Combination of His-CNHs, QDs, and a poly(oligo-(ethylene glycol)₉ methyl ether methacrylate)-*block*-poly(4-vinyl imidazole) copolymer using an interfacial complexation technique afforded stable ternary nanocomplexes with average hydrodynamic diameters under 100 nm. These ternary nanocomplexes represent promising materials for photothermal cancer theranostics due to their size and stability.

The efficient reaction of 2-isocyanatoethyl methacrylate with amines afforded urea-containing methacrylic monomers, where the amine-derived pendant groups determined the polymer T_g . Reversible addition-fragmentation chain-transfer (RAFT) polymerization enabled the synthesis of ABA triblock copolymers with urea-containing methacrylic outer blocks and poly(2-ethylhexyl methacrylate) inner blocks. These ABA triblocks copolymers displayed composition dependent phase-separated morphologies and desirable mechanical properties. The urea-containing polymers efficiently complexed gold nanoparticles through urea-gold interactions. Furthermore, urea-containing methacrylic polymers served as a useful matrix for incorporation of silica-coated upconverting nanoparticles, affording upconverting nanoparticle composite films. The novel ionene monomer N1,N2-bis(3-(dimethylamino)propyl)oxalamide permitted synthesis of novel oxalamide-containing ammonium ionenes. The hydrogen bonding, charge density, and counter anion tuned the ionene mechanical properties. The ionene structure also influenced water uptake and conductivity. The differences in physical properties correlated well with the morphology observed in small-angle X-ray scattering. The oxalamide-containing ionenes greatly enhance mechanical properties compared to typical ammonium ionenes, and further expand the library of ionene polymers.

ACKNOWLEDGEMENTS

One of the most daunting and rewarding tasks in completing a dissertation (besides writing all the chapters) is trying to thank everyone who has helped you reach this amazing achievement. It's your race to run, but many people help you get to the finish line, so many that it is probably not possible to thank them all. First off, I would like to thank Dr. Long for introducing me to the wonderful world of polymer science, which changed the course of my education, career, and life. Also, I want to thank him for the opportunity to conduct undergraduate research in his group, and for continued expert guidance after accepting me into his amazing group as a graduate student. I need to thoroughly acknowledge all Long group members past and present for their role in my accomplishments. I could not have done it without you! I would like to thank Dr. Erin B. Murphy for her guidance and a super fun first year, and for teaching me cowboy chemistry. I want to thank Evan Margaretta and Dan Buckwalter for countless awesome times in lab, and far out discussions about chemistry and life in general. I need to thank Joe, Keren, and Alie for being a great lab crew, and always being there to have some fun. I would like to thank Chainika for being a great friend and helping me with many experiments. I would also like to acknowledge the whole ICTAS crew for assistance with experiments and being a great group to hang out with when I was over there. I am very grateful for Mingtao, and for all his help this last semester, I know that graduate school will go great for him. Also, I would like to thank my undergraduate mentee Eric "Fergie" Ferguson for lots of hilarious times in lab, and for teaching me a lot, too. I bet everyone in the group wants to thank Brent for all his support!

I need to graciously acknowledge my committee members, Dr. Moore, Dr. Rylander, and Dr. Dorn for all of their guidance, collaboration, and support. Thank you all for coming to my committee meetings and exams, and for all of the helpful insight and advice. All of you embody what it means to be a great professor, and I am really lucky to have such intelligent committee members with such fascinating research. I would also like to thank all my collaborators for all the great work we've done together the past few years. I want to acknowledge Amanda Hudson for her expertise and massive assistance with IR experiments and data, and also Mingqiang and Greg for all of the X-ray scattering data collection and analysis. I had so much fun working on the carbon nanohorn project with Allison and Kristen, and think we have really found some interesting results that were truly a group effort. Also, I want to thank Dr. Giti Khodaparast, Travis Merritt, and Brenden Magill for their help with upconverting nanoparticle design and characterization. All my collaborators have been very kind, knowledgeable, and fun to work with.

I need to importantly thank my family and friends for their support as I've gone through graduate school. It is a long and stressful process that I could not have done without my family and friends. I want to thank my mom for all of her assistance and moral support, and the rest of my family for being there in any way they could help. I need to thank my dog, Cosmo, for being the best friend a graduate student could have. It's no mystery why so many graduate student have dogs, they are always there to pick you up when your experiments aren't going as planned. I want to thank my girlfriend and future wife, Abby, for her overwhelming support the last few years.

I need to thank Steve McCartney out at the NCFL for all his help over the years with countless experiments and many training hours. It was so fun and refreshing to work with you

and chat about music. Listen to *The Wall* Steve! The best Pink Floyd albums in order are *The Wall*>*Dark Side of the Moon*>*Wish You Were Here*. I also need to acknowledge Andrew Giordani for his assistance with XPS analysis. I also want to thank Kathy Lowe at the VetMed school for all her help with TEM experiments over the years, and for being one of the nicest people you'll ever meet. Finally, I want to thank my high school biology teacher, Dr. Cammer for challenging me and leading me down my eventual course toward this PhD. He cemented my love for science, and always made me strive for more, never being satisfied just to coast. Things have turned out pretty good so far! If I have forgotten you, or didn't mention you by name, I am sorry! If you helped me you know who you are, and I am forever in your debt. Like Dr. Long always says, if you could do the research all by yourself, it's probably not that great.

Table of Contents

Chapter 1: Introduction	1
1.1 Dissertation Overview	1
1.2 References	5
Chapter 2: Self-Assembly Strategies for Block Copolymer Nanocomposites	6
2.1 Abstract	6
2.2 Introduction	7
2.3 Block Copolymer Morphologies	8
2.3.1 Idealized Diblock Copolymer Equilibrium Morphologies	9
2.3.2 More Complex BCP Morphological Possibilities	12
2.4 Thermodynamic Factors in Self-Assembled Nanocomposites	12
2.5 Inorganic Nanoparticle Self-Assembly Strategies in Block Copolymers	15
2.6 Carbon Nanomaterial Self-Assembly Strategies in Block Copolymers.....	28
2.7 Conclusions	37
2.8 References	38
Chapter 3: Hydrogen Bond Containing Multi-walled Carbon Nanotubes in Polyurethane Composites.....	41
3.1 Abstract	41
3.2 Introduction	42
3.3 Experimental	44
3.4 Results and Discussion.....	49
3.5 Conclusions	66
3.6 References	67
3.7 Appendix 3A	69
Chapter 4: Temperature-Dependent Hydrogen Bonding Interactions in Polyurethane Multi- walled Carbon Nanotube Composites.....	70
4.1 Abstract	70
4.2 Introduction	71
4.3 Experimental	74
4.4 Results and Discussions	77

4.5 Conclusions	97
4.6 References	98
Chapter 5: Imidazole-Containing Block Copolymers as Stabilizers for Theranostic Carbon Nanohorn-Quantum Dot Nanocomplexes.....	100
5.1 Abstract	100
5.2 Introduction	101
5.3 Experimental	104
5.4 Results and Discussion.....	107
5.5 Conclusions	118
5.6 References	119
Chapter 6: Urea-Containing ABA Triblock Copolymers for Gold Nanoparticle Incorporation	123
6.1 Abstract	123
6.2 Introduction	123
6.3 Experimental	126
6.4 Results and Discussion.....	132
6.5 Conclusions	144
6.6 References	146
Chapter 7: Upconverting Nanocomposites Utilizing Urea-Containing Methacrylic Polymers..	148
7.1 Abstract	148
7.2 Introduction	149
7.3 Experimental	151
7.4 Results and Discussion.....	157
7.5 Conclusions	163
7.6 References	163
Chapter 8: Synthesis and Characterization of Oxalamide Ammonium Ionenes.....	165
8.1 Abstract	165
8.2 Introduction	166
8.3 Experimental	169
8.4 Results and Discussion.....	174
8.5 Conclusions	187

8.6 References	188
Chapter 9: Multi-walled Carbon Nanotubes Decorated with Inorganic Nanoparticles	191
9.1 Abstract	191
9.2 Introduction	192
9.3 Experimental	194
9.4 Results and Discussion.....	197
9.5 Conclusions	204
9.6 References	205
Chapter 10: Overall Conclusions	207
Chapter 11: Suggested Future Work.....	208

List of Figures

- Figure 2.1. Diblock copolymer morphologies: A.) Phase diagram of an idealized diblock copolymer as predicted by self-consistent mean-field theory. B.) Experimental phase diagram of poly(isoprene-*b*-styrene) diblock copolymers. C.) Schematic depiction of ideal diblock copolymer morphologies, determined by the volume fraction of each block. Reprinted with permission from reference 19. 10
- Figure 2.2. Bright field transmission electron microscopy (TEM) micrograph of ternary PS-PEP + Au NPs + SiO₂ NPs nanocomposite film with inorganic volume fraction = 0.02. Gold NPs appear as dark spots at the interface of the PS and PEP domains, and SiO₂ NPs reside in the center of the PEP domains. Inset: Schematic of particle distribution (size proportions altered for clarity). Reprinted from reference 47..... 15
- Figure 2.3. Ordered mesoporous materials from metal NP-BCP self-assembly: A.) Chemical structure of ionic liquid NP surface ligand imparting moderate hydrophilicity. B.) True-scale model of ligand coated Pt NPs. C.) PI-*b*-PDMAEMA BCP structure with hydrophobic poly(isoprene) blocks and hydrophilic poly(DMAEMA) blocks. D.) Model of NP-BCP self-assembly with inverse hexagonal morphology. E.) TEM image of annealed inverse hexagonal hybrid. F.) Higher magnification TEM image of E. showing individual Pt NPs (Inset: convergent-beam electron diffraction pattern from a single Pt NP, demonstrating its crystallinity. Figure adapted from reference 51. 17
- Figure 2.4. TEM analysis of the self-assembly behavior of PMMA-grafted magnetite NPs in PS-*b*-PMMA as a function of graft molecular weight and NP concentration: A.) Fe₃O₄-2.7K (1 wt%) in PS-*b*-PMMA annealed for 240 h. B.) Fe₃O₄-2.7K (4 wt%) in PS-*b*-PMMA annealed for 240 h. C.) Fe₃O₄-2.7K (10 wt%) in PS-*b*-PMMA annealed for 192 h. D.) Fe₃O₄-13.3K (4 wt%) in PS-*b*-PMMA annealed for 240 h. E.) Fe₃O₄-35.7K (16 wt%) in PS-*b*-PMMA annealed for 240 h. Arrows in the micrographs indicate the film/substrate surface. Figure adapted from reference 52. 19
- Figure 2.5. TEM micrographs of small molecule-directed NP self assembly in PS-*b*-P4VP: A.) PS-*b*-P4VP(PDP)₁ blend with ~4 nm CdSe NPs. B.) PS-*b*-P4VP(PDP)₁ blend with ~5.4 nm PbS NPs. C. Higher magnification image of B. showing NP orientation normal to the lamellar surface. D.) PS-*b*-P4VP(PDP)₂ blend with ~4 nm CdSe NPs. E.) Higher magnification image of D. Insets show schematic depictions of NP assembly. Adapted from reference 54..... 21
- Figure 2.6. Small molecule directed self-assembly of gold NPs in PS-*b*-P4VP: A.) Self-assembly mechanism utilizing the fan shaped small molecule L. B.) Phase diagram of PS-*b*-P4VP(L)_n-Au NP composites. Adapted from reference 55. 22

Figure 2.7. Self-assembly of magnetic L1₀-ordered FePt nanoparticles in PS-*b*-PEO BCP thin films: A.) TEM micrograph of PS-*b*-PEO nanocomposite containing 20 wt% FePt NPs (Inset at higher magnification shows the localization of FePt NPs in the PEO domains). B.) 3D topographic AFM image of PS-*b*-PEO nanocomposite containing 20 wt% FePt NPs. C.) Composite image of topography and magnetic phase shows each dark spot (magnetic signal) is contained within one hole corresponding to a PEO/FePt NP domain. Adapted from reference 56. 23

Figure 2.8. Effect of micelle size on surface plasmon resonance in PS-*b*-P4VP/Au/Ag NP composite films cast from micellar solutions. A.) Schematic of interparticle distance affected by BCP composition. B.) UV-Vis spectroscopy showing red-shifting with increased interparticle distance. C.-E.) TEM micrographs of films showing increased micelle-micelle distances in the films with varying BCP composition. Adapted from reference 58. 25

Figure 2.9. TEM images of PS-*b*-P2VP/Au NP nanocomposites with an overall volume fraction of PS-coated Au NPs of 0.3 displaying varying morphology as a function of distance from the top of the film: A.) 27 μm from film surface. B.) 46 μm from film surface. C.) 64 μm from film surface. D.) Schematic of film structure based on TEM images. All scale bars are 100 nm. Adapted from reference 59. 26

Figure 2.10. Ternary morphology diagram of various PI-*b*-PEO/aluminosilicate NP nanocomposite compositions (in weight fractions). Schematic representations of the pure BCP morphologies are shown at the bottom, with blue representing the PI domains and red representing the PEO domains. Each white region within the diagram is labeled with a schematic representing the morphology of the formed composites. The yellow regions in these schematic morphologies represent the PEO/NP domains. Closed dark points on a gray background indicate areas where biphasic morphologies were observed. Reproduced from reference 60. 28

Figure 2.11. Schematic representation of the effect of C₆₀ incorporation into PS-*b*-P4VP copolymers. Aging the composite solutions led to C₆₀ migration into the P4VP phase through the charge-transfer interaction of C₆₀ with 4-vinyl pyridine units. Reprinted from reference 67. 30

Figure 2.12. Scheme showing the synthesis of a polythiophene BCP and functionalized fullerene capable of ‘three-point’ complimentary hydrogen bonding. Figure adapted from reference 70. 31

Figure 2.13. Nanocomposites obtained from post-polymerization functionalization of a diene-containing BCP: A.) Scheme for anionic polymerization and post-polymerization functionalization with C₆₀ utilizing the Diels-Alder reaction. B.) TEM micrograph showing the phase-separated morphology of the BCP. C.) TEM micrograph of the BCP/C₆₀ nanocomposite. Adapted from reference 73. 32

Figure 2.14. Self-assembly of PS functionalized MWCNTs in PS-*b*-PI BCP composites: A.) Schematic of the self-assembly strategy. B.) TEM micrograph of PS functionalized MWCNT

showing the PS coverage of the MWCNT. C.) and D.) TEM micrographs of MWCNT sequestration in PS phases (PS domains are light and PI domains are dark). Adapted from reference 80..... 35

Figure 2.15. Selective self-assembly of DWCNTs in a SBS BCP: A.) Schematic of the self-assembly process. B.) TEM micrograph of the phase separated SBS BCP. C.) PSBS nanocomposite with short (<500 nm) PS-DWCNTs. D.) PSBS nanocomposite with long (>500 nm) PS-DWCNTs. Adapted from reference 81..... 36

Figure 3.1. Thermogravimetric analysis of MWCNTs..... 51

Figure 3.2. Raman spectra of MWCNTs. 52

Figure 3.3. Dispersion in varied pH conditions (MWCNTs dispersed at 1×10^{-2} wt%, photos taken after 1 day). 55

Figure 3.4. Comparison of MWCNT dispersibility in composites (1.8 wt% MWCNTs). 59

Figure 3.5. Effect of surface functionalization on thermal stability of composites (1.8 wt% MWCNTs). 60

Figure 3.6. Comparison of Dynamic Mechanical Properties at 1.8 wt% MWCNTs..... 61

Figure 3.7. Representative tensile curves of composites (1.8 wt% MWCNTs). 62

Figure 3.8. Stress at break as a function of MWCNT loading..... 64

Figure 3.9. Strain at break as a function of MWCNT loading..... 65

Figure 3.10. Young's modulus as a function of MWCNT loading. 65

Figure 3.11. Surface resistivity measurements of polyurethane-MWCNT composites. 69

Figure 4.1. Polyurethane and MWCNT structures with varying hydrogen bonding surface functionality utilized to form composites. 75

Figure 4.2. SAXS analysis of neat polyurethane. Inset shows AFM of microtomed surface of the segmented polyurethane displaying microphase separation. 78

Figure 4.3. DMA comparison of purified MWCNT loading in segmented polyurethane composites..... 80

Figure 4.4. DMA comparison of AO-MWCNT loading in segmented polyurethane composites. 81

Figure 4.5. DMA comparison of AA-MWCNT loading in segmented polyurethane composites. 81

Figure 4.6. DMA comparison of AU-MWCNT loading in segmented polyurethane composites. 82

Figure 4.7. Representative variable temperature FT-IR spectra (neat polyurethane shown). 85

Figure 4.8. Representative peak fitting (neat polyurethane at 35 °C).....	87
Figure 4.9. Representative peak fitting (neat polyurethane at 185 °C).....	87
Figure 4.10. Relative area of hydrogen bonding carbonyl peaks and free carbonyl peaks as a function of temperature (neat polyurethane).....	89
Figure 4.11. Relative area of hydrogen bonding carbonyl peaks and free carbonyl peaks as a function of temperature (0.18 wt% AO-MWCNTs polyurethane).....	91
Figure 4.12. Relative area of hydrogen bonding carbonyl peaks and free carbonyl peaks as a function of temperature (1.8 wt% AO-MWCNTs polyurethane).....	91
Figure 4.13. Relative area of hydrogen bonding carbonyl peaks and free carbonyl peaks as a function of temperature (5 wt% AO-MWCNTs polyurethane).....	92
Figure 4.14. Relative area of hydrogen bonding carbonyl peaks and free carbonyl peaks as a function of temperature (10 wt% AO-MWCNTs polyurethane).....	92
Figure 4.15. Percent hydrogen bonded carbonyl of purified MWCNT composites as a function of temperature.	94
Figure 4.16. Percent hydrogen bonded carbonyl of AO- MWCNT composites as a function of temperature.	94
Figure 4.17. Percent hydrogen bonded carbonyl of AA-MWCNT composites as a function of temperature.	95
Figure 4.18. Percent hydrogen bonded carbonyl of AU-MWCNT composites as a function of temperature.	95
Figure 4.19. Comparison of initial percent hydrogen bonded (35 °C) and final percent hydrogen bonded (185 °C) carbonyl values of each MWCNT composite series as a function of wt% MWCNTs.....	96
Figure 5.1. Synthesis of histamine functionalized CNHs: A.) CNH functionalization scheme. B.) Thermogravimetric analysis of AO-CNHS and His-CNHS. (C.) Raman spectroscopy of functionalized CNHs.....	108
Figure 5.2. Diblock copolymer synthesis by RAFT polymerization: A.) Copolymer synthesis scheme. B.) SEC analysis of macroCTA and diblock copolymer.	111
Figure 5.3. Interfacial complexation producing theranostic nanocomplexes.	113
Figure 5.4. Transmission electron microscopy of nanocomplexes: A.) His-CNHS + QDs. B.) HisCNHS + QDs. C.) AO-CNHS + QDs. D.) AO-CNHS + QDs. E.) AO-CNHS + QDs filtered.	114
Figure 5.5. Optimal concentration determination by DLS: A.) Variation of QD concentration in QD-polymer complexation. B.) Variation of His-CNHS in ternary nanocomplex formation. ..	115

Figure 5.6. Ideal nanocomplex formation: A.) Dynamic light scattering of ternary nanocomplexes and key components in water. B.) TEM of ternary nanocomplex.	117
Figure 6.1. Fit of urea-containing copolymers to the Fox Equation.	135
Figure 6.2. RAFT polymerization behavior: A.) macroCTA determined from SEC. B.) ABA triblocks determined from ¹ H NMR.	138
Figure 6.3. DMA of triblock copolymers: A.) Storage modulus. B.) Tan delta. Copolymers are labeled according to the wt % of outer block incorporation.	140
Figure 6.4. AFM of unannealed triblock copolymers (copolymers are labeled according to the wt % of outer block incorporation).	142
Figure 6.5. AFM of annealed triblock copolymers (copolymers are labeled according to the wt % of outer block incorporation).	142
Figure 6.6. Au nanoparticle complexation test: A.) No polymer before stirring.	144
Figure 7.1. Energy state diagram of the Yb ³⁺ /Er ³⁺ upconversion system. Reproduced from reference 10.	150
Figure 7.2. Schematic representation of the instrumental setup utilized in the measurement of upconverted optical emissions. The red arrow represents the exciting laser light, and the green arrow represents the backscattered upconverted emission.	156
Figure 7.3. TEM of upconverting nanoparticles: A.) Er/Yb doped NaYF ₄ core. B.) Er/Yb doped NaYF ₄ core with glass spacer. C.) and D.) UCNP@Au nanoshell.	159
Figure 7.4. Optical emission properties of UCNPs in solution.	161
Figure 7.5. Optical emission properties of UCNP@SiO ₂ polymer composites. Inset shows visible upconversion emission from UCNP@SiO ₂ composite film.	162
Figure 8.1. Dynamic mechanical analysis of oxalamide ionenes: A.) Storage modulus versus temperature. B.) Tan delta versus temperature.	179
Figure 8.2. Representative tensile curves of 3ox3,12 oxalamide ionenes.	181
Figure 8.3. Water sorption analysis of ionenes.	182
Figure 8.4. Conductivity analysis of ionenes: A.) Impedance spectroscopy. B.) Impedance spectroscopy normalized by T _g	184
Figure 8.5. SAXS analysis of ionenes.	185
Figure 9.1. Observation of magnetic behavior of mnp-MWCNTs.	198
Figure 9.2. TEM imaging of mnp-MWCNTs at various weight ratios of Fe(acac) ₃ :MWCNTs in the synthesis procedure. Red scale bars are 100 nm.	199

Figure 9.3. Alignment of mnp-MWCNTs in a magnetic field. mnp-MWCNTs (4:1 weight ratio of Fe(acac)₃:MWCNT in initial reaction) were dropped at 7.5 x 10⁻⁴ wt % in water on a silicon wafer and dried in a 1 T magnetic field. 200

Figure 9.4. TGA analysis of thiol functionalized MWCNTs..... 201

Figure 9.5. TEM imaging of thiol functionalized MWCNTs decorated with gold nanoparticles and control (AO-MWCNTs) showing no conjugation of gold nanoparticles. Red scale bars are 100 nm. 202

Figure 9.6. TEM imaging of A.) endohedral gold nanoparticles (Au@AO-MWCNTs) and B.) Au@mnp-MWCNTs. Red scale bars are 100 nm..... 204

Figure 11.1. Proposed gold-coated upconverting nanoparticle self-assembly in urea-containing block copolymers. 209

List of Tables

Table 3.1. Summary of relevant Raman peak area ratios.	52
Table 3.2. Elemental composition as determined by XPS.	53
Table 3.3. Deconvoluted oxygen 1s peak areas.	54
Table 3.4. Summary of composite tensile properties (1.8 wt% MWCNTs).	63
Table 5.1. XPS elemental composition and Raman peak area ratios of CNHs.	109
Table 6.1. Summary of urea-containing homopolymer properties.	133
Table 6.2. Summary of urea-containing copolymer properties for Fox Equation analysis.	135
Table 6.3. Summary of urea-containing triblock properties.	137
Table 8.1. Ionene molecular weights and thermal properties.	177
Table 8.2. Summary of 3ox3,12 oxalamide ionene tensile properties.	180
Table 9.1. Weight loss at magnetite degradation (~700 °C) of different mnp-MWCNTs.	200

List of Schemes

Scheme 3.1. Surface functionalization for the synthesis of urea functionalized MWCNTs.	49
Scheme 3.2. Synthesis of segmented PTMO based polyurethane.	56
Scheme 6.1. Synthesis of urea-containing methacrylic monomers and homopolymers.....	133
Scheme 6.2. Synthesis of urea-containing methacrylic copolymers.....	135
Scheme 6.3. Synthesis of urea-containing triblock copolymers.	136
Scheme 7.1. Synthesis and polymerization of HUrMA.....	157
Scheme 7.2. Synthesis of upconverting nanoparticles with silica spacer and gold nanoshell...	159
Scheme 8.1. Synthesis of N1,N2-bis (3-(dimethylamino)propyl)oxalamide.	174
Scheme 8.2. Synthesis of oxalamide ammonium ionenes.	175
Scheme 8.3. Synthesis of alkyl ammonium ionenes.....	175
Scheme 8.4. Anionic exchange of oxalamide ionenes.....	176
Scheme 9.1. Synthesis of mnp-MWCNTs.....	198
Scheme 9.2. Synthesis of thiol functionalized MWCNTs.	201
Scheme 9.3. Formation of endohedral gold nanoparticles and subsequent formation of exohedral magnetic nanoparticles.....	203
Scheme 11.1. Proposed functionalization for the synthesis of highly charged carbon nanotubes capable of ionic and electronic conductivity.	210

Chapter 1: Introduction

1.1 *Dissertation Overview*

Polymer-nanoparticle composite materials consist of nanoparticles complexed with polymers in solution or dispersed in polymer matrices.¹ Nanoparticles employed in polymer composite systems cover a wide range of materials including inorganic nanoparticles, clay nanoplatelets, and carbon nanomaterials, which include fullerenes, carbon nanotubes, and graphene. Formation of composites enables exploitation of desirable electrical, optical, and thermal nanoparticle properties in polymer systems and enhancement of polymer thermomechanical properties through nanoparticle reinforcement.² Also, incorporation into polymer matrices offers environmental protection for nanoparticles and provides the opportunity for nanoparticle self-assembly.³ The wide range of desirable nanoparticle properties and extreme diversity of polymers allowing for tunable composite properties gives rise to a plethora of potential composite materials with exciting applications covering all areas of materials and biomedical research.

Typically, composite property optimization relies on effective polymer-nanoparticle interactions which reduce nanoparticle aggregation and maximize polymer-nanoparticle interfacial adhesion. Therefore, integration of efficient polymer-nanoparticle intermolecular interactions into nanocomposite design is essential to maximize nanoparticle dispersion or allow for self-assembly. Incorporation of chemical functionality capable of intermolecular interactions with nanoparticles in polymer structures combined with complimentary nanoparticle surface functionalization ensures compatibilization of nanoparticles with polymers which may originally exhibit chemical incompatibility.⁴ This basic necessity of nanoparticle-polymer

compatibilization continues to represent one of the most important areas of polymer nanocomposite research. Novel polymer structures and nanoparticle functionalizations expand the library of materials for high-performance nanocomposites. In this dissertation we explore several novel nanoparticle functionalizations and polymer structures that afford efficient polymer-nanoparticle interactions enabling nanocomposite formation.

Carbon nanotubes (CNTs) represent a promising and intensively researched class of materials for use in nanocomposites. The unique electrical, thermal, and mechanical properties of CNTs offer many opportunities in nanocomposite design.⁵ CNTs enable mechanical reinforcement of polymer matrices when proper functionalization facilitates thorough dispersion and effective polymer-CNT interactions.⁶ Here, acid oxidation of multi-walled carbon nanotubes (MWCNTs) introduced carboxylic acid sites that permitted further functionalization to form amide-amine and amide-urea functionalized MWCNTs. Incorporation of hydrogen bonding functionalized MWCNTs provided mechanical enhancement of a segmented polyurethane matrix at optimized loadings. In contrast, non-functionalized MWCNTs reduced composite mechanical properties at all loadings. This is attributed to thorough dispersion and efficient polymer-MWCNT interactions in functionalized MWCNT composites, as opposed to the non-functionalized MWCNTs which aggregate heavily due to their hydrophobic surface and interact poorly with the polyurethane matrix. We further investigated the temperature-dependent properties of these polyurethane-MWCNT composites utilizing dynamic mechanical analysis (DMA) and variable temperature Fourier transform infrared spectroscopy (VT FT-IR). DMA demonstrated an increase in composite flow temperature with increasing loading of functionalized MWCNTs, in contrast with non-functionalized MWCNTs which did not significantly affect composite flow temperature. VT FT-IR revealed a profound effect of

MWCNT incorporation on hydrogen bonding in the polyurethane composites, which was intensified in the functionalized MWCNT composites. These results show that the hydrogen bonding functionalized MWCNTs disperse more thoroughly and interact more effectively with polymer chains in polyurethane-MWCNT composites compared to non-functionalized MWCNTs.

Carbon nanohorns (CNHs) represent promising nanocarbon materials for biomedical applications due to their size, shape, and lack of toxic metal catalysts.⁷ CNHs offer extensive opportunities for surface functionalizations that enable complexation with polymers and inorganic nanoparticles. Here, we investigate the stabilization of CNH-quantum dot (QD) nanocomplexes with a water-soluble diblock copolymer that contains a colloiddally stabilizing poly(oligo-(ethylene glycol)₉ methyl ether methacrylate) block and a QD-complexing poly(4-vinyl imidazole) block synthesized using reversible addition-fragmentation chain-transfer (RAFT) polymerization. Synthesis of histamine functionalized CNHs (His-CNHs) enabled efficient CNH-QD complexation through imidazole-QD interactions. Combination of the diblock copolymer, CNHs, and QDs through an interfacial complexation yielded stable ternary nanocomplexes with sizes desirable for cellular uptake. These ternary nanocomplexes represent promising candidates for photothermal cancer theranostics.

Incorporation of urea groups into polymers facilitates polymer-gold nanoparticle complexation through urea-gold interactions.⁸ These efficient urea-gold interactions provide the opportunity for gold nanoparticle dispersion and self-assembly in urea-containing polymers. Here, the facile reaction of 2-isocyanatoethyl methacrylate with amines afforded urea-containing methacrylic monomers, where the pendent amine-derived structures affected physical properties in the resulting polymers. RAFT polymerization enabled the synthesis of ABA

triblock copolymers with urea-containing outer blocks and low T_g poly(2-ethylhexyl methacrylate) inner blocks. These triblock copolymers displayed promising composition dependent mechanical properties and phase separation. Also, they effectively complexed gold nanoparticles through urea-gold interactions. The high levels of urea hydrogen bonding also provided a suitable matrix for silica-coated nanoparticle incorporation. Dispersion of silica-coated rare-earth doped NaYF_4 nanoparticles in urea-containing methacrylic polymers afforded upconverting nanocomposite films.

Ammonium ionenes contain positive charges in every repeat unit, leading to ionic conductivity and, typically, poor mechanical properties.⁹ Ammonium ionenes with bromide counterions exhibit brittle mechanical properties and also readily absorb water at ambient conditions, limiting their usefulness in mechanically demanding applications. Here, N1,N2-bis(3-(dimethylamino)propyl)oxalamide, a novel ditertiary amine monomer, enabled the synthesis of ammonium ionenes containing the multi-dentate hydrogen bonding oxalamide group. Oxalamide-containing ammonium ionenes displayed improved mechanical properties compared to ammonium ionene controls, where the charge density, oxalamide concentration, and counteranions determined the mechanical properties and water sorption. The polymer structure also influenced ionic conductivity determined using impedance spectroscopy and polymer morphology determined using small-angle X-ray scattering. The oxalamide-containing ionenes exhibit a significant improvement in mechanical properties over traditional ammonium ionenes, and offer opportunities for polymer matrices in nanocomposites with ionic or hydrogen bonding nanoparticles and nanocarbon materials.

1.2 References

1. Hussain, F.; Hojjati, M.; Okamoto, M.; Gorga, R. E. *J. Compos. Mater.* **2006**, *40*, 1511.
2. Moniruzzaman, M.; Winey, K. I. *Macromolecules* **2006**, *39*, 5194.
3. Bockstaller, M. R.; Mickiewicz, R. A.; Thomas, E. L. *Adv. Mater.* **2005**, *17*, 1331.
4. Kao, J.; Thorkelsson, K.; Bai, P.; Rancatore, B. J.; Xu, T. *Chem. Soc. Rev.* **2013**, *42*, 2654.
5. Sahoo, N. G.; Rana, S.; Cho, J. W.; Li, L.; Chan, S. H. *Prog. Polym. Sci.* **2010**, *35*, 837.
6. Rahmat, M.; Hubert, P. *Compos. Sci. Technol.* **2011**, *72*, 72.
7. Iijima, S.; Yudasaka, M.; Yamada, R.; Bandow, S.; Suenaga, K.; Kokai, F.; Takahashi, K. *Chem. Phys. Lett.* **1999**, *309*, 165.

Chapter 2: Self-Assembly Strategies for Block Copolymer Nanocomposites

David L. Inglefield Jr.^a and Timothy E. Long^{ab}

^aDepartment of Chemistry, ^bMacromolecules and Interfaces Institute

Virginia Tech, Blacksburg, VA 24061

2.1 Abstract

Nanocomposite materials continually attract intense interest from researchers across diverse disciplines due to their ability to combine the desirable properties of nanoparticles and host polymers through proper synthetic design. Employment of block copolymers greatly expands the utility of nanocomposite systems, and offers unique opportunities in the bottom-up approach to self-assembly of nanoparticle arrays with nanoscale order. State-of-the-art polymer synthesis techniques enable precise control of block copolymer structure and composition. These techniques provide tunable and well-defined phase-separated morphologies that serve as templates for nanoparticle self-assembly. Enthalpic compatibilization with block copolymer phases allows for the selective assembly of nanoparticles into specific phases, with nanoscale order provided by the block copolymer morphology. This review explores self-assembly strategies in block copolymer nanocomposites, with attention given to underlying thermodynamic considerations. Illustrative examples and recent developments in the field are discussed, highlighting the synthetic techniques that afford enthalpically favorable interactions between block copolymer phases and nanoparticles.

2.2 Introduction

Nanoparticles (NPs) continue to attract extensive academic and commercial interest due to their unique electrical, optical, mechanical, and catalytic properties imparted by their small size and the ability to precisely control NP shape and composition.¹⁻⁴ These unique properties and their tunability make NP research one of the fastest growing and most promising fields in nanotechnology, with potential applications in electronics, photovoltaics, optics, and medicine.⁵⁻⁸ The combination of NPs with polymers into nanocomposite materials increases NP efficacy, as polymers offer environmental protection, increased mechanical integrity, and the possibility of NP self-assembly.⁹ Rational design of nanocomposite materials involves tailored interactions towards improving NP dispersibility, which results in the retention of unique NP properties and possible enhancement of polymeric properties in the composite material, such as improved thermal and mechanical properties.¹⁰⁻¹² Block copolymers (BCPs) prove particularly promising for nanocomposite applications due to their tunable chemical, mechanical, and morphological properties.^{13,14} The ability for BCPs to self-assemble into phase separated morphologies allows NPs to assemble into specific nanoscale domains with defined patterns, spacing, and long-range order.

Selective self-assembly of NPs into specific BCP phases relies on favorable enthalpic interactions between the NPs and a specific phase.¹⁵ Tailored NP functionalization with a compatibilizing ligand or polymer (or intrinsic NP-polymer interactions) achieve favorable NP-polymer interactions that enable self-assembly. When properly designed, self-assembled BCP-NP composites reflect thermodynamically favorable systems with long-range order that retain desirable properties of NPs and polymers. Such composite systems aim to generate emergent

properties, where the regular nanoscale arrangement of NPs leads to new or synergistic properties. This area of self-assembled BCP nanocomposites represents a rapidly growing and diverse field of research at the interface of polymer synthesis, polymer morphology, nanoparticle design, and applied nanotechnology.

This review focuses on self-assembly strategies of pre-formed NPs, including carbon nanomaterials, in BCP films through intermolecular interactions. A brief introduction to BCP morphology as it relates to NP assembly is presented in addition to a general overview of thermodynamic effects on the generation and study of self-assembled nanocomposites. A discussion of illustrative examples of nanoparticle self-assembly in BCPs from the literature follows, including both inorganic nanoparticles and the less explored area of carbon nanomaterials. A special focus is given to the enthalpic compatibilization required for self-assembly achieved through tailored intermolecular interactions. This review is limited to applications in BCP films, not solution or dispersed systems which exemplify another exciting area of BCP-NP self-assembly and is reviewed elsewhere and continues to develop.¹⁶⁻¹⁸

2.3 Block Copolymer Morphologies

BCPs represent an extremely important and versatile class of materials, possessing a high degree of tunability in their thermal, mechanical, and morphological properties.¹⁹ BCPs combine desirable properties of different polymers into one material, and proper design enables new and exciting copolymer properties. Nanoscale and microscale phase separation in block and segmented copolymers lead to physical and mechanical properties difficult to achieve in homopolymers, such as elastomeric mechanical behavior and tunable transport properties.²⁰⁻²² A variety of controlled polymerizations, including atom-transfer radical-polymerization (ATRP),

nitroxide-mediated radical polymerization (NMP), reversible addition-fragmentation chain-transfer polymerization (RAFT), living anionic polymerization, and living cationic polymerization yield well-defined BCPs with correct synthetic design.²³⁻²⁷ The synthesis of well-defined BCPs using these techniques allows precise control of block lengths and narrow polydispersity indices (PDIs). These factors facilitate BCP self-assembly, as increases in PDI profoundly impact self-assembled morphologies.²⁸⁻³⁰ The more predictable and less complicated self-assembled morphology behavior of diblock copolymers make them the most thoroughly studied, although the variety of possible block structures include triblocks, pentablocks, and beyond. Step-growth polymerizations yield segmented copolymers also capable of self-assembly into distinct phases.³¹

2.3.1 Idealized Diblock Copolymer Equilibrium Morphologies

Although a thorough discussion of BCP morphologies falls outside the scope of this review, understanding the fundamentals of BCP self-assembly is essential for employing BCPs as templates for NP self-assembly. The phase separation of BCPs to form nanoscale and microscale domains arises from chemically distinct and enthalpically incompatible polymer species being covalently bonded to form a single macromolecular chain. In the absence of covalent connection, macroscale phase separation occurs. The covalent attachment of the blocks into a BCP structure prevents macroscale phase separation, leading to phase separation on the nano- and mesoscale. Minimization of the enthalpically unfavorable mixing of the incompatible polymer blocks and the entropically unfavorable stretching of the polymer chains induced by the incompatible chain segments stretching away from each other determines the resultant phase-separated morphology.³²

The equilibrium morphology of BCPs governed by the minimization of the entropy and enthalpy in the system depends on the chemical compatibility of the blocks, the degree of polymerization of each block, and the BCP composition (volume fraction of each block).¹⁹ The Flory-Huggins interaction parameter χ represents the compatibility between the blocks, which depends on the polymer structures. Most χ values between polymers are small and positive, where positive values indicate repulsion between the phases and negative values indicate that mixing is energetically favorable.¹⁹ The segregation product, χN , determines the degree of phase separation, where N is the total degree of polymerization of both blocks. The χN value and volume fraction of each block determine the resultant morphology.³³

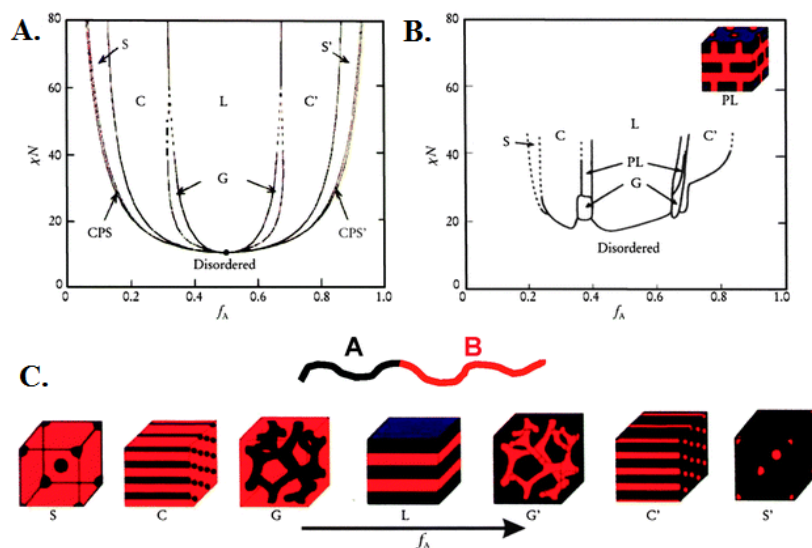


Figure 2.1. Diblock copolymer morphologies: A.) Phase diagram of an idealized diblock copolymer as predicted by self-consistent mean-field theory. B.) Experimental phase diagram of poly(isoprene-b-styrene) diblock copolymers. C.) Schematic depiction of ideal diblock copolymer morphologies, determined by the volume fraction of each block. Reprinted with permission from reference 19.

Figure 2.1 illustrates predicted behavior of an idealized diblock copolymer using simulation and its comparison to experimental observations. **Figure 2.1A** shows the theoretical

predictions of a diblock copolymer phase diagram as a function of χN and the volume fraction of each block. **Figure 2.1C** illustrates the predicted morphologies, which transition from spherical(S), to cylindrical(C), to gyroid(G), to lamellar(L) as the volume fraction of each block is altered, with lamellar representing the favored morphology in symmetrical compositions. **Figure 2.1B** shows how experimental results from a model system, poly(isoprene-*b*-styrene), differs from the theoretical predictions, while retaining a high degree of similarity. The asymmetry and the new, metastable perforated layer (PL) phases are examples of differences between ideal theoretical simulations and empirical observations.³⁴ There are several articles and reviews that thoroughly discuss the self-assembly behavior of BCPs.^{19,32,33,35}

These various morphologies represent different templates for the self-assembly of NPs, providing unique spatial arrangement possibilities for NPs that selectively assemble in one phase. Understanding the phase separation behavior and morphology of BCPs is crucial to proper design and implementation of high performance BCP nanocomposites. Altering the BCP structure and composition not only affects the physical properties of BCP films, but also their morphology which proves critically important for NP self-assembly. In addition to the spatial organization, the BCP composition will affect the interparticle distance in self-assembled NP nanocomposites, as block length affects domain size in phase-separated BCPs.³⁶ The synthetic techniques that afford well-defined BCPs enable phase-separated systems with predictable and reproducible order, as variation in block composition and polydispersity greatly affect BCP morphology.²⁸ In addition, the processing of BCPs for NP self-assembly requires thorough investigation to determine if an obtained morphology is in equilibrium and if the equilibrium morphology is desirable for the intended application.

2.3.2 More Complex BCP Morphological Possibilities

In addition to the idealized diblock copolymer morphologies discussed above, more complex morphologies are possible with added BCP complexity. In general, ABA triblock systems are more complex and less predictable than analogous AB diblocks. However, ABA triblock copolymers typically have improved mechanical properties when compared to analogous AB diblocks due to enhanced physical crosslinking.^{37,38} This tradeoff between mechanical properties and morphological predictability requires optimization in each system. The ABA triblock systems are still only capable of two distinct phases.

Vastly increased morphological complexity arises when three incompatible polymers are combined into a single macromolecule, as occurs in ABC triblocks, ABCBA pentablocks, and ABC miktoarm star polymers. The formed morphologies depend on the factors discussed earlier, as well as the polymer topology and relative χ parameters of the different blocks. Many investigations in the past two decades focus on the fundamental behavior and application of three-phase BCPs in films and micellar systems.³⁹⁻⁴² There are also several reviews that explore the synthesis and morphology of these three-phase BCP systems.⁴³⁻⁴⁵ Since research has focused mainly on diblock copolymers for NP self-assembly, three-phase systems represent an important future avenue for NP self-assembly. These three-phase systems greatly expand the complexity and diversity of available BCP morphologies. In the future, these systems may be employed to increase the geometric possibilities and functional capabilities of self-assembled nanocomposites.

2.4 Thermodynamic Factors in Self-Assembled Nanocomposites

In analogy to the factors in BCP self-assembly discussed above, the thermodynamic minimization of free energy determines the equilibrium self-assembled state of NPs in BCP

templates. The main factors that contribute to the self-assembly behavior of NPs in a BCP include the chemical compatibility of the NP with each block, the size of the NPs, and the processing conditions. The affinity for a nanoparticle P with a given domain X in a block copolymer system is represented by the Flory-Huggins interaction parameter χ_{PX} , which defines the enthalpic compatibility of a NP and a BCP phase, analogous to the χ parameters which define the affinity of polymer blocks.¹⁵ For a NP to selectively incorporate into a specific phase, it is expected that the χ value for the NP and that phase must be lower than the χ value for the NP and any other phase. This requirement of enthalpic compatibilization for NP assembly into a specific BCP phase creates the need for tailored NP-polymer interactions, which is a focus of this review.

The following equation expresses the overall self-assembly process of NPs in BCPs in terms of free energy change:

$$\Delta G = (\Delta H_{\text{NP-polymer}}) - T(\Delta S_{\text{con}} + \Delta S_{\text{trans}})$$

where $\Delta H_{\text{NP-polymer}}$ defines the enthalpic contribution from the NP-polymer interactions (as determined by the NP surface chemistry), ΔS_{con} denotes the change in conformational entropy of polymer chains induced by NP incorporation, and ΔS_{trans} represents the entropic contribution of the number of physical arrangements of the NPs (the overall level of order of NPs in the nanocomposite).⁴⁶

Conceptually, the goal of NP self-assembly in BCPs is to maximize the specific long-range order of the NPs in the composite system, which is represented by the ΔS_{trans} contribution in the above equation. The NP size determines how the BCP chains conform to accommodate the NPs, which corresponds to the ΔS_{con} term in the above equation. Usually the NP size is fixed to provide the desirable NP properties which are often size dependent.² Therefore, the enthalpic

contribution of the NP-polymer interactions, $\Delta H_{\text{NP-polymer}}$, is the most readily accessible parameter to alter through synthetic design to obtain well-ordered BCP-NP nanocomposites. Also, the processing conditions that determine how closely a nanocomposite resembles the thermodynamically favored equilibrium as opposed to a kinetically trapped state represent extremely important and tunable variables in nanocomposite design. Researchers must consider all of these factors when designing nanocomposites to achieve the desired nanostructure and properties.

The size-dependent assembly of silica and gold NPs in a symmetric poly(styrene-*b*-ethylene propylene) (PS-*b*-PEP) copolymer serves as an illustrative example of the interplay of thermodynamic effects on nanocomposite formation. Bockstaller *et al.* demonstrated that organization of similarly compatibilized gold and silica NPs in the PS-*b*-PEP BCP was dependent on the size of the NP (**Figure 2.2**).⁴⁷ In this study, both types of particles were prepared using aliphatic surface functionalization, compatibilizing the NPs with the PEP phase. Assuming equal enthalpic interactions between the different types of NPs and PEP, the observed behavior indicates the importance of entropic contributions to NP self-assembly. When composites were formed with smaller gold NPs (diameters ~ 4 nm), the NPs assembled at the domain interface. When larger SiO₂ NPs (diameters ~ 22 nm) were used, they assembled in the center of the PEP phases. Intriguingly, when a ternary nanocomposite was prepared, site selective assembly of each type of NP was conserved. Since equal enthalpic interactions were assumed, this size-dependent assembly behavior was explained by the conformational entropy change of the polymer chains and NP translational entropy. For the larger NPs, the conformational entropic penalty due to polymer chains stretching to accommodate the NPs dominates, so the NPs become sequestered in the center of the PEP to minimize this

conformational entropic penalty. For the smaller gold NPs, the decrease in conformational entropy is outweighed by the NP translational entropy. These experimental results agree well with theoretical simulations which predict entropically controlled assembly of NPs based on their size relative to BCP phases.^{48,49}

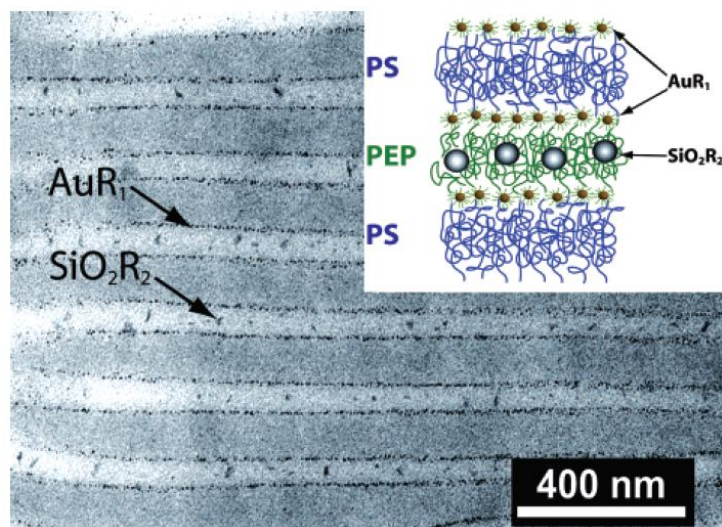


Figure 2.2. Bright field transmission electron microscopy (TEM) micrograph of ternary PS-PEP + Au NPs + SiO₂ NPs nanocomposite film with inorganic volume fraction = 0.02. Gold NPs appear as dark spots at the interface of the PS and PEP domains, and SiO₂ NPs reside in the center of the PEP domains. Inset: Schematic of particle distribution (size proportions altered for clarity). Reprinted from reference 47.

2.5 Inorganic Nanoparticle Self-Assembly Strategies in Block Copolymers

The majority of investigations into NP self-assembly in BCPs focus on inorganic nanoparticles (typically metal, metal oxide, or silica NPs). Various inorganic NPs display exceptional electrical, optical, thermal, and catalytic properties that make them promising candidates for nanocomposite applications.^{1,3,4,6,7} Using pre-formed NPs utilizing established synthetic techniques in nanocomposites allows for precise control of the NP structure and resulting properties, which are size, shape, and composition dependent.¹⁵ This contrasts with the *in-situ* “nanoreactor” approach that forms NPs in selected BCP domains from loaded precursors,

which leads to reduced synthetic precision in NP formation. Furthermore, the well understood surface modification techniques of metal and silica NPs allow for many compatibilization possibilities with BCPs.⁵⁰ Typical strategies to self-assemble inorganic NPs in BCPs include utilizing compatibilizing surface ligands, grafted polymers, and independent self-assembling supramolecular additives. As with any BCP system, the processing conditions and techniques of nanocomposites determine the final nanocomposite structure and properties.

In an example of employing tailored surface ligands, Warren and coworkers demonstrated the self-assembly of Pt NPs in a poly(isoprene-*b*-dimethylaminoethyl methacrylate) (PI-*b*-PDMAEMA) BCP with the goal of forming ordered mesoporous materials with high conductivities for fuel cell electrodes and related applications (**Figure 2.3**).⁵¹ They employed anionic polymerization to yield well-defined PI-*b*-PDMAEMA with narrow polydispersity, and used a hydrophilic ionic liquid surface ligand to compatibilize Pt NPs with the PDMAEMA block. They showed that aging in boiling water tuned the surface functionalized NP hydrophilicity to an optimal level by reducing the number of ligands per NP. Using these optimized NPs in a high weight fraction, they obtained nanocomposites with an inverse hexagonal morphology with hydrophilic NPs and PDMAEMA forming the continuous phase which was ordered with annealing (**Figure 2.3E and 2.3F**). The formed morphology depended on the volume fraction of the combined hydrophilic components (NPs and PDMAEMA) and they demonstrated formation of lamellar morphologies by adjusting this volume fraction. Using a rapid pyrolysis technique, they converted the polymer phases of these ordered composites to amorphous carbon which coated the platinum and preserved the platinum order. They additionally demonstrated the high conductivity of these ordered mesoporous Pt-C

composites and showed that selective etching removed the amorphous carbon to yield a mesoporous inverse hexagonal Pt structure, all from BCP templated self-assembly.

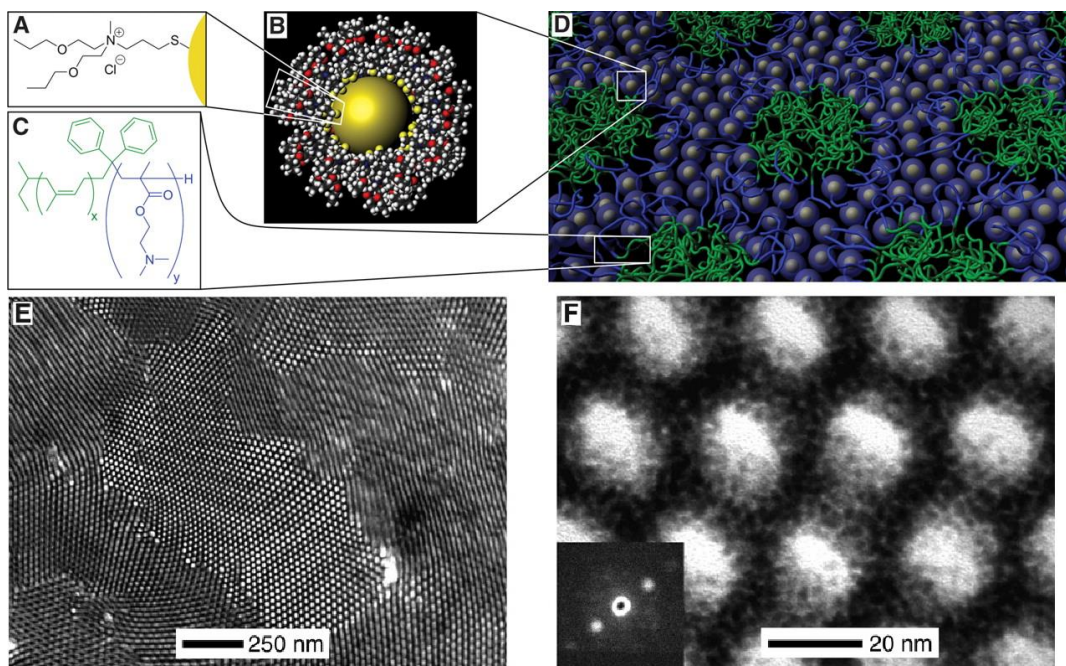


Figure 2.3. Ordered mesoporous materials from metal NP-BCP self-assembly: A.) Chemical structure of ionic liquid NP surface ligand imparting moderate hydrophilicity. B.) True-scale model of ligand coated Pt NPs. C.) PI-*b*-PDMAEMA BCP structure with hydrophobic poly(isoprene) blocks and hydrophilic poly(DMAEMA) blocks. D.) Model of NP-BCP self-assembly with inverse hexagonal morphology. E.) TEM image of annealed inverse hexagonal hybrid. F.) Higher magnification TEM image of E. showing individual Pt NPs (Inset: convergent-beam electron diffraction pattern from a single Pt NP, demonstrating its crystallinity. Figure adapted from reference 51.

Employing a NP-grafted polymer compatibilization strategy, Xu *et al.* investigated the self-assembly behavior of poly(styrene-*b*-methyl methacrylate) (PS-*b*-PMMA) with PMMA-grafted magnetite (Fe₃O₄) NPs (**Figure 2.4**).⁵² Using well-defined PS-*b*-PMMA with narrow PDI and approximately equal volume fractions, they systematically probed the obtained morphologies of BCP nanocomposites as a function of NP concentration and grafted PMMA molecular weight. Surface-initiated ATRP afforded PMMA-grafted magnetite NPs with PMMA

molecular weights of 2.7, 13.3, and 35.7 kg/mol (named Fe₃O₄-2.7K, Fe₃O₄-13.3K, and Fe₃O₄-35.7K, respectively) with narrow PDIs and equivalent grafting densities. The surface functionalization with PMMA led to selective NP incorporation into the PMMA phase of the BCP. The grafted PMMA molecular weight, NP concentration, and annealing conditions greatly affected the NP distribution and nanocomposite morphology. **Figure 2.4** illustrates the effect of PMMA graft molecular weight and NP concentration on the nanocomposite morphology with similar annealing conditions. The low graft molecular weight Fe₃O₄-2.7K NPs at 1 wt% displayed highly individualized and selective incorporation into the PMMA phase of a well-ordered lamellar morphology (**Figure 2.4A**). Increasing Fe₃O₄-2.7K concentration to 4 wt% (**Figure 2.4B**) and 10 wt% (**Figure 2.4C**) led to NP aggregation in annealed films which hindered the development of the well-ordered lamellar morphology, even though individualized NPs were observed in as-cast samples. As the graft molecular weight increased to 13.3K, NP aggregation in as-cast films was observed and remained after annealing (**Figure 2.4D**), further impeding the development of lamellae. This effect was amplified in Fe₃O₄-35.7K composites (**Figure 2.4E**), which displayed large NP aggregates at higher NP loadings which formed their own phases causing the BCP to assemble around these large aggregates in an onion-like arrangement. Investigating the magnetic properties of the composites, they observed the expected superparamagnetic behavior imparted by the NPs. These results highlight the importance of grafted polymer molecular weight and processing on the final morphology and NP self-assembly in BCP nanocomposites.

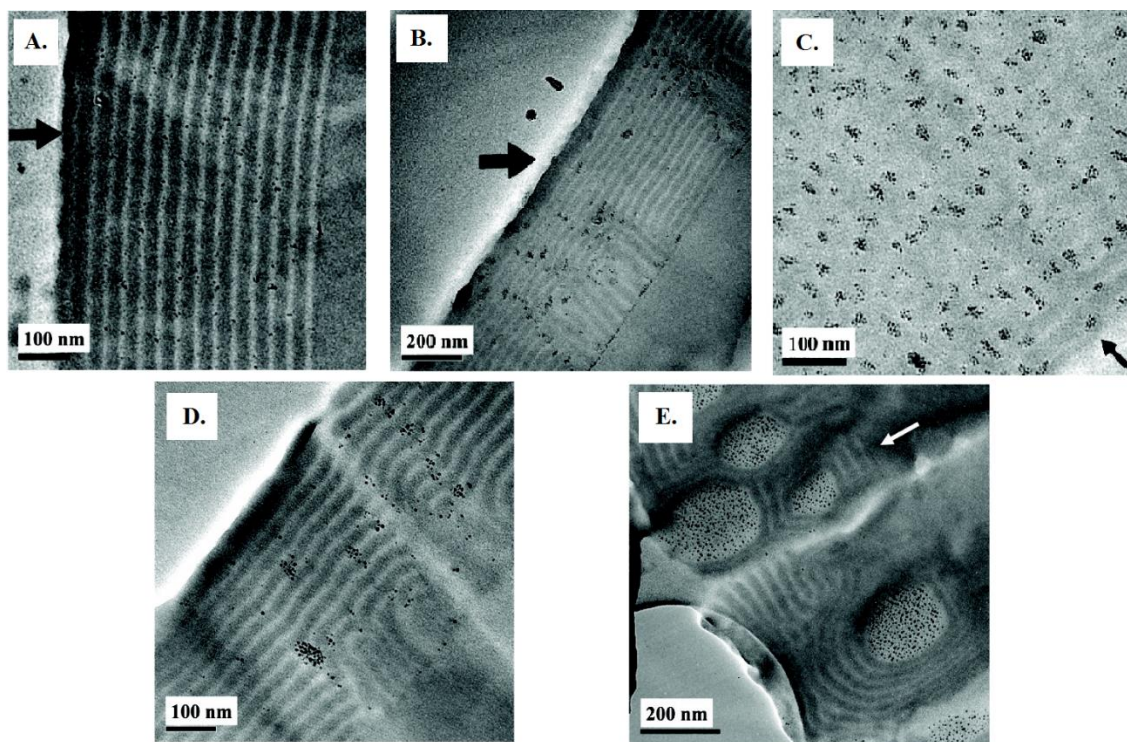


Figure 2.4. TEM analysis of the self-assembly behavior of PMMA-grafted magnetite NPs in PS-*b*-PMMA as a function of graft molecular weight and NP concentration: A.) Fe₃O₄-2.7K (1 wt%) in PS-*b*-PMMA annealed for 240 h. B.) Fe₃O₄-2.7K (4 wt%) in PS-*b*-PMMA annealed for 240 h. C.) Fe₃O₄-2.7K (10 wt%) in PS-*b*-PMMA annealed for 192 h. D.) Fe₃O₄-13.3K (4 wt%) in PS-*b*-PMMA annealed for 240 h. E.) Fe₃O₄-35.7K (16 wt%) in PS-*b*-PMMA annealed for 240 h. Arrows in the micrographs indicate the film/substrate surface. Figure adapted from reference 52.

Another versatile approach to NP self-assembly in BCP films utilizes small molecules capable of supramolecular assembly with the BCP and as-synthesized NPs. This technique avoids additional modification of BCP or NPs, typically relying on small molecules capable of hydrogen bonding at one end coupled with a long alkyl tail. This permits hydrogen bonding to polymers such as poly(4-vinyl pyridine) and favorable interactions with long alkyl chains on NP surfaces commonly used to stabilize NPs. These small molecules assemble into supramolecular assemblies with BCPs and allow for phase specific NP incorporation.⁵³ Adjusting the small molecule loading alters the obtained morphologies.

Zhao *et al.* demonstrated the versatility of this technique in a poly(styrene-*b*-4-vinyl pyridine) BCP (PS-*b*-P4VP, block lengths of 40 and 5.6 kg/mol, respectively) utilizing two small molecules, 3-*n*-pentadecylphenol (PDP) and 4-(4'-octylphenyl)azophenol (OPAP), to direct NP self-assembly.⁵⁴ They examined the supramolecular assembly of CdSe and PbS NPs in the supramolecular BCP system and demonstrated that altering the small molecule loading affected the nanocomposite morphology. The BCP self-assembled with PDP into PS-*b*-P4VP(PDP) supramolecular polymers, where PDP molecules and the P4VP blocks form distinct phases through hydrogen bonding interactions. The long alkyl chains of PDP molecules permitted compatibilization of the CdSe and PbS NPs which respectively possessed octadecylphosphonate and oleate capping ligands, leading to NP incorporation into the P4VP(PDP) phases (**Figure 2.5**). Adjusting the amount of PDP incorporation in the supramolecular PS-*b*-P4VP(PDP)_x blend, where x denotes the ratio of PDP to P4VP units, tuned the NP self-assembly and overall BCP morphology. Changing the PDP content afforded different morphologies due to increased P4VP(PDP) volume fraction. Increasing the PDP in PS-*b*-P4VP(PDP)₃ composites with PbS NPs lead to a hexagonal nanocomposite morphology. Furthermore, they demonstrated the temperature responsive nature of the PS-*b*-P4VP(PDP)₂/CdSe NP composites, observing changes in NP distribution with temperature. When utilizing the photoresponsive OPAP molecule in PS-*b*-P4VP(OPAP)_{1.5}-PbS NP composites, they observed photoreversible NP assembly through OPAP *cis-trans* isomerization. This study details small molecule-directed self-assembly of NPs and further incorporation of tunable, stimuli-responsive behavior.

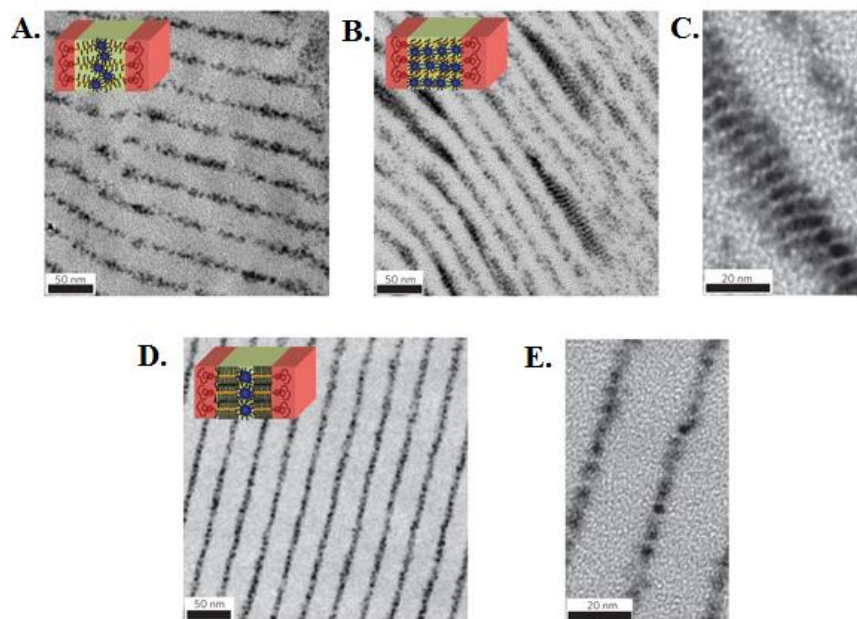


Figure 2.5. TEM micrographs of small molecule-directed NP self assembly in PS-*b*-P4VP: A.) PS-*b*-P4VP(PDP)₁ blend with ~4 nm CdSe NPs. B.) PS-*b*-P4VP(PDP)₁ blend with ~5.4 nm PbS NPs. C. Higher magnification image of B. showing NP orientation normal to the lamellar surface. D.) PS-*b*-P4VP(PDP)₂ blend with ~4 nm CdSe NPs. E.) Higher magnification image of D. Insets show schematic depictions of NP assembly. Adapted from reference 54.

Ye and coworkers expanded on the supramolecular approach, utilizing a fan-shaped small molecule to direct the self-assembly of gold nanoparticles in PS-*b*-P4VP (**Figure 2.6A**).⁵⁵ The fan-shaped small molecule (denoted L) has a structure similar to PDP with a hydroxyl head group and long chain alkyl tails but with much larger volume (see **Figure 2.6A**). Blends of PS-*b*-P4VP and L formed supramolecular PS-*b*-P4VP(L)_n BCPs through hydrogen bonding, where the molar ratio of L to P4VP units (denoted by n) controlled the supramolecular BCP morphology. The fan shape of L with increased volume compared to PDP allowed for highly tunable morphologies with small changes in L content. The alkyl chains in L enabled selective assembly of dodecanethiol capped Au NPs into the P4VP(L)_n domains. PS-*b*-P4VP(L)₁ nanocomposites with 5 vol% Au NPs exhibited a structure-within-structure morphology, where

the Au/P4VP(L)₁ chains displayed hexagonal packing within the lamellar morphology. Altering the L content and NP loading in the nanocomposites combined with small-angle X-ray scattering (SAXS) and TEM analysis allowed the authors to construct a phase diagram for this composite system (**Figure 2.6B**), which shows several differences upon the addition of Au NPs.

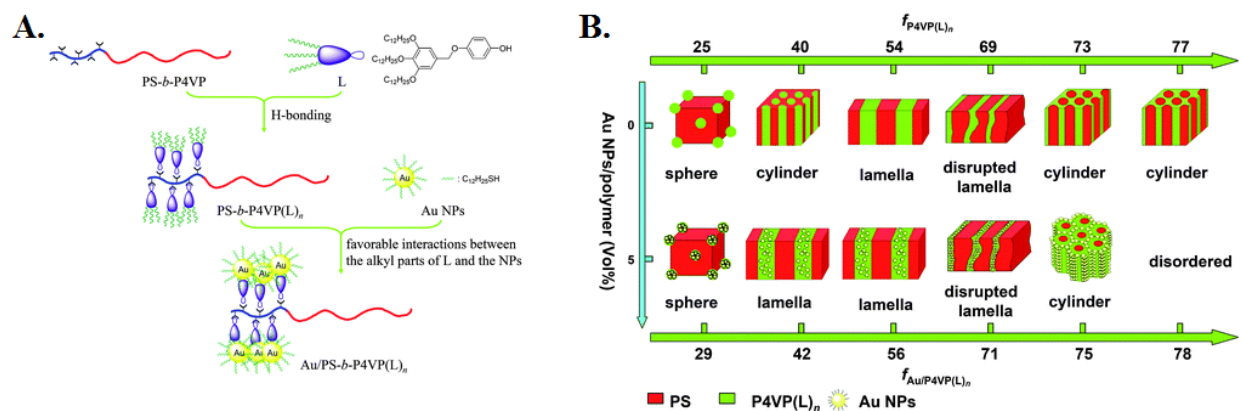


Figure 2.6. Small molecule directed self-assembly of gold NPs in PS-*b*-P4VP: **A.)** Self-assembly mechanism utilizing the fan shaped small molecule L. **B.)** Phase diagram of PS-*b*-P4VP(L)_n-Au NP composites. Adapted from reference 55.

Exploitation of the unique properties of NPs motivates the design of self-assembled NP nanocomposites. Towards the goal of nanoscale bit-patterned magnetic storage devices, Aisso *et al.* investigated the self-assembly behavior of FePt NPs in poly(styrene-*b*-ethylene oxide) (PS-*b*-PEO) thin films (**Figure 2.7**).⁵⁶ They utilized asymmetric PS-*b*-PEO with narrow PDI that assembled into a spherical morphology with PEO domains in a continuous PS matrix to serve as the BCP template for NP assembly. The L1₀-ordered FePt NPs employed in this study display desirable magnetic properties for nanoscale bit-storage applications through large uniaxial magnetocrystalline anisotropy which determines how strongly a particle can retain magnetic information. This large uniaxial magnetocrystalline anisotropy indicates L1₀-ordered FePt NPs as small as 2.8 nm in diameter show potential for permanent data storage.⁵⁷ A ligand exchange

technique yielded L1₀-ordered FePt NPs functionalized with dopamine-terminated-methoxy poly(ethylene oxide) chains (mPEO-Dopa). This enabled the selective self-assembly of the FePt-mPEO-Dopa NPs in the PEO domains through enthalpic compatibilization (**Figure 2.7A**). The authors demonstrated the localized magnetic properties in the nanocomposites through correlating atomic force microscopy (AFM) with magnetic force microscopy (MFM), which revealed magnetic signals arising from NPs confined in the PEO phases (**Figure 2.7B and 2.7C**). This study illustrates how desirable NP properties can be exploited in a nanoscale array.

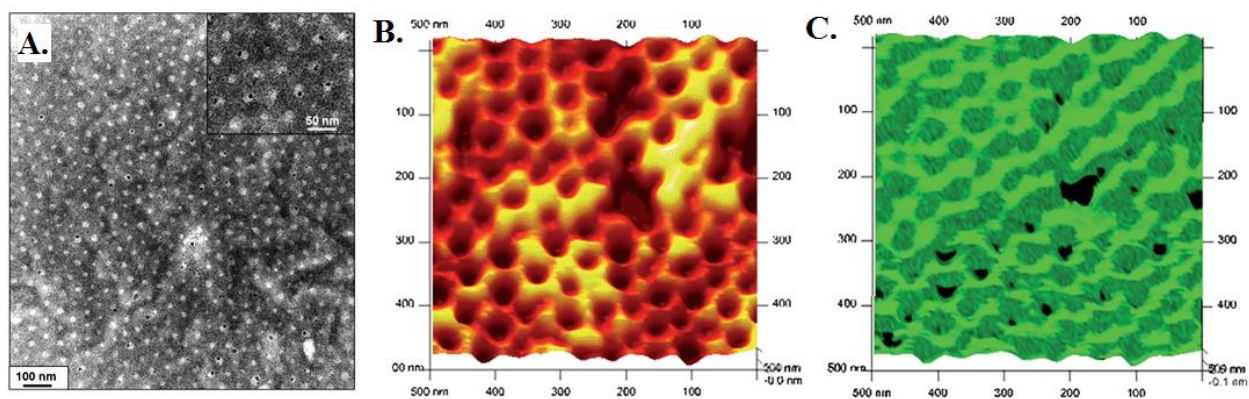


Figure 2.7. Self-assembly of magnetic L1₀-ordered FePt nanoparticles in PS-*b*-PEO BCP thin films: A.) TEM micrograph of PS-*b*-PEO nanocomposite containing 20 wt% FePt NPs (Inset at higher magnification shows the localization of FePt NPs in the PEO domains). B.) 3D topographic AFM image of PS-*b*-PEO nanocomposite containing 20 wt% FePt NPs. C.) Composite image of topography and magnetic phase shows each dark spot (magnetic signal) is contained within one hole corresponding to a PEO/FePt NP domain. Adapted from reference 56.

Ideally, adjusting the morphology of self-assembled BCP-NP nanocomposites enables tunability of macroscale nanocomposite properties. Acharya *et al.* demonstrated the tunability of surface plasmon resonance (SPR) in PS-*b*-P4VP/Au/Ag NP composites through variation of nanocomposite morphology (**Figure 2.8**).⁵⁸ They employed a micellar self-assembly process to form PS-*b*-P4VP micelles in toluene solution with the polar P4VP blocks forming the micelle

core. Silver acetate(AgAc) was loaded into the micelle cores through the interaction of P4VP lone pair electrons with silver ions in AgAc. Dodecanethiol capped Au NPs were incorporated at varying loadings into the micellar solution, and the density of the PS coronas led them to preferentially localize between the micelles. Spin casting the micellar solution and subsequent solvent evaporation led to well-ordered micellar films with pseudo-hexagonal packing. Thermal annealing reduced the AgAc in the micelle cores into Ag NPs. This process formed composites with Ag NPs in the micelle cores regularly spaced from Au NPs assembled at the corona edges, and a high degree of long range order. The investigators tuned the Ag NP-Au NP coupled SPR of the thin films through adjusting the amount of Au NP loaded into the composites. Also, changing the PS block length led to increased Ag-Au NP distance and red-shifted the SPR of the films. This investigation demonstrates how altering the nanocomposite morphology through BCP composition and NP loading can allow for tuning of macroscopic properties.

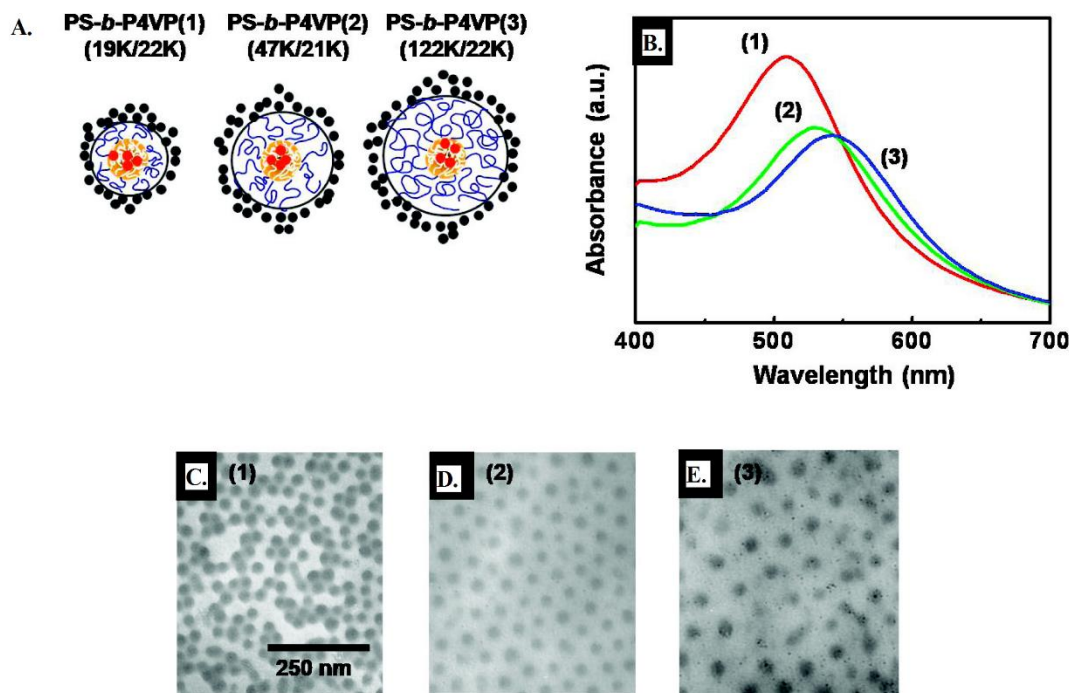


Figure 2.8. Effect of micelle size on surface plasmon resonance in PS-*b*-P4VP/Au/Ag NP composite films cast from micellar solutions. A.) Schematic of interparticle distance affected by BCP composition. B.) UV-Vis spectroscopy showing red-shifting with increased interparticle distance. C.-E.) TEM micrographs of films showing increased micelle-micelle distances in the films with varying BCP composition. Adapted from reference 58.

When employing BCPs to template the self-assembly of NPs, understanding how the NP loading and composite processing affects the overall morphology proves crucial. Kim *et al.* demonstrated how PS-functionalized Au NP loading altered the morphology of poly(styrene-*b*-2-vinylpyridine) (PS-*b*-P2VP) nanocomposites.⁵⁹ Living anionic polymerization yielded low molecular weight thiol-terminated PS with narrow PDI that stabilized Au NPs and facilitated their selective dispersion into PS phases of symmetric, well-defined, narrow PDI PS-*b*-P2VP BCPs. They found that the PS-coated Au NPs behaved similarly to PS homopolymers added to the BCPs and effectively increased PS volume fraction, leading to a shift from lamellar to cylindrical morphology. The Au NP concentration varied depending on the distance from the film-air interface, thus affecting the morphology as a function of the distance from the film-air

surface, with lamellar morphology formed at the top of the film transitioning to cylindrical morphology at the bottom where the Au NP volume fraction was highest. They attributed this behavior to preferential Au NP migration towards the substrate as solvent evaporated from the film. Although these structures represent kinetically trapped states and not equilibrium morphologies, this investigation illustrates how NP loading alters nanocomposite morphology and how processing conditions lead to complex structures appropriate for certain applications.

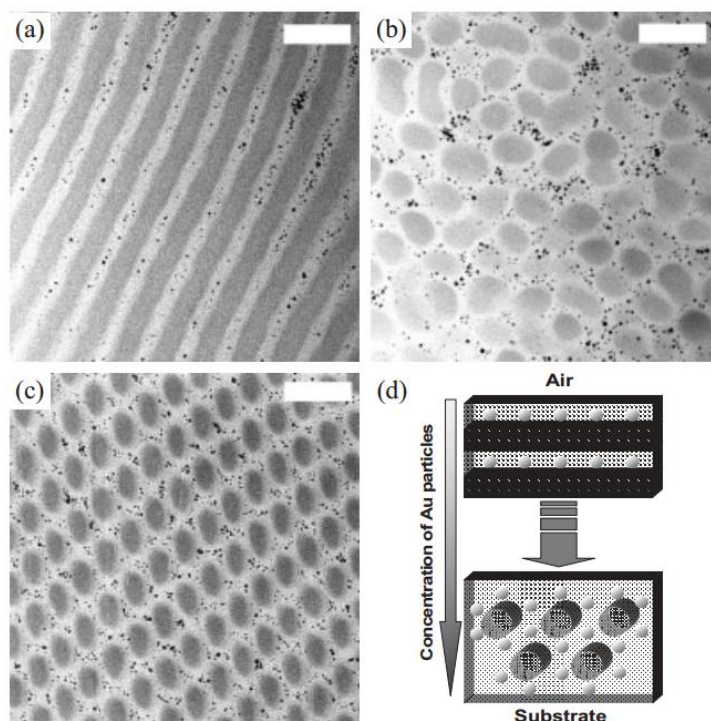


Figure 2.9. TEM images of PS-*b*-P2VP/Au NP nanocomposites with an overall volume fraction of PS-coated Au NPs of 0.3 displaying varying morphology as a function of distance from the top of the film: A.) 27 μm from film surface. B.) 46 μm from film surface. C.) 64 μm from film surface. D.) Schematic of film structure based on TEM images. All scale bars are 100 nm. Adapted from reference 59.

Garcia *et al.* detailed the effect of NP incorporation on the morphology of poly(isoprene-*b*-ethylene oxide) (PI-*b*-PEO) nanocomposites formed with aluminosilicate NPs.⁶⁰ Anionic polymerization afforded PI-*b*-PEO BCPs with varying compositions and narrow PDIs.

Hydrogen bonding and dipole-dipole interactions drove the selective incorporation of aluminosilicate NPs into PEO phases in nanocomposite films effectively forming PEO-NP phases. TEM and SAXS analysis of 64 nanocomposites obtained through adjusting the BCP composition and NP content generated a detailed ternary phase diagram of the nanocomposite system as a function of the weight fraction of each component (**Figure 2.10**). The nanocomposites exhibited morphologies typical to pure PI-*b*-PEO BCPs in addition to morphologies unique to the nanocomposite system that were stabilized by the presence of the NPs. Several compositions exhibited biphasic morphologies that contained regions of each of the neighboring morphologies. Although these structures likely represent kinetically trapped states, this study impressively demonstrates the near complete characterization of a nanocomposite morphology as a function of BCP composition and NP loading.

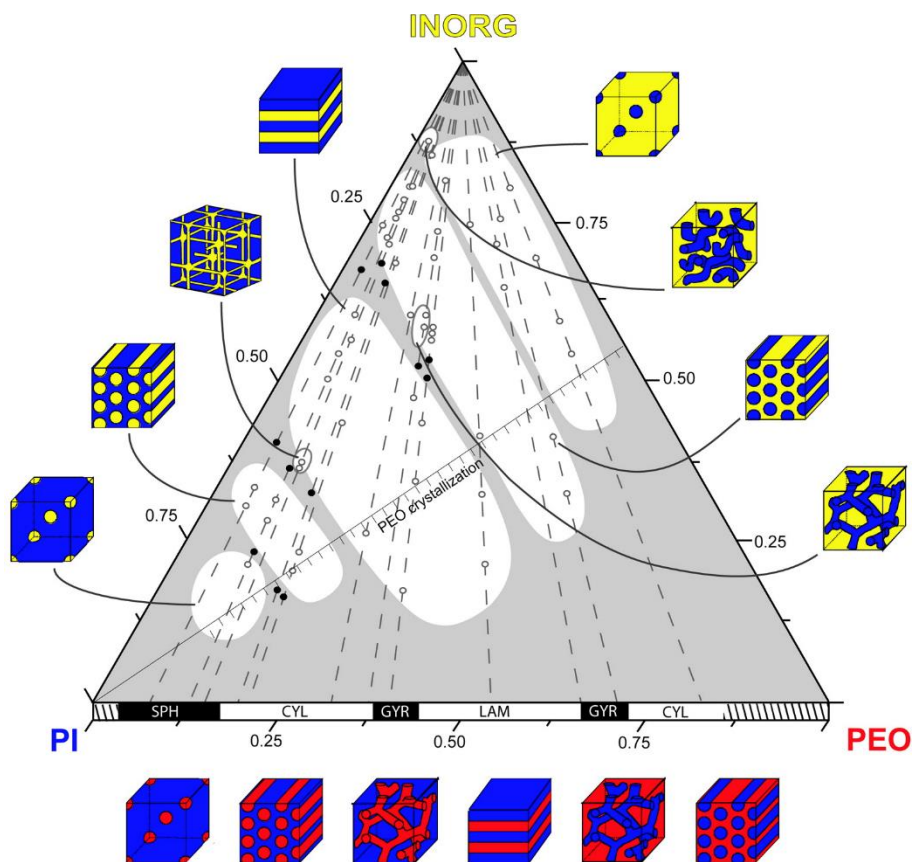


Figure 2.10. Ternary morphology diagram of various PI-b-PEO/aluminosilicate NP nanocomposite compositions (in weight fractions). Schematic representations of the pure BCP morphologies are shown at the bottom, with blue representing the PI domains and red representing the PEO domains. Each white region within the diagram is labeled with a schematic representing the morphology of the formed composites. The yellow regions in these schematic morphologies represent the PEO/NP domains. Closed dark points on a gray background indicate areas where biphasic morphologies were observed. Reproduced from reference 60.

2.6 Carbon Nanomaterial Self-Assembly Strategies in Block Copolymers

Carbon nanomaterials (CNMs) represent a diverse class of materials with a wide range of sizes, shapes, and material properties that prove extremely promising in the field of polymer nanocomposites due to their electrical, thermal, and mechanical properties.⁶¹ CNMs include fullerenes, single-walled carbon nanotubes (SWCNTs), multi-walled carbon nanotubes

(MWCNTs), and carbon nanohorns. These CNMs vary greatly in their size and aspect ratios. The graphene structure in CNMs generates strong van der Waals interactions, which lead to large scale aggregation and inhibit dispersion of CNMs in polymer matrices.⁶² However, this graphene structure also provides ample functionalization capability, leading to a plethora of functionalized CNMs.⁶³⁻⁶⁵ Self-assembly of CNMs is highly dependent on the size and aspect ratio of the NPs, and more research into BCP-mediated self-assembly exists for the relatively small, spherical fullerenes (C_{60} has a diameter of about 1 nm) than SWCNT and MWCNTs. The larger sizes and anisotropy makes self-assembly of carbon nanotubes (CNTs) more difficult to accomplish.^{15,66}

Several investigations demonstrate the ability of BCPs to serve as templates for fullerene self-assembly. Most of these studies aim to develop composites with potential applications in organic solar cells utilizing the electron-accepting capacity of fullerenes. Laiho and coworkers employed the electron-accepting property of fullerenes to affect C_{60} self-assembly in PS-*b*-P4VP (**Figure 2.11**).⁶⁷ They found that composites cast from fresh xylene solutions of PS-*b*-P4VP and led to C_{60} incorporation into the PS domains causing swelling of the continuous PS domains in the observed cylindrical morphology. This occurred because the PS-*b*-P4VP formed micelles with P4VP cores in xylene solution, and the PS and C_{60} affinity for the xylene solvent led to C_{60} incorporation into the PS phase. However, aging the PS-*b*-P4VP/ C_{60} xylene solutions led to C_{60} migration into the P4VP cores caused by a charge transfer between the C_{60} molecules and the 4-vinyl pyridine units as observed in UV-Vis and FT-IR spectroscopic measurements, and altered the observed morphology. Interestingly, instead of swelling the P4VP phase and leading to a lamellar morphology, the composites cast from aged solutions exhibited a spherical morphology. The authors attributed this effect to C_{60} molecules effectively crosslinking many P4VP chains

through the charge-transfer interaction combined with aggregation of C_{60} molecules, leading to condensed P4VP phases.

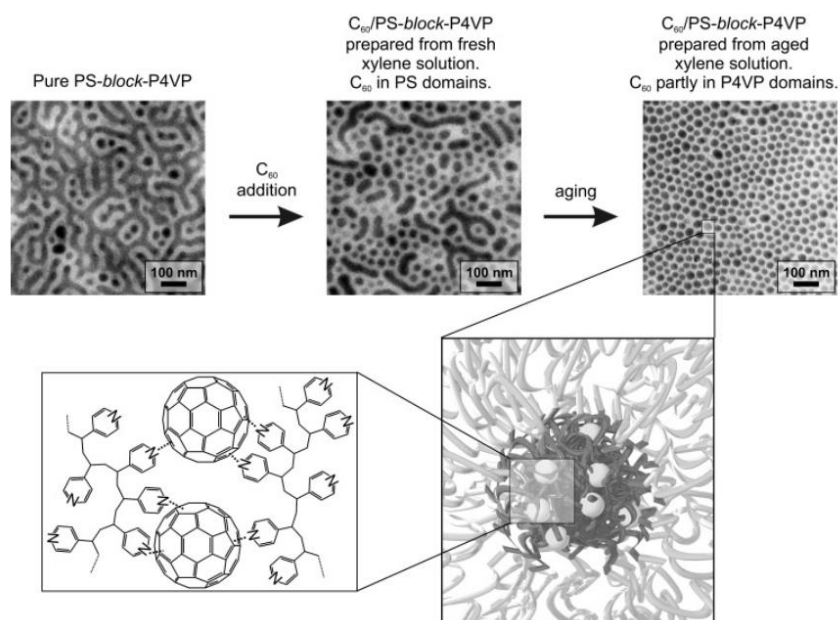


Figure 2.11. Schematic representation of the effect of C_{60} incorporation into PS-*b*-P4VP copolymers. Aging the composite solutions led to C_{60} migration into the P4VP phase through the charge-transfer interaction of C_{60} with 4-vinyl pyridine units. Reprinted from reference 67.

Fullerene self-assembly is also accomplished using polymer or small molecule functionalization leading to enhanced interaction with a specific phase of BCPs.⁶⁸ For example, Schmaltz *et al.* detailed the self-assembly behavior of PS-grafted C_{60} in poly(styrene-*b*-isoprene) and showed morphological dependence on the molecular weight and grafting density.⁶⁹ The PS functionalization allowed for effective fullerene incorporation into the PS domains, and the lamellar morphology was either preserved or altered depending on the molecular weight of the grafted PS. The amount of C_{60} that could be solubilized in the PS domain varied depending on the graft density.

Li and coworkers employed a complimentary hydrogen bonding strategy to direct the self-assembly of C₆₀ in a polythiophene BCP.^{70,71} They achieved strong hydrogen bonding interactions between an isorotac acid-functionalized polythiophene BCP and diaminopyridine fullerene derivative (**Figure 2.12**). The strong complimentary hydrogen bonding allowed for selective fullerene self-assembly. The researchers demonstrated promising device stability, and tuned the resultant morphologies through variation of amount and type of fullerene derivative added to the composites. This technique offers promising opportunities for the design of bulk heterojunction polymer solar cells.

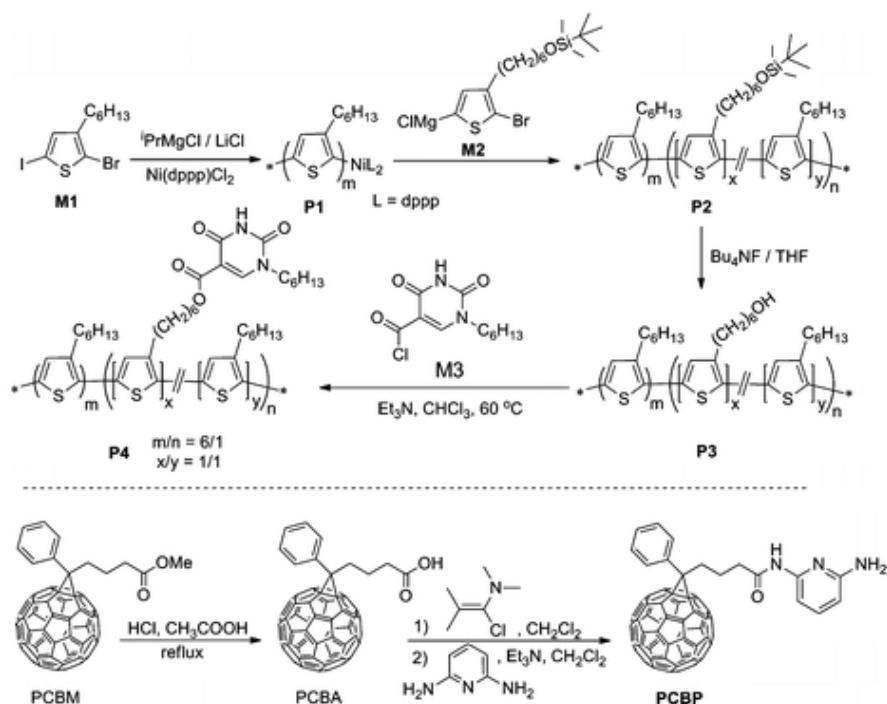


Figure 2.12. Scheme showing the synthesis of a polythiophene BCP and functionalized fullerene capable of ‘three-point’ complimentary hydrogen bonding. Figure adapted from reference 70.

Researchers also employ direct covalent reactions to achieve self-assembled fullerene-BCP nanocomposites.⁷² Min *et al.* recently detailed a versatile application of this approach

(Figure 2.13).⁷³ They utilized specialized anionic polymerization to yield well-defined poly(furfuryl isocyanate-*b*-hexyl isocyanate) (PFIC-*b*-PHIC) BCPs. These BCP displayed composition dependent morphologies which further changed through solvent selection, with solvents common to both blocks yielding different morphologies than solvents selective to one block. The furan ring in furfuryl isocyanate readily undergoes Diels-Alder reaction with dienophiles, such as maleimide and C₆₀. Reacting C₆₀ with the furan functionality resulted in selective incorporation of C₆₀ into the PFIC domains, and the composites retained the BCP morphology to a high degree.

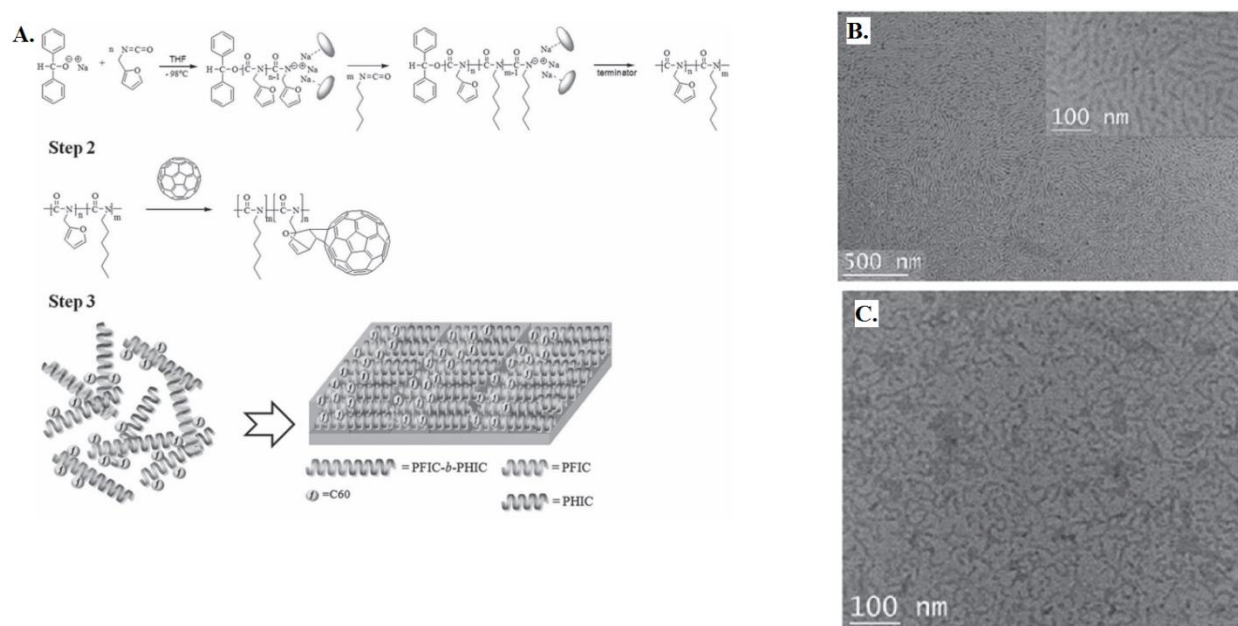


Figure 2.13. Nanocomposites obtained from post-polymerization functionalization of a diene-containing BCP: A.) Scheme for anionic polymerization and post-polymerization functionalization with C₆₀ utilizing the Diels-Alder reaction. B.) TEM micrograph showing the phase-separated morphology of the BCP. C.) TEM micrograph of the BCP/C₆₀ nanocomposite. Adapted from reference 73.

Selective self-assembly of CNTs, especially large MWCNTs, into specific phases of BCPs proves challenging due their anisotropy and relatively large sizes compared to the BCP

domains.¹⁵ The basic strategies for CNT self-assembly in BCPs remain the same as for other NPs, and many investigations explore the use of small molecule and polymer functionalizations to selectively disperse CNTs into BCP phases. Furthermore, CNTs themselves serve as self-assembly templates for various NPs, offering exciting hierarchical assembly possibilities when combined with BCPs.^{74,75} Effective incorporation of CNTs into BCP domains relies on the domain's ability to spatially accommodate the CNTs and depends on the size and aspect ratio of the CNTs. For example, using dodecanethiol as a surfactant Peponi *et al.* demonstrated the selective confinement of octadecylamine functionalized SWCNTs (ODA-SWCNTs) into the PS block of a poly(styrene-*b*-isoprene-*b*-styrene) (PSIS) triblock copolymer.⁷⁶ The incorporation of ODA-SWCNTs changed the self-assembled BCP morphology from cylindrical to lamellar. This strategy relied on the interaction of the alkyl chain functionalized CNTs and the PS blocks through the action of the dodecanethiol surfactant, and was not possible with non-functionalized SWCNTs. In a further study, Peponi and coworkers mapped the placement of ODA-SWCNTs in the PS blocks of the PSIS BCP using electrostatic force microscopy.⁷⁷ In comparison, when Garate *et al.* employed this surfactant aided strategy to disperse PS functionalized MWCNTs into the same PSIS BCP, the larger size of the MWCNTs prevented confinement in PS domains.⁷⁸ Instead the PS functionalized MWCNTs spanned several phases, although non-functionalized MWCNTs aggregated and did not effectively disperse in the PSIS matrix.

Forming composites using CNTs with sizes larger than the BCP matrix domains will in many cases drastically alters the BCP morphology.⁷⁹ Aggregates or individual CNTs impede the formation of the BCP morphology either during solvent evaporation or annealing. Li and coworkers showed how SWNTs affected the self-assembly of poly(flourenylstyrene-*b*-2-vinyl pyridine) BCPs.⁷⁶ Carboxylic acid functionalization of SWCNTs resulted in SWCNT miscibility

with the P2VP phases. They found that two-dimensional lamellar morphologies encapsulated the carboxylic acid functionalized SWCNTs more efficiently than one-dimensional cylindrical morphologies, and composites with lamellar morphology displayed higher conductivity than composites with cylindrical morphologies comprised of P2VP cylinders in a continuous PS phase. The presence of the SWCNTs resulted in changes in the order-order transitions in the BCP, requiring higher temperatures to achieve equilibrium morphologies, and overall the SWCNTs negatively impacted the ordering of the BCP.

Park *et al.* demonstrated the selective sequestration of PS functionalized MWCNTs in the PS phase of a poly(styrene-*b*-isoprene) (PS-*b*-PI) BCP (**Figure 2.14**).⁸⁰ Emulsion polymerization functionalized the MWCNTs with PS, thus compatibilizing the MWCNTs with the PS block. They selected ultra-high molecular weight PS-*b*-PI with narrow PDI that displayed lamellar morphology. The ultra-high molecular weight (760 kg/mol total, 400 kg/mol PS and 360 kg/mol PI blocks) ensured relatively large lamellar phases, minimizing the entropic cost for MWCNT incorporation into these phases. Although the authors reported that some MWCNTs spanned multiple phases, most of the MWCNTs remained in the PS lamellae and no large-scale MWCNT aggregation occurred. The enthalpic compatibilization through PS functionalization and utilization of ultra-high molecular weight BCP to minimize the entropic penalty of selective MWCNT incorporation enabled this degree of selective assembly.

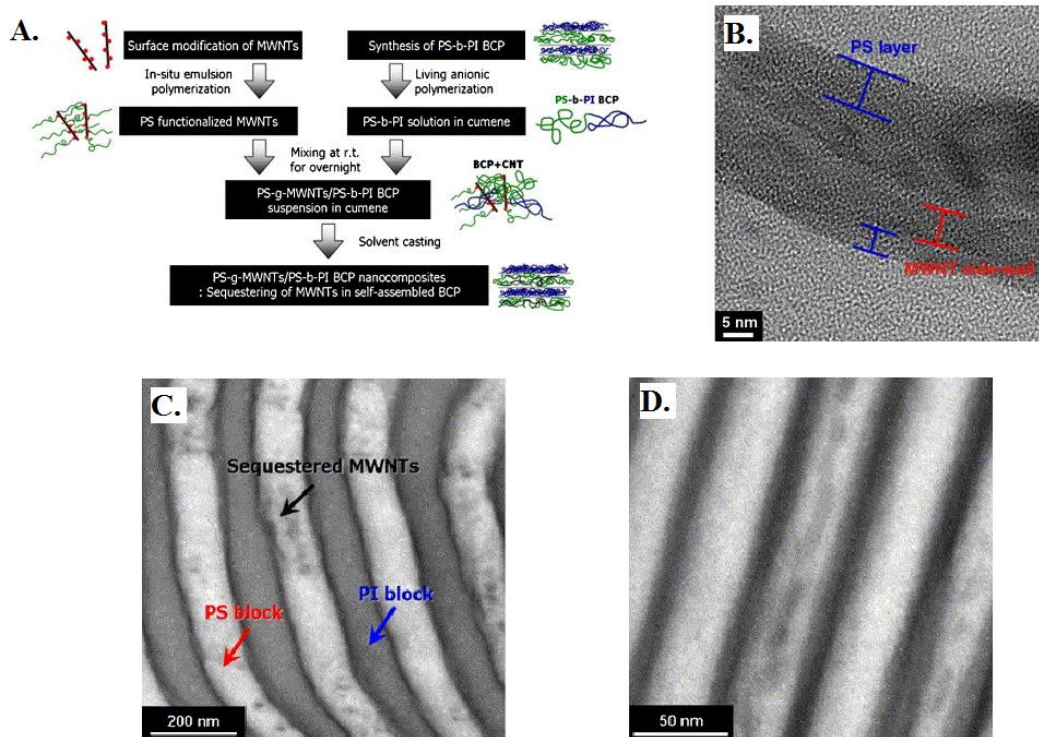


Figure 2.14. Self-assembly of PS functionalized MWCNTs in PS-*b*-PI BCP composites: A.) Schematic of the self-assembly strategy. B.) TEM micrograph of PS functionalized MWCNT showing the PS coverage of the MWCNT. C.) and D.) TEM micrographs of MWCNT sequestration in PS phases (PS domains are light and PI domains are dark). Adapted from reference 80.

Liu and coworkers investigated the selective self-assembly of polymer-functionalized double-walled carbon nanotubes (DWCNTs) in a poly(styrene-*b*-butadiene-*b*-styrene) (PSBS) BCP (**Figure 2.15**).⁸¹ They employed a grafting-to approach to covalently attach polystyrene-*g*-(glycidyl methacrylate-*co*-styrene) to DWCNTs, yielding DWCNTs that were wrapped with PS chains (PS-DWCNTs). The asymmetric BCP with a PS weight fraction of 30% displayed a cylindrical phase-separated morphology after annealing. The PS functionalization of PS-DWCNTs enabled their selective assembly into the PS domains of the PSBS BCP through enthalpic compatibilization. However, the size of the DWCNTs affected this self-assembly. Short PS-DWCNTs (<500 nm in length) were sequestered into the PS domain, and even

conformed their shapes to follow the PS domain structure. Longer PS-DWCNTs (>500 nm in length) were no longer able to self-assemble into the PS phases, and instead spanned multiple phases of the BCP. The authors attributed this behavior to an excessive entropic penalty required to assemble these longer PS-DWCNTs into the relatively smaller PS phases. Interestingly, they also discovered that increasing the molecular weight of the PS grafted onto the DWCNTs did not affect the self-assembly process. The PS chains wrapped around the DWCNTs instead of extending outward as in other types of NPs, where the molecular weight of grafted polymers does affect the self-assembly.

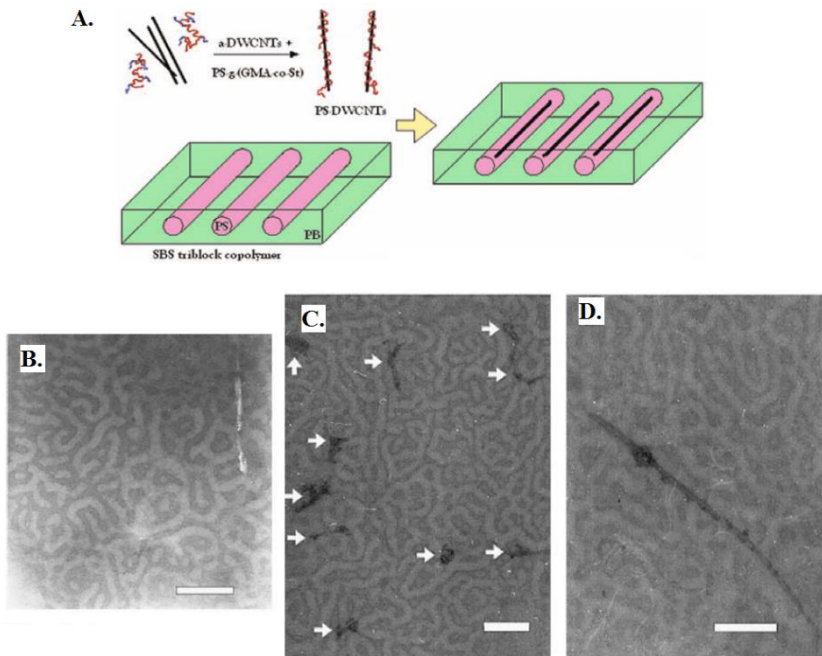


Figure 2.15. Selective self-assembly of DWCNTs in a SBS BCP: A.) Schematic of the self-assembly process. B.) TEM micrograph of the phase separated SBS BCP. C.) PSBS nanocomposite with short (<500 nm) PS-DWCNTs. D.) PSBS nanocomposite with long (>500 nm) PS-DWCNTs. Adapted from reference 81.

2.7 Conclusions

Controlled polymerization techniques facilitate the synthesis of well-defined BCPs, with specified block lengths and narrow PDIs. BCPs phase separate into nanoscale and microscale morphologies with proper BCP design, where the BCP composition and processing determines the morphology. These phase-separated BCP morphologies serve as effective templates for the self-assembly of NPs. Enthalpic compatibilization of NPs with specific BCP phases enables the selective incorporation of NPs into desired phases, with the BCP morphology determining the long-range nanoscale ordering of the NPs. Common strategies to promote this selective self-assembly include functionalizing NPs with compatibilizing ligands, NP-grafted polymers, and the use of small molecules that provide supramolecular interactions between specific BCP phases and NPs. Many investigations demonstrate the ability to self-assemble NPs using BCPs, and several detail the effect of NP incorporation on nanocomposite morphology or illustrate tunability of macroscale properties through nanocomposite design.

Although the results of the past decade in the field of BCP-mediated NP self-assembly are extremely promising, a formidable amount of investigation remains to attain the ultimate goals of NP self-assembly, including emergent properties of nanocomposites. The realization of high-performance self-assembled nanocomposites will rely on the continued interdisciplinary efforts of researchers at the interfaces of polymer synthesis, nanoparticle design, and nanocomposite engineering and fabrication. Applying the fundamental aspects of NP self-assembly in BCPs explored in the past two decades to specific problems and goals in nanocomposite design will lead to materials that fully exploit the desirable properties of NPs and BCPs. Future directions include utilization of three-phase or other morphologically complex systems to expand self-assembly possibilities, and the simultaneous assembly of different NPs

into different BCP phases. BCP-mediated self-assembly of NPs is a diverse and rapidly growing branch in the broadly impactful field of nanocomposite research, and will likely exponentially develop in coming years.

2.8 References

1. Daniel, M.-C.; Astruc, D. *Chem. Rev.* **2004**, *104*, 293.
2. Kelly, K. L.; Coronado, E.; Zhao, L. L.; Schatz, G. C. *The Journal of Physical Chemistry B* **2003**, *107*, 668.
3. El-Sayed, M. A. *Acc. Chem. Res.* **2001**, *34*, 257.
4. Balazs, A. C.; Emrick, T.; Russell, T. P. *Science* **2006**, *314*, 1107.
5. Haynes, C. L.; Van Duyne, R. P. *The Journal of Physical Chemistry B* **2001**, *105*, 5599.
6. Kruis, F. E.; Fissan, H.; Peled, A. *J. Aerosol Sci* **1998**, *29*, 511.
7. Saunders, B. R.; Turner, M. L. *Adv. Colloid Interface Sci.* **2008**, *138*, 1.
8. Salata, O. V. *Journal of nanobiotechnology* **2004**, *2*, 3.
9. Hussain, F.; Hojjati, M.; Okamoto, M.; Gorga, R. E. *J. Compos. Mater.* **2006**, *40*, 1511.
10. Tjong, S. C. *Materials Science and Engineering: R: Reports* **2006**, *53*, 73.
11. Kashiwagi, T.; Grulke, E.; Hilding, J.; Groth, K.; Harris, R.; Butler, K.; Shields, J.; Kharchenko, S.; Douglas, J. *Polymer* **2004**, *45*, 4227.
12. Leszczyńska, A.; Njuguna, J.; Pielichowski, K.; Banerjee, J. R. *Thermochim. Acta* **2007**, *453*, 75.
13. Alexandridis, P.; Lindman, B. *Amphiphilic block copolymers: self-assembly and applications*; Elsevier, 2000.
14. Schacher, F. H.; Ruper, P. A.; Manners, I. *Angew. Chem. Int. Ed.* **2012**, *51*, 7898.
15. Bockstaller, M. R.; Mickiewicz, R. A.; Thomas, E. L. *Adv. Mater.* **2005**, *17*, 1331.
16. Pochan, D. J.; Zhu, J.; Zhang, K.; Wooley, K. L.; Miesch, C.; Emrick, T. *Soft Matter* **2011**, *7*, 2500.
17. Li, W.; Liu, S.; Deng, R.; Zhu, J. *Angew. Chem.* **2011**, *123*, 5987.
18. Wang, J.; Li, W.; Zhu, J. *Polymer* **2014**, *55*, 1079.
19. Bates, F. S.; Fredrickson, G. H. *Physics today* **2008**, *52*, 32.
20. Hamley, I. W.; Wiley, J. *Developments in block copolymer science and technology*; Wiley Online Library, 2004.
21. Elabd, Y. A.; Napadensky, E.; Walker, C. W.; Winey, K. I. *Macromolecules* **2006**, *39*, 399.
22. Harrison, W. L.; Hickner, M. A.; Kim, Y. S.; McGrath, J. E. *Fuel cells* **2005**, *5*, 201.
23. Aoshima, S.; Kanaoka, S. *Chem. Rev.* **2009**, *109*, 5245.
24. Morton, M. *Anionic polymerization: principles and practice*; Elsevier, 1983.
25. Hawker, C. J.; Bosman, A. W.; Harth, E. *Chem. Rev.* **2001**, *101*, 3661.
26. Chiefari, J.; Chong, Y. K.; Ercole, F.; Krstina, J.; Jeffery, J.; Le, T. P. T.; Mayadunne, R. T. A.; Meijs, G. F.; Moad, C. L.; Moad, G. *Macromolecules* **1998**, *31*, 5559.
27. Matyjaszewski, K.; Xia, J. *Chem. Rev.* **2001**, *101*, 2921.
28. Lynd, N. A.; Meuler, A. J.; Hillmyer, M. A. *Prog. Polym. Sci.* **2008**, *33*, 875.

29. Widin, J. M.; Schmitt, A. K.; Schmitt, A. L.; Im, K.; Mahanthappa, M. K. *J. Am. Chem. Soc.* **2012**, *134*, 3834.
30. Widin, J. M.; Kim, M.; Schmitt, A. K.; Han, E.; Gopalan, P.; Mahanthappa, M. K. *Macromolecules* **2013**, *46*, 4472.
31. Rogers, M. E.; Long, T. E. *Synthetic methods in step-growth polymers*; Wiley Online Library, 2003.
32. Orilall, M. C.; Wiesner, U. *Chem. Soc. Rev.* **2011**, *40*, 520.
33. Mai, Y.; Eisenberg, A. *Chem. Soc. Rev.* **2012**, *41*, 5969.
34. Khandpur, A. K.; Foerster, S.; Bates, F. S.; Hamley, I. W.; Ryan, A. J.; Bras, W.; Almdal, K.; Mortensen, K. *Macromolecules* **1995**, *28*, 8796.
35. Matsen, M. W.; Schick, M. *Current Opinion in Colloid & Interface Science* **1996**, *1*, 329.
36. Clauss, J.; Schmidt-Rohr, K.; Spiess, H. W. *Acta Polym.* **1993**, *44*, 1.
37. Matsen, M. W.; Thompson, R. B. *The Journal of chemical physics* **1999**, *111*, 7139.
38. Song, C. X.; Feng, X. D. *Macromolecules* **1984**, *17*, 2764.
39. Li, Z.; Kesselman, E.; Talmon, Y.; Hillmyer, M. A.; Lodge, T. P. *Science* **2004**, *306*, 98.
40. Yamauchi, K.; Takahashi, K.; Hasegawa, H.; Iatrou, H.; Hadjichristidis, N.; Kaneko, T.; Nishikawa, Y.; Jinnai, H.; Matsui, T.; Nishioka, H. *Macromolecules* **2003**, *36*, 6962.
41. Mogi, Y.; Nomura, M.; Kotsuji, H.; Ohnishi, K.; Matsushita, Y.; Noda, I. *Macromolecules* **1994**, *27*, 6755.
42. Tanaka, Y.; Hasegawa, H.; Hashimoto, T.; Ribbe, A.; Sugiyama, K.; Hirao, A.; Nakahama, S. *Polym. J.* **1999**, *31*, 989.
43. Li, Z.; Hillmyer, M. A.; Lodge, T. P. *Langmuir* **2006**, *22*, 9409.
44. Hasegawa, H. *Complex Macromolecular Architectures: Synthesis, Characterization, and Self-Assembly* **2011**, 569.
45. Bates, F. S.; Hillmyer, M. A.; Lodge, T. P.; Bates, C. M.; Delaney, K. T.; Fredrickson, G. H. *Science* **2012**, *336*, 434.
46. Kao, J.; Thorkelsson, K.; Bai, P.; Rancatore, B. J.; Xu, T. *Chem. Soc. Rev.* **2013**, *42*, 2654.
47. Bockstaller, M. R.; Lapetnikov, Y.; Margel, S.; Thomas, E. L. *J. Am. Chem. Soc.* **2003**, *125*, 5276.
48. Huh, J.; Ginzburg, V. V.; Balazs, A. C. *Macromolecules* **2000**, *33*, 8085.
49. Thompson, R. B.; Ginzburg, V. V.; Matsen, M. W.; Balazs, A. C. *Science* **2001**, *292*, 2469.
50. Sperling, R. A.; Parak, W. J. *Philosophical Transactions of the Royal Society A: Mathematical, Physical and Engineering Sciences* **2010**, *368*, 1333.
51. Warren, S. C.; Messina, L. C.; Slaughter, L. S.; Kamperman, M.; Zhou, Q.; Gruner, S. M.; DiSalvo, F. J.; Wiesner, U. *Science* **2008**, *320*, 1748.
52. Xu, C.; Ohno, K.; Ladmiral, V.; Milkie, D. E.; Kikkawa, J. M.; Composto, R. J. *Macromolecules* **2009**, *42*, 1219.
53. Ruokolainen, J.; Saariaho, M.; Ikkala, O.; ten Brinke, G.; Thomas, E. L.; Torkkeli, M.; Serimaa, R. *Macromolecules* **1999**, *32*, 1152.
54. Zhao, Y.; Thorkelsson, K.; Mastroianni, A. J.; Schilling, T.; Luther, J. M.; Rancatore, B. J.; Matsunaga, K.; Jinnai, H.; Wu, Y.; Poulsen, D. *Nature materials* **2009**, *8*, 979.
55. Ye, T.; Chen, X.; Fan, X.; Shen, Z. *Soft Matter* **2013**, *9*, 4715.
56. Aissou, K.; Alnasser, T.; Pecastaings, G.; Goglio, G.; Toulemonde, O.; Mornet, S.; Fleury, G.; Hadziioannou, G. *Journal of Materials Chemistry C* **2013**, *1*, 1317.

57. Sun, S.; Fullerton, E. E.; Weller, D.; Murray, C. B. *Magnetics, IEEE Transactions on* **2001**, *37*, 1239.
58. Acharya, H.; Sung, J.; Sohn, B.-H.; Kim, D. H.; Tamada, K.; Park, C. *Chem. Mater.* **2009**, *21*, 4248.
59. Kim, B. J.; Chiu, J. J.; Yi, G. R.; Pine, D. J.; Kramer, E. J. *Adv. Mater.* **2005**, *17*, 2618.
60. Garcia, B. C.; Kamperman, M.; Ulrich, R.; Jain, A.; Gruner, S. M.; Wiesner, U. *Chem. Mater.* **2009**, *21*, 5397.
61. Sahoo, N. G.; Rana, S.; Cho, J. W.; Li, L.; Chan, S. H. *Prog. Polym. Sci.* **2010**, *35*, 837.
62. Chen, Q.; Saliel, C.; Manickavasagam, S.; Schadler, L. S.; Siegel, R. W.; Yang, H. *J. Colloid Interface Sci.* **2004**, *280*, 91.
63. Georgakilas, V.; Kordatos, K.; Prato, M.; Guldi, D. M.; Holzinger, M.; Hirsch, A. *J. Am. Chem. Soc.* **2002**, *124*, 760.
64. Shim, M.; Shi Kam, N. W.; Chen, R. J.; Li, Y.; Dai, H. *Nano Lett.* **2002**, *2*, 285.
65. Ma, P.-C.; Siddiqui, N. A.; Marom, G.; Kim, J.-K. *Composites Part A: Applied Science and Manufacturing* **2010**, *41*, 1345.
66. Wang, J.; Li, F.; Li, Q.; Sun, J.; Chen, G.-X. *Thin Solid Films* **2013**, *536*, 191.
67. Laiho, A.; Ras, R. H. A.; Valkama, S.; Ruokolainen, J.; Österbacka, R.; Ikkala, O. *Macromolecules* **2006**, *39*, 7648.
68. Wang, J.; Chen, G.-X.; Sun, J.; Li, Q. *The Journal of Physical Chemistry B* **2011**, *115*, 2824.
69. Schmaltz, B.; Brinkmann, M.; Mathis, C. *Macromolecules* **2004**, *37*, 9056.
70. Li, F.; Yager, K. G.; Dawson, N. M.; Yang, J.; Malloy, K. J.; Qin, Y. *Macromolecules* **2013**, *46*, 9021.
71. Li, F.; Yang, J.; Qin, Y. *J. Polym. Sci., Part A: Polym. Chem.* **2013**, *51*, 3339.
72. Barrau, S.; Heiser, T.; Richard, F.; Brochon, C.; Ngov, C.; van de Wetering, K.; Hadziioannou, G.; Anokhin, D. V.; Ivanov, D. A. *Macromolecules* **2008**, *41*, 2701.
73. Min, J.; Shah, P. N.; Chae, C.-G.; Lee, J.-S. *Macromol. Rapid Commun.* **2012**, *33*, 2029.
74. Tang, Z.; Kotov, N. A. *Adv. Mater.* **2005**, *17*, 951.
75. Correa-Duarte, M. A.; Liz-Marzán, L. M. *J. Mater. Chem.* **2006**, *16*, 22.
76. Peponi, L.; Valentini, L.; Torre, L.; Mondragon, I.; Kenny, J. M. *Carbon* **2009**, *47*, 2474.
77. Peponi, L.; Tercjak, A.; Gutierrez, J.; Cardinali, M.; Mondragon, I.; Valentini, L.; Kenny, J. M. *Carbon* **2010**, *48*, 2590.
78. Garate, H.; Fascio, M. L.; Mondragon, I.; D'Accorso, N. B.; Goyanes, S. *Polymer* **2011**, *52*, 2214.
79. Saint-Aubin, K.; Poulin, P.; Jaillet, C.; Maugey, M.; Zakri, C. *Polymer* **2013**, *54*, 2285.
80. Park, I.; Lee, W.; Kim, J.; Park, M.; Lee, H. *Sensors and Actuators B: Chemical* **2007**, *126*, 301.
81. Liu, Y.-T.; Zhang, Z.-L.; Zhao, W.; Xie, X.-M.; Ye, X.-Y. *Carbon* **2009**, *47*, 1883

Chapter 3: Hydrogen Bond Containing Multi-walled Carbon Nanotubes in Polyurethane Composites

David L. Inglefield, Jr.^a, Robert J. Bodnar^b, and Timothy E. Long^{ac}

^a*Department of Chemistry*, ^b*Department of Geosciences*, ^c*Macromolecules and Interfaces Institute*

Virginia Tech, Blacksburg, VA 24061

3.1 Abstract

Introduction of hydrogen bonding sites onto multi-walled carbon nanotubes (MWCNTs) included oxidized, amide-amine, and novel amide-urea MWCNTs for the formation of homogenous polyurethane composites. Acid oxidation and subsequent derivatization introduced hydrogen bonding functionality onto MWCNTs to compare the effect of surface functionalization on mechanical properties in a 45 wt% hard segment polyurethane matrix. Raman spectroscopy showed an increase in the D/G peak ratio, which indicated successful oxidation. X-ray photoelectron spectroscopy (XPS) also revealed elemental compositions that supported each step of the functionalization strategy. Thermogravimetric analysis (TGA) supported functionalization with an increase in weight loss for each functionalization, and the MWCNT surface functionalization determined pH dependent dispersibility. The non-functionalized MWCNT composites showed poor dispersion with transmission electron microscopy (TEM), and in sharp contrast, the functionalized composites displayed homogenous dispersions. Tensile testing revealed improved stress at break in the functionalized MWCNT composites at low loadings due to homogenous dispersion.

3.2 Introduction

The unique electrical,¹ thermal,^{2,3} optical,^{4,5} and mechanical^{6,7} properties of carbon nanotubes (CNTs) account for intense research since their discovery in 1991.⁸ Although a number of factors limit their full potential, researchers continue to demonstrate a wide variety of applications including energy storage,^{9,10} high performance electrical materials,¹¹ and composites.^{12,13} The field of polymer-carbon nanotube composites represents one of the most promising and active areas in CNT research.¹⁴ CNTs are attractive fillers due to their ability to enhance the electrical and mechanical properties of the polymer matrix.^{15,16} The hydrophobic structure of CNTs limits the efficacy of CNT polymer composites, causing aggregation through van der Waals interactions, which reduces CNT interactions with polymer matrices leading to poor composite properties.¹⁷ Increasing dispersion and interfacial interactions within a polymer matrix allows for improved mechanical and electrical properties because the desirable mechanical properties are possessed by non-aggregated CNTs, and effective interactions improve interfacial strength and assist in CNT dispersion through interacting with polymer chains during dispersion.¹⁸

Modification with either covalent or non-covalent sites on the CNT surface¹⁹ is an essential strategy for attaining dispersion and suitable polymer composites, particularly for matrices of polar polymers²⁰. Typically, the introduction of surface bound polymers or functionalities increases the CNTs dispersion through non-covalent intermolecular interactions or covalent bonding with the polymer matrix. MWCNTs are particularly promising for structural composites due to the opportunity for highly functionalized outer walls while retaining the structure of the inner walls.²¹ Researchers introduced hydrogen bonding groups onto CNTs through a number of functionalization techniques to increase CNT interaction with polar

polymers or solvents. Acid oxidation²²⁻²⁴ of CNTs introduces hydrogen bonding carboxylic acid sites, increasing CNT dispersibility in a number of polymers.²⁵⁻²⁷ Further reacting these sites provides a myriad of functionalized CNTs using efficient carboxylic acid chemistry. Reactions of nucleophiles such as diamines with the carboxylic acid sites through an acyl chloride precursor or carbodiimide coupling is typical.^{28,29} Pulikkathara et al. also reported the synthesis of urea-functionalized, single-walled carbon nanotubes (SWCNTs) through a hydrofluoric acid route.³⁰ The reaction of urea with fluorinated CNTs yielded a high degree of urea functionality and retained a high level of sidewall fluorination. The urea-functionalized CNTs showed improved dispersion over the fluorinated precursor in an epoxy resin. The urea groups on the SWCNT surface also served as curing sites for the epoxy resin, which led to improved dispersion through covalent bonding.

The mechanical properties, efficient synthesis, and high tailorability of segmented compositions make segmented polyurethanes an industrially and academic valued class of polymers. The prepolymer method³¹ allows for incorporation of hard and soft segments that often lead to microphase separated elastomeric materials.^{32,33} The structural diversity and desirable properties associated with polyurethanes make them a promising candidate for polymeric composites, but the highly polar character of polyurethanes requires proper functionalization of CNTs for homogenous composite formation. Many techniques allow for improved CNT dispersion in polyurethanes, which include non-covalent means using dispersing agents and *in situ* polymerization,³⁴ covalent incorporation achieved through amine functionalized CNTs present in the polyurethane reaction mixture,^{29,35} and non-covalent dispersion of CNTs functionalized with low molecular weight and polymeric functionality.³⁶⁻³⁸

CNTs improved the properties of polyurethanes with varied effects on composite mechanical and electrical properties due to the rich diversity of polyurethanes and CNTs.

Long et al. recently reported the successful synthesis of novel dendritic ammonium functionalized MWCNTs and demonstrated successful dispersion in a charged polyurethane matrix.³⁹ In a sulfonated soft segment polyurethane⁴⁰, permanently charged MWCNTs showed better dispersibility than pristine controls. This demonstrated that tailored functionality improved the dispersion of MWCNTs in the polymer matrix using electrostatic interactions. In the present study, functionalization of MWCNTs through acid oxidation to form amide-amine and novel amide-urea derivatives enabled homogenous MWCNT dispersion in a polyurethane matrix. Raman spectroscopy, TGA, and XPS confirmed successful functionalization. Comparison of the dispersibility of the functionalized MWCNTs to non-functionalized MWCNTs required TEM analysis and an investigation of thermal stability and mechanical properties as a function of surface functionality at various MWCNT loadings. Functionalized MWCNT composites showed a significant improvement of mechanical properties and improved dispersibility compared to non-functionalized MWCNT composites.

3.3 Experimental

Materials

Ethylene diamine (99.5%), thionyl chloride (99%), and n-heptyl isocyanate (97%), were purchased from Sigma Aldrich and used as received. Poly(tetramethylene oxide) (PTMO, Terathane®, $M_n = 2272$ g/mol as determined from hydroxyl titration) was purchased from Sigma Aldrich and dried *in vacuo* overnight. Triethyl amine (99%) and 1,4-butanediol (BDO) (99%) were purchased from Sigma Aldrich and distilled from calcium hydride prior to use. Dibutyltin

dilaurate (95%) was purchased from Sigma Aldrich and diluted to a 1 wt% solution in anhydrous tetrahydrofuran (THF). Dimethylformamide (DMF) and THF were purchased from Fischer Scientific and passed through an Innovative Technology, Inc. PureSolv solvent purification system to remove impurities and water. Concentrated nitric acid (ACS Reagent Plus) and concentrated hydrochloric acid (ACS Reagent Plus) were obtained from Fischer Scientific and used as received. Pristine multi-walled carbon nanotubes (Baytubes®, C70P, carbon purity > 95%, outer diameter: 10-30 nm, catalyst: cobalt metal nanoparticle) and dicyclohexylmethane-4,4'-diisocyanate (HMDI) (99.5%) were supplied through Bayer and used as received. All MWCNTs were gently powderized before sonication. All dry MWCNTs were handled with care and the proper protective equipment, including respirators.

Instrumentation

Size exclusion chromatography (SEC) was performed using a Waters size exclusion chromatograph equipped with an auto sampler, three 5 μm PLgel Mixed-C columns, a Waters 2410 refractive index detector operating at 880 nm, and a Wyatt Technologies miniDAWN multi-angle laser light scattering detector operating at 690 nm. Samples were run at 50 °C in 0.01 M LiBr DMF solution with a flow rate of 1 mL/min. The specific refractive index increment values (dn/dc) for the polyurethane sample were determined with a Wyatt Optilab T-rEX refractive index detector operating at 658 nm and 35 °C. Polymer unimers in 0.01 M LiBr DMF solution were confirmed through dynamic light scattering using a Malvern Zetasizer Nano ZS. XPS analysis was performed on a Phi Quantera Scanning XPS Microprobe. XPS data was analyzed using CASA XPS software version 2.3.14. Raman spectroscopy was performed using a JY Horiba LabRam HR800 Raman Spectrometer with a 514 nm argon laser. Raman spectra were analyzed and deconvoluted in Labspec Raman software version 5.25.15. TGA was

performed using a TA Instruments HiRes 2950 thermogravimetric analyzer using a ramp rate of 10 °C/min under a nitrogen atmosphere. Sonication was performed with a Branson 2510R-MTH sonicator bath or a Hielscher UP400S Ultrasonicator probe (only for water dispersion tests), both operating at full capacity. Dynamic mechanical analysis (DMA) was performed on a TA Instruments Q800 dynamic mechanical analyzer using a heating rate of 3 °C/min and an amplitude of 50 µm in tension mode. Tensile data was collected on an Instron 5500 R using a ramp rate of 50 mm/min. The tensile samples were cut using a Pioneer Dietec dog bone cutter (ASTM D-638-V) and 6 trials were performed for all samples. Cryo ultramicrotomy was performed with a Diatome MT12610 diamond blade on a RMC Products Powertome PC ultramicrotome equipped with a RX cryo attachment cutting 100 nm sections. TEM images were generated using a Phillips EM 420 transmission electron microscope operating at 100 kV accelerating voltage.

MWCNT Functionalization

Acid oxidized MWCNTs (AO-MWCNTs, **Scheme 3.1-b**) were prepared with as received Baytubes® C70P using nitric acid. For a typical procedure, in a 2-L, round-bottomed, flask equipped with a magnetic stirrer, pristine Baytubes (12 g, C70P, **Scheme 3.1-a**) were dispersed at 1 wt% in 8 M HNO₃ (1200 mL) using the sonicator probe and magnetic stirring for 1.5 h. This mixture was refluxed at 110 °C for 72 h and allowed to cool to room temperature. The reaction mixture was diluted with deionized (DI) water and decanted several times. The MWCNTs were subsequently filtered and washed with DI water until the filtrate reached a neutral pH. In a 2-L, round-bottomed, flask equipped with magnetic stir bar, the resulting MWCNTs were dispersed in 1 M HCl (1200 mL) through sonication and stirred for 1 h at 110 °C reflux for 16 h to ensure protonation of carboxylic acid groups. The MWCNTs were rinsed

with DI water and decanted several times, then washed with DI water until the filtrate reached a neutral pH. The MWCNTs were rinsed with isopropyl alcohol (200 mL) to aid in the drying process. The resulting AO-MWCNTs were then dried at 60 °C *in vacuo* until they achieved a constant weight after 36 h.

Amide-amine functionalized MWCNTs (AA-MWCNTs, **Scheme 3.1 – d**) were prepared according to the following procedure. In a 250-mL, round-bottomed, flask equipped with magnetic stir bar, AO-MWCNTs (3.5 g) were dispersed in thionyl chloride (80 mL) through sonication for 2 h under an inert argon atmosphere and then refluxed at 80 °C for 16 h. The excess thionyl chloride was removed with distillation, leaving behind the acid chloride functionalized MWCNTs (**Scheme 3.1-c**). A solution of 3.8 mL ethylenediamine and 8 mL triethylamine in 200 mL of dry DMF was cannulated into the reaction solution dropwise under magnetic stirring and argon purge over 1 h. After this addition, the reaction mixture was homogenized through sonication for 2 h, then the reaction was allowed to proceed for 48 h at 25 °C under magnetic stirring. The reaction was diluted with DMF (200 mL) and filtered. The MWCNTs were rinsed with DMF (500 mL), DI water (300 mL), and finally isopropyl alcohol (200 mL). The resulting AA-MWCNTs were dried at 60 °C *in vacuo* for 36 h until a constant weight was achieved.

Amide-urea functionalized MWCNTs (AU-MWCNTs) were synthesized according to the following procedure. In a 250-mL, round-bottomed, flask equipped with magnetic stirrer, AA-MWCNTs (2g) were dispersed in a mixture of dry DMF (50 mL) and heptyl isocyanate (4 g) through sonication for 2 h under an argon purge. The reaction was stirred at 25 °C for 48 h, then diluted with DMF (100 mL) and filtered. The MWCNTs were rinsed with DMF (300 mL), and

then chloroform (300 mL) to aid in the drying process. The resulting AU-MWCNTs were dried at 60 °C *in vacuo* for 36 h until a constant weight was observed.

Purified MWCNTs, which serve as an important control, were prepared according to the following procedure. Pristine MWCNTs (5 g) were dispersed in 1 M HCl (500 mL) through sonication in a round-bottomed flask equipped with magnetic stir bar. The MWCNTs were then refluxed at 110 °C for 16 h, ensuring removal of metal catalyst nanoparticles and amorphous carbon impurities.⁴¹ The MWCNTs were diluted with DI water and decanted several times, and rinsed with DI water until the filtrate was neutral. Then, the MWCNTs were rinsed with isopropyl alcohol to aid in the drying process. The resulting purified MWCNTs were dried at 60 °C *in vacuo* until they achieved a constant weight after 36 h.

Composite Formation and Water Dispersion Test

A three-necked, round-bottomed flask equipped with addition funnels and mechanical stirrer was charged with 2k PTMO (29.58 g), dibutyltin dilaurate (10 wt % in THF, 50 ppm), and HMDI (22.05 g) in an addition funnel. After 30 min of argon purge, HMDI was added dropwise and allowed to react for 4 h at 80 °C under argon and mechanical stirring. BDO (6.80 g) in dry DMF (255 mL, 20 wt% total solids) was added to an addition funnel and allowed to purge with argon for 1 h. BDO in DMF was added dropwise over the course of 30 min and the polymerization proceeded for 24 h at 80 °C. The solution was stirred at room temperature for a day and then stored in glass jars for film casting and composite formation.

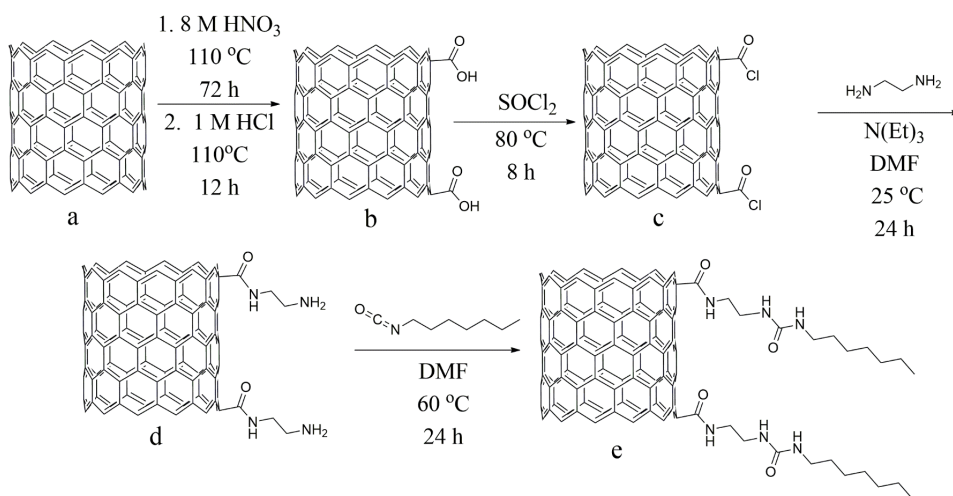
MWCNTs were dispersed into the polymer solution using the following procedure: MWCNTs were dispersed in DMF (1.5 mL) through sonication for 30 min. The polymer solution (4.65 g of 20 wt% polymer in DMF) was added and stirred magnetically for 30 min. The entire mixture was again sonicated in the sonicator bath for 100 min. The composite

mixtures were then immediately cast as films. All films and composites were cast using the same method and had an identical same thermal history prior to testing. Polymer or composite solutions were cast onto glass plates and placed in a drying oven at 80 °C and dried for 2 h, then for 5 h *in vacuo* at 80 °C. Soaking the films in water for 5 min and then gently peeling them from the glass allowed for removal from the glass plates. The films air dried for 48 h before testing. The wt% of MWCNTs in the sample is reported relative to the polymer weight.

For the water dispersion test, all MWCNT samples were dispersed using the sonicator probe for 15 min in a glass vial and allowed to settle for 5 min before observation. The test was conducted in reverse osmosis (RO) purified water with a of pH 6.8, and RO water adjusted to pH 3 upon addition of HCl or pH 11 with the addition of NaOH. The vials were observed for several months to monitor dispersion stability.

3.4 Results and Discussion

MWCNT Functionalization and Characterization



Scheme 3.1. Surface functionalization for the synthesis of urea functionalized MWCNTs.

Acid oxidation introduced hydrogen bonding sites to the sidewalls of MWCNTs as depicted in **Scheme 3.1**. A large excess of reagents for each functionalization promoted reaction of the MWCNTs, and thorough rinsing and drying removed unreacted reagents. TGA showed the weight loss upon heating of the functionalized MWCNTs and supported successful functionalization (**Figure 3.1**). The functionalized MWCNTs had an onset of weight loss near 200 °C, which corresponded to the onset of decarboxylation of the carboxyl sites.⁴² The non-functionalized MWCNTs demonstrated excellent thermal stability to 500 °C. The purified MWCNTs showed less weight loss at high temperatures than the pristine MWCNTs because the acid wash removed metal catalyst nanoparticles and carbonaceous fragments that degrade at high temperatures.⁴¹ Acid oxidation had the same effect of purifying and removing metal catalyst particles as the purification procedure because the second step of the acid oxidation was identical to the purification technique. Furthermore, the functionalized MWCNTs showed an increased weight loss in the 200-500 °C range for each additional functionalization step, supporting successful functionalization with organic substituents.

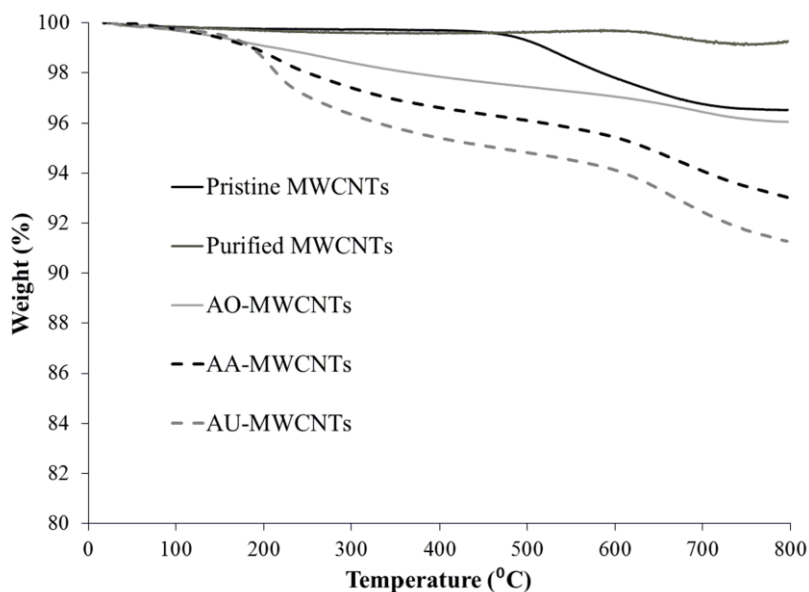


Figure 3.1. Thermogravimetric analysis of MWCNTs.

Raman spectroscopy supported successful functionalization according to the ratios of the D (or disorder) peaks to the G (or order) peak areas shown in **Table 3.1** (Raman spectra, **Figure 3.2**). Phonons arising from the perfect order in the graphene lattice result in the G peak positioned around 1585 cm^{-1} .⁴³ The defect-induced double-resonance intervalley (D) and intravalley (D') scattering processes that cause the D and D' peaks located near 1350 cm^{-1} and 1615 cm^{-1} respectively, arise from areas of the graphene lattice surrounding defect sites.⁴⁴ The level of disorder, due to defects in the graphene structure, will affect the D to G peak area ratio observed in Raman, and a change in the D to G ratio is indicative of damage to the graphene walls.⁴⁵ Deconvolution of the D' peak from the G peak was essential for proper analysis because of the peak overlap. The D peak to G peak area ratio as well as the sum of the D and D' peaks to the G peak area ratios for the MWCNTs are shown in **Table 3.1**, and the same trends were seen for both ratios. For this functionalization scheme, the D to G ratio increased with the first acid

oxidation step. The acid oxidation introduced defect sites into the graphene lattice causing the increase. In the subsequent AA-MWCNTs and AU-MWCNT functionalizations, the D to G ratios did not change significantly compared to the AO-MWCNTs, which indicated no damage during functionalization that would further affect the order in the graphene lattice. The purified MWCNTs showed a lower D to G peak ratio because the purification process removed amorphous carbon impurities and small carbonaceous fragments with high levels of disorder.

Table 3.1. Summary of relevant Raman peak area ratios.

MWCNT sample	D/G	(D and D')/G
Pristine MWCNTs	1.21	1.25
Purified MWCNTs	1.12	1.17
AO-MWCNTs	1.28	1.32
AA-MWCNTs	1.30	1.37
AU-MWCNTs	1.32	1.41

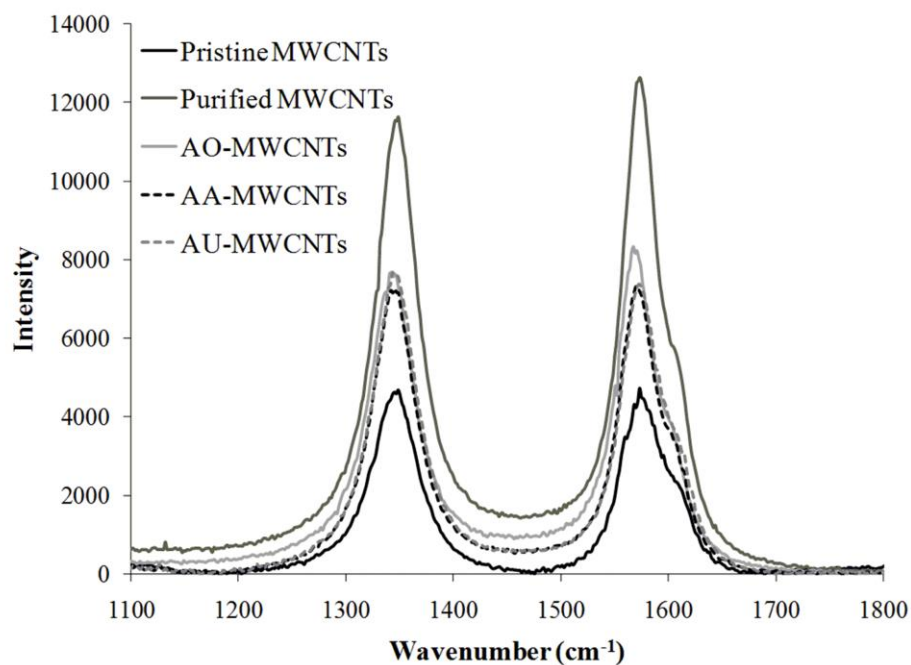


Figure 3.2. Raman spectra of MWCNTs.

XPS also showed evidence for successful functionalization. **Table 3.2** shows the elemental composition of the MWCNT samples according to XPS. The pristine MWCNTs were nearly entirely carbon with a small amount of oxygen, likely due to atmospheric oxidation of the carbon nanotubes during the chemical vapor deposition process and subsequent storage. The purified MWCNTs exhibited similar oxygen levels compared to the pristine MWCNTs, which showed that acid purification did not significantly affect the oxygen content of the MWCNTs. After acid oxidation, there was a significant increase in the oxygen content as a result of the introduction of oxygen-containing groups onto the MWCNT surface.²³ The AA-MWCNTs showed a significant increase in nitrogen content, which was negligible for the other samples, which indicated successful functionalization with ethylene diamine. Reaction with heptyl isocyanate to form AU-MWCNTs enriched the carbon content compared to the oxygen content as more carbon was added relative to oxygen, and this was reflected in the XPS results.

Table 3.2. Elemental composition as determined by XPS.

MWCNT sample	C (%)	O (%)	N (%)
Pristine MWCNTs	98.8	1.2	0
Purified MWCNTs	99.1	0.9	0
AO-MWCNTs	96.1	3.9	0
AA-MWCNTs	94.5	4.0	1.5
AU-MWCNTs	95.3	2.7	2.0

Deconvolution of the oxygen 1s region provided insight into the types of oxygen species present in each sample and provides further support for successful covalent functionalization. Deconvolution revealed two peaks centered around binding energies of 533 eV and 531 eV, which corresponded to oxygen singly bonded to carbon and oxygen doubly bonded to carbon, respectively.²³ The purified MWCNT sample failed to reveal any contribution from the peak at

531 eV. The amount of oxygen doubly bonded to carbon relative to oxygen singly bonded to carbon increased going from AO-MWCNT to AA-MWCNTs to AU-MWCNTs. **Table 3.3** shows the area under the deconvoluted peaks of the oxygen 1s region, which further supported successful covalent functionalization of the MWCNTs. Doubly bonded oxygen increased from AO-MWCNTs to AA-MWCNTs because amide groups replaced the hydroxyl groups of the carboxylic acid sites. Doubly bonded oxygen also relatively increased going from the AA-MWCNTs to the AU-MWCNTs, due to the new carbonyl groups in urea.

Table 3.3. Deconvoluted oxygen 1s peak areas.

MWCNT Sample	C=O (531-532 eV)	C-O (533-534 eV)
Pristine MWCNTs	63	37
Purified MWCNTs	100	-
AO-MWCNTs	50	50
AA-MWCNTs	57	43
AU-MWCNTs	67	33

An analysis of the water dispersibility water dispersion test served as a qualitative indication of MWCNT functionalization and probed how surface functionalizations effected aqueous dispersibility at different pHs (**Figure 3.3**). Probe sonication dispersed the MWCNTs in aqueous solutions of different pH ranges, either low (3), neutral (6.8), or high (11). The surface functionality determined the stability of the dispersion at different pHs. The state of dispersion after 24 h was nearly identical to immediately after sonication, and MWCNTs that were not dispersible immediately precipitated. The dispersions remained stable for over 6 mo and surface functionality allowed for a prediction of the aqueous dispersion at a given pH.

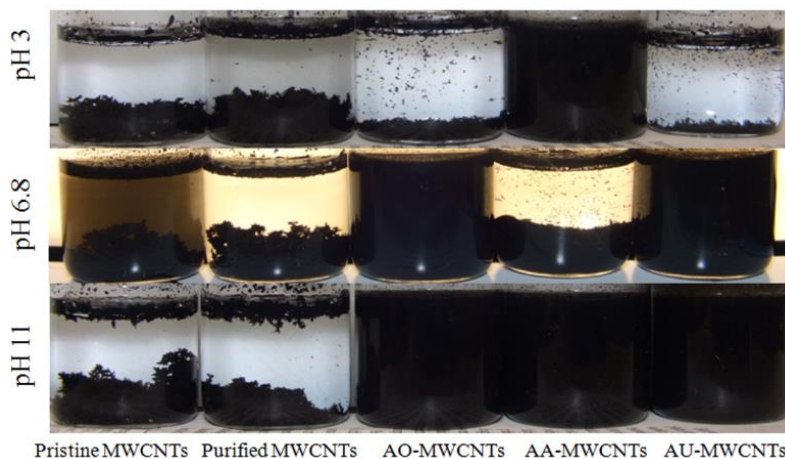
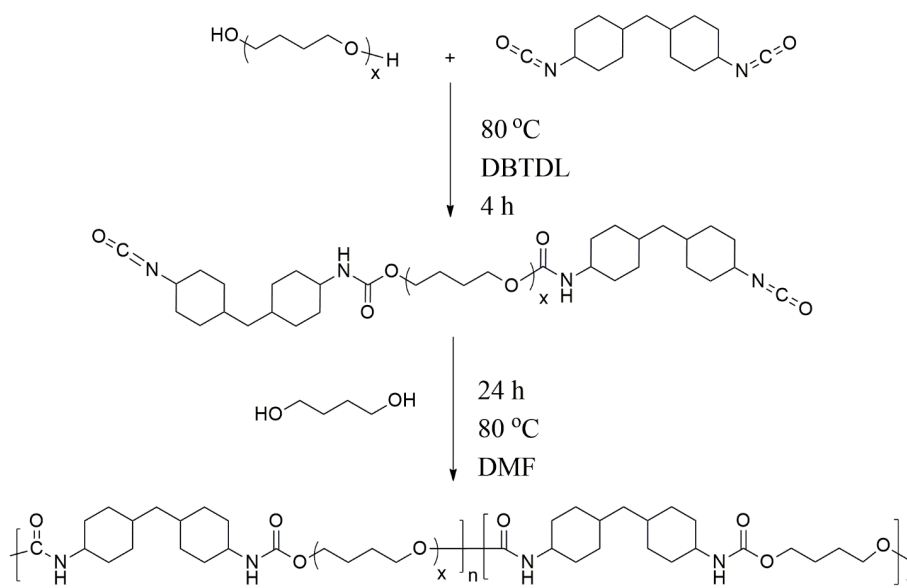


Figure 3.3. Dispersion in varied pH conditions (MWCNTs dispersed at 1×10^{-2} wt%, photos taken after 1 day).

The completely hydrophobic nature and lack of pH-responsive functional groups rendered the non-functionalized MWCNTs nondispersible at any pH. The AO-MWCNTs formed a stable dispersion at neutral and high pHs since carboxylic acid groups were deprotonated and the MWCNTs were rendered hydrophilic. Protonation of the carboxylic acid sites at low pHs reverted the MWCNTs to hydrophobic, leading to aggregation. The AA-MWCNTs displayed very different dispersibility that suggests that ethylene diamine did not react quantitatively with the carboxylic acid sites when synthesizing the AA-MWCNTs due to the high reactivity of the acyl chloride with trace amounts of water. Any remaining carboxylic acid groups affected the pH-dependent dispersibility of the AA-MWCNTs and AU-MWCNTs. The ionized amine groups on the surface the AA-MWCNTs at low pH imparted hydrophilicity and charge repulsion leading to dispersibility. Neutral amine groups with the deprotonated remaining carboxylic acid groups allowed for dispersibility similar to the AO-MWCNTs at high pH. The protonated and positively charged amine groups combined with the deprotonated and negatively charged carboxylic acid groups led to aggregation at neutral pH. The AA-MWCNTs

effectively experienced an isoelectric point, and the presence of the attracting opposite charges caused the AA-MWCNTs to aggregate at neutral pH. The AU-MWCNTs exhibited the same dispersion behavior as the AO-MWCNTs. This was attributed to the isocyanate quantitatively converting all amines to urea groups, and the remaining carboxylic acid groups determined dispersibility.

Effect of Surface Functionalization on MWCNT Composite Properties



Scheme 3.2. Synthesis of segmented PTMO based polyurethane.

A 45 wt% hard segment polyurethane served as the polymer matrix as shown in **Scheme 3.2**. The hard segment content ensured good mechanical properties and provided a high concentration of urethane sites for non-covalent, hydrogen bonding, intermolecular interactions with the functionalized MWCNTs. Light scattering determined the polyurethane absolute M_w of 50,200 g/mol using a dn/dc of 0.0633 that was determined offline. This molecular weight provided a polyurethane with good mechanical properties including high stress and strain at

break in tensile without high viscosities for higher molecular weights. The viscosity of the polymer due to its molecular weight will greatly affect dispersibility.⁴⁶ The hard segment based on HMDI limited the effect of hard segment crystallization as a complicating factor in composite formation. The soft segment PTMO imparts desirable mechanical properties in elastomers,⁴⁷ and a low molecular weight (2000 g/mol) limits soft segment crystallization. The incorporation of MWCNTs into the optically clear polyurethane matrix led to black composites, except at the lowest loading (0.18 wt% MWCNTs) which displayed a transparent, grayish color.

Functionalization of MWCNTs with hydrogen bonding groups served to increase non-covalent intermolecular interactions with the polyurethane matrix in an attempt to increase MWCNT dispersion and thus composite properties. TEM, TGA, and tensile analysis all supported increased dispersion and improved composite properties with functionalized MWCNTs compared to non-functionalized controls. **Figure 3.4** depicts TEM images of microtomed sections of the neat polyurethane and composites with 1.8 wt% MWCNTs. This intermediate loading allowed for investigation of the dispersion state without overloading the composites. The images in **Figure 3.4** were representative of the entire sample, however, there was minimal aggregation and areas of good dispersion in all samples, but the functionalized and non-functionalized MWCNTs had very different overall dispersion. The neat polyurethane sample (**Figure 3.4a**) displayed a speckled light and dark pattern, which may correspond to the areas of higher and lower electron density in the hard and soft phases.⁴⁸ Although phase separation is not as apparent in composite TEM images, it is not clear whether this is a contrast issue in TEM or whether MWCNT incorporation affects phase separation. Determination of the effect of MWCNT incorporation on polyurethane morphology would require more detailed morphological studies. The non-functionalized MWCNT samples (**Figure 3.4b and 3.4c**) had a

significant number of aggregates over 1 μm in diameter with very few well dispersed regions. The non-polar nature of the non-functionalized tubes caused them to interact with each other through van der Waals interactions as opposed to interacting with the polymer matrix, which led to poor dispersion with many large aggregates after the dispersion process. The specifics of MWCNT behavior during dispersion are still largely not understood, but in the case of non-functionalized MWCNTs, the end result was poor dispersion, whether the aggregates reformed after sonication or were never dispersed. In contrast, MWCNTs functionalized with hydrogen bonding groups (**Figure 3.4d-f**) displayed thorough dispersion in the polymer matrix where most regions exhibited non-aggregated MWCNTs and a small number of small aggregates (less than 100 nm in diameter). This enhanced dispersion resulted from the polar nature of the functionalized MWCNTs and the hydrogen bonding interactions with the urethane and ether groups in the polymer backbone. The polar solvent aided in the dispersion of the functionalized MWCNTs over the non-functionalized MWCNTs, despite the ability of DMF to disperse non-functionalized MWCNTs. At this loading of the three functionalized MWCNTs, there was an insignificant difference in the quality of dispersion as evident in TEM.

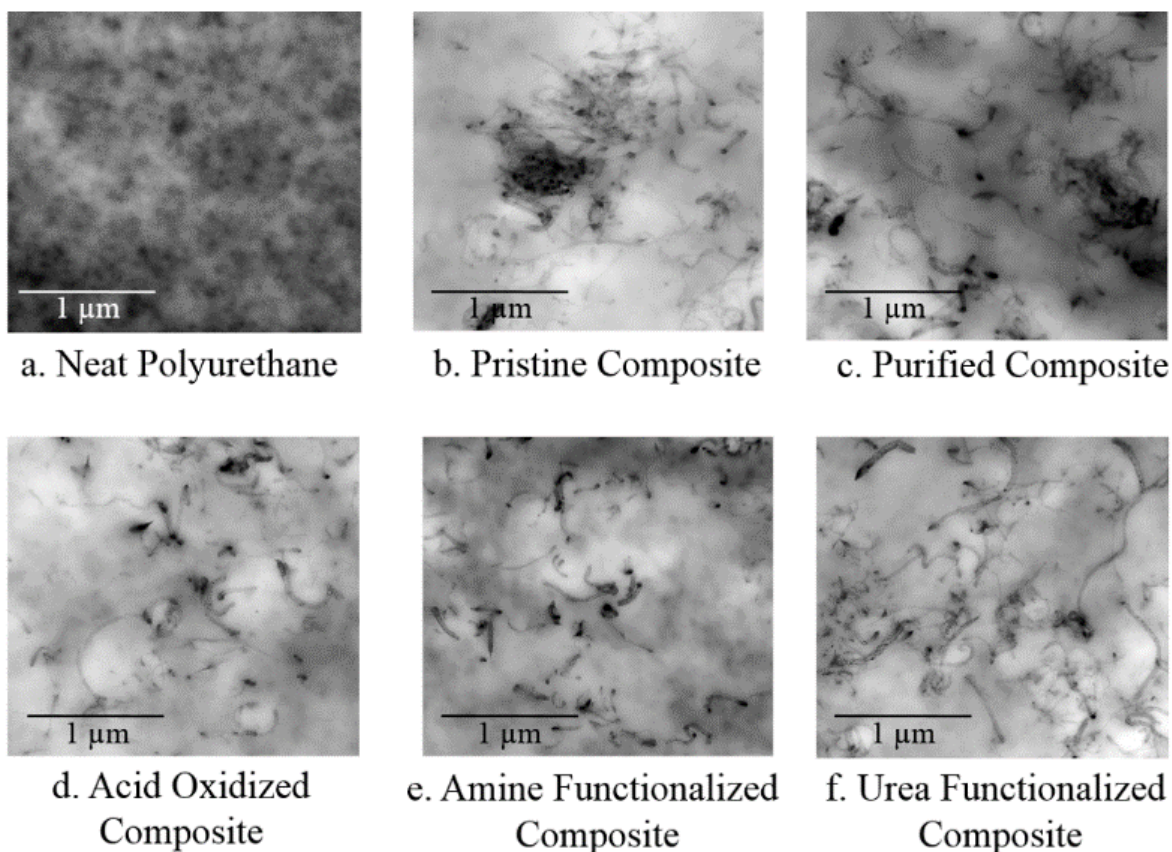


Figure 3.4. Comparison of MWCNT dispersibility in composites (1.8 wt% MWCNTs).

TGA revealed the thermal stability of the polyurethane and the MWCNT composites at 1.8 wt % MWCNT loading (**Figure 3.5**). The polymer and composites minimal weight loss up to ~ 300 °C and displayed similar degradation profiles except for pristine MWCNT composites, which showed a slightly reduced degradation temperature. The slight difference was reproducible, and was likely due to the presence of the cobalt metal catalyst particles that were present in the sample. Cobalt catalyst particles have the ability to drastically reduce the thermal stability of polymers through radical chain scission at elevated temperatures.⁴⁹ Scission of polymer chains likely occurred at room temperature in the pristine composites as well. Pristine composites showed a drastic change in bulk mechanical properties over time. Mechanical

integrity degraded after a few months and the composites became fragile, even when they initially displayed suitable mechanical properties. This indicated that certain applications in polymer composites require removal of cobalt-containing metal catalyst particles. Typically MWCNT loading will increase the thermal stability with increasing MWCNTs,⁵⁰ but the loading of 1.8 wt% MWCNTs did not produce a significant difference.

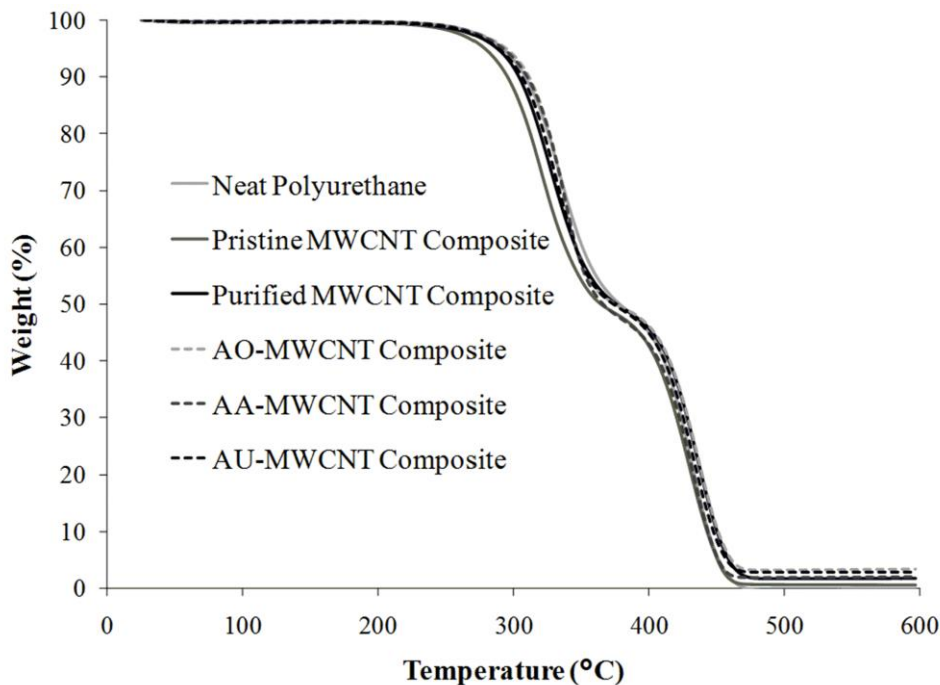


Figure 3.5. Effect of surface functionalization on thermal stability of composites (1.8 wt% MWCNTs).

DMA was used to probe the thermomechanical properties of the composites, shown in **Figure 3.6** for the neat polyurethane and 1.8 wt% MWCNT composites. The neat polyurethane displayed the characteristic transitions of a segmented polyurethane⁴⁷. The first transition near -75 °C was attributed to the T_g of the PTMO soft segment, which has a reported value of about -79°C⁵¹, and this indicates the presence of a PTMO rich domain. After this transition, there was a rubbery plateau in which the PTMO rich domains are mobile but the hard segments serve as

physical crosslinks in phase separated hard domains, providing viscoelastic properties. This rubbery plateau ends as the polymer goes through a second transition from 50-100 °C. This corresponded to the softening of the hard domains as the hard segment chains go through their T_g and become mobile⁴⁷. The polymer flowed in the DMA near 140 °C in the temperature range where the urethane hydrogen bonds begin to dissociate rapidly and the majority of the population of carbonyl groups in the hard segment are not involved in hydrogen bonding⁵². The composites displayed very similar behavior in DMA, except for the pristine MWCNT composite which flowed at an earlier temperature near 110 °C likely due to poor dispersion and the aforementioned thermal instability due to the cobalt catalyst particles. Rheological measurements would further elucidate the effect of these MWCNTs on the flow behavior of the polyurethane composite.

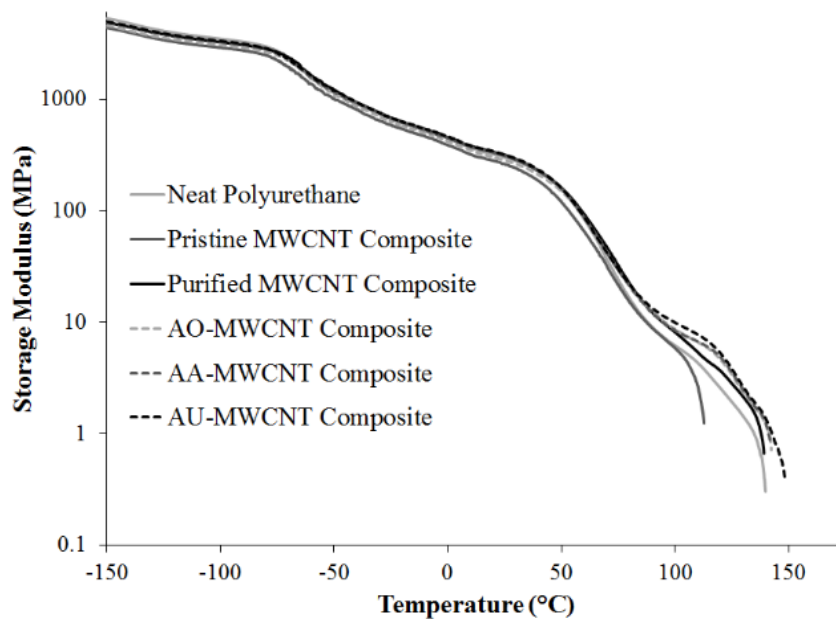


Figure 3.6. Comparison of Dynamic Mechanical Properties at 1.8 wt% MWCNTs.

Tensile testing proved extremely important for evaluating the performance of polymer composites, and particularly useful for evaluating dispersion as it relates to mechanical

properties. Aggregates and imperfections in the composite film in combination with limited filler-matrix interactions reduces mechanical properties in composites, and tensile testing clearly reveals the effects.⁵³ **Figure 3.7** shows representative tensile curves for the neat polyurethane and 1.8 wt% MWCNT composites, and **Table 3.4** summarizes the data. A loading of 1.8 wt% resulted in a slight increase in the stress at break with insignificant change in the strain at break or Young's modulus of the functionalized MWCNT composites compared to the neat polymer. The non-functionalized MWCNT composites displayed lower mechanical properties with lower stress and strain at break.

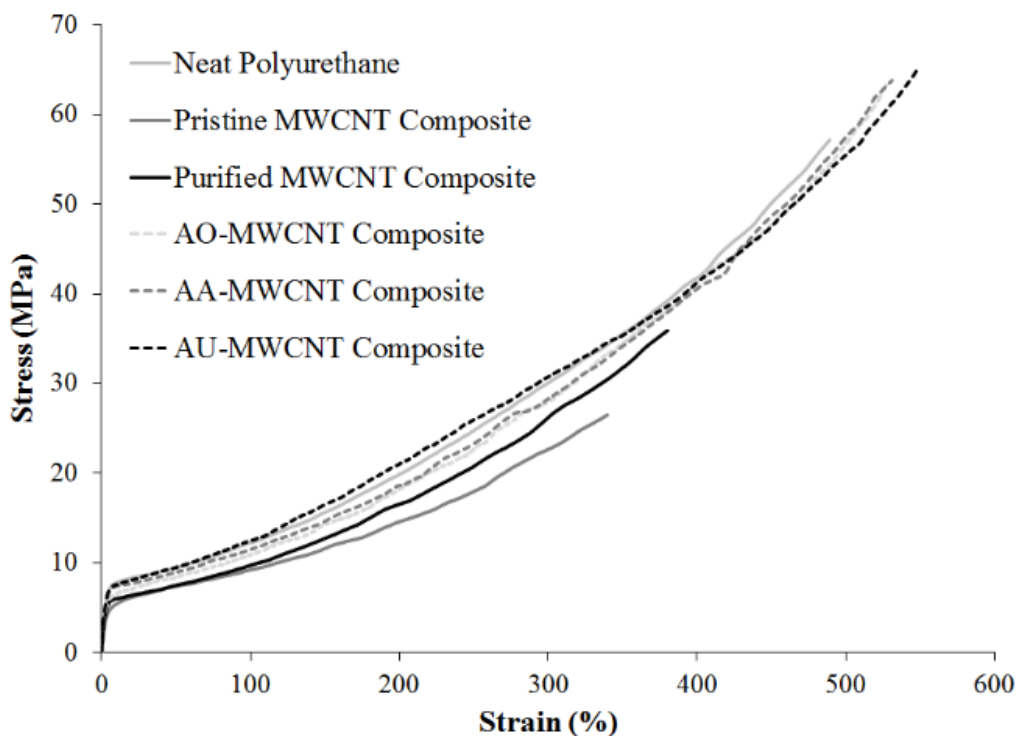


Figure 3.7. Representative tensile curves of composites (1.8 wt% MWCNTs).

Table 3.4. Summary of composite tensile properties (1.8 wt% MWCNTs).

Sample	Stress at Break (MPa)	Strain at Break (%)	Modulus (MPa)
Neat PU	58.2 ± 0.6	576 ± 52	194 ± 26
Pristine MWCNT Composite	26.6 ± 2.1	371 ± 30	170 ± 24
Purified MWCNT Composite	42.1 ± 15.3	412 ± 44	220 ± 4
AO-MWCNT Composite	63.4 ± 0.8	513 ± 24	240 ± 36
AA-MWCNT Composite	63.3 ± 0.7	516 ± 17	244 ± 8
AU-MWCNT Composite	62.4 ± 1.9	544 ± 19	270 ± 21

Formulation of composites at 0.18, 0.6, 1.8, 2.4, 3, 5, 7.5, and 10 wt% MWCNTs (using functionalized MWCNTs and purified MWCNTs) further investigated the influence of MWCNT loading on tensile properties. The plot of stress at break *versus* loading of MWCNTs showed an increase in the stress at break as loading increased in the functionalized MWCNT composites to 2.4 wt % MWCNTs (**Figure 3.8**). At higher loadings, the stress at break declined, presumably due to the presence of aggregates and imperfections formed at higher loadings. Higher MWCNT levels caused tensile properties to further decline, which indicated the dispersion process was not sufficient for the high loading of MWCNTs, despite thorough MWCNT dispersion at lower loadings.⁵⁴ However, purified MWCNTs demonstrated a gradual decline and increased variability in stress at break between trials. This was due to the limited interactions and poor dispersion in the polyurethane matrix. The strain at break gradually decreased as MWCNT loading was increased in all composites (**Figure 3.9**), consistent with MWCNT composites.⁵⁵ The well-dispersed, functionalized MWCNTs initially increased the Young's moduli for the functionalized MWCNTs. The high modulus of the MWCNTs increased the composite bulk modulus until reaching higher levels, and tensile properties declined as heterogeneity increased (**Figure 3.10**). The poor dispersion of the purified MWCNTs, at loadings that could affect the modulus, caused the Young's modulus to remain the same for the purified MWCNT series. The

tensile data showed an improvement in the stress at break and Young's moduli of the composites at lower loadings for functionalized MWCNTs compared to neat polyurethane without a change in the strain at break. The three surface functionalizations displayed very similar properties. The increase in tensile properties in the functionalized composites arise from thorough dispersion and effective intermolecular interactions between the MWCNTs and the polyurethane matrix in the well-dispersed state which allows for efficient stress transfer between the matrix and MWCNTs. Higher loadings of the functionalized MWCNTs and all purified MWCNT loadings caused a reduction in mechanical properties compared to the neat polymer. This was due to MWCNT aggregation and imperfections in the polymer film, which drastically influenced tensile properties.

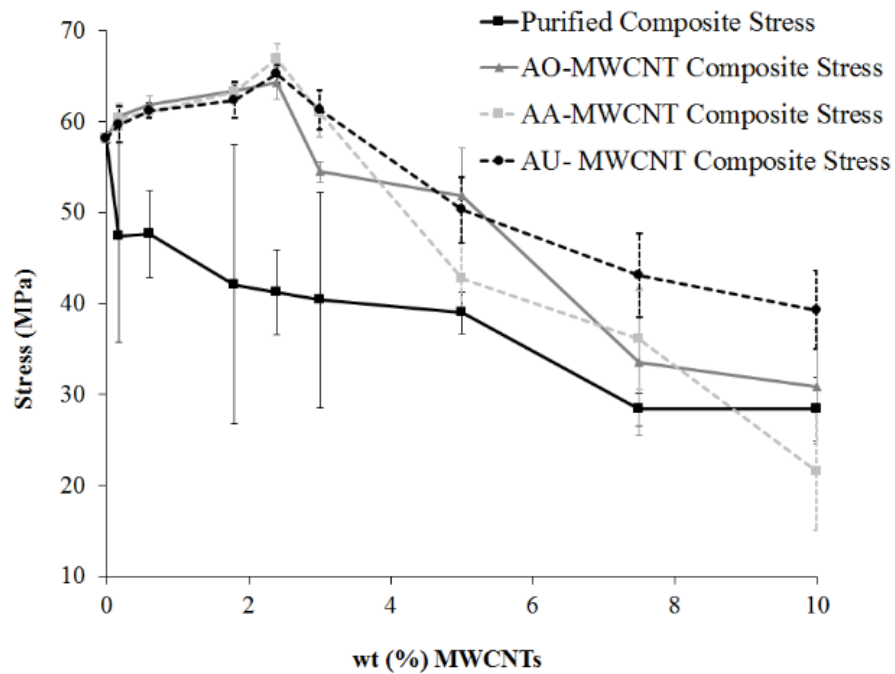


Figure 3.8. Stress at break as a function of MWCNT loading.

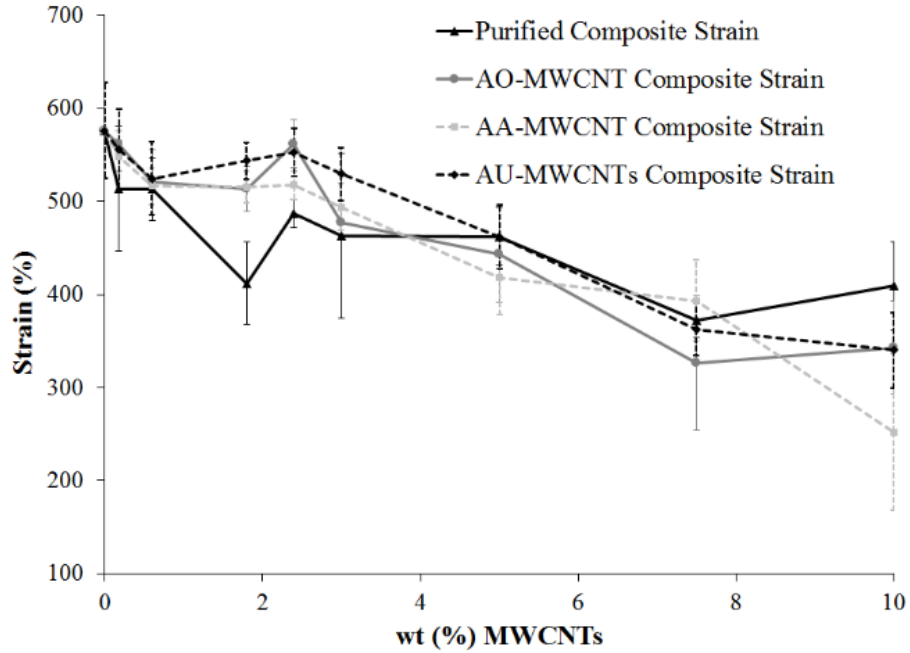


Figure 3.9. Strain at break as a function of MWCNT loading.

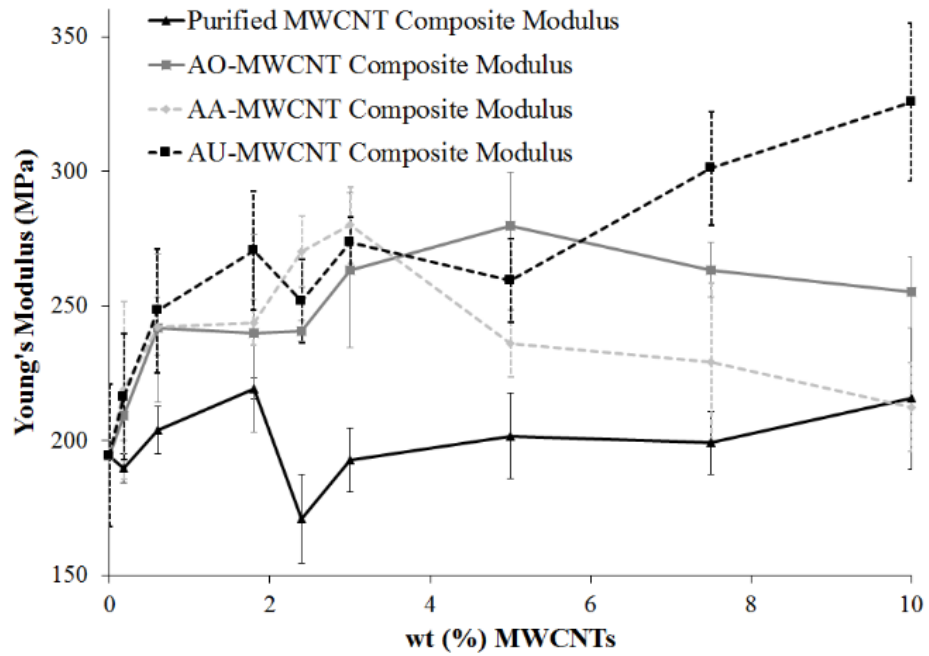


Figure 3.10. Young's modulus as a function of MWCNT loading.

The tensile data in combination with TEM showed that incorporation of hydrogen bonding groups on the MWCNT surface allowed for thorough dispersion and improved composite mechanical properties. This was not possible with non-functionalized MWCNTs. The presence of hydrogen bonding groups on the functionalized MWCNT surface allowed for non-covalent intermolecular interactions with the polymer matrix. These hydrogen bonding sites enabled enhanced initial dispersion and increased interactions with the polymer in the final composite. Although mechanical properties decline at higher functionalized MWCNT levels, properties improved at low MWCNT loadings, which are desirable in composite applications due to MWCNT cost and aggregation behavior at higher loadings.

3.5 Conclusions

An acid oxidation functionalization coupled with a derivatization scheme introduced hydrogen bonding functionality onto the surface of MWCNTs, yielding AO-MWCNTs, AA-MWCNTs, and novel AU-MWCNTs. This is the first reported functionalization with urea groups through the acid oxidation route and the first detailed comparison of the influence MWCNT hydrogen bonding on composite properties. All functionalizations provided hydrogen bonding sites and yielded polar MWCNTs that interacted heavily with polar sites in polyurethanes. Raman spectroscopy, TGA, and XPS confirmed successful MWCNT functionalization. The functionalized MWCNTs also displayed pH and surface functionalization dependent aqueous dispersion. Sonication successfully dispersed functionalized MWCNTs into a 45 wt% hard segment segmented polyurethane matrix. TEM confirmed thorough dispersion of the functionalized MWCNTs, and the tensile properties of the functionalized MWCNT composites improved at low loadings. The non-functionalized MWCNT composites, in contrast,

displayed high levels of aggregation in TEM. Also, non-functionalized MWCNT composites displayed reduced tensile properties compared to the neat polyurethane. The mechanical properties of the three functionalized MWCNTs composites showed insignificant differences. These results indicated that the introduction of hydrogen bonding functionality allowed for MWCNT dispersion in the polyurethane matrix and an increase in mechanical properties, which was dependent on the polymer composition and dispersion process.

Acknowledgements. This work was supported by collaboration with Bayer MaterialScience. The authors would like to thank Karl Haider and Tao Yu for their guidance on the project. TEM was performed at the Nanoscale Characterization and Fabrication Laboratory (NCFL) operated by the Institute for Critical Technology and Applied Science (ICTAS) at Virginia Tech. The authors would like to acknowledge the technical expertise of Steve McCartney at the NCFL, and would like to thank Charles Farley for assistance with Raman spectroscopy.

3.6 References

1. Ebbesen, T. W.; Lezec, H. J.; Hiura, H.; Bennett, J. W.; Ghaemi, H. F.; Thio, T. *Nature* **1996**, 382, 54.
2. Fujii, M.; Zhang, X.; Xie, H.; Ago, H.; Takahashi, K.; Ikuta, T.; Abe, H.; Shimizu, T. *Phys. Rev. Lett.* **2005**, 95, 065502.
3. Hone, J.; Llaguno, M. C.; Biercuk, M. J.; Johnson, A. T.; Batlogg, B.; Benes, Z.; Fischer, J. E. *Appl. Phys. A* **2002**, 74, 339.
4. Kataura, H.; Kumazawa, Y.; Maniwa, Y.; Umez, I.; Suzuki, S.; Ohtsuka, Y.; Achiba, Y. *Synth. Met.* **1999**, 103, 2555.
5. Lin, M. F.; Shung, K. W. K. *Physical Review B* **1994**, 50, 17744.
6. Ruoff, R. S.; Lorents, D. C. *Carbon* **1995**, 33, 925.
7. Salvetat, J. P.; Bonard, J. M.; Thomson, N. H.; Kulik, A. J.; Forro, L.; Benoit, W.; Zuppiroli, L. *Appl. Phys. A* **1999**, 69, 255.
8. Iijima, S. *Nature* **1991**, 354, 56.
9. Dillon, A. C.; Jones, K. M.; Bekkedahl, T. A.; Kiang, C. H.; Bethune, D. S.; Heben, M. J. *Nature* **1997**, 386, 377.
10. Liu, C.; Chen, Y.; Wu, C.-Z.; Xu, S.-T.; Cheng, H.-M. *Carbon* **2010**, 48, 452.

11. Niu, C.; Sichel, E. K.; Hoch, R.; Moy, D.; Tennent, H. *Appl. Phys. Lett.* **1997**, *70*, 1480.
12. Andrews, R.; Weisenberger, M. C. *Curr. Opin. Solid State Mater. Sci.* **2004**, *8*, 31.
13. Spitalsky, Z.; Tasis, D.; Papagelis, K.; Galiotis, C. *Prog. Polym. Sci.* **2010**, *35*, 357.
14. Moniruzzaman, M.; Winey, K. I. *Macromolecules* **2006**, *39*, 5194.
15. Byrne, M. T.; Gun'ko, Y. K. *Adv. Mater.* **2010**, *22*, 1672.
16. Coleman, J. N.; Khan, U.; Blau, W. J.; Gun'ko, Y. K. *Carbon* **2006**, *44*, 1624.
17. Bose, S.; Khare, R. A.; Moldenaers, P. *Polymer* **2010**, *51*, 975.
18. Rasheed, A.; Dadmun, M. D.; Ivanov, I.; Britt, P. F.; Geohegan, D. B. *Chem. Mater.* **2006**, *18*, 3513.
19. Balasubramanian, K.; Burghard, M. *Small* **2005**, *1*, 180.
20. Gojny, F. H.; Wichmann, M. H. G.; Köpke, U.; Fiedler, B.; Schulte, K. *Compos. Sci. Technol.* **2004**, *64*, 2363.
21. Ventura, D. N.; Stone, R. A.; Chen, K.-S.; Hariri, H. H.; Riddle, K. A.; Fellers, T. J.; Yun, C. S.; Strouse, G. F.; Kroto, H. W.; Acquah, S. F. A. *Carbon* **2010**, *48*, 987.
22. Aviles, F.; Cauich-Rodriguez, J. V.; Moo-Tah, L.; May-Pat, A.; Vargas-Coronado, R. *Carbon* **2009**, *47*, 2970.
23. Datsyuk, V.; Kalyva, M.; Papagelis, K.; Parthenios, J.; Tasis, D.; Siokou, A.; Kallitsis, I.; Galiotis, C. *Carbon* **2008**, *46*, 833.
24. Rosca, I. D.; Watari, F.; Uo, M.; Akasaka, T. *Carbon* **2005**, *43*, 3124.
25. Yang, S.-Y.; Ma, C.-C. M.; Teng, C.-C.; Huang, Y.-W.; Liao, S.-H.; Huang, Y.-L.; Tien, H.-W.; Lee, T.-M.; Chiou, K.-C. *Carbon* **2010**, *48*, 592.
26. Wang, S.-F.; Shen, L.; Zhang, W.-D.; Tong, Y.-J. *Biomacromolecules* **2005**, *6*, 3067.
27. Kokil, A.; Saito, T.; Depolo, W.; Elkins, C. L.; Wilkes, G. L.; Long, T. E. *Journal of Macromolecular Science, Part A* **2011**, *48*, 1016.
28. Peng, H.; Alemany, L. B.; Margrave, J. L.; Khabashesku, V. N. *J. Am. Chem. Soc.* **2003**, *125*, 15174.
29. Kuan, H.-C.; Ma, C.-C. M.; Chang, W.-P.; Yuen, S.-M.; Wu, H.-H.; Lee, T.-M. *Compos. Sci. Technol.* **2005**, *65*, 1703.
30. Pulikkathara, M. X.; Kuznetsov, O. V.; Khabashesku, V. N. *Chem. Mater.* **2008**, *20*, 2685.
31. Sheth, J. P.; Unal, S.; Yilgor, E.; Yilgor, I.; Beyler, F. L.; Long, T. E.; Wilkes, G. L. *Polymer* **2005**, *46*, 10180.
32. Camberlin, Y.; Pascault, J. P. *Journal of Polymer Science: Polymer Chemistry Edition* **1983**, *21*, 415.
33. Garrett, J. T.; Xu, R.; Cho, J.; Runt, J. *Polymer* **2003**, *44*, 2711.
34. Xia, H.; Song, M. *Soft Matter* **2005**, *1*, 386.
35. Xiong, J.; Zheng, Z.; Qin, X.; Li, M.; Li, H.; Wang, X. *Carbon* **2006**, *44*, 2701.
36. Chen, W.; Tao, X.; Liu, Y. *Compos. Sci. Technol.* **2006**, *66*, 3029.
37. Fernández-d'Arlas, B.; Khan, U.; Rueda, L.; Coleman, J. N.; Mondragon, I.; Corcuera, M. A.; Eceiza, A. *Compos. Sci. Technol.* **2011**, *71*, 1030.
38. Zhao, J.-C.; Du, F.-P.; Zhou, X.-P.; Cui, W.; Wang, X.-M.; Zhu, H.; Xie, X.-L.; Mai, Y.-W. *Composites Part B: Engineering* **2011**, *42*, 2111.
39. Gao, R.; Ramirez, S. M.; Inglefield, D. L.; Bodnar, R. J.; Long, T. E. *Carbon* **2013**, *54*, 133.
40. Gao, R.; Zhang, M.; Dixit, N.; Moore, R. B.; Long, T. E. *Polymer* **2012**, *53*, 1203.
41. Hou, P.-X.; Liu, C.; Cheng, H.-M. *Carbon* **2008**, *46*, 2003.
42. Ranjan, S.; Jue, Z.-F.; Chen, F. L. *J. Compos. Mater.* **2010**, *44*, 1305.

43. Dresselhaus, M. S.; Eklund, P. C. *Advances in Physics* **2000**, *49*, 705.
44. Jorio, A.; Lucchese, M. M.; Stavale, F.; Ferreira, E. H. M.; Moutinho, M. V. O.; Capaz, R. B.; Achete, C. A. *J. Phys.: Condens. Matter* **2010**, *22*, 334204.
45. Dresselhaus, M. S.; Jorio, A.; Hofmann, M.; Dresselhaus, G.; Saito, R. *Nano Lett.* **2010**, *10*, 751.
46. Jakubka, F.; Schießl, S. P.; Martin, S.; Englert, J. M.; Hauke, F.; Hirsch, A.; Zaumseil, J. *ACS Macro Letters* **2012**, *1*, 815.
47. Klinedinst, D. B.; Yilgör, I.; Yilgör, E.; Zhang, M.; Wilkes, G. L. *Polymer* **2012**, *53*, 5358.
48. Serrano, M.; MacKnight, W. J.; Thomas, E. L.; Ottino, J. M. *Polymer* **1987**, *28*, 1667.
49. Li, Z.; Lin, W.; Moon, K.-S.; Wilkins, S. J.; Yao, Y.; Watkins, K.; Morato, L.; Wong, C. *Carbon* **2011**, *49*, 4138.
50. Kashiwagi, T.; Grulke, E.; Hilding, J.; Harris, R.; Awad, W.; Douglas, J. *Macromol. Rapid Commun.* **2002**, *23*, 761.
51. Yoon, S. C.; Ratner, B. D. *Macromolecules* **1988**, *21*, 2392.
52. Teo, L.-S.; Chen, C.-Y.; Kuo, J.-F. *Macromolecules* **1997**, *30*, 1793.
53. Ogasawara, T.; Ishida, Y.; Ishikawa, T.; Yokota, R. *Composites Part A: Applied Science and Manufacturing* **2004**, *35*, 67.
54. Graff, R. A.; Swanson, J. P.; Barone, P. W.; Baik, S.; Heller, D. A.; Strano, M. S. *Adv. Mater.* **2005**, *17*, 980.
55. McNally, T.; Pötschke, P.; Halley, P.; Murphy, M.; Martin, D.; Bell, S. E. J.; Brennan, G. P.; Bein, D.; Lemoine, P.; Quinn, J. P. *Polymer* **2005**, *46*, 8222.

3.7 Appendix 3A

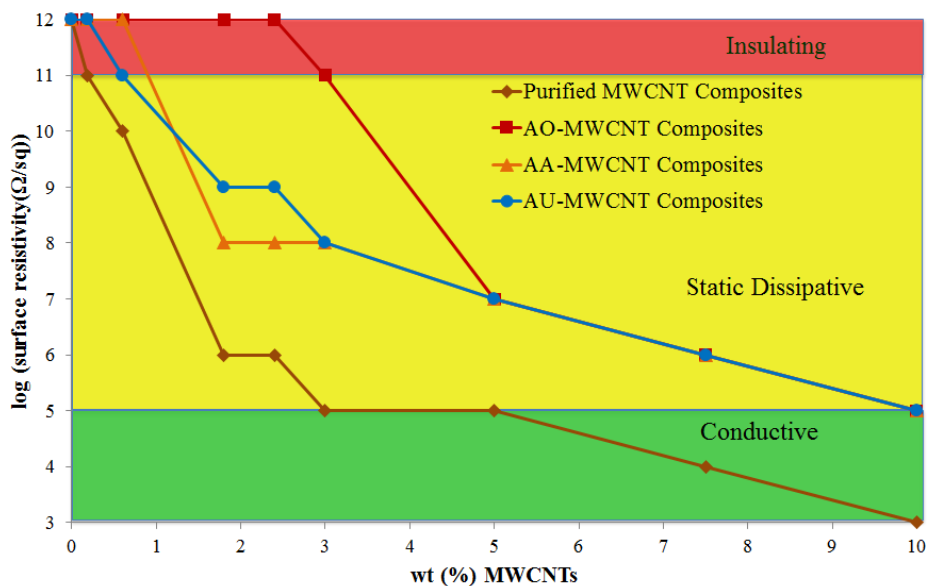


Figure 3.11. Surface resistivity measurements of polyurethane-MWCNT composites.

Chapter 4: Temperature-Dependent Hydrogen Bonding Interactions in Polyurethane Multi-walled Carbon Nanotube Composites

David L. Inglefield Jr.^a, Amanda Hudson^a, Mingqiang Zhang^a, Robert B. Moore^{ab}, and Timothy E. Long^{ab}

*^aDepartment of Chemistry, ^bMacromolecules and Interfaces Institute
Virginia Tech, Blacksburg, VA 24061*

4.1 Abstract

Multi-walled carbon nanotubes represent promising nanofillers for polymer matrix composites due to their inner walls retaining desirable properties after extensive surface functionalization. Surface functionalization is essential for formation of useful composites with polar polymers such as polyurethanes. Logically, utilizing hydrogen bonding surface functionality to disperse carbon nanotubes in polyurethanes and enable polymer-carbon nanotube intermolecular interactions will likely affect the overall state of hydrogen bonding in the polymer matrix. Understanding of the effect of nanofiller incorporation on polyurethane hydrogen bonding impacts the applicability and processing techniques of these composite systems due to the high levels of hydrogen bonding in polyurethanes. Here, variable temperature Fourier transform infrared spectroscopy and dynamic mechanical analysis investigate the effect of incorporating multi-walled carbon nanotubes surface functionalized with hydrogen bonding groups on hydrogen bonding in polyurethane composites. Acid oxidation enabled synthesis of multi-walled carbon nanotubes with different hydrogen bonding surface functionalities, and non-functionalized multi-walled carbon nanotubes served as analogs with limited capacity for

intermolecular interactions with the polymer matrix. The functionalized multi-walled carbon nanotubes displayed a more pronounced effect on the state of hydrogen bonding and flow temperature in the composites than the non-functionalized multi-walled carbon nanotubes. These findings correlate well with previous investigations of these composites, which show that functionalization affords enhanced dispersion and increased intermolecular interactions with the polymer matrix.

4.2 Introduction

Carbon nanotube polymer-matrix composites continue to generate intense interest due to the unique thermal, electrical, and mechanical properties imparted by carbon nanotubes (CNTs), despite the shortcomings of these composite systems.¹⁻³ In their native form, CNTs possess hydrophobic graphene surfaces prone to aggregation through van der Waals interactions. Aggregation and limited polymer-CNT interfacial interactions reduce the efficacy of CNT composites.⁴ Thorough dispersion and effective CNT-polymer interactions are essential for optimal composite properties.^{5,6} Due to these factors, understanding the fundamental effects of CNT incorporation on polymer properties and intermolecular interactions, such as hydrogen bonding, is of utmost importance to the realization of high-performance composites.

Functionalizing CNTs with surface bound functionalities or polymers improves CNT dispersion and interactions with the polymer matrix.^{7,8} This is especially important for applications in polar polymer matrices such as polyurethanes which are chemically incompatible with the non-polar surface of non-functionalized CNTs.^{9,10} Multi-walled carbon nanotubes (MWCNTs) are particularly promising for mechanically reinforced composites because they retain their inner walls which preserve their mechanical properties after extensive surface

functionalization.¹¹ Researchers introduce polar functionalities onto the surface of CNTs through a number of functionalization techniques, including the popular acid oxidation route.¹²⁻¹⁴ Acid oxidation introduces carboxylic acid groups onto the CNT surface which permit further functionalization through typical carboxylic acid chemistry, enabling a large number of possible surface functionalizations.¹⁵ This approach prepared MWCNTs with various hydrogen bonding surface functionalities for this study, including acid oxidized MWCNTs (AO-MWCNTs), amide-amine functionalized MWCNTs (AA-MWCNTs) and amide-urea functionalized (AU-MWCNTs). Functionalization with these hydrogen bonding groups enables effective dispersion in a segmented polyurethane matrix leading to increased composite tensile properties (see Chapter 3).

The highly tunable and desirable mechanical properties that arise from phase-separated morphologies and hydrogen bonding make segmented polyurethanes a heavily researched and industrially important family of polymers. Synthesis using the prepolymer method allows for incorporation of soft segment oligomers and hard segments derived from diisocyanates and diol chain extenders into segmented polymer structures, which often leads to phase separated systems due to chemical incompatibility between the hard and soft segments.¹⁶⁻¹⁸ Adjusting the hard and soft segment structures and overall composition provides a wide range of physical properties for a variety of polyurethane applications. The nature of hydrogen bonding in the segmented polyurethane hard domains depends on the polyurethane structure and level of crystallinity.^{19,20} Fourier transform infrared spectroscopy (FT-IR) permits investigation of hydrogen bonding in polyurethanes and related polymers through analyzing the hydrogen bond donor and acceptor group absorbance signals, which vary depending on the state of hydrogen bonding.²¹ Furthermore, utilization of variable temperature FT-IR (VT FT-IR) elucidates the temperature-

dependent behavior of hydrogen bonding in polyurethanes and related polymers.²²⁻²⁵ For example, typical analysis of urethane carbonyl region reveals a shift to higher wavenumbers as hydrogen bonds dissociate with increasing temperature.

The effect of nanofillers such as CNTs, nanoclays, and inorganic nanoparticles on hydrogen bonding in polyurethane nanocomposites represents an important parameter in polyurethane nanocomposite design which commands further scrutiny. A limited number of investigations probe the nature of hydrogen bonding in polyurethane nanocomposites and the effect of nanofiller incorporation.²⁶⁻³⁰ The influence of nanofillers on hydrogen bonding greatly depends on the type of nanoparticle and its surface functionality. Incorporation of nanoparticles with efficient hydrogen bonding surface functionality into polyurethane composites provides the opportunity for effective polymer-nanoparticle hydrogen bonding, but the presence of the nanoparticles may also affect the overall polyurethane morphology and chain mobility which in turn will influence the physical properties and polymer-polymer hydrogen bonding. To our knowledge, no studies thoroughly examine the effect of CNTs on temperature dependent hydrogen bonding behavior in polyurethane-CNT composites.

In the present study, we investigate the effect of MWCNT loading on hydrogen bonding in polyurethane-MWCNT nanocomposites. Surface functionalization through the acid oxidation route enabled synthesis of hydrogen bonding AO-MWCNTs, AA-MWCNTs, and AU-MWCNTs. Analysis of the temperature-dependent hydrogen bonding behavior using VT FT-IR revealed the effect of MWCNT incorporation on the extent of hydrogen bonding as a function of MWCNT content and surface functionality, which correlated with dynamic mechanical analysis (DMA). MWCNTs functionalized with hydrogen bonding groups display a more pronounced effect on the hydrogen bonding content and dissociation behavior in the polyurethane composites compared to

non-functionalized MWCNT control composites. The VT FT-IR results correlated with DMA, where incorporation of functionalized MWCNTs increased the flow temperature.

4.3 *Experimental*

Materials and Instrumentation

A detailed description of the materials, instrumentation, and synthetic techniques employed along with basic characterization of the polyurethane and MWCNTs is found elsewhere (see Chapter 3 entitled Hydrogen Bond Containing Multi-walled Carbon Nanotubes in Polyurethane Composites). In brief, a high molecular weight ($M_w = 50,200$ g/mol) 45 wt% hard segment segmented polyurethane was prepared using the prepolymer method with ~2,000 g/mol poly(tetramethylene oxide (PTMO) as the soft segment, dicyclohexylmethane-4,4'-diisocyanate (HMDI) as the diisocyanate, and butanediol as the chain extender. The resultant polyurethane displayed good mechanical properties with significant hydrogen bonding and levels of crystallinity below detection. MWCNTs with various levels of hydrogen bonding were prepared from acid oxidized precursors synthesized using nitric acid oxidation. Non-functionalized MWCNTs purified using hydrochloric acid served as control MWCNTs with minimal hydrogen bonding capacity (purified MWCNTs). This purification process removes metal catalyst particles present in the pristine MWCNTs that negatively affect composite thermal properties through catalyzing polymer chain scission.³¹ Dispersion in the polyurethane matrix was achieved using sonication of the MWCNTs in dimethylformamide (DMF), stirring this dispersion with polyurethane solution in DMF, and subsequent sonication of the polymer-MWCNT mixture in DMF. Polymer and composite solutions were cast onto glass plates, dried in a drying oven at 80 °C for 2 h, then dried for 5 h *in vacuo* at 80 °C. Films were removed from

the glass plates by soaking in water for 5 minutes and gently peeled off to avoid film deformation, and were allowed to dry in air for 48 h before testing. Composites with various loadings from 0.18 wt% up to 10 wt% MWCNTs were formed for testing, where the reported wt% MWCNTs is relative to the polymer weight. **Figure 4.1** illustrates the polyurethane and MWCNT structures utilized to form composites in this investigation.

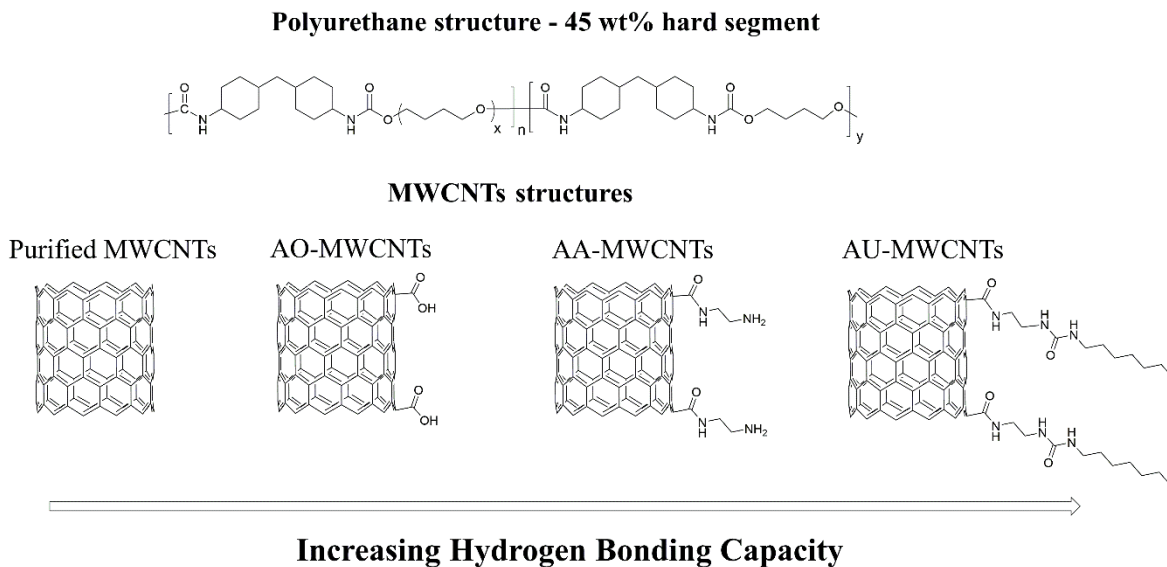


Figure 4.1. Polyurethane and MWCNT structures with varying hydrogen bonding surface functionality utilized to form composites.

SAXS experiments were performed on a Rigaku S-Max 3000 3 pinhole SAXS system, equipped with a rotating anode emitting X-ray with a wavelength of 0.154 nm (Cu K α), using a sample-to-detector distance of 1603 mm. The q-range was calibrated using a silver behenate standard. Two-dimensional SAXS patterns were acquired using a fully integrated 2D multiwire, proportional counting, gas-filled detector, using an exposure time of 1 hour. The SAXS data has been corrected for sample thickness, sample transmission and background scattering. All the SAXS data was analyzed using the SAXSGUI software package to obtain radially integrated SAXS intensity versus scattering vector q, where $q = (4\pi/\lambda)\sin(\theta)$, and θ is one half of the

scattering angle and λ is the wavelength of X-ray. WAXD was performed using a Rigaku S-Max 3000 3 pinhole SAXS system, equipped with a rotating anode emitting X-rays with a wavelength of 0.154 nm (Cu K α). Scattering from a silver behenate standard calibrated the sample-to-detector distance. The sample-to-detector distance was 80.0 mm. WAXD two-dimensional diffraction patterns were obtained using an image plate, with an exposure time of 2 hours. All WAXD data were analyzed using the SAXSGUI software package to obtain azimuthal averaged WAXD intensity versus 2θ profiles, where θ is one half of the scattering angle. Cryo ultramicrotomy was performed using a Diatome MT12610 diamond blade in a RMC Products Powertome PC ultramicrotome equipped with a RX cryo attachment cutting 100 nm sections to generate a smooth surface for bulk atomic force microscopy (AFM) imaging. AFM of the bulk morphology was achieved by imaging the microtomed surface of the segmented polyurethane mounted in an epoxy block using a Veeco Multimode atomic force microscope in tapping mode with 42 N/m spring constant tips and a set point ratio of 0.65. DMA was performed using a TA Instruments Q800 dynamic mechanical analyzer utilizing a heating rate of 3 °C/min and amplitude of 50 μ m in tension mode. Variable temperature Fourier transform infrared spectroscopy (VT FT-IR) was performed using a Varian 670-IR equipped with a PIKE® GladiATR diamond heated stage accessory. Each sample was analyzed over a temperature range of 35 – 185 °C with a ramping rate of 1 °C/min. Spectra were collected every 5 °C and each spectrum was an average of 32 scans at a resolution of 4 cm⁻¹.

Peak Fitting

As seen in previous literature, curve fitting was used in the carbonyl stretching region to quantitatively compare the three peaks seen in the data, corresponding to two different states of hydrogen bonding bands and one “free” carbonyl band.²¹ Each spectrum was ATR corrected and

then adjusted with linear base line correction. Points for the base line were selected at minima in the spectra between 4000 and 400 cm^{-1} where no visible absorptions were detected, with specific emphasis near 1780 and 1565 cm^{-1} , on either side of the carbonyl-stretching region. The exact location of these minima adjacent to the carbonyl bands that were used to draw the linear base line were noted and also used as the upper and lower limits for peak fitting. Each of the three carbonyl bands were fit with a Gaussian peak shape using nonlinear least squares fitting in Microsoft® Excel. Initial estimates for the width, frequency (ν), and amplitude of each peak were made, and then fitting iterations were repeated in the software until constant values were reached. Afterward, the values for these three parameters were used in Wolfram Mathematica® to solve for the area under each curve. In an effort to address the fact that the absorption coefficient for the hydrogen bonding carbonyl bands is larger than that of the free carbonyl band, a correction factor, k , of 1.71 was used in accordance with the literature, to ensure that the total carbonyl region remains constant with changing temperature.^{21,22} To further evaluate the hydrogen bonded and free carbonyl bands across the different temperatures, CNT loadings, etc., the areas of the two hydrogen bonding bands for each spectra were combined. Then the relative areas for hydrogen bonded versus free carbonyl were compared for each sample.

4.4 Results and Discussions

Composite Synthetic Design

The simplicity of the polymer structure and resulting phase-separated morphology combined with desirable mechanical properties motivated the selection of polyurethane employed in this investigation. The diisocyanate selection and hard segment content utilized combined with the molecular weight of the PTMO soft segment limited crystallization of both

hard and soft segments. The non-planar aliphatic diisocyanate reduces hard segment crystallization.^{32,33} The ~2,000 g/mol PTMO soft segment and 45 wt% hard segment content ensured desirable mechanical properties while limiting soft segment crystallization. The hard segment content ensured plentiful hydrogen bonding sites to interact with hydrogen bonding groups on the MWCNTs. Targeting an amorphous system simplified composite characterization. The film casting procedure employed which included annealing at 80 °C for 7 h resulted in desirable tensile properties (see Chapter 3). SAXS and AFM analysis confirmed the presence of a phase separated morphology (**Figure 4.2**). SAXS displays a single scattering peak due to polyurethane phase separation, and the corresponding distance of ~18 nm correlates well to the domain spacing seen in AFM of the bulk morphology achieved through imaging a microtomed bulk surface. WAXD showed no observable crystallinity in the neat polyurethane, only displaying an amorphous halo (data not shown).

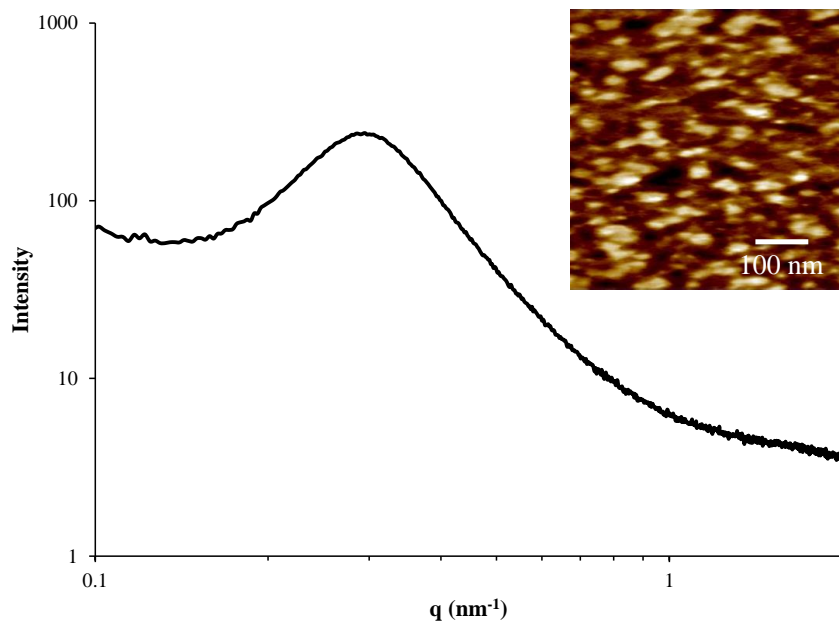


Figure 4.2. SAXS analysis of neat polyurethane. Inset shows AFM of microtomed surface of the segmented polyurethane displaying microphase separation.

The MWCNT structures utilized in this investigation provided varying levels of hydrogen bonding close to the MWCNT surface. Surface functionalization with hydrogen bonding groups is essential for thorough dispersion in hydrogen bonding polyurethane although no significant difference in ultimate tensile properties were found between the different types of hydrogen bonding MWCNTs (see Chapter 3). Purified MWCNTs represent a control with very limited hydrogen bonding capacity, with an almost completely carbon surface. Acid oxidation yielded MWCNTs functionalized with carboxylic acid groups (AO-MWCNTs), possessing a high degree of hydrogen bonding carboxylic acid groups on the MWCNT surface (see Chapter 3). Theoretically, hydrogen bonding capacity is increased in amide-amine functionalized MWCNTs (AA-MWCNTs) and further in amide-urea functionalized MWCNTs (AU-MWCNTs) through increasing the strength and number of hydrogen bonding groups. AO-MWCNTs, AA-MWCNTs, and AU-MWCNTs all possess a high degree of hydrogen bonding that affords efficient dispersibility in the polyurethane matrix and desirable composite mechanical properties (see Chapter 3). DMA and VT FT-IR experiments are employed here to further elucidate the nature of dynamic hydrogen bonding in these composites and differences between the types of MWCNTs.

Dynamic Mechanical Analysis

DMA investigated the thermomechanical properties of polyurethane-MWCNT composites. **Figure 4.3**, **Figure 4.4**, **Figure 4.5**, and **Figure 4.6** show the DMA analysis of polyurethane composites formed with purified MWCNTs, AO-MWCNTs, AA-MWCNTs, and AU-MWCNTs, respectively. A wide range of MWCNT loadings including 0.18, 0.6, 1.8, 2.4, 5, 7.5, and 10 wt% MWCNTs probed the effect of MWCNT loading on the thermomechanical

properties of the composites. All of the composites display similar behavior, exhibiting transitions characteristic of a segmented polyurethane, with notable differences in the high temperature region above 100 °C. The first transition around -75 °C was attributed to the PTMO soft segment T_g , which has a reported literature value of -79 °C.³⁴ The temperature of this transition indicates a PTMO rich phase and thorough phase separation, which correlates well with the morphological analysis in **Figure 4.2**. A rubbery plateau exists after this transition, in which the PTMO soft segment domains are mobile and the phase-separated hard segment domains serve as physical crosslinks, leading to viscoelastic properties. This plateau ends as the polymer begins to go through a second transition which spans 50-100 °C. This transition is attributed to softening of hard segments as the hard segment chains become mobile as they go through their T_g .³⁵

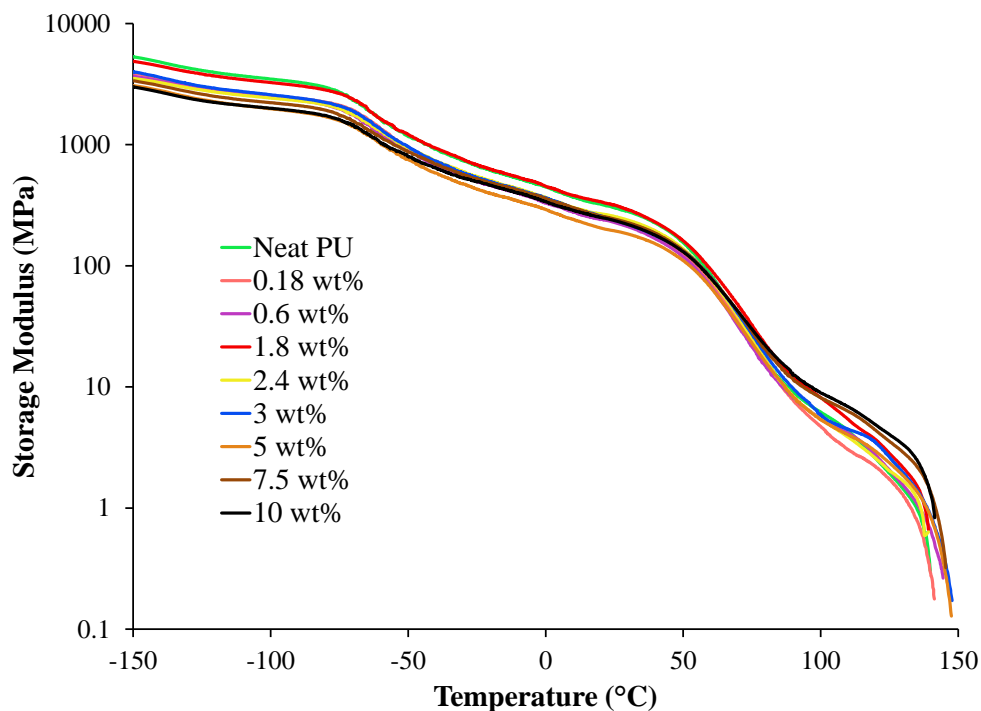


Figure 4.3. DMA comparison of purified MWCNT loading in segmented polyurethane composites.

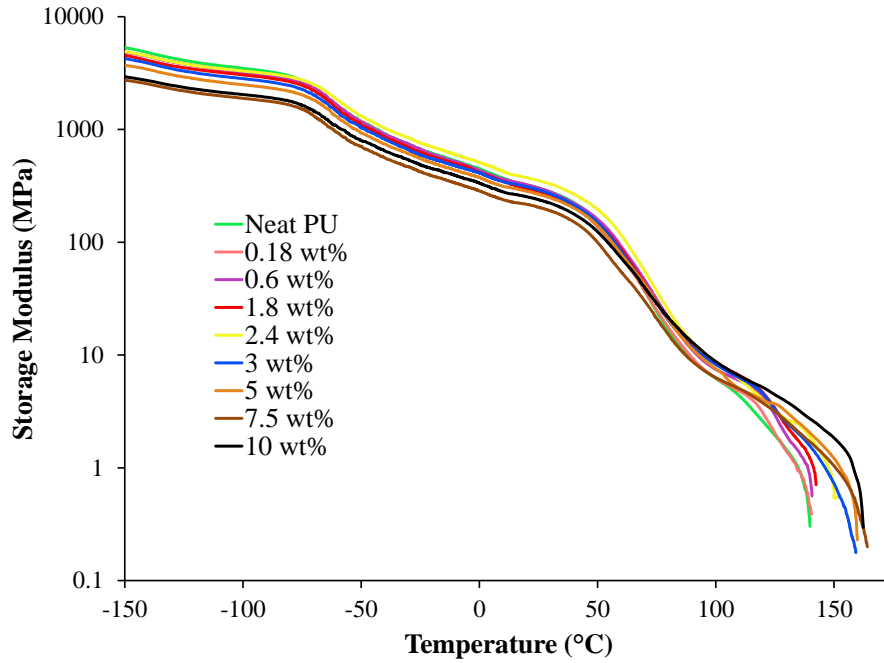


Figure 4.4. DMA comparison of AO-MWCNT loading in segmented polyurethane composites.

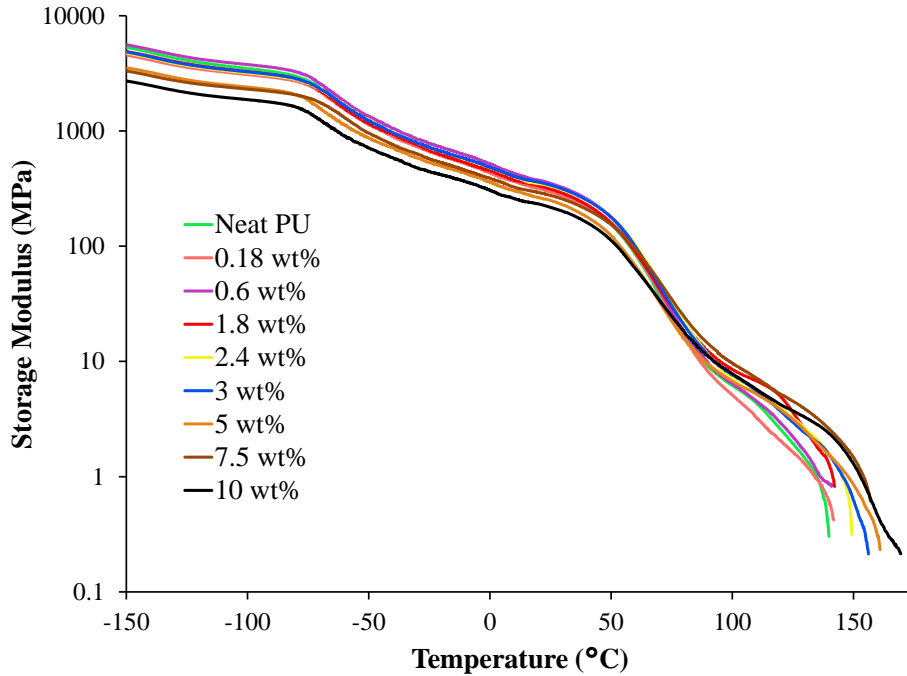


Figure 4.5. DMA comparison of AA-MWCNT loading in segmented polyurethane composites.

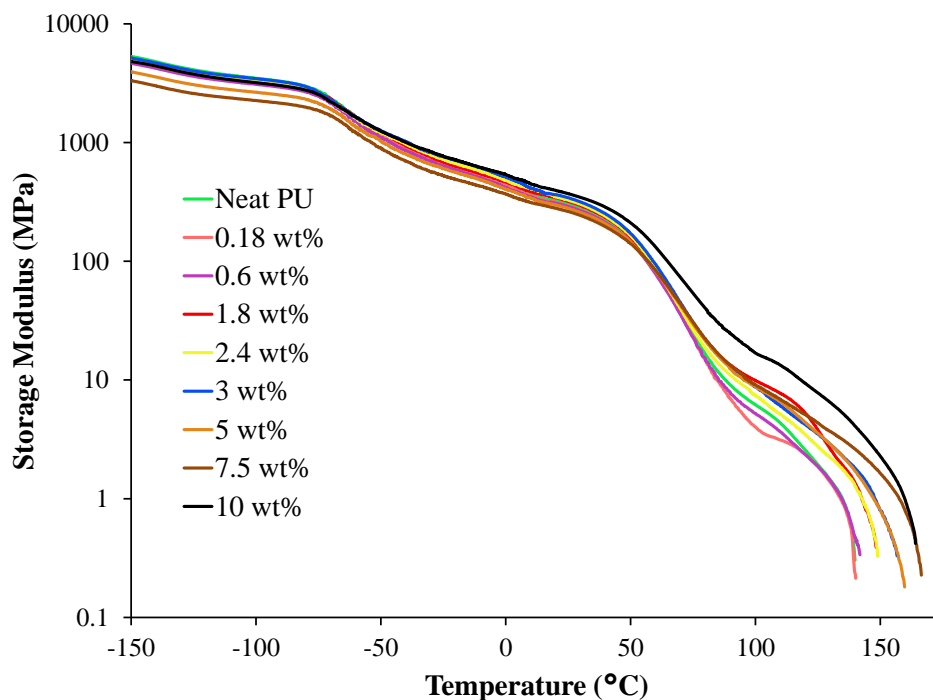


Figure 4.6. DMA comparison of AU-MWCNT loading in segmented polyurethane composites.

The first two transition occur similarly for all the composites, with no significant differences observable for changes in MWCNT loading or functionalization, indicating that the presence of MWCNTs did not significantly affect the soft or hard segment T_g s. However, the high temperature region above 100 °C where the neat polyurethane and composite films flow due to hydrogen bond dissociation does show significant differences. The neat polyurethane flowed around 140 °C where the urethane hydrogen bonds started to rapidly dissociate.²⁵ Varying the loading of purified MWCNTs which lack hydrogen bonding sites resulted in no significant difference or observable trend in the flow temperature, shown in **Figure 4.3**. All of the purified MWCNT composites flow at or before 150 °C. In contrast, varying the loading of MWCNTs functionalized with hydrogen bonding groups affected the composite flow temperature. The flow temperature in AO-MWCNT, AA-MWCNT, and AU-MWCNT composites shown in

Figure 4.4, Figure 4.5, and Figure 4.6, respectively, increases with increasing MWCNT loading. The flow temperature at the highest loadings of AO-MWCNT, AA-MWCNT, and AU-MWCNTs exceeds 170 °C. The incorporation of MWCNTs likely restricts polymer chain mobility at these temperatures necessitating higher temperatures to provide the chain motion required to dissociate the hydrogen bonds, resulting in higher flow temperatures. Purified MWCNTs do not disperse effectively in the polyurethane matrix, mostly existing as large aggregates in the composites (see Chapter 3), which likely accounts for the observed behavior compared to the functionalized MWCNTs which disperse effectively through intermolecular interactions with the polyurethane. The overall effect on the polymer chain mobility at these temperatures is likely related to the MWCNT dispersion, amount of MWCNTs, and intermolecular interactions with the polymer chains via the surface functionality. The intermolecular interactions with the polymer also initially influence the dispersion of the MWCNTs in the polymer matrix, allowing for individualized dispersion at low loadings with proper surface functionalization. Even with effective intermolecular interactions through surface functionalization, the hydrogen bonding MWCNTs likely form some large aggregates at higher loadings (see Chapter 3). VT FT-IR further investigated the state of hydrogen bonding in the polyurethane-MWCNT composites.

Variable Temperature FT-IR – Basic Data Collection and Peak Fitting

VT FT-IR enables investigation of temperature-dependent hydrogen bonding in the polyurethane-MWCNT composites. Analysis of the carbonyl region in FT-IR (about 1600 – 1800 cm^{-1}) as a function of temperature reveals the temperature-dependent nature of hydrogen bonding in this polyurethane and the composites. The carbonyl region in this polymer is

comprised of overlapping peaks of carbonyls in different hydrogen bonding states that display different FT-IR absorbance due to the effect of hydrogen bonding on the vibration of the carbonyl bond. Stretching of the C=O bond gives rise to the characteristic absorbances, and hydrogen bonding of the oxygen atom to amine protons in other urethane linkages affects the vibration of the bond. Carbonyls not associating in hydrogen bonding, or “free” carbonyls, are found at higher wavenumbers than carbonyls in identical structures that are participating in hydrogen bonding.^{21,22,25} Hydrogen bonding to the carbonyl oxygen reduces the vibrational frequency of the carbonyl stretch, shifting the FT-IR absorbance to lower wavenumbers, and the type and strength of the hydrogen bonding affect this change in absorbance. The populations of free carbonyls and carbonyls associating in hydrogen bonding changes as a function of temperature in the neat polyurethane (shown in **Figure 4.7**) and composites. At 35 °C, most of the carbonyls are associating in hydrogen bonding. Increased temperatures led to increased chain motion, disrupting hydrogen bonding and changing the dynamic hydrogen bonding equilibrium at high temperatures, which shifted the carbonyl absorbance to higher wavenumbers. Performing the VT FT-IR experiment on all composites and analyzing the carbonyl regions revealed the effect of MWCNT surface functionality and loading on the temperature-dependent hydrogen bonding in the composites.

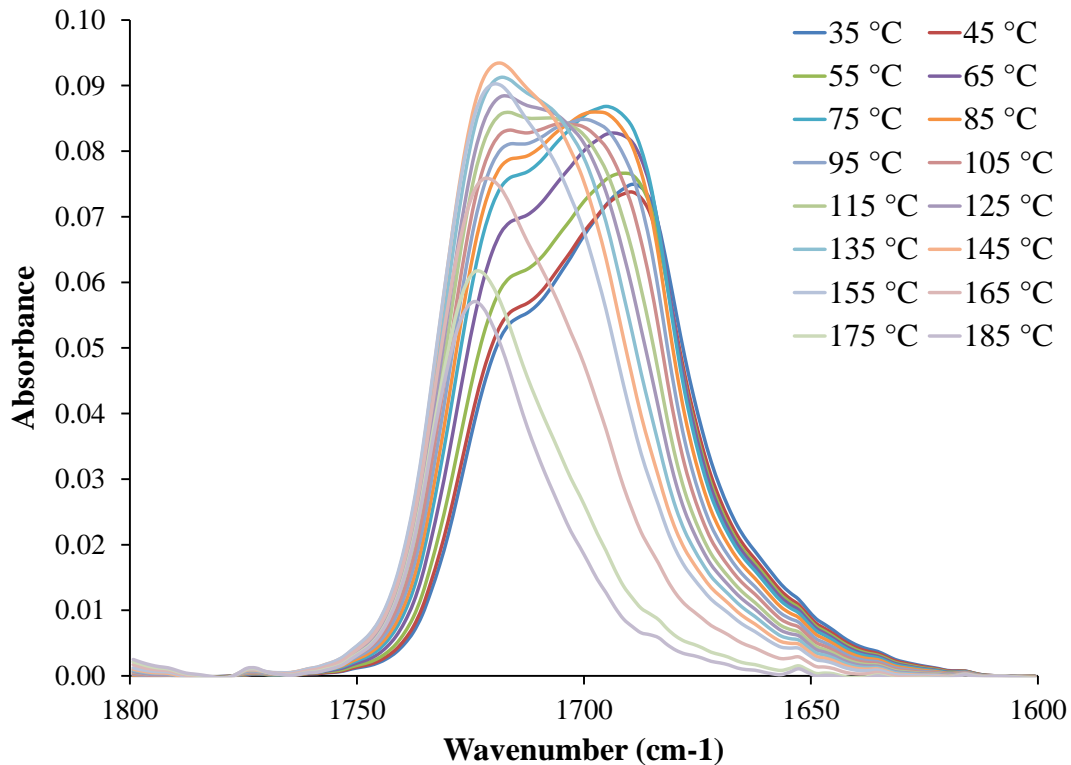


Figure 4.7. Representative variable temperature FT-IR spectra (neat polyurethane shown).

The spectra at each temperature were peak fitted to further analyze and quantify the extent of hydrogen bonding as a function of temperature. Different states of hydrogen bonding exist for the same structure, which relate to the order in the hydrogen bonding domains.^{21,22,25} The peak fitting of the neat polyurethane at 35 °C is shown in **Figure 4.8** which reveals three peaks, all attributed to carbonyl bond vibrations in the urethane linkages. The highest wavenumber peak centered around 1720 cm^{-1} is attributed to the free carbonyls not associating in hydrogen bonding. The other two peaks centered around 1690 and 1670 cm^{-1} are attributed to carbonyls participating in hydrogen bonding, designated as disordered and ordered hydrogen bonding, respectively.²¹ Disordered hydrogen bonding is attributed to hard segment carbonyls in an amorphous region, whereas ordered hydrogen bonding is associated with highly-ordered, or

possibly crystalline, hard segment domains.^{19,21,23} There is a small amount of ordered hydrogen bonding (relative to the disordered hydrogen bonding carbonyl content, which contrasts with the WAXD analysis. The amount of hard segment crystallization is likely to low to be observed in WAXD or is hidden under the amorphous halo. **Figure 4.9** shows the peak fitting of the neat polyurethane at 185 °C, where most of the carbonyl absorbance shifted to higher wavenumbers as the hydrogen bonds have largely dissociated. The position of the peak maxima shift slightly in the peak fitting, moving to higher wavenumbers as the temperature is increased. The relative area (out of 1) of each peak in the carbonyl region allows for quantitation of the hydrogen bonding character as a function of temperature. Although thermal fission of the urethane bonds leading to chain scission and hydrogen bond disruption may occur at the highest temperatures probed, the all aliphatic polyurethane structure limits this possibility as aliphatic isocyanates and alcohols lead to the highest thermal stabilities and bond fission temperatures.^{36,37} Unfortunately, the diamond crystal window in the IR spectrometer prevents the analysis of isocyanate evolution during the VT FT-IR experiments.

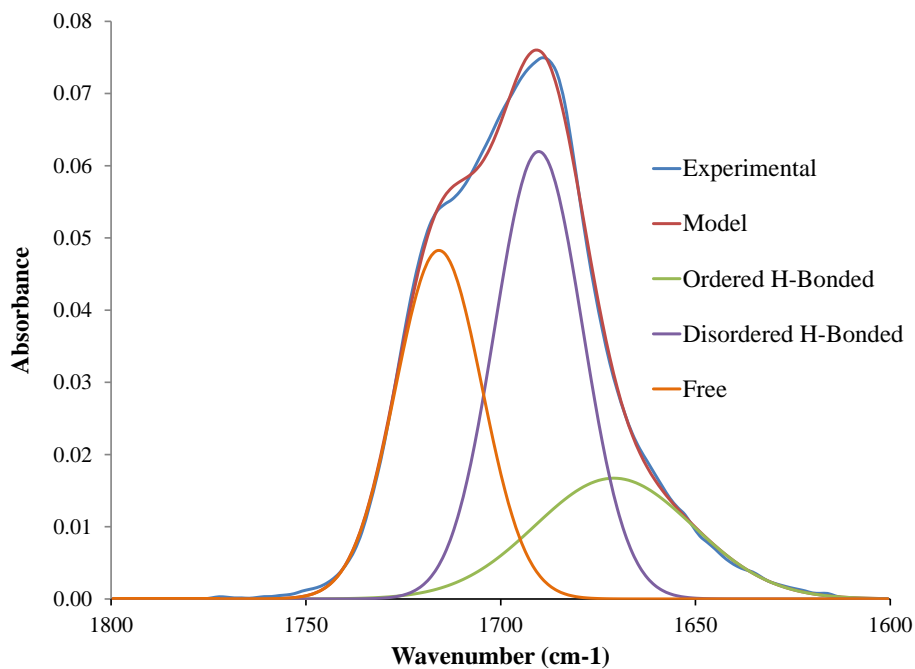


Figure 4.8. Representative peak fitting (neat polyurethane at 35 °C).

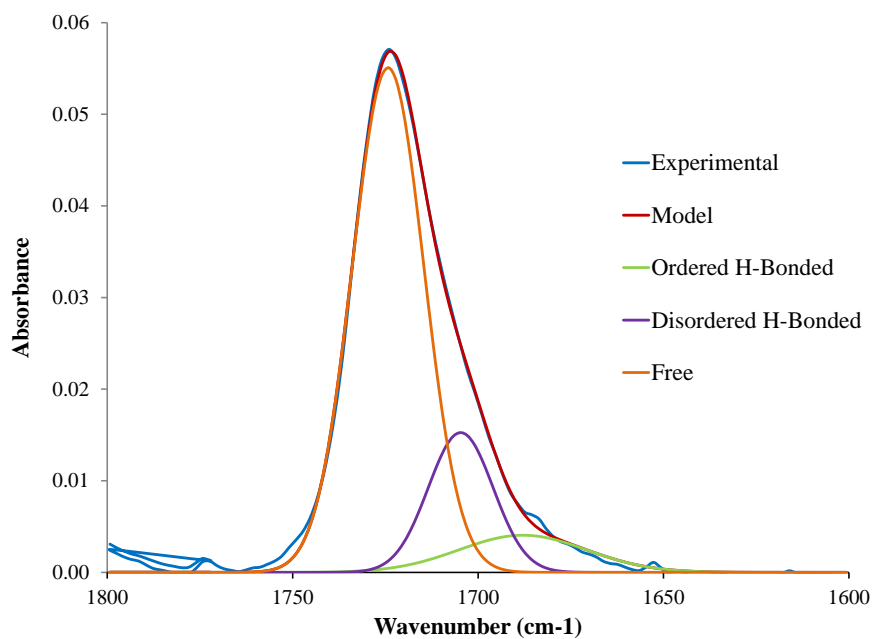


Figure 4.9. Representative peak fitting (neat polyurethane at 185 °C).

Variable Temperature FT-IR – Analysis of Hydrogen Bonding Populations and R Index

Peak fitting of each spectra into the three carbonyl peaks allows for analysis of hydrogen bonding in the composites as a function of temperature. The large amount of data led to selective peak fitting of MWCNT loadings of 0.18, 1.8, 5, and 10 wt % every 10 degrees from 35 to 185 °C to investigate the effect of loading level and surface functionality on hydrogen bonding in the composites. Adjusting the free carbonyl content using a factor of 1.71 corrected for the difference in absorption coefficients between the free and hydrogen bonding carbonyls according to literature.^{21,22} The following analysis combines ordered and disordered relative peak areas into a single hydrogen bonding population and compares the hydrogen bonding urethane carbonyls to the free carbonyls as a function of temperature. The ordered hydrogen bonding content was low overall, and analysis of the three peaks independently did not reveal any additional information. Other analytical methods did not detect crystalline content for this hard segment structure and polyurethane composition, and any crystalline hard segment likely only contributes slightly to the overall hard segment content. We assume that carbonyl groups on the MWCNTs are not observed due to their relatively low concentration and that the polymer carbonyl groups hydrogen bond to hydrogen bond donors in the polymer hard segments or on the surface of the MWCNTs. Plotting the hydrogen bonding and free carbonyl populations for each composite versus temperature reveals the effect of MWCNT surface functionality and loading on the composite hydrogen bonding. **Figures 4.10-4.14** show this analysis for the AO-MWCNT composites.

Figure 4.10 shows the relative areas of the combined hydrogen bonding peaks and free carbonyl peak versus temperature for the neat polyurethane. Initially the hydrogen bonding

content comprises a slight majority of the carbonyl groups, and around temperatures corresponding to the beginning of the hard segment T_g the relative free carbonyl content begins to increase. Although direct comparisons between the DMA results and VT FT-IR experiments are not accurate due to the different heating rates and nature of the experiments, and these correlations may not be significant, many intriguing similarities are observed for the neat polyurethane. The relative areas of the free and hydrogen bonded peaks changed slowly over the temperature range of the hard segment T_g , about 50 -100 °C, until they begin to level out remaining relatively constant from 115 – 155 °C. After this, the hydrogen bonds began to rapidly dissociate leading to a sharp change in the relative peak areas in the temperature range above 155 °C. This beginning of rapid change in hydrogen bonding content also correlated roughly with the flow in DMA. Most importantly this identifies the temperature region above 150 °C as where the hydrogen bonds begin to rapidly dissociate in the neat polyurethane.

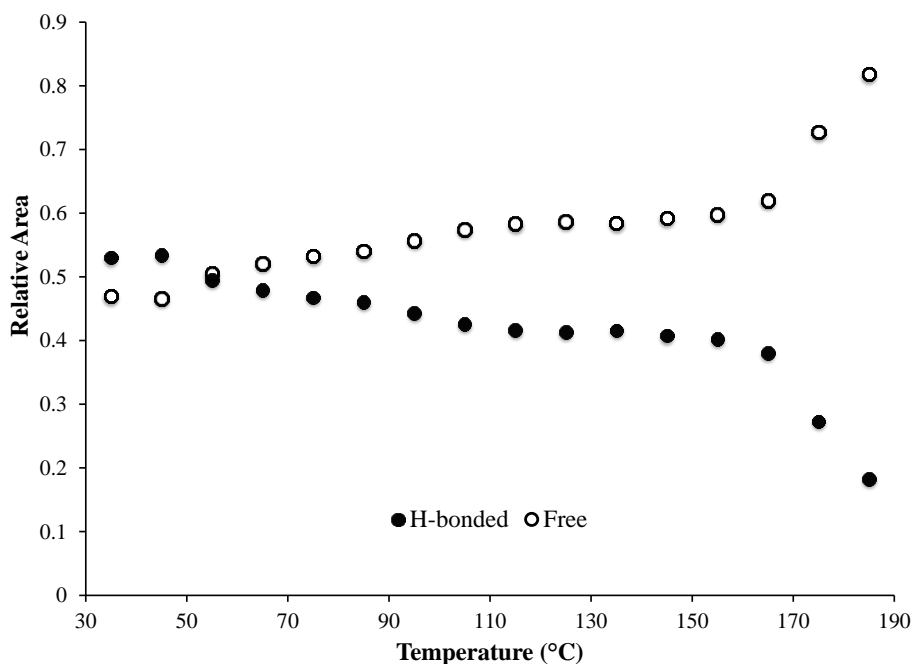


Figure 4.10. Relative area of hydrogen bonding carbonyl peaks and free carbonyl peaks as a function of temperature (neat polyurethane).

Figures 4.11-4.14 show the effect of adding AO-MWCNTs on the temperature-dependent hydrogen bonding in polyurethane composites. Even low loadings of 0.18 wt % drastically effect the appearance of this plot. Overall, adding AO-MWCNTs increased the relative hydrogen bonded content across the temperature range. Addition of AO-MWCNTs also prevented the crossover of the populations at higher AO-MWCNT loadings, where the relative free carbonyl content overtakes the relative hydrogen bonding carbonyl content. In addition, introduction of the AO-MWCNTs led to a different behavior in these relative area plots, most pronounced in the 1.8 ad 5 wt % AO-MWCNT composites. Initially the hydrogen bonding content decreased similar to in the neat polyurethane, but after the hard segment T_g around 100 °C the hydrogen bonding content increases until the high temperature range above 150 °C where the hydrogen bonds began to dissociate, although less rapidly than in the neat polyurethane. This effectively represents an annealing region where increased chain mobility after the hard segment T_g allowed for urethane reorganization and increased hydrogen bonding before high temperature dissociation. This contrasts with the neat polyurethane where this region between 100 – 150 °C is a plateau, and the reason for this difference is not yet understood. The other MWCNT composite series displayed similar trends to the AO-MWCNT series, where the overall hydrogen bonding content and temperatures required for similar dissociation of hydrogen bonding increased with increasing MWCNT content. The magnitude of these effects, however, depended on the surface functionality, which is compared below in terms of the hydrogen bonding index values.

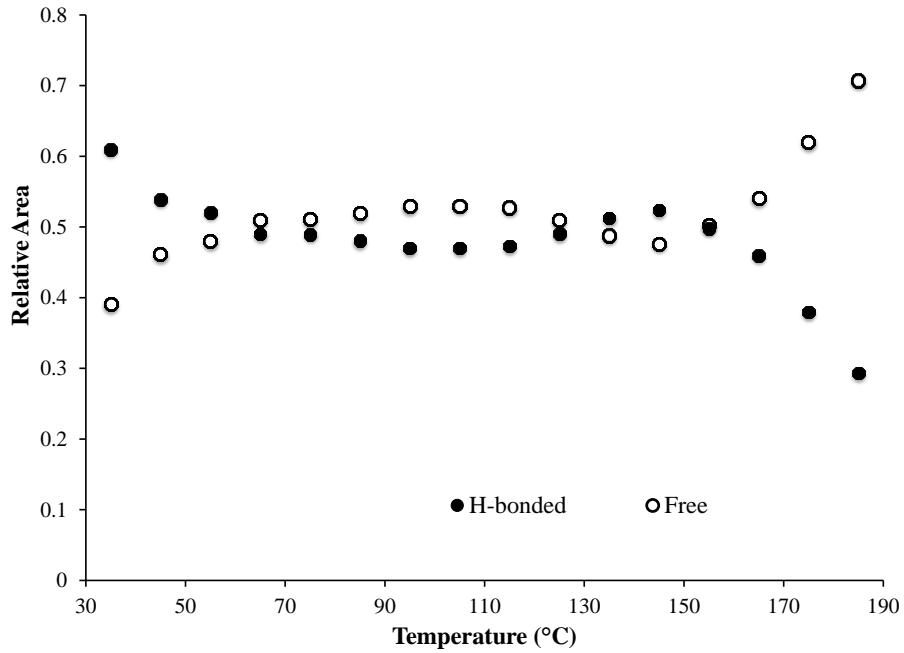


Figure 4.11. Relative area of hydrogen bonding carbonyl peaks and free carbonyl peaks as a function of temperature (0.18 wt% AO-MWCNTs polyurethane).

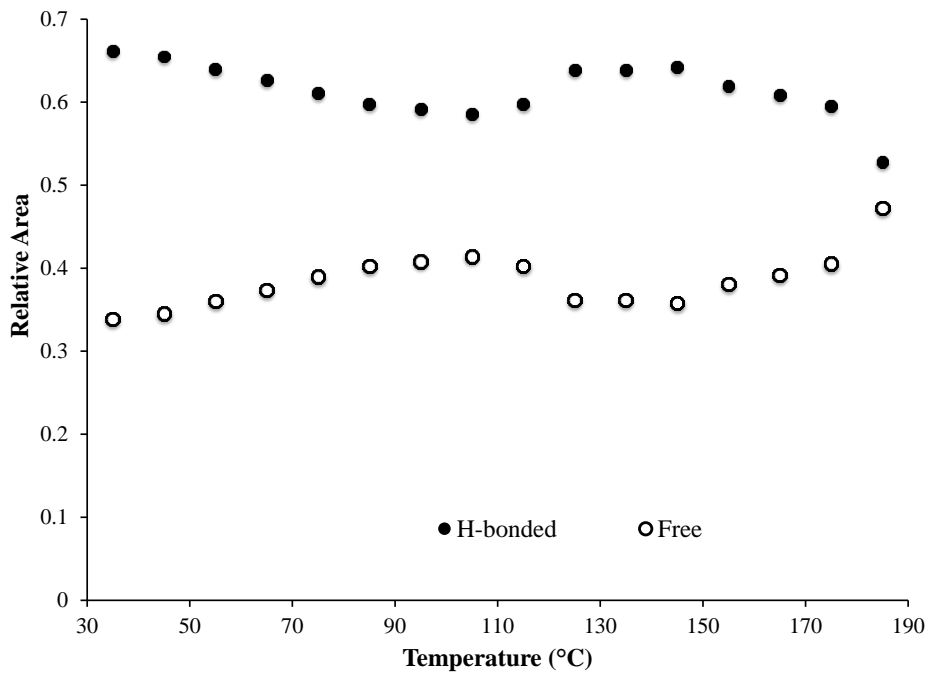


Figure 4.12. Relative area of hydrogen bonding carbonyl peaks and free carbonyl peaks as a function of temperature (1.8 wt% AO-MWCNTs polyurethane).

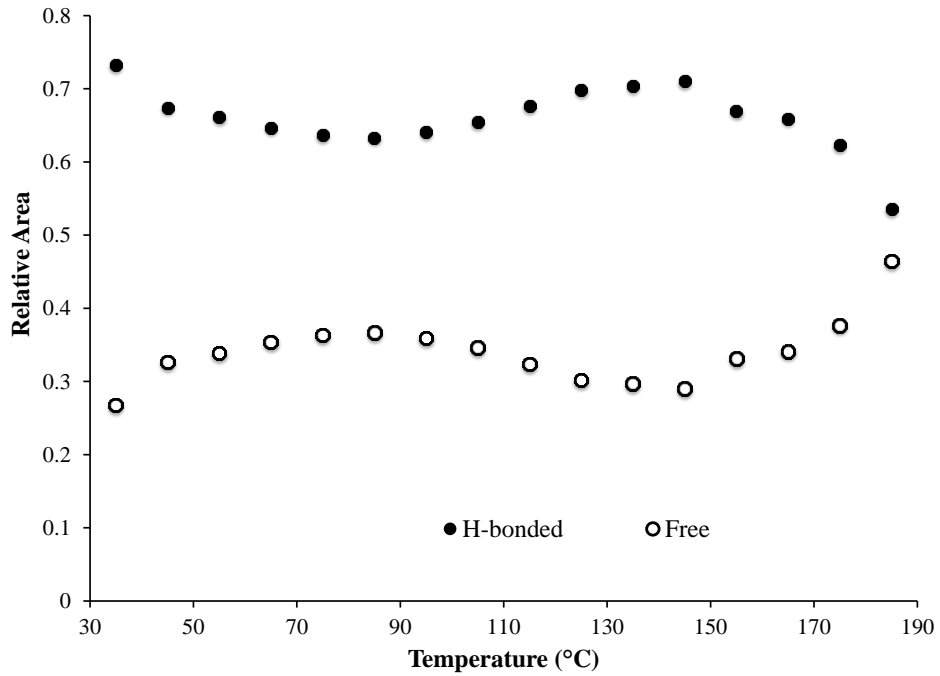


Figure 4.13. Relative area of hydrogen bonding carbonyl peaks and free carbonyl peaks as a function of temperature (5 wt% AO-MWCNTs polyurethane).

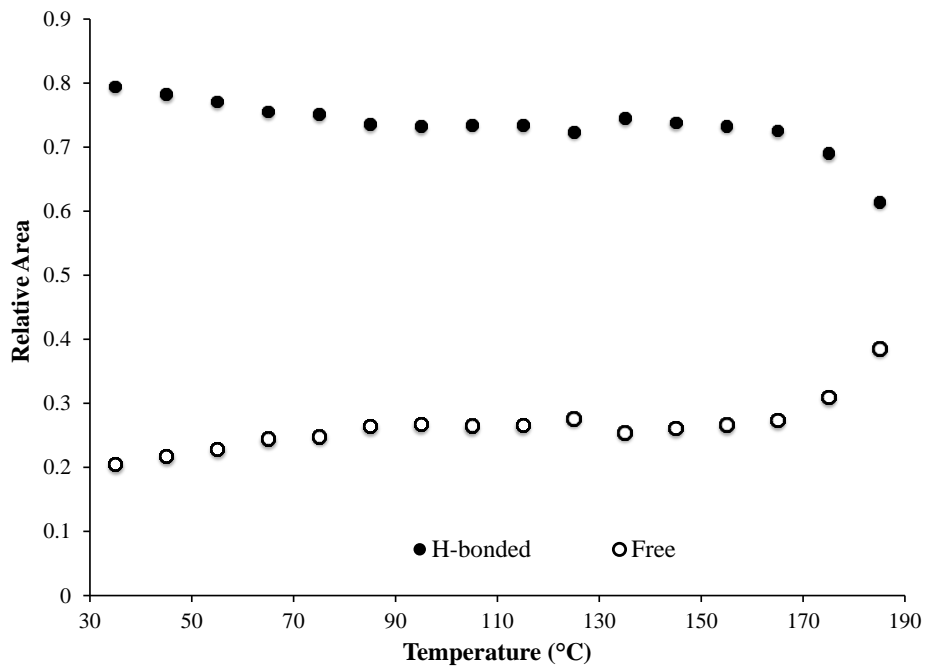


Figure 4.14. Relative area of hydrogen bonding carbonyl peaks and free carbonyl peaks as a function of temperature (10 wt% AO-MWCNTs polyurethane).

Percent hydrogen bonding is a convenient way to express the level of hydrogen bonding in polyurethanes and similar polymers, analogous to the hydrogen bonding index shown in the literature.³⁰ **Figures 4.15-4.18** show the percent hydrogen bonding values as a function of temperature for purified MWCNT, AO-MWCNT, AA-MWCNT, and AU-MWCNT composites, respectively. Comparing percent hydrogen bonding reveals the effect of the surface functionality on the hydrogen bonding in the composites. For all of the MWCNT series, increasing the MWCNT loading typically increased percent hydrogen bonding at any given temperature. This effect is amplified as the hydrogen bonding capacity of the MWCNT surface functionalization is increased, with a few exceptions. **Figure 4.19** summarizes the initial percent hydrogen bonded carbonyl values (at 35 °C) and final percent hydrogen bonded carbonyl values (at 185 °C) for the different MWCNT composites series as a function of MWCNT loading. It is evident that the hydrogen bonding functionalized MWCNTs affect the percent hydrogen bonded carbonyl content more drastically than the non-hydrogen bonding purified MWCNTs. Incorporation of MWCNTs with hydrogen bonding surface functionality increases percent hydrogen bonded carbonyl values and necessitates higher temperatures for hydrogen bonding dissociation, which correlates well with the observed DMA flow temperatures.

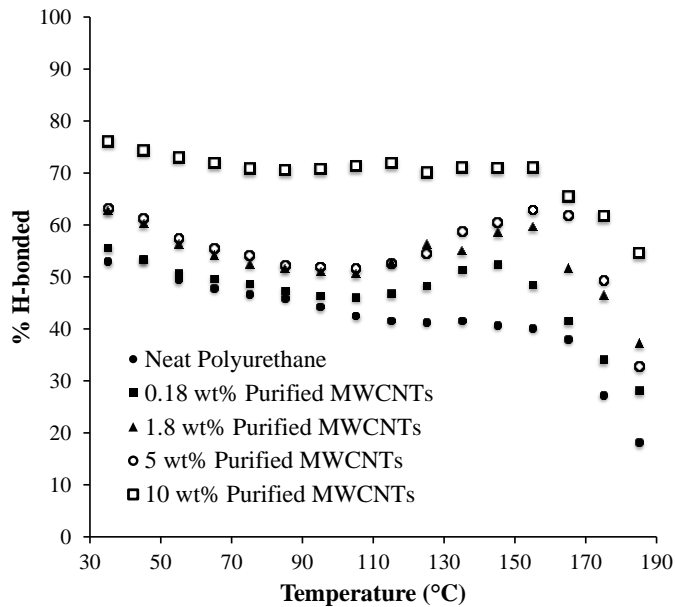


Figure 4.15. Percent hydrogen bonded carbonyl of purified MWCNT composites as a function of temperature.

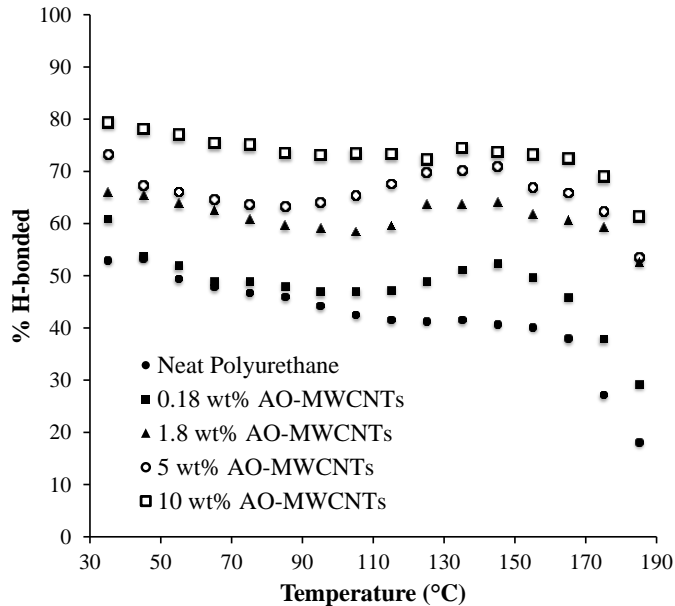


Figure 4.16. Percent hydrogen bonded carbonyl of AO-MWCNT composites as a function of temperature.

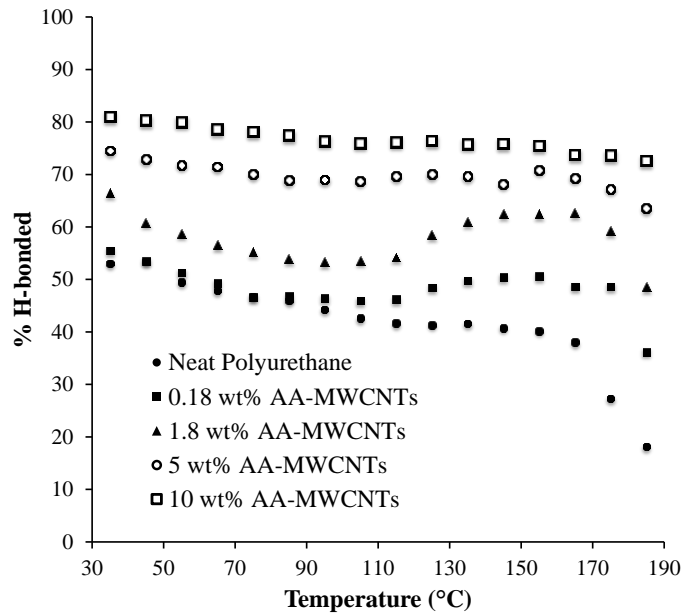


Figure 4.17. Percent hydrogen bonded carbonyl of AA-MWCNT composites as a function of temperature.

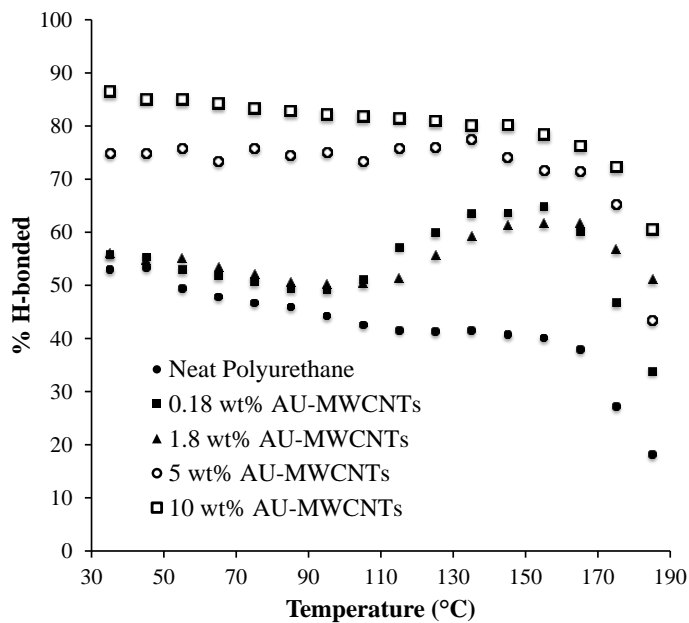


Figure 4.18. Percent hydrogen bonded carbonyl of AU-MWCNT composites as a function of temperature.

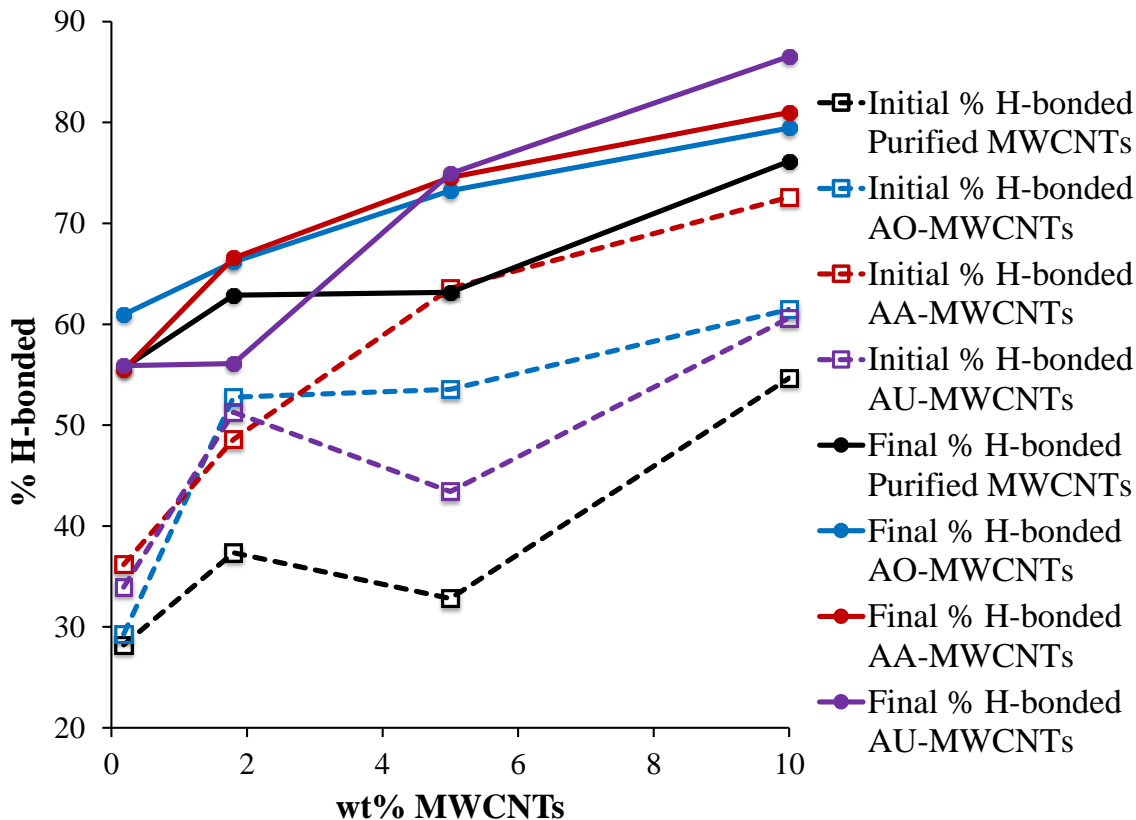


Figure 4.19. Comparison of initial percent hydrogen bonded (35 °C) and final percent hydrogen bonded (185 °C) carbonyl values of each MWCNT composite series as a function of wt% MWCNTs.

Dispersion and interfacial interactions with the polyurethane matrix, which are related, explain the differences between the purified MWCNTs and hydrogen bonding carbon nanotubes in these composites. Improved interactions with a polymer matrix typically lead to enhanced dispersion, which is evident in TEM of these composites, where the functionalized MWCNTs are well dispersed compared to the purified MWCNTs (see Chapter 3). Once the MWCNTs are dispersed, the hydrogen bonding surface functionality serves to increase interfacial interactions between the MWCNTs and the polyurethane matrix. The thorough dispersion and high degree of hydrogen bonding surface functionality in the functionalized MWCNT composites provided

efficient hydrogen bonding sites over a large accessible area for the polymer urethane groups to hydrogen bond with which may increase the hydrogen bonded carbonyl content in these composites. In addition, the presence of rigid MWCNTs in the composites should reduce the overall polymer chain mobility, requiring higher temperatures to dissociate hydrogen bonds in the flow temperature region, which is amplified in well-dispersed composites with efficient polymer-MWCNT interactions. These effects influence the processing procedures and capabilities for polyurethane-MWCNT composites, and the end state of the composite hydrogen bonding. Further work is required to clarify the drastic increase of percent hydrogen bonding at low temperatures in composites with high loadings of MWCNTs, observed regardless of the surface functionality. Analysis of the -NH stretching region in the VT FT-IR data would further elucidate the state of hydrogen bonding in these composites, and provides a way of expressing the phase separation in addition to SAXS analysis of composites. Differential scanning calorimetry studies of the composites would also help corroborate the findings of this study.

4.5 Conclusions

In this study, DMA and VT FT-IR investigated the effect of MWCNT incorporation on mechanical properties and hydrogen bonding in polyurethane nanocomposites. MWCNTs with carboxylic acid, amide-amine, and amide-urea functionalities provided MWCNTs with varied hydrogen bonding on the MWCNT surface. VT FT-IR revealed that MWCNTs functionalized with hydrogen bonding groups displayed a more pronounced effect on urethane carbonyl hydrogen bonding in the nanocomposites than non-functionalized MWCNTs. Addition of the hydrogen bonding MWCNTs increased carbonyl hydrogen bonding and necessitated higher temperatures for comparable hydrogen bonding dissociation. DMA showed that incorporation of

the functionalized MWCNTs raised the composite flow temperature, in contrast to non-functionalized MWCNTs that displayed a marginal effect. These results correlate well with previous findings, which show these hydrogen bonding MWCNTs possess greater dispersion and intermolecular interactions with polyurethanes than non-functionalized MWCNTs.

4.6 References

1. Andrews, R.; Weisenberger, M. C. *Curr. Opin. Solid State Mater. Sci.* **2004**, *8*, 31.
2. Moniruzzaman, M.; Winey, K. I. *Macromolecules* **2006**, *39*, 5194.
3. Du, J. H.; Bai, J.; Cheng, H. M. *Express Polymer Letters* **2007**, *1*, 253.
4. Bose, S.; Khare, R. A.; Moldenaers, P. *Polymer* **2010**, *51*, 975.
5. Rahmat, M.; Hubert, P. *Compos. Sci. Technol.* **2011**, *72*, 72.
6. Ma, P.-C.; Siddiqui, N. A.; Marom, G.; Kim, J.-K. *Composites Part A: Applied Science and Manufacturing* **2010**, *41*, 1345.
7. Balasubramanian, K.; Burghard, M. *Small* **2005**, *1*, 180.
8. Sahoo, N. G.; Rana, S.; Cho, J. W.; Li, L.; Chan, S. H. *Prog. Polym. Sci.* **2010**, *35*, 837.
9. Gojny, F. H.; Wichmann, M. H. G.; Köpke, U.; Fiedler, B.; Schulte, K. *Compos. Sci. Technol.* **2004**, *64*, 2363.
10. Spitalsky, Z.; Tasis, D.; Papagelis, K.; Galiotis, C. *Prog. Polym. Sci.* **2010**, *35*, 357.
11. Ventura, D. N.; Stone, R. A.; Chen, K.-S.; Hariri, H. H.; Riddle, K. A.; Fellers, T. J.; Yun, C. S.; Strouse, G. F.; Kroto, H. W.; Acquah, S. F. A. *Carbon* **2010**, *48*, 987.
12. Aviles, F.; Cauich-Rodriguez, J. V.; Moo-Tah, L.; May-Pat, A.; Vargas-Coronado, R. *Carbon* **2009**, *47*, 2970.
13. Datsyuk, V.; Kalyva, M.; Papagelis, K.; Parthenios, J.; Tasis, D.; Siokou, A.; Kallitsis, I.; Galiotis, C. *Carbon* **2008**, *46*, 833.
14. Rosca, I. D.; Watari, F.; Uo, M.; Akasaka, T. *Carbon* **2005**, *43*, 3124.
15. Banerjee, S.; Hemraj-Benny, T.; Wong, S. S. *Adv. Mater.* **2005**, *17*, 17.
16. Camberlin, Y.; Pascault, J. P. *Journal of Polymer Science: Polymer Chemistry Edition* **1983**, *21*, 415.
17. Garrett, J. T.; Xu, R.; Cho, J.; Runt, J. *Polymer* **2003**, *44*, 2711.
18. Sheth, J. P.; Unal, S.; Yilgor, E.; Yilgor, I.; Beyler, F. L.; Long, T. E.; Wilkes, G. L. *Polymer* **2005**, *46*, 10180.
19. Heintz, A. M.; McKiernan, R. L.; Gido, S. P.; Penelle, J.; Hsu, S. L.; Sasaki, S.; Takahara, A.; Kajiyama, T. *Macromolecules* **2002**, *35*, 3117.
20. Yilgör, E.; Burgaz, E.; Yurtsever, E.; Yilgör, İ. *Polymer* **2000**, *41*, 849.
21. Coleman, M. M.; Lee, K. H.; Skrovanek, D. J.; Painter, P. C. *Macromolecules* **1986**, *19*, 2149.
22. Wang, W.; Wang, W.; Chen, X.; Jing, X.; Su, Z. *J. Polym. Sci., Part B: Polym. Phys.* **2009**, *47*, 685.
23. Buckwalter, D. J.; Inglefield, D. L.; Enokida, J. S.; Hudson, A. G.; Moore, R. B.; Long, T. E. *Macromol. Chem. Phys.* **2013**, *214*, 2073.

24. Buckwalter, D. J.; Zhang, M.; Inglefield Jr, D. L.; Moore, R. B.; Long, T. E. *Polymer* **2013**, *54*, 4849.
25. Teo, L.-S.; Chen, C.-Y.; Kuo, J.-F. *Macromolecules* **1997**, *30*, 1793.
26. Bistričić, L.; Baranović, G.; Leskovic, M.; Bajsić, E. G. *Eur. Polym. J.* **2010**, *46*, 1975.
27. Ciobanu, L.-C.; Ciobanu, C.; Dorohoi, D. *High Perform. Polym.* **2010**, *22*, 56.
28. Phua, S. L.; Yang, L.; Toh, C. L.; Huang, S.; Tsakadze, Z.; Lau, S. K.; Mai, Y.-W.; Lu, X. *ACS Applied Materials & Interfaces* **2012**, *4*, 4571.
29. Chen, G.; Wei, M.; Chen, J.; Huang, J.; Dufresne, A.; Chang, P. R. *Polymer* **2008**, *49*, 1860.
30. Xia, H.; Song, M. *Soft Matter* **2005**, *1*, 386.
31. Li, Z.; Lin, W.; Moon, K.-S.; Wilkins, S. J.; Yao, Y.; Watkins, K.; Morato, L.; Wong, C. *Carbon* **2011**, *49*, 4138.
32. Seneker, S. D.; Born, L.; Schmelzer, H. G.; Eisenbach, C. D.; Fischer, K. *Colloid. Polym. Sci.* **1992**, *270*, 543.
33. Lee, D.-K.; Tsai, H.-B. *J. Appl. Polym. Sci.* **2000**, *75*, 167.
34. Yoon, S. C.; Ratner, B. D. *Macromolecules* **1988**, *21*, 2392.
35. Klinedinst, D. B.; Yilgör, I.; Yilgör, E.; Zhang, M.; Wilkes, G. L. *Polymer* **2012**, *53*, 5358.
36. Song, Y. M.; Chen, W. C.; Yu, T. L.; Linliu, K.; Tseng, Y. H. *J. Appl. Polym. Sci.* **1996**, *62*, 827.
37. Joel, D.; Hauser, A. *Die Angewandte Makromolekulare Chemie* **1994**, *217*, 191.

Chapter 5: Imidazole-Containing Block Copolymers as Stabilizers for Theranostic Carbon Nanohorn-Quantum Dot Nanocomplexes

David L. Inglefield Jr.^a, Allison Pekkanen^b, Michael H. Allen Jr.^a, Marissa Nichole Rylander^{b,c}, Robert J. Bodnar^d, and Timothy E. Long^{ab}

^a*Department of Chemistry*, ^b*Macromolecules and Interfaces Institute*, ^b*School of Biomedical Engineering and Sciences*, ^c*Department of Mechanical Engineering*, ^d*Department of Geosciences*

Virginia Tech, Blacksburg, VA 24061

5.1 Abstract

Unique material properties of carbonaceous nanomaterials combined with their synthetic versatility continues to catalyze research into their fundamental properties and applications. Various forms of graphene based nanomaterials, including fullerenes, single-walled carbon nanotubes, multi-walled carbon nanotubes, and graphene sheets remain at research frontiers, enabling numerous applications in emerging technologies ranging from energy to medicine. Carbon nanohorns, spherical aggregates of conical single-walled carbon nanotubes, display particularly promising properties for medical applications of carbonaceous nanomaterials because of their size, shape, and limited toxicity. Carbonaceous nanomaterials, and carbon nanohorns in particular, represent attractive candidates for photothermal cancer therapy, which employs laser induced heating of nanoparticles at tumor sites and thermally destroys cancer cells. Combining diagnostic bioimaging with photothermal therapy increases the utility of nanoparticles in cancer therapy. Herein, we report the formation of theranostic nanocomplexes that combine carbon nanohorns, quantum dots, and a diblock copolymer into a stable nanocomplex with an average size < 100 nm. As promising candidates for photothermal cancer

therapy, these nanocomplexes offer further versatility to include anticancer drugs and targeting ligands in their multifunctional design.

5.2 Introduction

The ability of carbonaceous nanomaterials (CNMs) to serve as scaffolds for the attachment of drugs, targeting ligands, polymers, and inorganic nanoparticles drives research into novel multifunctional nanomaterials for a variety of applications, including energy production and storage, bioimaging, and cancer therapy.¹⁻¹⁵ Currently, intense investigation focuses on CNMs such as fullerenes, single-walled carbon nanotubes, multi-walled carbon nanotubes, carbon nanohorns, and graphene sheets for many biological applications relating to cancer treatment, including gene delivery, anticancer drug delivery, and photothermal cancer therapy.^{10,16-23} Due to the complexity of cancer and devastating side-effects and complications of many established treatments, new cancer therapies that efficiently destroy tumor tissue with limited invasion and healthy tissue damage are highly desirable. Photothermal cancer therapy represents one of the more promising and intensely researched areas of emerging cancer treatments.

Theranostic materials combine therapeutic and diagnostic features.^{24,25} The synergistic combination of polymers and nanoparticles creates hybrid theranostic systems capable of delivering photothermal cancer therapy and bioimaging diagnostics.²⁶⁻²⁸ Quantum dots (QDs) prove extremely useful in bioimaging and theranostic applications due to their efficient and precise size-dependent fluorescent imaging, and commercial availability of QDs with ZnS shells allow for a variety of conjugations.²⁹⁻³¹ QDs possess many advantages over other fluorescent probes such as chemical resistance, low propensity to photobleach, and the ability to fine tune

fluorescence with QD core diameter.²⁹ Although CdSe/ZnS core/shell quantum dots display cytotoxicity due to the heavy metal core, the cytotoxicity depends on the environment and surface coating.³² QDs provided diagnostic capabilities in a number of recent CNM-based photothermal cancer theranostic materials. Hu *et al.* demonstrated the formation of QD-tagged reduced graphene oxide sheet nanocomposites and their photothermal therapy, and local heating quenched the fluorescence of the QDs, leading to spatial and temporal monitoring of photothermal therapy through QD imaging.²⁶

Carbon nanohorns (CNHs) are spherical aggregates of single-walled carbon nanotubes with conical ends that display potential for biological applications due to their size range, shape, and lack of cytotoxic metal catalysts.^{33,34} Laser ablation techniques produce CNHs in a variety of diameters with low systemic toxicity, and their graphene surface allows for a variety of surface functionalizations.³⁵ Also, the unique structure of CNHs facilitates anticancer drug loading into cone interiors.^{22,36-38} Many successful studies demonstrate the utility of CNHs in biomedical applications relating to photothermal cancer therapy.^{39,40} Zhang *et al.* demonstrated complexation of encapsulated trimetallic nitride endohedral metallofullerene peapod CNHs with QDs using carbodiimide coupling to introduce surface thiols to oxidized CNHs for subsequent QD complexation, enabling imaging of the cellular uptake of these particles using the QD fluorescence.²⁸ Zimmerman *et al.* described similar CNH-QD complexes to elucidate the intracellular tracking of these nanoparticles. Endocytosis of the nanocomplexes depended on cell type, and the particles displayed localization in the cytoplasm and nuclei of cells as a function of time.²⁷

Although widely utilized for biological applications, evidence suggests that single thiol ligands are ineffective for stable QD attachment. Moreover, molecules containing two thiol

linkages in an attempt to increase QD affinity are readily exchanged with poly-histamine sequences that possess a stronger metal affinity.^{41,42} In many cases, quantum dots initially assembled using a thiol-based capping polymer are subsequently exchanged with a stronger bond.⁴¹⁻⁴⁵ Histamine-containing sequences in proteins possess a high affinity to QDs, rivaling the strong attachment observed between antibodies and antigens.⁴³⁻⁴⁵ Recently, imidazole rings in polymers enabled the immobilization of QDs for biological applications.^{46,47} The transition from thiol-functionalized ligands to imidazole-based ligands highlights the importance of creating stable complexes with QDs for biological applications.

This work demonstrates the formation of stable, ternary nanocomplexes incorporating histamine functionalized carbon nanohorns (His-CNHs), quantum dots (QDs), and a colloiddally stabilizing diblock copolymer. CNHs are readily functionalized using an acidic oxidation and subsequent reaction with histamine to produce novel His-CNHs. The imidazole ring on the surface of these CNHs facilitates efficient complexation with QDs. A diblock copolymer synthesized using reversible addition-fragmentation chain-transfer (RAFT) polymerization combines a poly(oligo-(ethylene glycol)₉ methyl ether methacrylate) (poly(OEG)) block that provides colloidal stability with a poly(4-vinyl imidazole) (poly(4-VIm)) block that complexes QDs. An interfacial complexation technique achieved complexation of QDs with the water dispersible His-CNHs and poly(OEG)-block-poly(4-VIm). Dynamic light scattering (DLS) measured the size of the ternary nanocomplexes showing desirable sizes under 100 nm, and transmission electron microscopy (TEM) revealed the structure of the nanocomplexes. These ternary nanocomplexes represent exciting candidates for photothermal cancer theranostics, and provide many opportunities for further functionalization with anticancer drugs and targeting ligands.

5.3 *Experimental*

Materials and Instrumentation:

SWNHs were obtained from Dr. David Geohegan at Oak Ridge National Laboratory. In this investigation, CNHs were synthesized by laser vaporization of carbon into an argon atmosphere at 1150 °C (Nd:YAG laser, $\lambda = 1.064 \mu\text{m}$, 20 ms pulse length).⁴⁸ These CNHs are highly monodisperse in size with an average diameter around 50 nm according to TEM observation.⁴⁹ All solvents were obtained from Fischer Scientific and all reagents were obtained from Sigma Aldrich and used without further purification, except where noted. Triethyl amine was distilled before use, 4,4'-azobis(4-cyanopentanoic acid) (V-501) was recrystallized from methanol twice before use, and OEG was purified using a basic alumina column before use. Glacial acetic acid was obtained from Alfa Aesar (99.7 %) and used as received. 4-cyano-4-(ethylsulfanylthiocarbonyl)sulfanylpentanoic acid (CEP) and 4-vinyl imidazole (4-VIm) were synthesized as previously reported.^{50,51} Pure and dry dimethylformamide was obtained by passing DMF through an Innovative Technology, Inc. PureSolv solvent purification system. CdSe/ZnS Core/Shell quantum dots (QDs) with octadecylamine capping agent were purchased from Ocean NanoTech.

Thermogravimetric analysis (TGA) was performed using a TA Instruments Q500 thermogravimetric analyzer using a ramp rate of 10 °C/min under a nitrogen atmosphere. Raman spectroscopy was performed on a JY Horiba LabRam HR800 Raman Spectrometer using a 514 nm argon laser. Raman spectra were deconvoluted and analyzed in Labspec Raman software, version 5.25.15. Sonication was performed using a Branson 2510R-MTH sonicator bath. X-ray photoelectron spectroscopy (XPS) was performed on a PHI Quantera SXM scanning photoelectron spectrometer microprobe. DLS was performed using a Malvern Zetasizer Nano

ZS. All samples were passed through a 45 μm teflon filter prior to DLS measurements. Size exclusion chromatography (SEC) was performed using an aqueous eluent of 54/23/23 (v/v/v %) water/methanol/acetic acid with 0.1 M sodium acetate with a Waters 1515 isocratic HPLC pump, a Waters 717plus autosampler, two Waters Ultrahydrogel linear columns, one Waters Ultrahydrogel 250 column, a Wyatt MiniDAWN, and a Waters 2414 refractive index detector at a flow rate of 0.8 mL/min. Absolute molecular weights were determined from SEC using dn/dc values measured offline using an Optilab T-rEX refractometer ($\lambda = 658 \text{ nm}$). TEM was performed using a Joel JEM 1400 TEM operating at an accelerating voltage of 80 kV.

Polymer Synthesis

A 500-mL, round-bottomed flask equipped with a magnetic stirrer was charged with a solution of CEP (868.9 mg, 3.29 mmol), OEG (40.0 g, 82.5 mmol), and V-501 (184.9 mg, 6.60 mmol) in dimethylsulfoxide (DMSO) (330 mL). The solution was sparged with nitrogen for 40 min and polymerized in a temperature controlled oil bath at 70 $^{\circ}\text{C}$ for 250 min. The reaction mixture was dialyzed against water (pH 4-5) and lyophilized to yield the OEG macro chain transfer agent (CTA) as a viscous yellow oil with a M_n of 13,700 g/mol and polydispersity index (PDI) of 1.01 as determined by SEC.

The isolated OEG macroCTA was chain extended with 4-VIm to form the diblock copolymer. A 100-mL, round-bottomed, flask equipped with a magnetic stirrer was charged with OEG macroCTA (580 mg, 0.042 mmol), V-501 (5.96 mg, 0.021 mmol), and 4-VIm (1.00 g, 10.6 mmol) in glacial acetic acid (21.25 mL). The solution was sparged for 30 min with nitrogen and polymerized in a temperature controlled oil bath at 70 $^{\circ}\text{C}$ for 90 min. The reaction mixture was dialyzed against water and lyophilized to yield the diblock copolymer with a M_n of 39,200 g/mol and PDI of 1.02 as determined by SEC.

CNH Functionalization and Characterization:

To prepare acid oxidized CNHs (AO-CNHs), pristine CNHs (1g) were dispersed in 8 M HNO₃ (100 mL) by sonication in a sonicator bath for 2h in a 250-mL, round-bottomed, flask equipped with magnetic stirrer. The mixture was refluxed at 110 °C for 24 h under magnetic stirring, then filtered and rinsed three times with 100 mL of deionized water. Protonation of the carboxylic acid sites was ensured by reaction with hydrochloric acid. The carbon nanohorns (1g) were redispersed in 1 M HCl (100 mL) by sonicator bath for 2 h in a 250-mL, round-bottomed, flask equipped with magnetic stirrer, then refluxed at 110 °C for 16 h under magnetic stirring. The resulting AO-CNTs were rinsed three times with 100 mL of deionized water and then rinsed with 50 mL of acetone to aid in drying. The AO-CNHs were dried under reduced pressure at 60 °C until achieving a constant weight.

To react histamine onto the carboxylic acid sites, the carboxylic acid sites were first chlorinated using thionyl chloride. AO-CNTs (400 mg) were dispersed in 20 mL of thionyl chloride by sonicator bath for 1 h in 100-mL, round-bottomed flask equipped with magnetic stirrer under an argon atmosphere, then refluxed at 80 °C for 16 h under magnetic stirring. The thionyl chloride was distilled, leaving reactive acyl chloride carbon nanohorns which were immediately reacted. A mixture of histamine (0.2 g) and triethylamine (0.3 mL) in dry DMF (25 mL) was added to the acyl chloride CNHs in a 100 mL, round-bottomed flask equipped with magnetic stirrer by cannulation slowly over 15 min. The mixture was dispersed by sonicator bath under an argon atmosphere for 2 h, then reacted under magnetic stirring at room temperature for 48 h to react histamine onto the acyl chloride sites. The resulting His-CNHs were rinsed three times with 30 mL of DMF and once with 30 ml of tetrahydrofuran, and dried at 60 °C until achieving a constant weight.

Interfacial complexation procedure:

For complexations between diblock copolymer and QDs: 10 mg of diblock copolymer was dissolved in deionized water (2 mL) in a 50-mL, round-bottomed, flask equipped with a magnetic stirrer. QDs were diluted to the desired concentration in chloroform (1 mL) and added drop-wise to the vigorously stirred copolymer solution. Reported concentrations of QDs and CNHs are relative to the water in the interfacial complexation procedure (2 mL). pH of the solution was adjusted to neutral (7) using NaOH/HCl, and the mixture stirred for 12 h. The aqueous layer containing copolymer-QD nanocomplexes was then isolated using a separatory funnel.

For complexations between His-CNHs, diblock copolymer and QDs: His-CNHs were sonicated at a concentration of 0.1 mg/mL for 1 h to yield a homogenous dispersion. They were diluted to the desired concentration and added to the diblock copolymer solution (total volume remained at 2 mL) in a 50-mL, round-bottomed, flask equipped with a magnetic stirrer. QDs were diluted to the desired concentration in chloroform (1 mL) and added drop-wise to the vigorously stirred copolymer/His-CNH solution. pH of the solution was adjusted to neutral (7) using NaOH/HCl, and the mixture stirred for 12 h. The aqueous layer containing copolymer-QD-His-CNH nanocomplexes was then isolated using a separatory funnel. These aqueous nanocomplex dispersions were then sonicated for 10 minutes before DLS and TEM observation.

5.4 Results and Discussion

CNH Functionalization and Characterization

Raman spectroscopy, TGA, and XPS collectively confirmed the successful functionalization of CNHs in accordance with **Figure 5.1A**. XPS shows logical changes in

elemental composition upon functionalization (**Table 5.1**). Reaction with nitric acid increased the oxygen content of the pristine CNHs, indicating the introduction of carboxylic acid sites in AO-CNHS.⁵² Formation of the acyl chloride and subsequent reaction with histamine introduced nitrogen, supporting successful synthesis of His-CNHS. Thermogravimetric analysis (**Figure 5.1B**) shows an increasing weight loss with each functionalization in the important range of 200–500 °C where organic functionality attached to carboxylic acid sites degrade.⁵³ This indicates added functionality with each synthetic step, supporting successful functionalization.

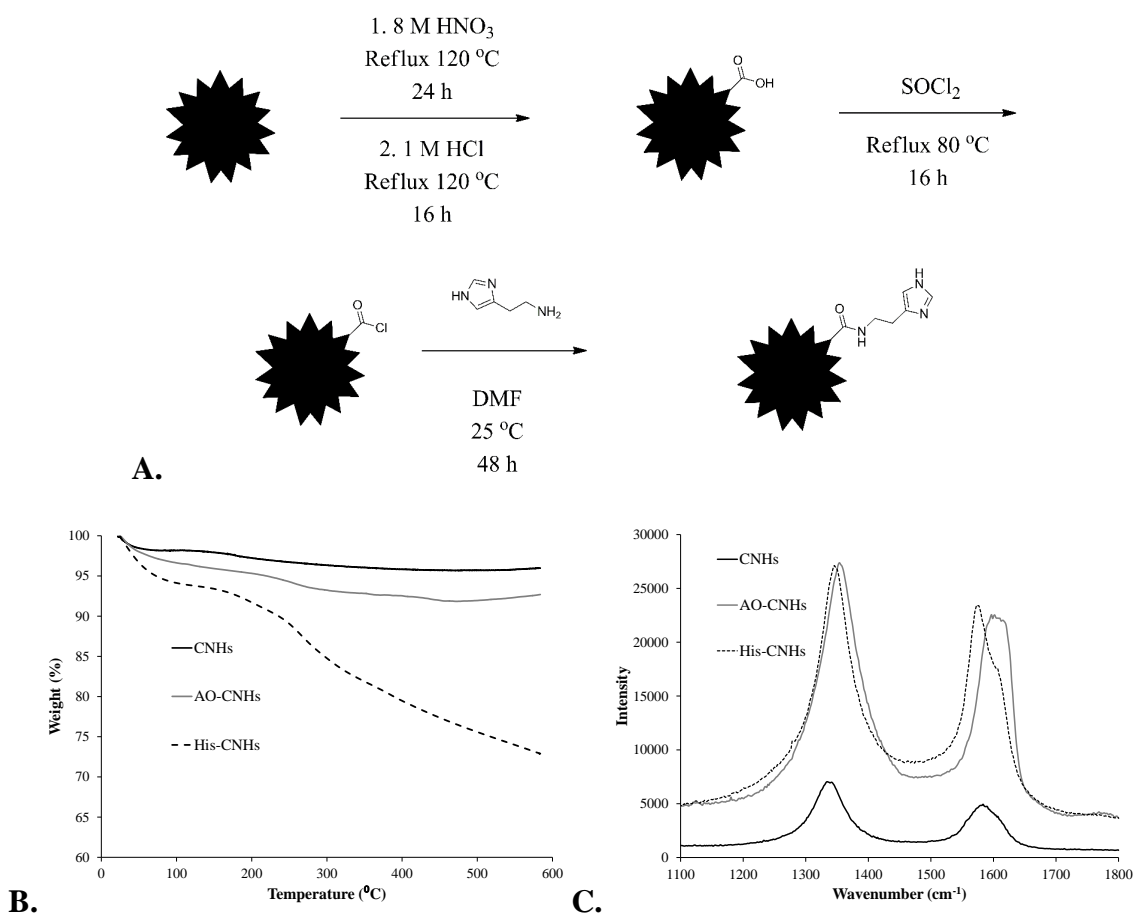


Figure 5.1. Synthesis of histamine functionalized CNHs: A.) CNH functionalization scheme. B.) Thermogravimetric analysis of AO-CNHS and His-CNHS. (C.) Raman spectroscopy of functionalized CNHs.

Raman spectroscopy (**Figure 5.1C**) supports successful oxidation of pristine CNHs with an increase in the D/G peak area ratio from pristine CNHs to AO-CNHs. The G (order) peak is attributed to phonons arising from perfect order in the graphene lattice and is centered at 1585 cm^{-1} .⁵⁴ Areas in the graphene lattice surrounding defect sites give rise to defect-induced double-resonance intervalley (D) and intravalley (D') scattering processes that lead to D and D' (disorder) peaks centered around 1350 cm^{-1} and 1615 cm^{-1} , respectively.⁵⁵ The D/G peak area ratio is indicative of the level of disorder in the graphene lattice of the CNH and successful oxidation will introduce defect sites in the graphene sidewall increasing the D/G ratio.⁵⁶ Due to peak overlap, deconvolution of the D' peak from the G peak was essential for proper analysis of the Raman spectra. The ratio of D to G peak areas (D/G) along with the ratio of the sum of the D and D' peak areas to the G peak area ((D and D')/G) both display similar results (**Table 5.1**). The D/G ratio increases going from pristine CNHs to AO-CNHs, indicating an increase in the level of disorder due to successful oxidation. Similar D/G ratios should be expected in the His-CNHs compared to AO-CNHs as new defect sites aren't introduced, but a strong Raman signal due to the ring stretching of the imidazole ring in histamine observed around 1625 cm^{-1} complicates analysis and leads to lower D/G ratios while confirming the presence of the imidazole ring.⁵⁷

Table 5.1. XPS elemental composition and Raman peak area ratios of CNHs.

CNH sample	C (%)	O (%)	N (%)	$\frac{D}{G}$	$\frac{D \text{ and } D'}{G}$
Pristine CNHs	89.8	9.2	-	1.95	2.00
AO-CNHs	84.6	15.4	-	2.15	2.40
His-CNHs	77.5	12.6	9.9	1.51	1.60

Polymer Synthesis and Characterization

RAFT polymerization enabled the formation of a diblock copolymer containing an poly(OEG) block capable of providing colloidal stability to nanocomplexes and an imidazole block that binds to QDs (**Figure 5.2A**). RAFT polymerization allows for precise molecular weight control and narrow PDIs with facile synthetic techniques.⁵⁸ RAFT polymerization of oligo-(ethylene glycol)₉ methyl ether methacrylate (OEG) in DMSO using the water soluble trithiocarbonate CTA, CEP, to control the radical polymerization yielded an OEG macroCTA. Use of V-501 as the initiator with this CTA ensured chain end fidelity. Dialysis in slightly acidic water purified the macroCTA. Hemp *et al.* previously demonstrated the utility of this macroCTA in providing colloidal stability for polyplexes between phosphonium-based AB diblock copolymers and plasmid DNA for non-viral gene delivery.⁵⁹ This macroCTA provides colloidal stability to a variety of nanoparticles with addition of a second complexing block.

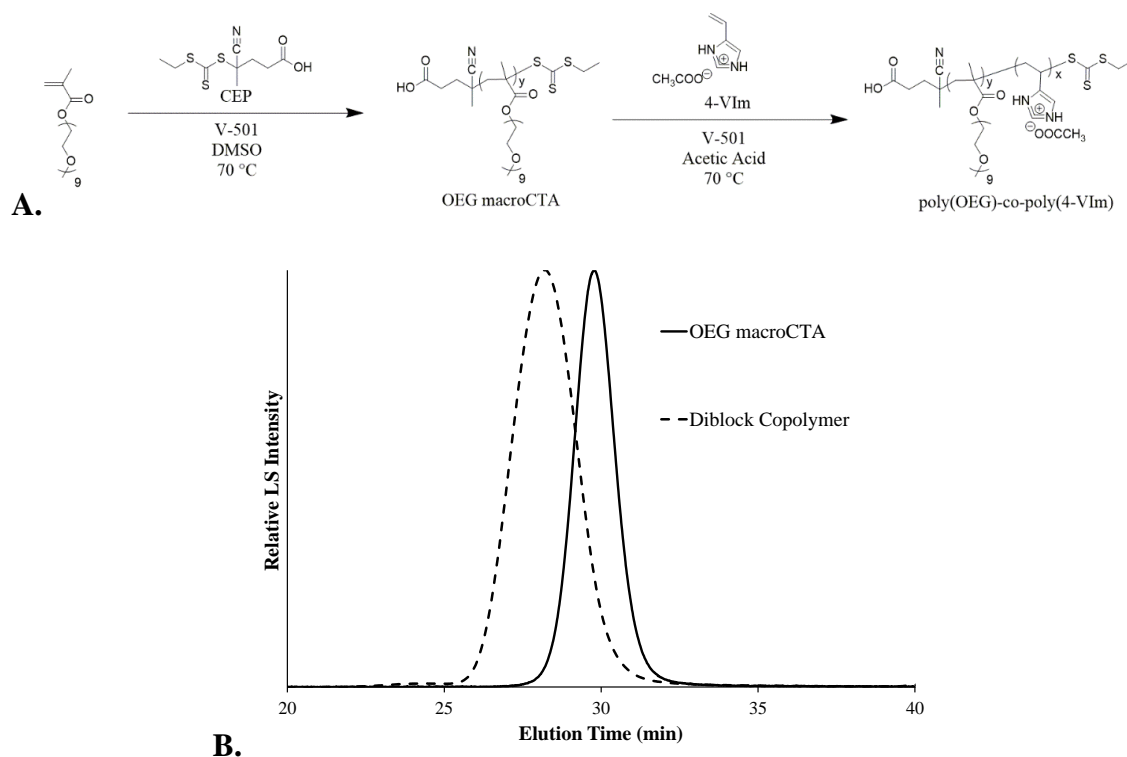


Figure 5.2. Diblock copolymer synthesis by RAFT polymerization: A.) Copolymer synthesis scheme. B.) SEC analysis of macroCTA and diblock copolymer.

The OEG macroCTA was chain extended with 4-VIm to yield a water soluble diblock copolymer, poly(OEG)-co-poly(4-VIm). Allen *et al.* recently reported the controlled radical polymerization of 4-VIm with RAFT in glacial acetic acid, which enabled molecular weight control and the formation of block copolymers.^{50,60} 4-VIm was polymerized in glacial acetic acid with the OEG macroCTA and V-501 to form a well-defined diblock copolymer. Dialysis against water purified the diblock copolymer. At the neutral pH conditions during interfacial complexation with QDs, this block copolymer is in a partially protonated form with the charged units of the poly(4-VIm) block affording water solubility and the lone pair electrons on the remaining unit of the poly(4-VIm) block enabling efficient QD complexation.⁶¹

SEC analysis (**Figure 5.2B**) using offline calculated dn/dc values revealed absolute molecular weights and narrow PDIs. The OEG macroCTA had a M_n of 13,700 g/mol and PDI of 1.01, and the diblock copolymer had a M_n of 39,200 g/mol and PDI of 1.02. The block lengths of 13,700 g/mol (DP of 28) for the OEG block and 25,500 g/mol (DP of 270) proved sufficient to complex QDs and provide colloidal stability to the formed nanocomplexes. However, block lengths require further optimization, and different block lengths could provide similar results.

Formation of Nanocomplexes Through Interfacial Complexation

An interfacial complexation procedure utilizing water chloroform phases successfully formed nanocomplexes of various compositions (**Figure 5.3**). Water soluble or dispersible components reside in the water phase, while QDs are dispersed in the chloroform phase. Vigorous stirring led to interfacial exchange of the QDs from the chloroform phase to the water phase when there is a component in the water phase capable of complexing the QDs, leading to water dispersible QD-containing nanocomplexes. The well-documented complexation of the imidazole ring with QDs provided efficient and stable complexation of the imidazole-containing diblock copolymer and His-CNHs with the QDs in this interfacial complexation.⁶² This interaction provides a more stable interaction compared to other QD complexation strategies such as the thiol-Zn interaction. Nanocomplexes using this strategy remain stable in solution for weeks.³¹

and TEM analysis of the filtered sample showed similarly well dispersed AO-CNHS (**Figure 5.4E**). It should be noted that pristine CNHs are not readily water- dispersible.

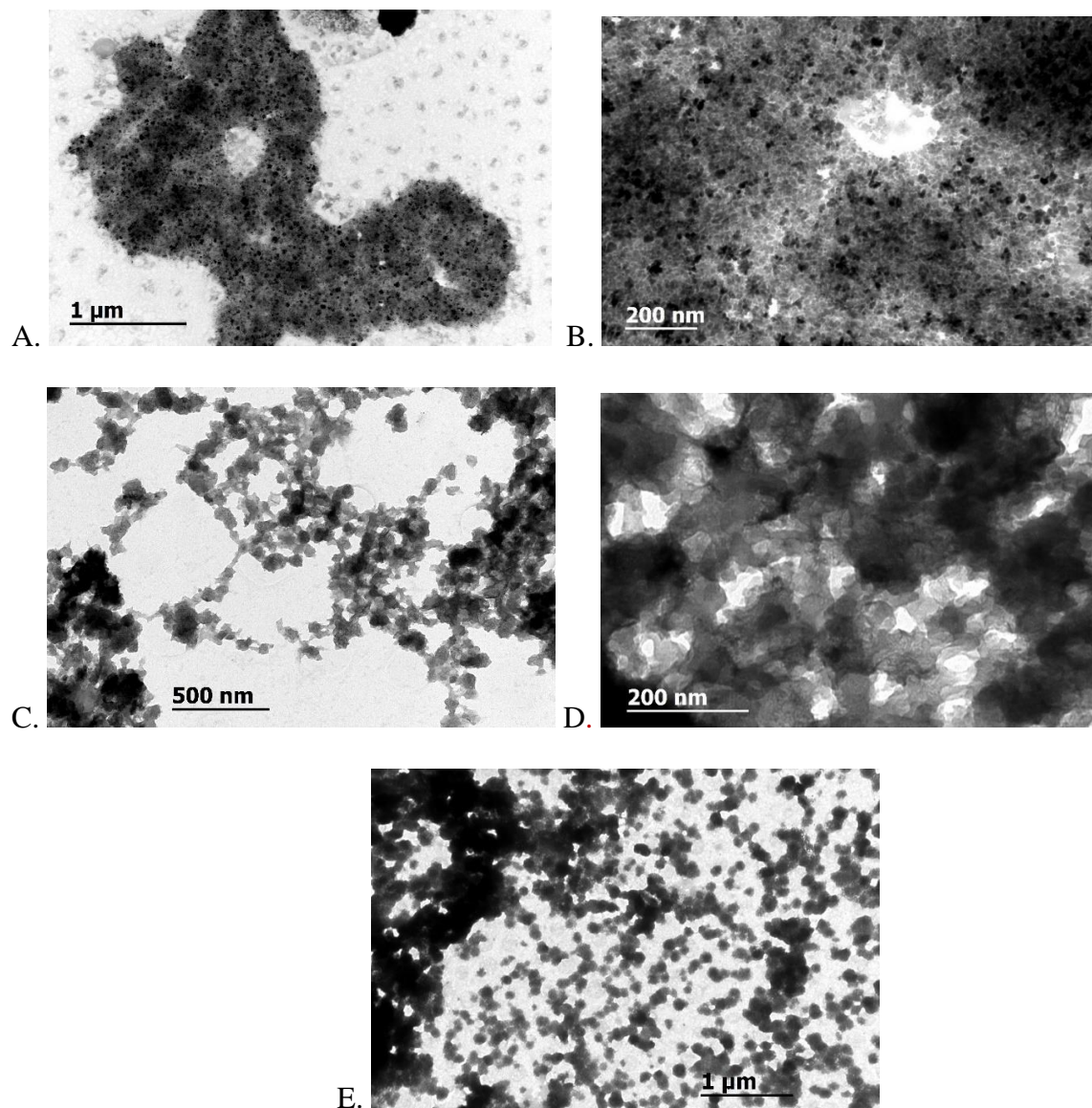


Figure 5.4. Transmission electron microscopy of nanocomplexes: A.) His-CNHS + QDs. B.) HisCNHS + QDs. C.) AO-CNHS + QDs. D.) AO-CNHS + QDs. E.) AO-CNHS + QDs filtered.

Formation of stable ternary nanocomplexes of diblock copolymer, QDs, and His-CNHs required the proper concentration of all components. Systematic variation of component concentrations with DLS analysis determined optimal concentrations to achieve an aggregate size under 100 nm, which is desirable for cellular uptake. First, variation of QD concentration with a constant polymer concentration (5 mg/mL) determined a starting point for addition of CNHs to the procedure. The QD concentration determined the ability to form nanocomplexes between the polymer and QDs and the nanocomplex size (**Figure 5.5A**). A low QD concentration of 0.0025 mg/mL did not produce nanocomplexes, and DLS observed dissolved polymer unimers in solution similar to the neat polymer dissolved in water. Higher concentrations (0.005, 0.015, and 0.025 mg/mL) produced nanocomplexes with size directly dependent on the QD concentration with more QDs leading to a larger nanocomplex. These nanocomplexes are presumably aggregates of several QDs surrounded by the diblock copolymer, with the imidazole block complexing the QDs and the OEG block providing colloidal stability. A QD concentration of 0.015 mg/mL proved ideal, due to the relatively small sized nanocomplexes obtained while retaining relative monodispersity.

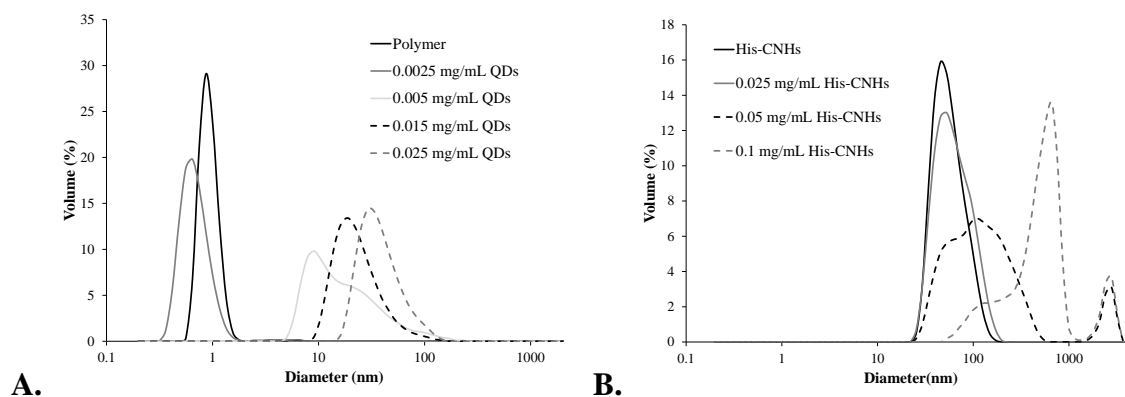


Figure 5.5. Optimal concentration determination by DLS: A.) Variation of QD concentration in QD-polymer complexation. B.) Variation of His-CNHs in ternary nanocomplex formation.

Addition of His-CNHs to the interfacial complexation procedure with varying concentration of His-CNHs probed the ideal formulation (**Figure 5.5B**), using the ideal QD concentration of 0.015 mg/mL and polymer concentration of 5 mg/mL determined from the previous study. The concentration of His-CNHs determined the size of the formed ternary nanocomplexes. A His-CNH concentration of 0.025 mg/mL yielded stable nanocomplexes of desirable size with a high degree of monodispersity. Higher concentrations of 0.05 and 0.01 mg/mL formed larger, more polydisperse, aggregates that were not deemed ideal for cellular uptake. This most likely results from a lack of sufficient diblock copolymer available to stabilize the aggregates of His-CNHs and QDs forming, leading to large His-CNHs aggregates with the QDs.

The lowest concentration of 0.025 mg/mL His-CNHs allowed for the amount of polymer present (5 mg/mL) to successfully complex and stabilize nanocomplexes of QDs (0.015 mg/mL) and highly individualized His-CNHs (**Figure 5.6**). DLS analysis of individual components and the nanocomplexes supports this conclusion (**Figure 5.6A**). The polymer dissolved at 10 mg/mL was fully solvated and displayed polymer unimers in solution around 1 nm in hydrodynamic diameter. The highly dispersible nature of the His-CNHs in water was evident in the DLS of the His-CNH dispersed at 0.025 mg/mL using sonication. The His-CNHs displayed a monodisperse peak with average hydrodynamic diameter of around 50 nm. The complexation of 0.015 mg/mL QDs and 5 mg/mL of polymer displayed a nanocomplex with an average diameter of approximately 20 nm as discussed above. When all three components are utilized in the interfacial complexation at the ideal concentrations, i.e. 0.025 mg/mL His-CNHs, 0.015 mg/mL QDs, and 5 mg/mL of polymer, the nanocomplex formed was similar in size to the dispersed His-CNHs but slightly larger with a slight shoulder at larger hydrodynamic diameters.

Importantly, large aggregates are absent, and there are no smaller peaks, which indicate free polymer or polymer-QD nanocomplexes. This indicated nanocomplexes of individual His-CNHs coated with QDs and the diblock copolymer complexed to the QDs on the outside stabilizing the entire structure (**Figure 5.3**). TEM analysis of the ternary nanocomplex also supported this conclusion (**Figure 5.6B**). TEM of the ternary nanocomplex showed particles around the size of a His-CNH that appear to be covered with QDs. Some free QDs are also observed in this dried sample, which likely does not accurately represent the ternary nanocomplexes as they exist dispersed in water. These ternary nanocomplexes are also very stable, and display the same average size in DLS after a month. TEM could not image QD-polymer nanocomplexes, as no CNH templated structures formed in this samples, and TEM only observed a high-contrast film of QDs and polymer.

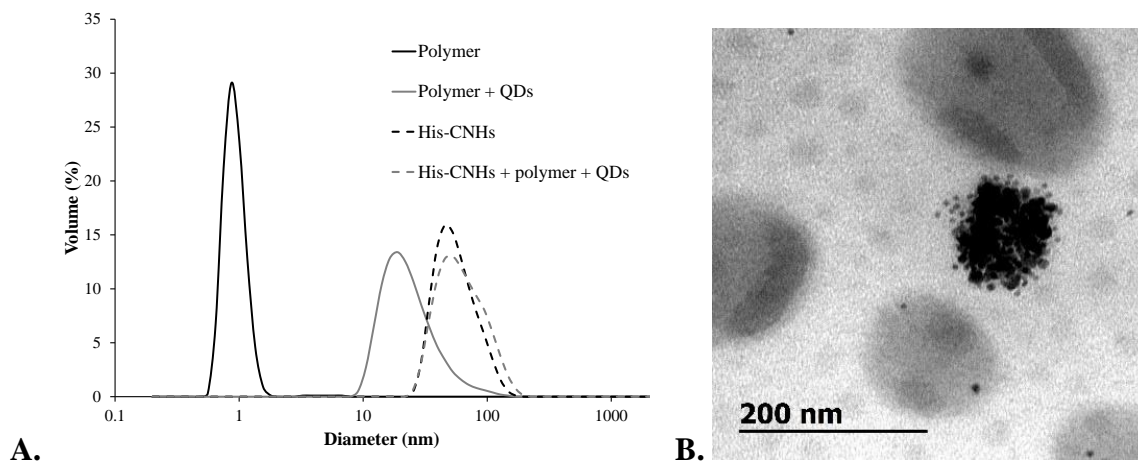


Figure 5.6. Ideal nanocomplex formation: A.) Dynamic light scattering of ternary nanocomplexes and key components in water. B.) TEM of ternary nanocomplex.

These ternary nanocomplexes based on individualized His-CNHs coated with QDs and stabilized on the outside with the diblock copolymer represent ideal and exciting nanoparticles for photothermal theranostic cancer treatment. Using the proper formulation, formation of

particles of ideal size for cellular uptake occurred without the presence of large scale aggregation. Each particle has His-CNHs, polymer, and QDs present allowing for theranostic capabilities. The diblock copolymer facilitated effective water dispersibility, but also allowed future improvements on the nanocomplex's functionality through the ability to incorporate cancer cell targeting ligands such as folic acid and epidermal growth factor through covalent linkage at the carboxylic acid on the OEG block side of the polymer.⁶³⁻⁶⁶ This would present targeting ligands on the outside of the particle, allowing for possible enhanced cancer cellular uptake. Anticancer drugs such as cisplatin and doxorubicin could also be incorporated into this ternary nanocomplex by physical loading into the His-CNHs.^{37,38}

Future investigations will focus on engineering an optimized ternary nanocomplex based on the imidazole-QD complexation that is capable of cellular uptake and fluorescent confocal imaging in a cellular environment for the eventual goal of photothermal cancer therapy. The uptake and localization of these nanoparticles in cells and their stability in a cellular environment is of key interest. The addition of targeting ligands may increase the cellular uptake and efficacy of these nanocomplexes for cancer cell therapy, and this will be explored by attaching targeting ligands to the colloidal stabilizing block of the diblock copolymer. Also, cryo-TEM will be investigated to observe the ternary nanocomplexes as they are dispersed in water more accurately.

5.5 Conclusions

Acid oxidation of carbon nanohorns and subsequent reaction of the introduced carboxylic acid sites led to the successful synthesis of water dispersible His-CNHs capable of complexing QDs. RAFT polymerization yielded a water soluble diblock copolymer containing an poly(OEG) block providing colloidal stability and an imidazole-containing block enabling QD

complexation. An interfacial complexation method utilizing water and chloroform phases allowed for the transfer of QDs from chloroform into water through His-CNHs and diblock copolymer complexation. This method formed stable, water dispersible nanocomplexes of QDs with the diblock copolymer whose size depended on the QD concentration, as evidenced by DLS. Combining all three components, His-CNHs, QDs, and diblock copolymer in the interfacial complexation method formed stable ternary nanocomplexes at the right His-CNH concentration with an average size < 100 nm. These ternary nanocomplexes represent promising candidates for cancer theranostics, combining possibilities of photothermal cancer therapy through local heating of CNHs and diagnostic tracking of nanoparticles through fluorescent imaging of the QDs.

Acknowledgements. The authors would like to thank Andrew Giordani for assistance with XPS, which was performed at the Nanoscale Characterization and Fabrication Laboratory (NCFL) operated by the Institute for Critical Technology and Applied Science (ICTAS) at Virginia Tech. SWNHs were generously donated from Dr. David Geohegan at Oak Ridge National Laboratory, Oak Ridge, TN. TEM was performed at the Virginia-Maryland Regional College of Veterinary Medicine in the Morphology Lab at the Virginia Tech campus with the assistance of Kathy Lowe. The authors would like to acknowledge Charles Farley for assistance with Raman spectroscopy.

5.6 References

1. Bianco, A.; Kostarelos, K.; Prato, M. *Curr. Opin. Chem. Biol.* **2005**, *9*, 674.
2. Brownson, D. A. C.; Kampouris, D. K.; Banks, C. E. *J. Power Sources* **2011**, *196*, 4873.
3. Chen, X.; Li, C.; Graetzel, M.; Kostecky, R.; Mao, S. S. *Chem. Soc. Rev.* **2012**, *41*, 7909.

4. Dai, L.; Chang, D. W.; Baek, J. B.; Lu, W. *Small* **2012**, *8*, 1130.
5. Georgakilas, V.; Tzitzios, V.; Gournis, D.; Petridis, D. *Chem. Mater.* **2005**, *17*, 1613.
6. Ji, S.; Liu, C.; Zhang, B.; Yang, F.; Xu, J.; Long, J.; Jin, C.; Fu, D.; Ni, Q.; Yu, X. *Biochimica et Biophysica Acta (BBA)-Reviews on Cancer* **2010**, *1806*, 29.
7. Jiang, K.; Eitan, A.; Schadler, L. S.; Ajayan, P. M.; Siegel, R. W.; Grobert, N.; Mayne, M.; Reyes-Reyes, M.; Terrones, H.; Terrones, M. *Nano Lett.* **2003**, *3*, 275.
8. Kim, B.; Sigmund, W. M. *Langmuir* **2004**, *20*, 8239.
9. Liu, P. *Eur. Polym. J.* **2005**, *41*, 2693.
10. Liu, Z.; Chen, K.; Davis, C.; Sherlock, S.; Cao, Q.; Chen, X.; Dai, H. *Cancer research* **2008**, *68*, 6652.
11. Liu, Z.; Tabakman, S.; Welsher, K.; Dai, H. *Nano research* **2009**, *2*, 85.
12. Lu, F.; Gu, L.; Meziani, M. J.; Wang, X.; Luo, P. G.; Veca, L. M.; Cao, L.; Sun, Y.-P. *Adv. Mater.* **2009**, *21*, 139.
13. Mehra, N. K.; Mishra, V.; Jain, N. K. *Biomaterials* **2014**, *35*, 1267.
14. Prato, M.; Kostarelos, K.; Bianco, A. *Acc. Chem. Res.* **2007**, *41*, 60.
15. Sun, Y.-P.; Fu, K.; Lin, Y.; Huang, W. *Acc. Chem. Res.* **2002**, *35*, 1096.
16. Burke, A.; Ding, X.; Singh, R.; Kraft, R. A.; Levi-Polyachenko, N.; Rylander, M. N.; Szot, C.; Buchanan, C.; Whitney, J.; Fisher, J.; Hatcher, H. C.; D'Agostino, R.; Kock, N. D.; Ajayan, P. M.; Carroll, D. L.; Akman, S.; Torti, F. M.; Torti, S. V. *Proceedings of the National Academy of Sciences* **2009**, *106*, 12897.
17. Chakravarty, P.; Marches, R.; Zimmerman, N. S.; Swafford, A. D. E.; Bajaj, P.; Musselman, I. H.; Pantano, P.; Draper, R. K.; Vitetta, E. S. *Proceedings of the National Academy of Sciences* **2008**, *105*, 8697.
18. Feazell, R. P.; Nakayama-Ratchford, N.; Dai, H.; Lippard, S. J. *J. Am. Chem. Soc.* **2007**, *129*, 8438.
19. Fisher, J. W.; Sarkar, S.; Buchanan, C. F.; Szot, C. S.; Whitney, J.; Hatcher, H. C.; Torti, S. V.; Rylander, C. G.; Rylander, M. N. *Cancer Research* **2010**, *70*, 9855.
20. Kam, N. W. S.; Liu, Z.; Dai, H. *J. Am. Chem. Soc.* **2005**, *127*, 12492.
21. Markovic, Z. M.; Harhaji-Trajkovic, L. M.; Todorovic-Markovic, B. M.; Kepić, D. P.; Arsić, K. M.; Jovanović, S. P.; Pantovic, A. C.; Dramićanin, M. D.; Trajkovic, V. S. *Biomaterials* **2011**, *32*, 1121.
22. Murakami, T.; Ajima, K.; Miyawaki, J.; Yudasaka, M.; Iijima, S.; Shiba, K. *Molecular pharmaceutics* **2004**, *1*, 399.
23. Singh, R.; Pantarotto, D.; McCarthy, D.; Chaloin, O.; Hoebeke, J.; Partidos, C. D.; Briand, J.-P.; Prato, M.; Bianco, A.; Kostarelos, K. *J. Am. Chem. Soc.* **2005**, *127*, 4388.
24. Fernandez-Fernandez, A.; Manchanda, R.; McGoron, A. J. *Appl. Biochem. Biotechnol.* **2011**, *165*, 1628.
25. McCarthy, J. R. *Nanomedicine* **2009**, *4*, 693.
26. Hu, S. H.; Chen, Y. W.; Hung, W. T.; Chen, I. W.; Chen, S. Y. *Adv. Mater.* **2012**, *24*, 1748.
27. Zimmermann, K.; Inglefield, D., Jr.; Zhang, J.; Dorn, H.; Long, T.; Rylander, C.; Rylander, M. N. *J. Nanopart. Res.* **2013**, *16*, 1.
28. Zhang, J.; Ge, J.; Shultz, M. D.; Chung, E.; Singh, G.; Shu, C.; Fatouros, P. P.; Henderson, S. C.; Corwin, F. D.; Geohegan, D. B. *Nano Lett.* **2010**, *10*, 2843.
29. Chan, W. C. W.; Maxwell, D. J.; Gao, X.; Bailey, R. E.; Han, M.; Nie, S. *Curr. Opin. Biotechnol.* **2002**, *13*, 40.

30. Dabbousi, B. O.; Rodriguez-Viejo, J.; Mikulec, F. V.; Heine, J. R.; Mattoussi, H.; Ober, R.; Jensen, K. F.; Bawendi, M. G. *The Journal of Physical Chemistry B* **1997**, *101*, 9463.
31. Igor, L. M.; Uyeda, H. T.; Ellen, R. G.; Hedi, M. *Nature Materials* **2005**, *4*, 435.
32. Derfus, A. M.; Chan, W. C. W.; Bhatia, S. N. *Nano Lett.* **2003**, *4*, 11.
33. Iijima, S.; Yudasaka, M.; Yamada, R.; Bandow, S.; Suenaga, K.; Kokai, F.; Takahashi, K. *Chem. Phys. Lett.* **1999**, *309*, 165.
34. Yudasaka, M.; Iijima, S.; Crespi, V. In *Carbon Nanotubes*; Springer Berlin Heidelberg: 2008; Vol. 111, p 605.
35. Zhang, M.; Yamaguchi, T.; Iijima, S.; Yudasaka, M. *Nanomedicine : nanotechnology, biology, and medicine* **2013**, *9*, 657.
36. Matsumura, S.; Ajima, K.; Yudasaka, M.; Iijima, S.; Shiba, K. *Molecular Pharmaceutics* **2007**, *4*, 723.
37. Dewitt, M.; Pekkanen, A.; Robertson, J.; Rylander, M. N. *Journal of Biomechanical Engineering*.
38. Ajima, K.; Murakami, T.; Mizoguchi, Y.; Tsuchida, K.; Ichihashi, T.; Iijima, S.; Yudasaka, M. *ACS nano* **2008**, *2*, 2057.
39. Hood, R. L.; Carswell, W. F.; Rodgers, A.; Kosoglu, M. A.; Rylander, M. N.; Grant, D.; Robertson, J. L.; Rylander, C. G. *Lasers in medical science* **2012**, *1*.
40. Miyako, E.; Deguchi, T.; Nakajima, Y.; Yudasaka, M.; Hagihara, Y.; Horie, M.; Shichiri, M.; Higuchi, Y.; Yamashita, F.; Hashida, M. *Proceedings of the National Academy of Sciences* **2012**, *109*, 7523.
41. Sapsford, K. E.; Pons, T.; Medintz, I. L.; Higashiya, S.; Brunel, F. M.; Dawson, P. E.; Mattoussi, H. *The Journal of Physical Chemistry C* **2007**, *111*, 11528.
42. Delehanty, J. B.; Medintz, I. L.; Pons, T.; Brunel, F. M.; Dawson, P. E.; Mattoussi, H. *Bioconjugate Chem.* **2006**, *17*, 920.
43. Boeneman, K.; Deschamps, J. R.; Buckhout-White, S.; Prasuhn, D. E.; Blanco-Canosa, J. B.; Dawson, P. E.; Stewart, M. H.; Susumu, K.; Goldman, E. R.; Ancona, M. *Acs Nano* **2010**, *4*, 7253.
44. Goldman, E. R.; Medintz, I. L.; Hayhurst, A.; Anderson, G. P.; Mauro, J. M.; Iverson, B. L.; Georgiou, G.; Mattoussi, H. *Anal. Chim. Acta* **2005**, *534*, 63.
45. Medintz, I. L.; Clapp, A. R.; Brunel, F. M.; Tiefenbrunn, T.; Uyeda, H. T.; Chang, E. L.; Deschamps, J. R.; Dawson, P. E.; Mattoussi, H. *Nature materials* **2006**, *5*, 581.
46. Liu, W.; Greytak, A. B.; Lee, J.; Wong, C. R.; Park, J.; Marshall, L. F.; Jiang, W.; Curtin, P. N.; Ting, A. Y.; Nocera, D. G. *J. Am. Chem. Soc.* **2009**, *132*, 472.
47. Jana, N. R.; Patra, P. K.; Saha, A.; Basiruddin, S. K.; Pradhan, N. *The Journal of Physical Chemistry C* **2009**, *113*, 21484.
48. Poretzky, A. A.; Styers-Barnett, D. J.; Rouleau, C. M.; Hu, H.; Zhao, B.; Ivanov, I. N.; Geohegan, D. B. *Appl. Phys. A* **2008**, *93*, 849.
49. Whitney, J. R.; Sarkar, S.; Zhang, J.; Do, T.; Young, T.; Manson, M. K.; Campbell, T. A.; Poretzky, A. A.; Rouleau, C. M.; More, K. L.; Geohegan, D. B.; Rylander, C. G.; Dorn, H. C.; Rylander, M. N. *Lasers in Surgery and Medicine* **2011**, *43*, 43.
50. Allen, M. H.; Hemp, S. T.; Smith, A. E.; Long, T. E. *Macromolecules* **2012**, *45*, 3669.
51. Convertine, A. J.; Benoit, D. S. W.; Duvall, C. L.; Hoffman, A. S.; Stayton, P. S. *J. Controlled Release* **2009**, *133*, 221.

52. Datsyuk, V.; Kalyva, M.; Papagelis, K.; Parthenios, J.; Tasis, D.; Siokou, A.; Kallitsis, I.; Galiotis, C. *Carbon* **2008**, *46*, 833.
53. Ranjan, S.; Jue, Z.-F.; Chen, F. L. *J. Compos. Mater.* **2010**, *44*, 1305.
54. Dresselhaus, M. S.; Eklund, P. C. *Advances in Physics* **2000**, *49*, 705.
55. Ado, J.; Marcia, M. L.; Fernando, S.; Erlon, H. M. F.; Marcus, V. O. M.; Rodrigo, B. C.; Carlos, A. A. *J. Phys.: Condens. Matter* **2010**, *22*, 334204.
56. Dresselhaus, M. S.; Jorio, A.; Hofmann, M.; Dresselhaus, G.; Saito, R. *Nano Lett.* **2010**, *10*, 751.
57. Collado, J. A.; Ramírez, F. J. *Journal of Raman Spectroscopy* **2000**, *31*, 925.
58. Chiefari, J.; Chong, Y. K.; Ercole, F.; Krstina, J.; Jeffery, J.; Le, T. P. T.; Mayadunne, R. T. A.; Meijs, G. F.; Moad, C. L.; Moad, G. *Macromolecules* **1998**, *31*, 5559.
59. Hemp, S. T.; Smith, A. E.; Bryson, J. M.; Allen, M. H.; Long, T. E. *Biomacromolecules* **2012**, *13*, 2439.
60. Allen, M. H.; Hemp, S. T.; Zhang, M.; Zhang, M.; Smith, A. E.; Moore, R. B.; Long, T. E. *Polymer Chemistry* **2013**, *4*, 2333.
61. Ihm, J. E.; Han, K.-O.; Hwang, C. S.; Kang, J. H.; Ahn, K.-D.; Han, I.-K.; Han, D. K.; Hubbell, J. A.; Cho, C.-S. *Acta Biomaterialia* **2005**, *1*, 165.
62. Dennis, A. M.; Sotto, D. C.; Mei, B. C.; Medintz, I. L.; Mattoussi, H.; Bao, G. *Bioconjugate Chem.* **2010**, *21*, 1160.
63. Bae, Y.; Jang, W.-D.; Nishiyama, N.; Fukushima, S.; Kataoka, K. *Molecular BioSystems* **2005**, *1*, 242.
64. Bhirde, A. A.; Patel, V.; Gavard, J.; Zhang, G.; Sousa, A. A.; Masedunskas, A.; Leapman, R. D.; Weigert, R.; Gutkind, J. S.; Rusling, J. F. *ACS nano* **2009**, *3*, 307.
65. Kukowska-Latallo, J. F.; Candido, K. A.; Cao, Z.; Nigavekar, S. S.; Majoros, I. J.; Thomas, T. P.; Balogh, L. P.; Khan, M. K.; Baker, J. R. *Cancer research* **2005**, *65*, 5317.
66. Sulistio, A.; Lowenthal, J.; Blencowe, A.; Bongiovanni, M. N.; Ong, L.; Gras, S. L.; Zhang, X.; Qiao, G. G. *Biomacromolecules* **2011**, *12*, 3469.

Chapter 6: Urea-Containing ABA Triblock Copolymers for Gold Nanoparticle Incorporation

David L. Inglefield Jr.^a and Timothy E. Long^{ab}

^aDepartment of Chemistry, ^bMacromolecules and Interfaces Institute

Virginia Tech, Blacksburg, VA 24061

6.1 Abstract

The facile and efficient reaction of amines with isocyanates afforded urea-containing methacrylic monomers. Subsequent free radical polymerization of these monomers revealed logical trends in the homopolymers' glass transition temperature. Reversible addition-fragmentation chain-transfer polymerization yielded poly(2-ethylhexyl methacrylate) macro chain transfer agents with low PDIs and well-controlled polymerization behavior. Chain extension of the poly(2-ethylhexyl methacrylate) macro chain transfer agent with urea-containing methacrylic monomers yielded ABA triblock copolymers which displayed desirable mechanical properties and phase separation. The strong interaction of urea groups with gold enabled triblock copolymer complexation of gold nanoparticles. These urea-containing triblocks represent promising candidates for gold nanoparticle composites and possible templates for gold nanoparticle self-assembly due to efficient interactions with gold nanoparticles.

6.2 Introduction

Combination of polymers and nanoparticles into nanocomposite systems increases their utility.¹ This permits incorporation of desirable mechanical, optical, or thermal nanoparticle

properties into the polymer composite.²⁻⁶ Also, the incorporation of nanoparticles into polymer matrices protects and immobilizes the nanoparticles, providing protection from the environment. Furthermore, use of block copolymers for the polymer matrix in nanocomposites allows for the possibility of stimuli-responsive behavior and polymer-mediated nanoparticle self-assembly.⁷⁻⁹ In all of these instances, proper design of polymer-nanoparticle interactions proves essential for obtaining useful nanocomposites.

Atom transfer radical polymerization (ATRP), nitroxide-mediated polymerization (NMP), and reversible addition-fragmentation chain-transfer polymerization (RAFT) are forms of controlled radical polymerization that allow synthesis of well-defined block copolymers with narrow polydispersity indices (PDIs) using a wide range of monomers.¹⁰⁻¹³ These controlled radical polymerization techniques continue to receive intense interest because of their versatility for many applications, from mechanically useful polymers to diverse biological applications including drug delivery and nanomedicine.¹⁴⁻¹⁶ RAFT is attractive due to its mild reaction conditions, lack of catalyst, and wide selection of RAFT chain transfer agents that allow polymerization of many classes of monomers and post-polymerization functionalization.¹⁷⁻¹⁹ RAFT permits incorporation of many novel functional monomers, including hydrogen-bonding groups and charged monomers that lead to structural and functional complexity in the resulting block copolymers.^{20,21} Recently, the Long research group investigated RAFT polymerization for a number of applications of well-defined diblock and triblock copolymers including nonviral gene delivery and mechanical properties.²²⁻²⁶

Urea-containing methacrylic polymers (and their acrylic analogues) represent a potentially versatile and under studied class of polymers. A vast range of monomers are conceivable using the commercially available 2-isocyanatoethyl methacrylate and amines as

starting materials, with urethane analogues possible when hydroxyl compounds are used in place of amines. These urea-containing methacrylate (UrMA) monomers afford a high degree of strong hydrogen bonding in methacrylic polymers, with precise control of the amount of hydrogen bonding by dilution with other monomers such as methyl methacrylate in copolymers. This ability to introduce and control hydrogen bonding levels in copolymers represents possible applications in adhesives and mechanically useful polymers. So far, a limited number of studies involving these types of monomers exist, especially in controlled radical polymerization and block copolymers. Previously, the Long research group investigated the synthesis and properties of self-complimentary hydrogen bonding 2-ureido-4[1H]-pyrimidone methacrylate (UPyMA) copolymers with either butyl acrylate or 2-ethylhexyl methacrylate and revealed the effects of the strong self-complimentary hydrogen bonding on the rheological and mechanical properties of these random copolymers.^{27,28} Patton *et al.* demonstrated the surface initiated radical polymerization of 2-isocyanatoethyl methacrylate and subsequent base catalyzed click chemistry with amine and thiol compounds to form micropatterned multicomponent functional surfaces.²⁹ Nelson *et al.* used RAFT polymerization to form poly(methyl methacrylate-co-UrMA) random copolymers and studied their host-guest binding behavior of the pendant urea groups with carboxylate, phosphonate, and sulfonate guest molecules.³⁰ No investigations report utilizing controlled radical polymerization methods to form block copolymers with these urea-containing methacrylic monomers.

Gold nanoparticles are intriguing due to their unique optical and electrical properties.³¹⁻³³ These properties along with their biocompatibility make Au nanoparticles attractive candidates for polymer nanocomposites for a variety of applications.³³⁻³⁵ Many polymers including vinyl pyridine and imidazole-containing polymers effectively complex Au ions and nanoparticles.³⁶⁻³⁸

The urea group also strongly complexes a number of metals, including gold.³⁹⁻⁴¹ Therefore, the current work hypothesizes that urea-containing polymers will effectively complex Au ions and nanoparticles. Furthermore, incorporation of Au nanoparticles into phase separated urea-containing block copolymers may lead to selective incorporation of Au nanoparticles into urea-containing phases, as is seen with other Au complexing polymers.⁴²

Here we present the synthesis and characterization of urea-containing ABA triblock copolymers capable of complexing gold nanoparticles through the urea-gold interaction. RAFT polymerization enabled the controlled polymerization of a poly(2-ethylhexyl methacrylate) macro chain transfer agent and subsequent chain extension with urea-containing methacrylic monomers to form ABA triblock copolymers. These ABA triblocks copolymers display phase separated morphologies and dynamic mechanical analysis revealed promising mechanical properties at optimal hard segment levels. Furthermore, these urea-containing copolymers complex gold nanoparticles in solution through an interfacial exchange. These triblock copolymers represent promising candidates for use in gold nanoparticle composites, providing the possibility for selective incorporation of gold nanoparticles into urea-containing domains.

6.3 *Experimental*

Materials

Dimethylformamide (DMF), dichloromethane (DCM), hexane, ethyl acetate, diethyl ether, and tetrahydrofuran (THF) were purchased from Fisher Scientific and used as received. HPLC grade water was obtained from Spectrum Chemical and used as received. 2-Isocyanatoethyl methacrylate (2-ICMA, >98%, stabilized with butylated hydroxytoluene) was purchased from TCI America and used as received. N-N'-Dicyclohexylcarbodiimide (DCC,

$\geq 99\%$) was purchased from Fluka and used as received. Aniline (99%), propylamine ($\geq 99\%$), and hexylamine (99%) were obtained from Sigma Aldrich and distilled before use. Hexanediamine (99.5%) was obtained from Acros Organics and distilled before use. Azobisisobutyronitrile (AIBN, 98%) and 4-4'-azobis(4-cyanovaleric acid) (V-501, $\geq 98\%$) were purchased from Sigma Aldrich and recrystallized twice from methanol prior to use. 4-Cyano-4-[(dodecylsulfanylthiocarbonyl)sulfanyl] pentanoic acid (CDP, 97%) was obtained from Sigma Aldrich and recrystallized from hexane before use. 2-Ethylhexyl methacrylate (2-EHMA) was purchased from Sigma Aldrich and passed through an alumina column before use. Methylamine (2 M in THF), 4-(dimethylamino)pyridine (DMAP, $\geq 99\%$), anhydrous dimethyl sulfoxide (DMSO), anhydrous chloroform, anhydrous 1,4-dioxane, and neutral alumina (activated) were obtained from Sigma Aldrich and used as received. Gold nanoparticle solution (Pelco NanoXact 5 nm T.Cap, 0.05mg/mL) for gold nanoparticle complexation testing was purchased from Ted Pella, Inc. and used as received.

Instrumentation

^1H nuclear magnetic resonance (NMR) spectroscopy was performed on a Varian Unity 400 MHz NMR spectrometer using 64 scans. Mass spectrometry was performed on an Agilent 6220 Accurate Mass TOF LC-MS system. Differential scanning calorimetry (DSC) was performed using a TA Instruments Q 2000 differential scanning calorimeter with a heating rate of $10\text{ }^\circ\text{C}/\text{min}$, and all reported values are from the second heat of a heat/cool/heat cycle using a cooling rate of $5\text{ }^\circ\text{C}/\text{min}$. Thermogravimetric analysis (TGA) was performed using a TA Instruments Q500 thermogravimetric analyzer with a heating rate of $10\text{ }^\circ\text{C}/\text{min}$ under a nitrogen atmosphere. Dynamic mechanical analysis (DMA) was performed on a TA Instruments Q800

dynamic mechanical analyzer in tension mode using a heating rate of 3 °C/min and an amplitude of 15 μm. Sonication was performed using a Bransonic 2510R-MTH sonicator bath. Size exclusion chromatography (SEC) of urea-containing methacrylic homopolymers was performed using a Waters size exclusion chromatograph equipped with an auto sampler, three 5 μm PLgel Mixed-C columns, a Waters 2410 refractive index detector operating at 880 nm, and a Wyatt Technologies miniDAWN multi-angle laser light scattering detector operating at 690 nm. The urea-containing methacrylic homopolymer samples were run at 50 °C in 0.01 M LiBr DMF solution with a flow rate of 1 mL/min. THF SEC was performed using a Waters 515 HPLC pump equipped with a Waters 717plus auto sampler, a Wyatt Technology miniDawn MALLS detector and Waters 2414 refractive index detector with a flow rate of 1 mL/min. Offline dn/dc values for free radical poly(2-EHMA) and poly(2-EHMA) macroCTA polymers were determined using an Optilab T-rEX refractometer ($\lambda = 658$ nm) to provide absolute M_w values in SEC analysis. Atomic force microscopy (AFM) analysis of triblocks copolymer morphology was performed on a Veeco Multimode AFM in tapping mode using 42 N/m spring constant tips and a set point ratio of 0.62.

Urea Methacrylate Monomer Synthesis

For a typical synthesis of urea-containing methacrylate monomers with liquid amine reactant (hexylamine, propylamine, or aniline): a 100-mL, round-bottomed, flask equipped with a magnetic stir bar was charged with one equivalent of liquid amine at 20 wt % in chloroform and purged with argon for 10 min. One equivalent of 2-ICMA was added dropwise with stirring at 0°C. The reaction was allowed to stir for 4 h at 0 °C, and then warmed slowly to room temperature and stirred for an additional 20 h. Chloroform was removed under reduced pressure, yielding white solid in quantitative yield.

For the reaction of methylamine with 2-ICMA, a 2M solution of methylamine in THF was used. One equivalent of methylamine in THF was charged to a 100-mL, round-bottomed, flask equipped with a magnetic stirrer and purged with argon for 10 min. One equivalent of 2-ICMA was added dropwise with stirring at 0°C. The reaction was allowed to stir for 4 h at 0 °C, and then warmed slowly to room temperature and stirred for an additional 20 h. THF was removed under reduced pressure, yielding white solid in quantitative yield.

The monomers were redissolved at 10 wt% in chloroform and passed through a neutral alumina column to remove inhibitor, then chloroform was removed under reduced pressure and the product was dried *in vacuo* at 25 °C for 12 h. The purity and structure of the monomers were confirmed by ¹H NMR, with the isolated yields after column listed in **Table 6.1**. The aromatic derivative 2-(3-phenylureido)ethyl methacrylate (ArUrMA), and the hexyl derivative 2-(3-hexylureido)ethyl methacrylate (HUrMA) were selected for triblock copolymer synthesis based on their physical properties and solubility.

Free Radical Polymerization of Urea Methacrylate Monomers

For a typical free radical polymerization of urea methacrylate monomers for urea methacrylate homopolymers and copolymers: a 25-mL, round-bottomed, flask equipped with a magnetic stirrer was charged with 0.5 g of urea methacrylate monomer dissolved at 5 wt% in DMF (10.6 ml) with 0.1 mol % of AIBN relative to the monomer. The mixture was sparged with argon for 25 minutes, and reacted at 65 °C for 24 h. The polymers were isolated by precipitation in the solvents listed in **Table 6.1**, and dried *in vacuo* at 65 °C for 12 h. The isolated polymer yields and molecular weights as determined by 0.05 M LiBr DMF SEC using a dn/dc estimate of 0.007 are listed in **Table 6.1**.

Free Radical Polymerization of 2-EHMA

For a typical free radical polymerization of 2-EHMA: a 25-mL, round-bottomed, flask equipped with a magnetic stirrer was charged with 0.5 g of 2-EHMA dissolved at 5 wt% in dioxane (9.7 ml) with 0.1 mol % of AIBN relative to 2-EHMA. The mixture was sparged with argon for 25 minutes, and reacted at 65 °C for 24 h. The polymer was isolated by dialysis against 1 L of THF three times for 12 h, and dried *in vacuo* at 65 °C for 12 h. The isolated polymer yield was 80%. Molecular weight as determined by THF SEC and offline determined dn/dc was 132,100 g/mol with a polydispersity index (PDI) of 2.07.

Difunctional Chain Transfer Agent Synthesis

Carbodiimide coupling synthesized a difunctional RAFT chain transfer using commercially available CDP, according to an adapted literature procedure.²⁵ In a representative synthesis, a 50-mL, round-bottomed, flask equipped with a magnetic stirrer was charged with CDP (1.12 g, 2.77 mmol) dissolved in 12 mL anhydrous DCM and stirred at 0 °C. A solution of hexamethylenediamine (0.107 g, 0.92 mmol) and catalytic DMAP (20 mg) dissolved in 4 mL of anhydrous DCM was added to the CDP solution. Upon the addition of the hexamethylenediamine and DMAP, DCC (0.635 g, 3.1 mmol) was immediately added. The reaction was allowed to stir under an argon atmosphere for 4 h at 0 °C, and then warmed slowly to room temperature and stirred for an additional 20 h. The solution was filtered to remove dicyclohexylurea precipitate and washed three times with saturated sodium bicarbonate solution. The resulting organic layer was dried over MgSO₄ and concentrated under reduced pressure. The difunctional CTA was purified by a silica gel column using 80:20 (v:v%) hexane:ethyl acetate to elute impurities. The product was then eluted using 50:50 (v:v%) ethyl acetate:methanol and the solvent was removed under reduce pressure. The product was dried for 16 h *in vacuo* at 25 °C to obtain the yellow-orange solid 1,6-bis(4-cyano-4-

[(dodecylsulfanylthiocarbonyl)sulfanyl] pentanoic acid)-hexane diamide (dCDP, 70% yield). MS-TOF confirmed the purity of dCDP ($m/z = 887.45$ g/mol ($M+H$)⁺).

RAFT Polymerization of 2-EHMA Difunctional macroCTA

In a representative synthesis, a 500-mL, round-bottomed, flask equipped with a magnetic stirrer was charged with 2-EHMA (20 g, 100.8 mmol), dCDP (112 mg, 126.2 μ mol), and V-501 (17.7 mg, 63.1 μ mol) dissolved in 202 mL dioxane. The solution was sparged with argon for 50 min, then reacted at 65 °C for given time intervals. The macroCTA was purified by dialysis against THF three times for 12 h. The solvent was removed under reduced pressure, and the polymer was dried *in vacuo* for 16 h at 65 °C. The molecular weight and PDI for given reaction times was determined by THF SEC using an offline determined dn/dc for absolute molecular weight determination. A reaction time of 10 h yielded a macroCTA with M_n of 48,900 g/mol and PDI of 1.16 in 28 % isolated yield, which was used for the synthesis of triblock copolymers.

RAFT Polymerization of ABA Triblock Copolymers

In a typical polymerization, a 25-mL, round-bottomed, flask equipped with a magnetic stirrer was charged with ArUrMA (157 mg, 630 μ mol), HUrMA (648 mg, 2.52 mmol), macroCTA (287 mg, 5.87 μ mol), and V-501 (1.36 mg, 4.85 μ mol) dissolved in 6.32 mL of 65:35 (v:v %) dioxane:DMF. The solution was sparged with argon for 25 min and then reacted at 65 °C for given time intervals. The triblock copolymers were precipitated into 4:1 MeOH:H₂O and dried *in vacuo* at 65 °C for 16 h. Comparing the integration at δ 3.8 which corresponds to the methylene protons adjacent to the ester present in all repeat units to the integration at δ 7.5 which corresponds to the aromatic protons closest to the urea linkage on the ArUrMA repeat units estimated molecular weights using ¹H NMR. This integration comparison combined with the molecular weight of the macroCTA as determined by THF SEC allowed for the estimation of

triblock M_n , which are summarized in **Figure 6.2B**. The triblocks are referred to by the wt% of the outerblocks incorporated as estimated from ^1H NMR with the naming convention UrMA-wt%. Triblock copolymer films were cast from 100 mg/mL THF solutions into teflon molds and dried at 25 °C for 48 h, then dried *in vacuo* at 25 °C for 16 h. To anneal, the films were further dried *in vacuo* at 100 °C for 16 h.

Gold Nanoparticle Complexation Test

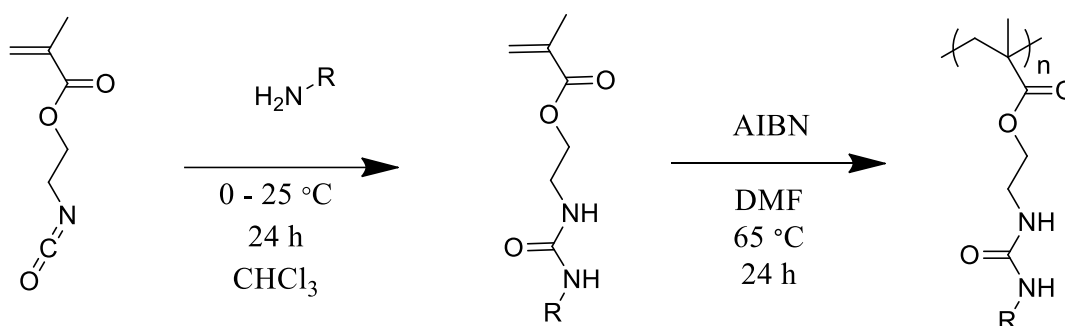
To confirm triblock copolymer complexation with Au nanoparticles, an interfacial complexation test was employed. 200 mg of either poly(2-EHMA) macroCTA or UrMA-45 were dissolved in 5 mL of chloroform, and 3 mL of Au nanoparticle solution (Sigma Aldrich) was added. The mixture was stirred vigorously for 16 h, then allowed to settle. A vial with 5 mL of chloroform and 3 mL Au nanoparticle solution served as a control with no polymer present. Pictures were taken before and after stirring to show the complexation of Au nanoparticles (**Figure 6.6**).

6.4 Results and Discussion

Urea Methacrylate Monomer Synthesis and Homopolymer Properties

The facile reaction of amines with 2-ICMA achieved the synthesis of urea-containing methacrylic monomers in high purity and quantitative yield (**Scheme 6.1**). However, alumina separation of inhibitor reduced the overall yield. Free radical polymerization using AIBN as initiator yielded urea-containing methacrylic polymers. **Table 6.1** summarizes the overall yields and polymer properties. The urea-containing methacrylic polymers are extremely brittle regardless of the T_g , presumably due to the high degree of hydrogen bonding in the polymers. All of the polymers possess a sufficiently high molecular weight for characterization of physical

properties, and begin to degrade in TGA at temperatures greater than 220 °C. The T_g of the urea-containing methacrylate polymers logically follows changes in the polymer side-chain structure. The aromatic derivative has the highest T_g and increasing the alkyl side-chain length decreases the T_g , presumably due to increasing free volume in the polymer. The high density of urea groups makes these polymers effective at complexing metal ions and nanoparticles due to the well documented urea-metal interaction.³⁹⁻⁴¹ Incorporation into ABA triblock copolymers with the low T_g polymer poly(2-EHMA) increases the physical usefulness of these polymers.



Scheme 6.1. Synthesis of urea-containing methacrylic monomers and homopolymers.

Table 6.1. Summary of urea-containing homopolymer properties.

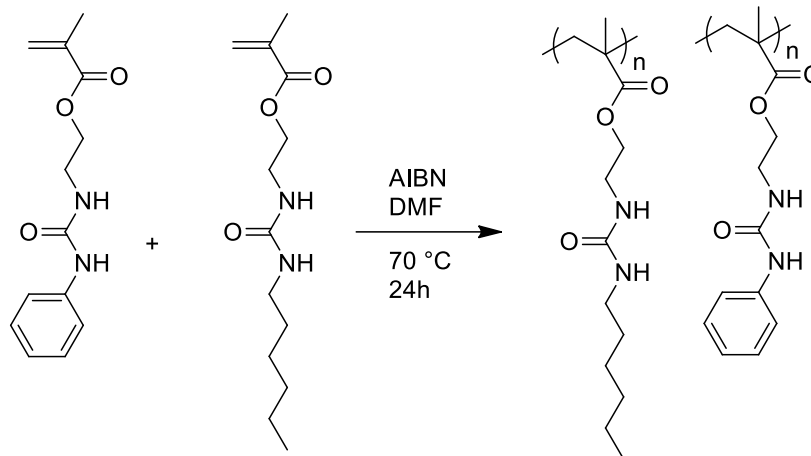
Polyme r	T_g (°C)	M_n	M_w	PDI	$T_d^{5\%}$ (°C)	Monomer Yield After Alumina Column	Precipitation solvent	Polymer Yield
R =								
Aryl	128	150,000	171,000	1.14	235	75%	4:1 MeOH:H ₂ O	66%
Methyl	106	61,000	101,000	1.6	225	84%	Diethyl ether	62%
Propyl	99	236,000	272,000	1.15	220	86%	1:1 MeOH:H ₂ O	60%
Hexyl	77	255,000	315,000	1.23	230	70%	4:1 MeOH:H ₂ O	55%

Free Radical Synthesis of ArUrMA/HUrMA Random Copolymers

Based on the physical properties and solubility of poly(HUrMA), and the high T_g and stainability of poly(ArUrMA) for TEM analysis, a copolymer of these monomers was targeted for use in RAFT triblock synthesis. To ensure the random polymerization behavior and miscibility of these monomers, a series of copolymers was prepared using free radical polymerization (**Scheme 6.2**). **Table 6.2** summarizes the properties of these copolymers. The copolymers are of sufficiently high molecular weight, and the molar ratio of each monomer charged in the polymerization is very close to the molar ratio in the resulting polymer as determined by ^1H NMR, comparing the integrations of HUrMA urea protons to ArUrMA urea protons. The copolymers closely follow the Fox equation:

$$\frac{1}{T_g} = \frac{w_1}{T_{g1}} + \frac{w_2}{T_{g2}}$$

where w_1 and w_2 are the weight fractions of monomer 1 and 2, respectively, and T_{g1} and T_{g2} are the T_g s of monomers 1 and 2, respectively. The fit of poly(HUrMA-co-ArUrMA) T_g s to the Fox equation is shown in **Figure 6.1**. The close fit to the theoretical T_g line demonstrates the miscibility of the monomers and suggests random statistical copolymerization.⁴³ The 80:20 HUrMA:ArUrMA copolymer composition was selected due to its relatively high T_g while retaining THF solubility for film casting.



Scheme 6.2. Synthesis of urea-containing methacrylic copolymers.

Table 6.2. Summary of urea-containing copolymer properties for Fox Equation analysis.

Fed Molar Ratio of ArUrMA to HUrMA	Obtained ratio by ¹ H NMR	M _n (g/mol)	M _w (g/mol)	PDI	T _g (°C)
100:0	100:0	150,000	171,000	1.14	128
80:20	78:20	162,600	185,400	1.14	114
60:40	58:42	145,900	166,800	1.14	106
40:60	39:61	123,300	150,300	1.21	91
20:80	20:80	140,600	174,400	1.24	86
0:100	0:100	255,200	315,700	1.23	77

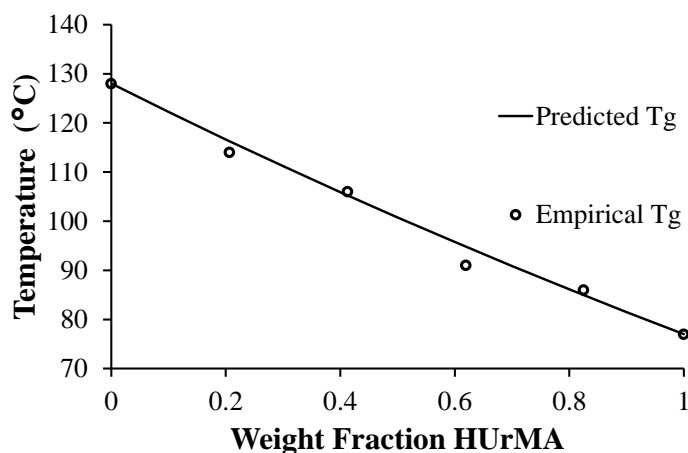
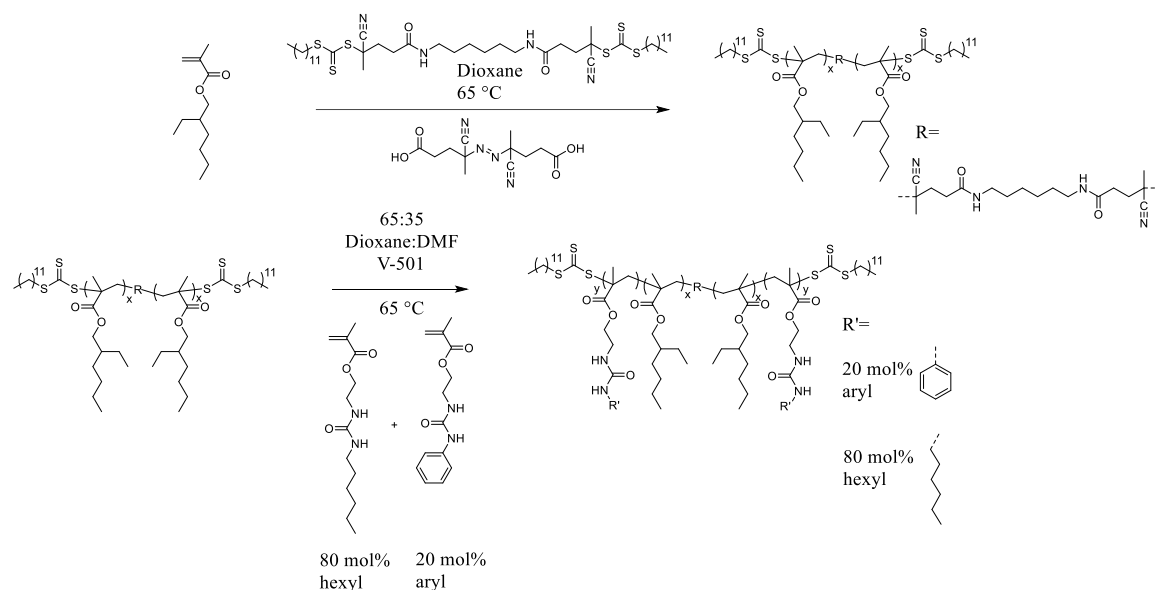


Figure 6.1. Fit of urea-containing copolymers to the Fox Equation.

Polymerization of 2-EHMA in the presence of dCDP in dioxane using V-501 as initiator (Scheme 6.3) enabled controlled growth of difunctional poly(2-EHMA) macro CTA as shown in Figure 6.2A. This RAFT polymerization provided near linear molecular weight growth over time and acceptably low PDIs at the longer reaction times according to THF SEC and offline determined dn/dc giving absolute M_w values. Dialysis ensured complete removal of residual monomer, purification of this polymer using precipitation from dioxane into cold methanol proves difficult because of dioxane's melting temperature. The molecular weight of 49,000 g/mol obtained from a 10 h polymerization served as the macroCTA for subsequent triblock synthesis due to its high molecular weight and low PDI.



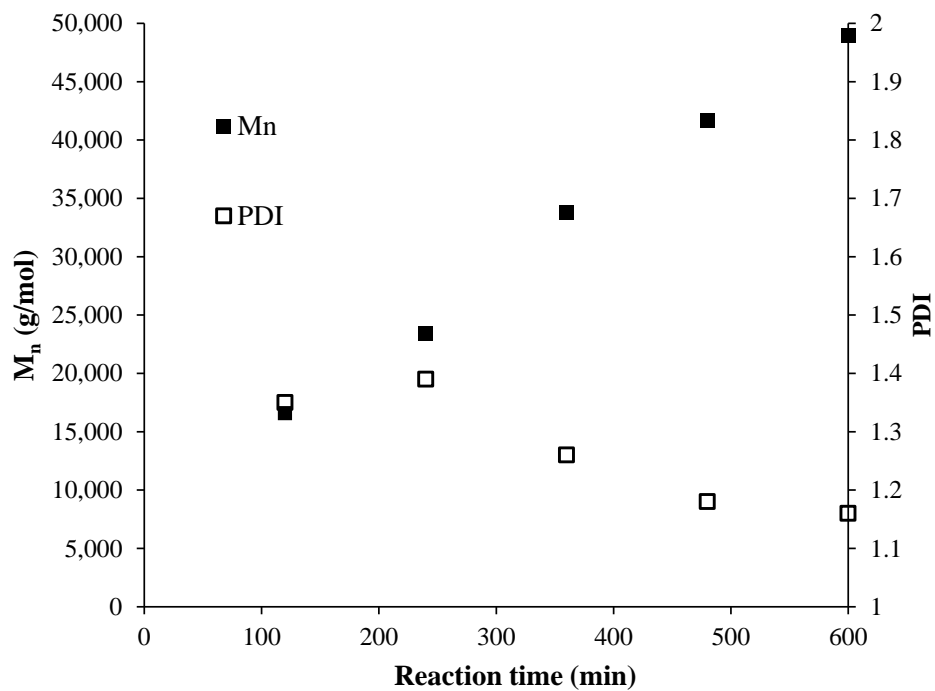
Scheme 6.3. Synthesis of urea-containing triblock copolymers.

Chain extension of the difunctional poly(2-EHMA) macroCTA using an 80:20 molar ratio of HUArMA:ArUrMA yielded urea-containing ABA triblock copolymers (Scheme 6.3).

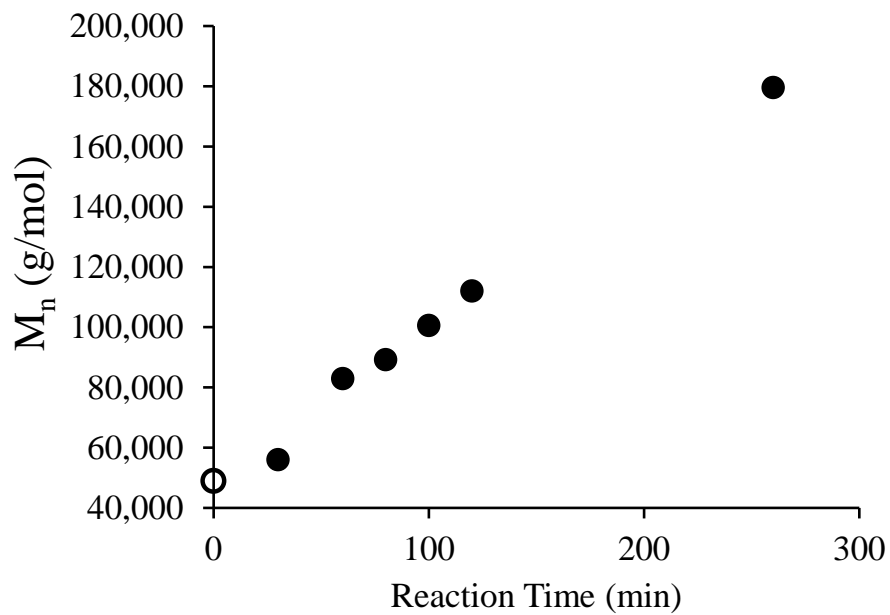
Because of the complex solubility of the obtained triblocks with a non-polar central block and polar outer blocks, a 65:35 dioxane:DMF (v:v%) solvent mixture was used to ensure solvation of the macroCTA and final triblocks at the polymerization temperature. Precipitation into 4:1 methanol:water (v:v%) purified the triblock copolymers. SEC could not reliably determine molecular weights because of the complex solubility. Therefore, triblock copolymer molecular weight was determined from the known molecular weight of the macro CTA using ^1H NMR comparing the integration of ester adjacent methylene protons (present in all repeat units) to the urea adjacent aromatic protons (present in the ArUrMA repeat units). This calculation assumed 20 mol% incorporation of ArUrMA into the outer blocks, which is a reasonable assumption from the incorporation in poly(HUrMA-co-ArUrMA) copolymers (**Table 6.2**). The molecular weights are summarized in **Table 6.3** and the polymerization behavior is shown in **Figure 6.2B**, which displays a nearly linear molecular weight growth over time, indicating good control of the reaction. However, PDIs could not be determined without SEC data. Each triblock composition retained THF solubility which was used to cast films.

Table 6.3. Summary of urea-containing triblock properties.

Polymer	Mn (g/mol)	Wt % Outer Blocks	T _g (°C) UrMA	T _{d5%} (°C)
Free Radical poly(2-EHMA)	132,100	-	-	270
MacroCTA	49,000	0	-	182
UrMA-12	55,900	12	-	178
UrMA-41	82,900	41	84	184
UrMA-45	89,200	45	67	184
UrMA-51	100,000	51	67	190
UrMA-56	112,000	56	79	196
UrMA-73	179,000	73	73	201
Free Radical 80:20 poly(HUrMA-co-ArUrMA)	140,600	-	86	224



A.



B.

Figure 6.2. RAFT polymerization behavior: A.) macroCTA determined from SEC. B.) ABA triblocks determined from ^1H NMR.

ABA Triblock Copolymer Physical Properties and Morphology

DSC and TGA investigated the thermal properties of the ABA triblock copolymers and free radical controls of each block, which are summarized in **Table 6.3**. The $T_{d\ 5\%}$ at 270 °C of the free radical poly(2-EHMA) is significantly higher than the $T_{d\ 5\%}$ of the poly(2-EHMA) macroCTA at 184 °C because of the trithiocarbonate functionality that begins degrading around this temperature, greatly reducing the thermal stability of the macroCTA. Increasing the incorporation of UrMA outer blocks increases the $T_{d\ 5\%}$, due to dilution of the trithiocarbonate endgroups. The $T_{d\ 5\%}$ of the poly(UrMA) free radical control polymer at 224 °C is significantly lower than the free radical poly(2-EHMA), likely due to the urea group reducing the thermal stability. DSC analysis reveals the presence of poly(UrMA) phases in triblocks with significant outer block incorporation, however with slightly depressed T_g s compared to the poly(UrMA) free radical control which is likely the consequence of some phase mixing during the DSC experiment. However, the poly(2-EHMA) T_g was not observable under these DSC conditions, even in the poly(2-EHMA) homopolymers. The literature value for poly(2-EHMA) T_g is about -13 °C.²⁸ The lack of an observable transition here in DSC is likely due to the broad nature of this transition, which was further elucidated in DMA.

DMA and AFM further investigated the phase separated morphology and mechanical properties of the triblock copolymers. Although the triblocks were fairly brittle which limited their mechanical testing, the triblocks with lower incorporations of outer block were testable by DMA. DMA of annealed films revealed a more defined rubbery plateau and an increase in rubbery plateau storage modulus with increase in outer block incorporation, as in shown in **Figure 6.3A**. The UrMA-12 triblock copolymer did not contain enough outer block to form a

rubbery plateau region, and its behavior resembled the poly(2-EHMA) free radical control, which contains a broad T_g transition around $-20\text{ }^\circ\text{C}$ and did not flow until $40\text{ }^\circ\text{C}$. The triblocks with a defined rubbery plateau also showed this broad poly(2-EHMA) transition around $-20\text{ }^\circ\text{C}$, and flowed around $100\text{ }^\circ\text{C}$ after going through the poly(UrMA) T_g . The tan delta (**Figure 6.3B**) clearly shows the nature of these transitions, with a very broad poly(2-EHMA) transition and flow after going through the poly(UrMA) T_g .

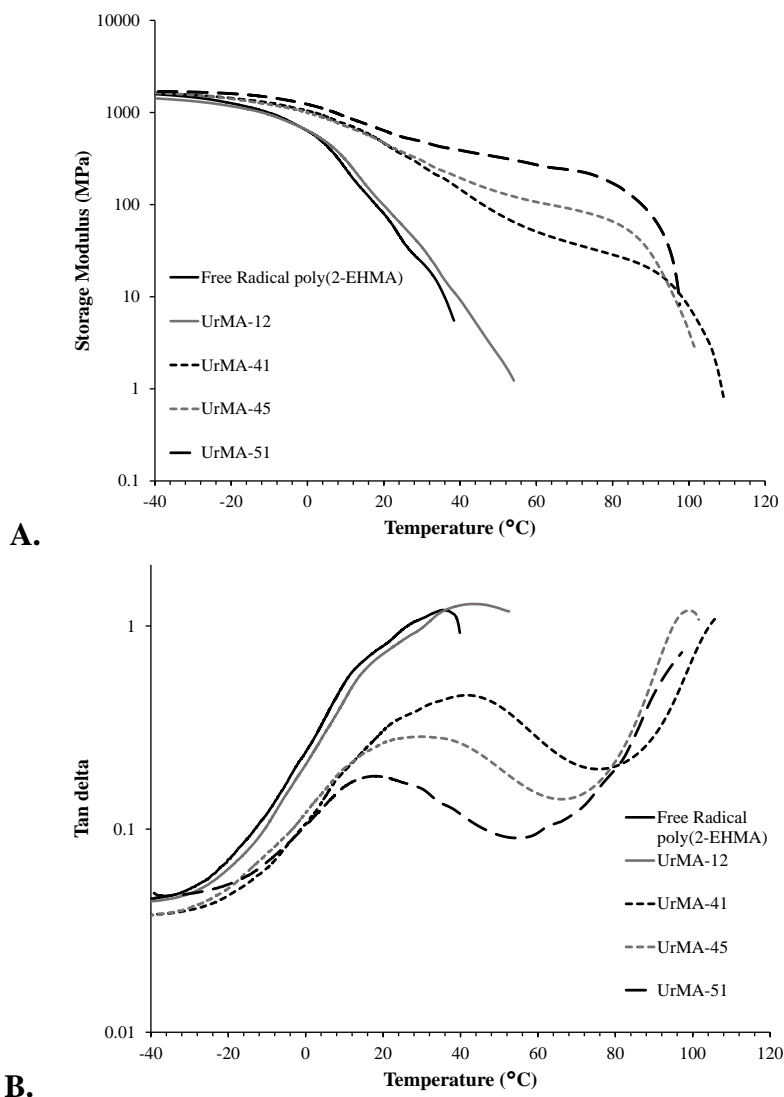


Figure 6.3. DMA of triblock copolymers: A.) Storage modulus. B.) Tan delta. Copolymers are labeled according to the wt % of outer block incorporation.

AFM reveals the phase separated surface morphology of the triblock copolymers. AFM imaged films in both the unannealed (**Figure 6.4**) and annealed (100 °C *in vacuo* for 16 h, **Figure 6.5**) states. In the unannealed films, the surface morphology follows a logical trend with increasing wt% of outer block incorporation. The hard domains formed by the poly(UrMA) outer blocks grow in size, starting as small spherical domains and growing into lamella-like structures lacking long-range order, and eventually forming large domains with inclusions of soft segment formed by the poly(2-EHMA) inner block. Annealing significantly changes the surface morphology, serving to coalesce the hard domains and yielding larger soft domains on the surface of the film. Although different in appearance compared to the unannealed films, the annealed films also follow a visible trend with increasing outer block incorporation. Unfortunately, limited contrast in small-angle X-ray scattering (SAXS) prevented SAXS analysis of the bulk morphology. In addition, preliminary attempts at TEM resulted in severe beam damage to the polymer sample, preventing TEM analysis of the bulk morphology. TEM analysis, if possible, requires further optimization.

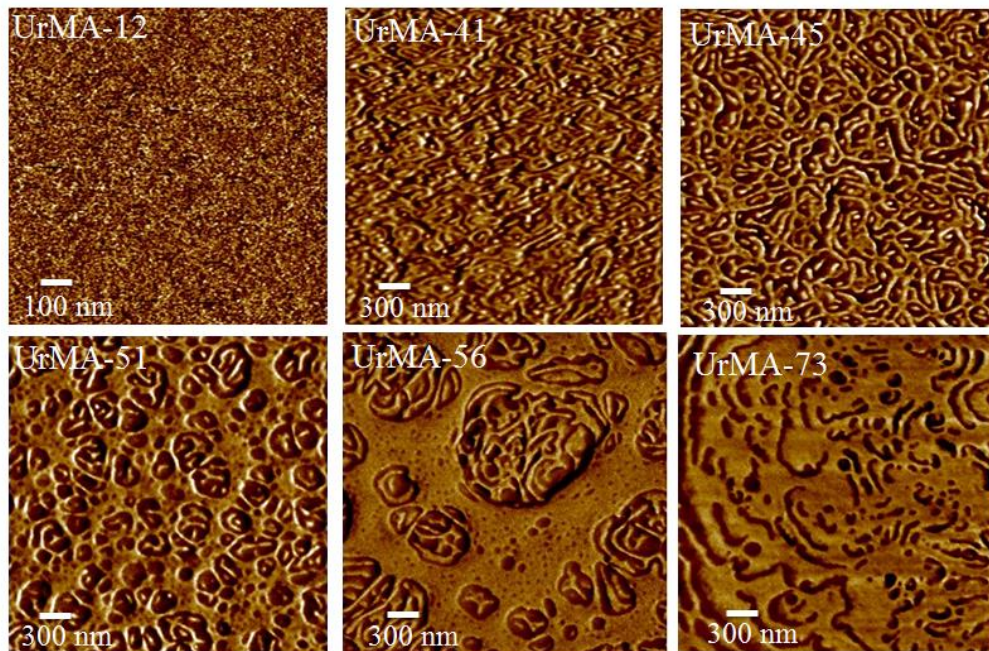


Figure 6.4. AFM of unannealed triblock copolymers (copolymers are labeled according to the wt % of outer block incorporation).

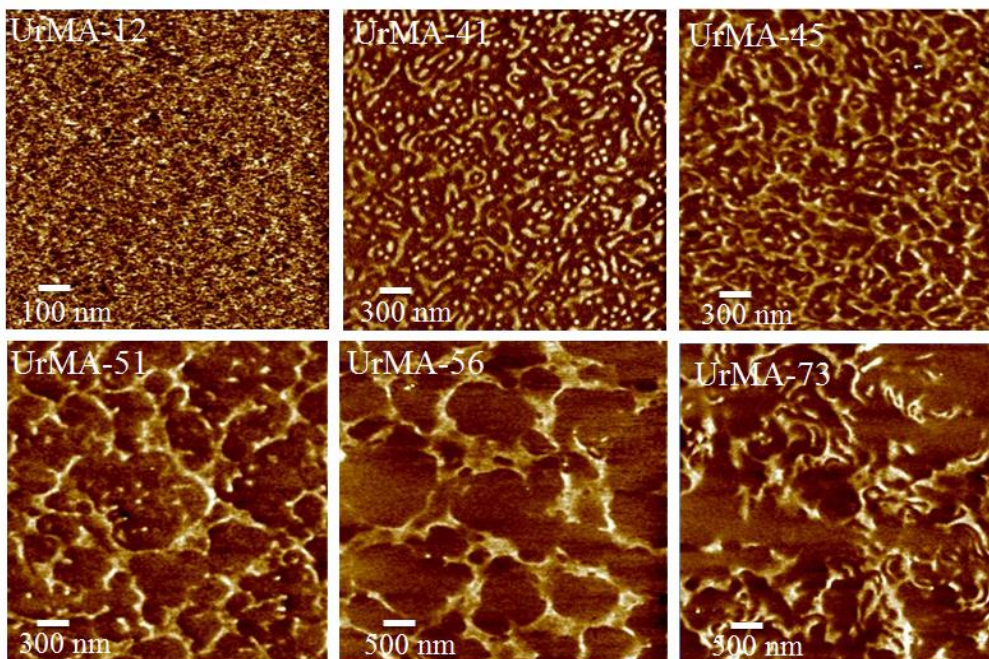


Figure 6.5. AFM of annealed triblock copolymers (copolymers are labeled according to the wt % of outer block incorporation).

Au Nanoparticle Complexation Test

The gold nanoparticle complexation of the UrMA-45 triblock copolymer in solution is shown in **Figure 6.6**. In this complexation test, a chloroform layer either containing no polymer, macroCTA, or UrMA-45 triblock, was stirred vigorously overnight with an aqueous Au nanoparticle solution. Before stirring, the chloroform layer is seen on the bottom with the reddish gold nanoparticle solution on top (**Figure 6.6 A-C**). After stirring and allowing the mixture to settle, the layers appear the same when no polymer or macroCTA was used in the chloroform layer (**Figure 6.6 D,E**), indicating that no gold nanoparticles have left the aqueous layer. However in the case of the urea-containing triblock (**Figure 6.6 F**), the top aqueous layer is now colorless and lacking the gold nanoparticles, which have been transferred to the chloroform layer which now has a pink hue. This is due to the urea-containing blocks complexing the gold nanoparticles at the chloroform-water interface during stirring and pulling them into the organic phase. This demonstrates how the UrMA blocks of these triblocks effectively complex gold nanoparticles. This interfacial method represents an effective way to form composites with aqueous metal nanoparticles.

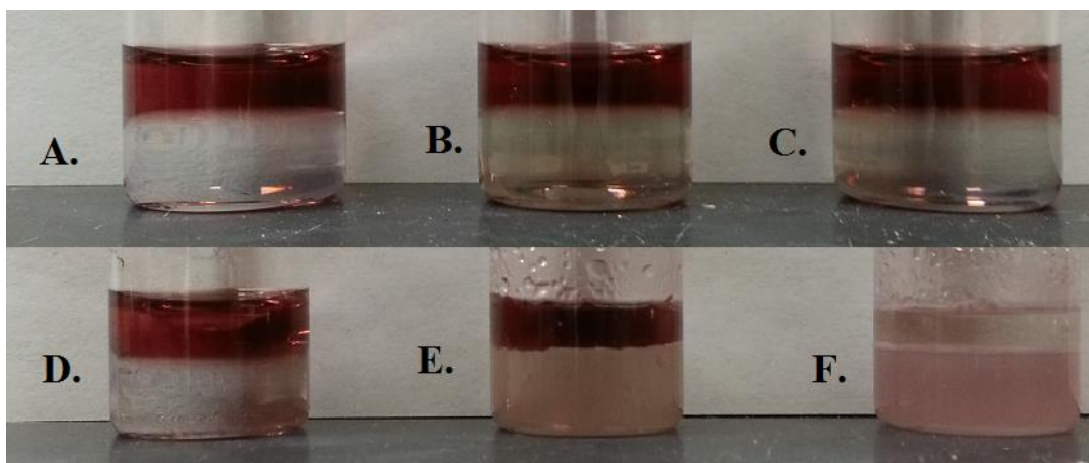


Figure 6.6. Au nanoparticle complexation test: A.) No polymer before stirring. B.) macroCTA before stirring. C.) UrMA-45 before stirring. D.) no polymer after stirring. E.) macroCTA after stirring. F.) UrMA-45 after stirring.

6.5 Conclusions

The facile reaction of 2-isocyanatoethyl methacrylate with amines afforded several urea-containing methacrylic monomers. Subsequent radical polymerization of these monomers revealed logical trends in the homopolymer T_g . Copolymers of HUrMA and ArUrMA followed the Fox equation, suggesting statistical copolymerization. RAFT polymerization enabled the controlled polymerization of poly(2-EHMA) with near linear molecular weight increase and low PDI. Chain extension of the poly(2-EHMA) with 80:20 HUrMA:ArUrMA yielded triblocks with varying outer block compositions. ^1H NMR estimated the molecular weight and composition of the triblock copolymers. TGA revealed reduced thermal degradation temperatures for polymers synthesized using RAFT compared to polymers prepared through conventional free radical polymerization. DMA demonstrated desirable triblock mechanical properties and increasing plateau modulus with increasing hard block composition. AFM analysis exhibited composition dependent phase-separated morphologies whose complicated appearance necessitates further analysis of the bulk morphology. An interfacial complexation

technique demonstrated the ability of the urea-containing triblocks to complex gold nanoparticles and transfer them from an aqueous phase to an organic phase, being stabilized by the polymer. These triblock copolymers represent promising candidates for mechanically useful matrices for gold nanoparticle composites, able to complex gold through the urea-gold interaction. Phase-separated morphologies also provide the opportunity for possible self-assembly of gold nanoparticles into urea-containing domains.

Acknowledgements. The authors would like to thank Steve McCartney and Chris Winkler for assistance with nanoscale characterization, performed at the Nanoscale Characterization and Fabrication Laboratory (NCFL) operated by the Institute for Critical Technology and Applied Science (ICTAS) at Virginia Tech. We would like to thank Bill Bebout for performing TOF-MS, and acknowledge from NSF (CHE-0722638) for the acquisition of our Agilent 6220 LC-TOF-MS.

6.6 References

1. Hussain, F.; Hojjati, M.; Okamoto, M.; Gorga, R. E. *J. Compos. Mater.* **2006**, *40*, 1511.
2. Tjong, S. C. *Materials Science and Engineering: R: Reports* **2006**, *53*, 73.
3. Crosby, A. J.; Lee, J. Y. *Polymer reviews* **2007**, *47*, 217.
4. Han, Z.; Fina, A. *Prog. Polym. Sci.* **2011**, *36*, 914.
5. Porter, D.; Metcalfe, E.; Thomas, M. J. K. *Fire and Materials* **2000**, *24*, 45.
6. Beecroft, L. L.; Ober, C. K. *Chem. Mater.* **1997**, *9*, 1302.
7. Shenhar, R.; Norsten, T. B.; Rotello, V. M. *Adv. Mater.* **2005**, *17*, 657.
8. Bockstaller, M. R.; Mickiewicz, R. A.; Thomas, E. L. *Adv. Mater.* **2005**, *17*, 1331.
9. Motornov, M.; Roiter, Y.; Tokarev, I.; Minko, S. *Prog. Polym. Sci.* **2010**, *35*, 174.
10. Patten, T. E.; Matyjaszewski, K. *Adv. Mater.* **1998**, *10*, 901.
11. Hawker, C. J.; Bosman, A. W.; Harth, E. *Chem. Rev.* **2001**, *101*, 3661.
12. Nicolas, J.; Guillauneuf, Y.; Lefay, C.; Bertin, D.; Gigmès, D.; Charleux, B. *Prog. Polym. Sci.* **2013**, *38*, 63.
13. Chiefari, J.; Chong, Y. K.; Ercole, F.; Krstina, J.; Jeffery, J.; Le, T. P. T.; Mayadunne, R. T. A.; Meijs, G. F.; Moad, C. L.; Moad, G. *Macromolecules* **1998**, *31*, 5559.
14. Matyjaszewski, K.; Tsarevsky, N. V. *Nature chemistry* **2009**, *1*, 276.
15. Rösler, A.; Vandermeulen, G. W. M.; Klok, H.-A. *Advanced drug delivery reviews* **2012**, *64*, 270.
16. York, A. W.; Kirkland, S. E.; McCormick, C. L. *Advanced drug delivery reviews* **2008**, *60*, 1018.
17. Moad, G.; Chong, Y. K.; Postma, A.; Rizzardo, E.; Thang, S. H. *Polymer* **2005**, *46*, 8458.
18. Boyer, C.; Bulmus, V.; Davis, T. P.; Ladmiral, V.; Liu, J.; Perrier, S. *Chem. Rev.* **2009**, *109*, 5402.
19. Boyer, C.; Bulmus, V.; Liu, J.; Davis, T. P.; Stenzel, M. H.; Barner-Kowollik, C. *J. Am. Chem. Soc.* **2007**, *129*, 7145.
20. Lowe, A. B.; McCormick, C. L. *Prog. Polym. Sci.* **2007**, *32*, 283.
21. Schilli, C. M.; Zhang, M.; Rizzardo, E.; Thang, S. H.; Chong, Y. K.; Edwards, K.; Karlsson, G.; Müller, A. H. E. *Macromolecules* **2004**, *37*, 7861.
22. Wu, T.; Wang, D.; Zhang, M.; Heflin, J. R.; Moore, R. B.; Long, T. E. *ACS applied materials & interfaces* **2012**, *4*, 6552.
23. Hemp, S. T.; Allen Jr, M. H.; Smith, A. E.; Long, T. E. *ACS Macro Letters* **2013**, *2*, 731.
24. Hemp, S. T.; Smith, A. E.; Bryson, J. M.; Allen Jr, M. H.; Long, T. E. *Biomacromolecules* **2012**, *13*, 2439.
25. Allen, M. H.; Hemp, S. T.; Zhang, M.; Zhang, M.; Smith, A. E.; Moore, R. B.; Long, T. E. *Polymer Chemistry* **2013**, *4*, 2333.
26. Allen Jr, M. H.; Hemp, S. T.; Smith, A. E.; Long, T. E. *Macromolecules* **2012**, *45*, 3669.
27. Yamauchi, K.; Lizotte, J. R.; Long, T. E. *Macromolecules* **2003**, *36*, 1083.
28. Elkins, C. L.; Park, T.; McKee, M. G.; Long, T. E. *J. Polym. Sci., Part A: Polym. Chem.* **2005**, *43*, 4618.
29. Hensarling, R. M.; Rahane, S. B.; LeBlanc, A. P.; Sparks, B. J.; White, E. M.; Locklin, J.; Patton, D. L. *Polymer Chemistry* **2011**, *2*, 88.
30. Kamps, A. C.; Magbitang, T.; Nelson, A. *Chem. Commun.* **2007**, 954.

31. Wessels, J. M.; Nothofer, H.-G.; Ford, W. E.; von Wrochem, F.; Scholz, F.; Vossmeier, T.; Schroedter, A.; Weller, H.; Yasuda, A. *J. Am. Chem. Soc.* **2004**, *126*, 3349.
32. Daniel, M.-C.; Astruc, D. *Chem. Rev.* **2004**, *104*, 293.
33. Huang, X.; Jain, P. K.; El-Sayed, I. H.; El-Sayed, M. A. **2007**.
34. Park, J. H.; Lim, Y. T.; Park, O. O.; Kim, J. K.; Yu, J.-W.; Kim, Y. C. *Chem. Mater.* **2004**, *16*, 688.
35. Li, D.; He, Q.; Li, J. *Adv. Colloid Interface Sci.* **2009**, *149*, 28.
36. Pekel, N.; Güven, O. *Colloid. Polym. Sci.* **1999**, *277*, 570.
37. Orhan, T.; Kaleli, K.; Uyar, T.; Kayran, C.; Hacaloglu, J. *J. Anal. Appl. Pyrolysis* **2014**.
38. Sidorov, S. N.; Bronstein, L. M.; Kabachii, Y. A.; Valetsky, P. M.; Soo, P. L.; Maysinger, D.; Eisenberg, A. *Langmuir* **2004**, *20*, 3543.
39. Sadeek, S. A.; Refat, M. S. *J. Coord. Chem.* **2005**, *58*, 1727.
40. Nishat, N.; Ahmad, S.; Tansir Ahamad, R. *J. Appl. Polym. Sci.* **2006**, *100*, 928.
41. Penland, R. B.; Mizushima, S.; Curran, C.; Quagliano, J. V. *J. Am. Chem. Soc.* **1957**, *79*, 1575.
42. Leong, W. L.; Lee, P. S.; Lohani, A.; Lam, Y. M.; Chen, T.; Zhang, S.; Dodabalapur, A.; G Mhaisalkar, S. *Adv. Mater.* **2008**, *20*, 2325.
43. Lejars, M.; Margaille, A.; Bressy, C. *Polymer Chemistry* **2014**, *5*, 2109.

Chapter 7: Upconverting Nanocomposites Utilizing Urea-Containing Methacrylic Polymers

David L. Inglefield Jr.^a, Travis Merritt^c, Brenden Magill^c, Giti A. Khodaparast^c, and Timothy E. Long^{ab}

^a*Department of Chemistry*, ^b*Macromolecules and Interfaces Institute*, ^c*Department of Physics*
Virginia Tech, Blacksburg, VA 24061

7.1 Abstract

Upconverting materials receive intense interest due to their ability to convert lower energy light to higher energy emissions. Upconverting nanoparticles present possible applications ranging from bio-imaging to solar energy technology. Combination with polymers in nanocomposites increases the utility of upconverting nanoparticles for biological or materials applications. Here, trifluoroacetate salt decomposition enables Er/Yb doped NaYF₄ upconverting nanoparticle synthesis. Subsequent deposition of a silica nanoshell yielded polar silica-coated upconverting nanoparticles, enabling composite formation with polar urea-containing methacrylic polymers. Hydrogen bonding between urea groups in the polymer and the silica-coated nanoparticles allowed for dispersion of the upconverting nanoparticles to form upconverting composite films. These films exhibit desirable upconversion comparable to the nanoparticles dispersed in methanol. Urea-containing polymers represent promising candidates for matrices in nanocomposites formed with polar silica and metal-coated nanoparticles due to favorable polymer-nanoparticle interactions. Possible applications of upconverting composite

films include components in photovoltaic cell components, being able to increase photovoltaic efficiency through upconverting sub-photonic band gap photons.

7.2 Introduction

Upconverting nanoparticles have recently attracted much interest for energy and bioimaging applications.¹⁻⁴ Photon upconversion is an anti-Stokes emission process that converts lower energy light to higher energy light.⁵ Although various types of anti-Stokes mechanisms exist, perhaps the most applicable is the energy transfer upconversion process due to the types of excitation sources required.^{6,7} Lanthanide-doped glasses represent the most popular energy transfer upconversion systems due to their emission tunability.⁸ In these systems, sensitizer ions absorb photons which excite electrons, and this energy is transferred non-radiatively to activator ions whose subsequent relaxation leads to emission of higher energy photons.^{6,7} A popular sensitizer-activator pair is the Yb³⁺-Er³⁺ system, usually found in NaYF₄ nanoparticles. This system absorbs near-IR light around 980 nm in wavelength, and emits visible emissions around 550 and 650 nm in wavelength.⁹ **Figure 7.1** shows the upconversion process for this system.¹⁰ However, when miniaturized in nanoparticles, surface quenching leads to low upconversion efficiencies.¹¹

Metal-enhanced fluorescence (MEF) increases the efficiency of upconverting nanoparticles (UCNPs) with proper design. MEF relies on the scattering component of the surface plasmon resonance (SPR) of metal nanostructures overlapping with the absorption or emission wavelengths of an upconverting system.¹²⁻¹⁴ The SPR depends on the size and shape of the metal nanostructure and in addition, enhancement of upconverted emissions from UCNPs depends on the distance of the metal nanostructure to the UCNP.¹⁵ If the plasmonic surface is

too close it will quench the upconverted emission, and if it is too far the enhancement is absent.¹⁴ This creates the need for a precisely tuned spacer between the UCNP and the plasmonic surface, typically achieved using a silica spacer. Many studies in recent years demonstrate MEF of UCNPs, with the magnitude of the MEF depending on the composition, size, shape, and distance to the upconverting core of the metallic nanostructures employed.^{12,14,16-19}

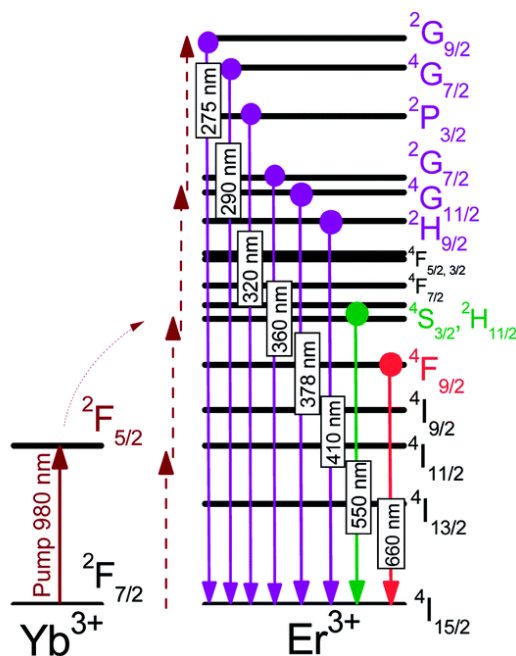


Figure 7.1. Energy state diagram of the Yb³⁺/Er³⁺ upconversion system. Reproduced from reference 10.

Although few studies investigate the use of UCNPs in polymer composites, the initial results appear promising.²⁰⁻²² These upconverting composites represent materials with possible applications in light curable polymers and solar energy technology. For example, upconversion offers the potential for increasing the efficiency of photovoltaic cells through converting light below the optical band gap to light within the photovoltaic cell's optical band gap. Here we present initial results toward the goal of utilizing urea-containing polymers in upconverting

nanocomposites. Urea-containing polymers appear particularly promising for applications with silica and metal coated UCNPs, due to the high levels of hydrogen bonding between urea groups with silica and the well-known urea-metal interaction.²³⁻²⁷ Employing urea-containing methacrylic polymers in block copolymer structures also presents the possibility for mechanically useful upconverting nanocomposites and self-assembly of upconverting nanoparticles into urea-containing phases.

7.3 Experimental

Materials

Dimethylformamide (DMF), methanol, and hexane were purchased from Fisher Scientific and used as received. HPLC grade water was obtained from Spectrum Chemical and used as received. 2-Isocyanatoethyl methacrylate (2-ICMA, >98%, stabilized with butylated hydroxytoluene) was purchased from TCI America and used as received. Hexylamine (99%) was obtained from Sigma Aldrich and distilled before use. Azobisisobutyronitrile (AIBN, 98%) was purchased from Sigma Aldrich and recrystallized twice from methanol before use. Anhydrous chloroform, neutral alumina (activated), oleic acid (90%), 1-octadecene (90%), gold(III) chloride hydrate (99.999%), thioglycolic acid (≥ 98), poly-L-histidine hydrochloride (PLH), sodium hydroxide ($\geq 98\%$), sodium nitrate ($\geq 99\%$), potassium nitrate (≥ 99), IGEPAL CO-520 (average M_n 441), hydroxylamine (50 wt% in water, 99.999%), ammonium hydroxide (28 wt% ammonia in water, 99.99%), sodium trifluoroacetate (98%) and tetraethyl orthosilicate (TEOS, $\geq 99\%$) were obtained from Sigma Aldrich and used as received. Erbium trifluoroacetate (99.9%), yttrium trifluoroacetate (99.9%), and ytterbium trifluoroacetate (99.9%) were obtained from GFS Chemicals and used as received.

Instrumentation

¹H nuclear magnetic resonance (NMR) spectroscopy was performed on a Varian Unity 400 MHz NMR spectrometer using 64 scans. Differential scanning calorimetry (DSC) was accomplished using a TA instruments Q 2000 differential scanning calorimeter with a heating rate of 10 °C/min, and all reported values are from the second heat of a heat/cool/heat cycle using a cooling rate of 5 °C/min. Thermogravimetric analysis (TGA) was performed with a TA Instruments Q500 thermogravimetric analyzer with a heating rate of 10 °C/min under a nitrogen atmosphere. Sonication was achieved using a Bransonic 2510R-MTH sonicator bath. Size exclusion chromatography (SEC) of urea-containing methacrylic homopolymers was performed using a Waters size exclusion chromatograph equipped with an auto sampler, three 5 µm PLgel Mixed-C columns, a Waters 2410 refractive index detector operating at 880 nm, and a Wyatt Technologies miniDAWN multi-angle laser light scattering detector operating at 690 nm, with a 0.01 M LiBr DMF eluent with a flow rate of 1 mL/min and column temperature of 50 °C. Transmission electron microscopy (TEM) of nanoparticles was performed using a Joel JEM 1400 TEM operating at an accelerating voltage of 80 kV. Instrumentation used in optical characterization of nanoparticles and composites is detailed below.

Urea Methacrylate Monomer Synthesis

A 100-mL, round-bottomed, flask equipped with a magnetic stirrer was charged with one equivalent of hexylamine at 20 wt % in chloroform and purged with argon for 10 min. One equivalent of 2-ICMA was added dropwise with stirring at 0 °C. The reaction was allowed to stir for 4 h at 0 °C, and then warmed slowly to room temperature and stirred for an additional 20 h. Chloroform was removed under reduced pressure, yielding white solid in quantitative yield. The monomer was redissolved at 10 wt% in chloroform and passed through a neutral alumina column

to remove inhibitor, then chloroform was removed under reduced pressure and the product was dried *in vacuo* at 25 °C for 12 h. The purity and structure of 2-(3-hexylureido)ethyl methacrylate (HUrMA) was confirmed using ¹H NMR. The isolated yield of HUrMA after alumina column was 70 %.

Free Radical Polymerization of Urea Methacrylate Monomers

For a typical free radical polymerization of urea methacrylate monomers: a 25-mL, round-bottomed, flask equipped with a magnetic stirrer was charged with 0.5 g of urea methacrylate monomer dissolved at 5 wt% in DMF (10.6 ml) with 0.1 mol % of AIBN relative to the monomer. The mixture was sparged with argon for 25 minutes, and reacted at 65 °C for 24 h. The polymer was precipitated in 4:1 MeOH:water, and dried *in vacuo* at 65 °C for 12 h. The isolated polymer yield was 55% and the M_n as determined using SEC in 0.01 M LiBr DMF was 255,000 g/mol, with an estimated dn/dc value of 0.07.

Upconverting Nanoparticle Synthesis

Er/Yb doped NaYF₄ upconverting nanoparticles with a silica spacer and gold nanoshell were achieved in a three part synthesis (**Scheme 2**). First, upconverting cores were synthesized from the high temperature decomposition of trifluoroacetate salts to yield rare earth doped NaYF₄ nanoparticles (UCNPs) from an adapted literature procedure, where the time of reaction determines the nanoparticle size and morphology.⁹ In a typical synthesis targeting spherical nanoparticles with diameters of 20-30 nm, a 500-mL, three-necked, round-bottomed, flask equipped with a magnetic stirrer was charged with sodium trifluoroacetate (0.66 g), yttrium trifluoroacetate (1.87g), ytterbium trifluoroacetate (560 mg), and erbium trifluoroacetate (56 mg) dissolved in a mixture of 22.5 mL of oleic acid and 22.5 mL of 1-octadecene. The mixture was stirred under vacuum at 100 °C for 45 min, forming a transparent yellow solution. Then the

reaction flask was purged with argon for 5 minutes, and placed in a molten salt bath (1:1 NaNO₃:KNO₃ weight) stabilized at 342 °C. The solution was refluxed for 25 min under constant argon flow and vigorous stirring, after which the nanoparticle growth was halted by removing the flask from the molten salt bath and immediately adding 15 mL octadecene to cool the reaction mixture. After the mixture reached room temperature, 200 mL ethanol was added to precipitate the UCNPs. The UCNPs were isolated by centrifugation at 4,000 rpm for 30 min, and then redispersed in 30 mL of cyclohexane by sonication for 30 min. The final concentration of UCNPs in cyclohexane was 48 mg/mL.

Deposition of a silica spacer on the UCNPs was achieved by base catalyzed hydrolysis of TEOS from an adapted literature procedure.¹⁸ In a typical synthesis, a 50-mL, round-bottomed, flask equipped with a magnetic stirrer was charged with 6 mL of the aforementioned UCNP solution in cyclohexane, 18 mL of cyclohexane, and 1.2 mL of CO-520, and the mixture was stirred for 20 min. Then, 252 µL of ammonia solution (28 wt%) was added and the mixture was sonicated for 20 min. 189 µL of TEOS was added and the mixture was stirred at 25°C at 400 rpm for 45 h. UCNPs containing silica spacers (UCNP@SiO₂) were precipitated by adding acetone to the reaction mixture, filtered, and washed two times with 50:50 ethanol:water. The UCNP@SiO₂ were dried *in vacuo* for 16 h at 25 °C and redispersed in water (3 mg/mL) for the gold nanoshell deposition.

Deposition of a gold nanoshell onto UCNP@SiO₂ was achieved using a modified literature procedure.¹⁸ 3 mL of the above UCNP@SiO₂ dispersion in water was sonicated for 30 min, then 4.5 mg of PLH was added and the mixture was stirred for 16 h at 300 rpm. The UCNP@SiO₂ were centrifuged at 12,000 rpm for 20 min and the water was decanted to remove excess PLH. The UCNP@SiO₂ were redispersed in 1.5 mL of water by sonication for 20 min.

400 μL of this dispersion was added to 200 μL of 1 wt% HAuCl_4 trihydrate in water. This mixture was diluted to 1 mL by the addition of 400 μL of water, and the pH was adjusted to 10 by the addition of 12 μL of 1 M NaOH. The mixture was sonicated for 1 min, then stirred for 180 min. 100 μL of 20 mM hydroxylamine was added to initiate reduction of Au^{3+} to metallic gold, and upon observation of color change 6 μL of thioglycolic acid was added to stabilize the nanoparticles in solution. The mixture was allowed to stir for 30 min, then centrifuged at 12,000 rpm for 30 min, decanted, and the nanoparticles were redispersed in 5 mL of water to remove excess reactants, then centrifuged again at 12,000 rpm for 30 min and decanted. The UCNP@Au were finally redispersed in 5 mL water by sonication for 10 min, with a final concentration of 1.4 mg/mL.

Optical Characterization of UCNPs and UCNP Composites

Upconverting samples were illuminated with a Coherent Chameleon II Ultra pulse laser (140 femtosecond pulse width) through a lens with a 7 cm focal length. The power at the sample was 668 mW for nanoparticles in solution and 680 mW for polymer composite films. Light from the upconversion was collected through the same lens then diverted by a dichroic beam splitter and focused via a 20cm lens to a Horiba iHR550 spectrometer equipped with a Symphony II CCD camera. Extra 980 nm light from the laser was filtered out before the spectrometer using a 700 nm short pass filter. A schematic of the instrumental setup is shown in **Figure 7.2**. The filtering was not completely successful and the increasing signal near 700 nm in the optical emission data is from backscattered laser light. For measurement of the nanoparticles in solution the UCNP cores were measured in cyclohexane, and UCNP@ SiO_2 and UCNP@Au were measured in methanol. Solvents with similar solubility were chosen to disperse the nanoparticles for optical measurements. Methanol was used in place of water because of water's absorbance in

the IR range. The weight percent of the UCNP cores in cyclohexane and UCNP@SiO₂ methanol was kept constant at 16 mg/mL, and the UCNP@Au nanoparticles were dispersed in methanol at the same particle concentration as the UCNP@SiO₂ sample to facilitate the most accurate comparison. The spectrometer exposure times for the samples were adjusted to attain an optimal signal with as little noise as possible, and are as follows: 2 s for UNCPS in cyclohexane, 5 s for UCNP@SiO₂ in methanol, 10 s for UCNP@Au in methanol, and 2s for UCNP@SiO₂ in the polymer composite film. The exposure times were chosen to optimize signal to noise.

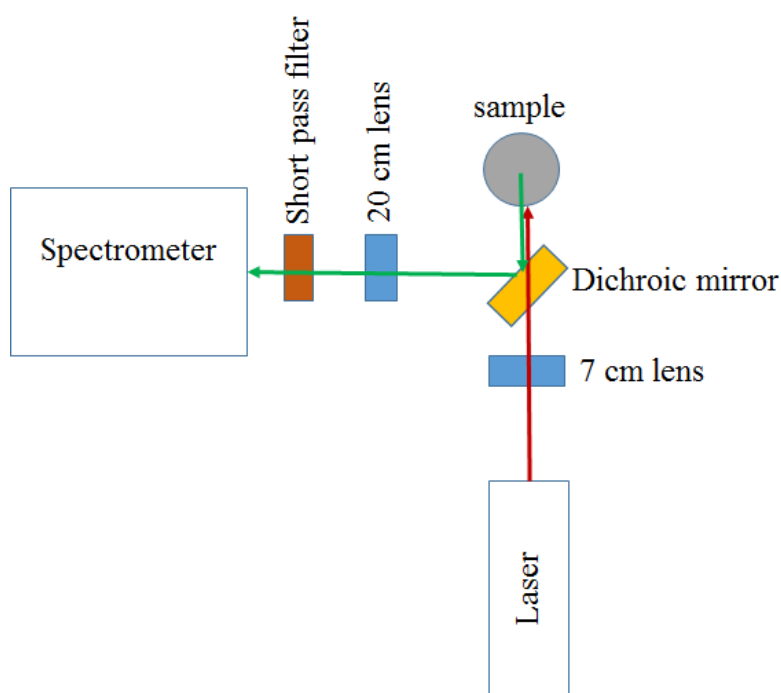


Figure 7.2. Schematic representation of the instrumental setup utilized in the measurement of upconverted optical emissions. The red arrow represents the exciting laser light, and the green arrow represents the backscattered upconverted emission.

Formation of UCNP@SiO₂ Composites

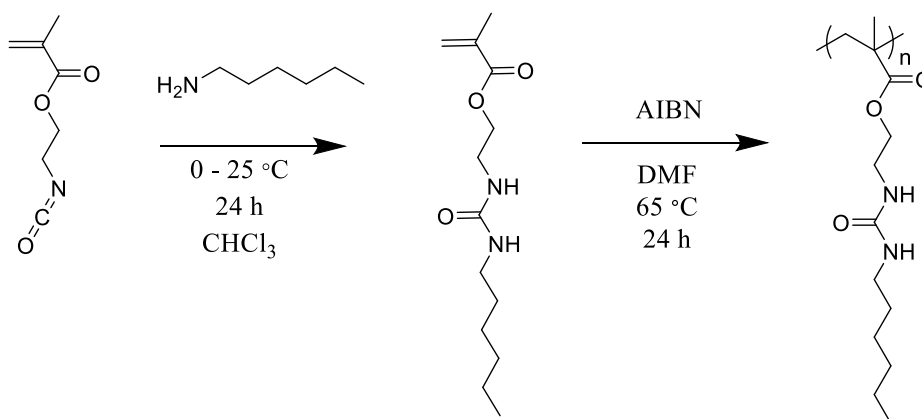
Urea-containing methacrylic polymers were combined with UCNP@SiO₂ to form upconverting composites according to following method. Dry UCNP@SiO₂ (25 mg) were

dispersed in MeOH (1 mL) by sonication for 1 h. Urea-containing methacrylic polymer (100 mg, 80:20 HUrMA:ArUrMA molar ratio) was dissolved in 1 mL of MeOH and added to the UCNP@SiO₂ dispersion in MeOH and the mixture was stirred for 5 min. The mixture was sonicated for 20 minutes before casting into a polytetrafluoroethylene mold, and dried at 25 °C for 16 h then at 65 °C for 8 h to ensure complete solvent removal.

7.4 Results and Discussion

Urea-containing polymer synthesis and properties

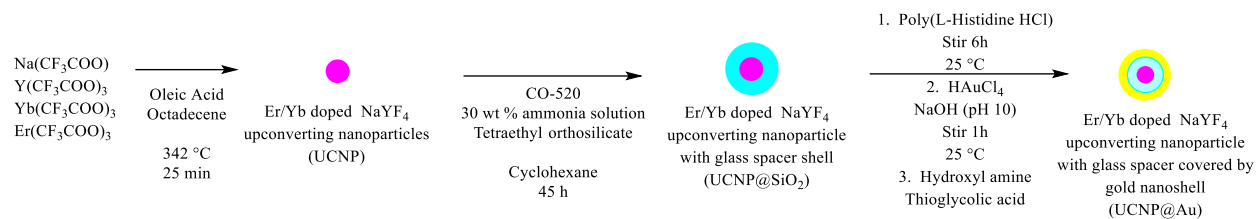
The efficient reaction of hexylamine with 2-ICMA yielded HUrMA in high purity and quantitative yield as shown in **Scheme 7.1**. However, passing the monomer through an alumina column to remove inhibitor reduced the overall yield. Free radical polymerization initiated using AIBN afforded poly(HUrMA) (**Scheme 7.1**) with high molecular weight and an isolated polymer yield of 60%. The polymer is extremely brittle, presumably due to the high degree of hydrogen bonding. The polymer possesses a sufficiently high molecular weight for characterization of physical properties, displaying a 5 wt% degradation temperature of 230 °C in TGA and a T_g of 77 °C in DSC.



Scheme 7.1. Synthesis and polymerization of HUrMA.

UCNP@Au Synthesis

A three-layer core/shell/shell nanoparticle structure with NaYF₄:Er,Yb core, SiO₂ inner spacer, and Au outer nanoshell was targeted in order to increase the upconversion efficiency of the NaYF₄:Yb,Er core through metal-enhanced fluorescence and allow for incorporation into poly(UrMA) block copolymer phases through Au-urea interactions (**Scheme 7.2**). High temperature degradation of trifluoroacetate salts accomplished formation of NaYF₄:Er,Yb nanoparticles. Use of a molten salt bath ensures uniform and rapid heating required to decompose the different trifluoroacetate salts with varying decomposition temperatures together in the reaction mixture. The length of this reaction effects the size and shape of the formed NaYF₄:Er,Yb nanoparticles.⁹ In this study, a reaction time of 25 min targeted spherical particles with a diameter of around 15 nm to serve as an ideal core for subsequent glass spacer growth and final Au nanoshell size. TEM analysis showed spherical particles with diameters around 10-15 nm (**Figure 7.3A**). Using these core particles, a glass spacer was deposited using base catalyzed hydrolysis of TEOS, where the concentration of reactants and length of reaction determines the glass spacer thickness. A reaction time of 45 h resulted in an ideal glass spacer thickness of about 10 nm (**Figure 7.3B**). The NaYF₄:Er,Yb cores are seen as the dark particles with a much less electron dense SiO₂ shell around them. The final diameter of UCNP@SiO₂ ranged from about 20-30 nm due to differences in core size and glass deposition. A glass spacer of around 10 nm ensures the metal nanoshell is spaced far enough away from the core to prevent quenching of the upconversion fluorescence.¹⁸



Scheme 7.2. Synthesis of upconverting nanoparticles with silica spacer and gold nanoshell.

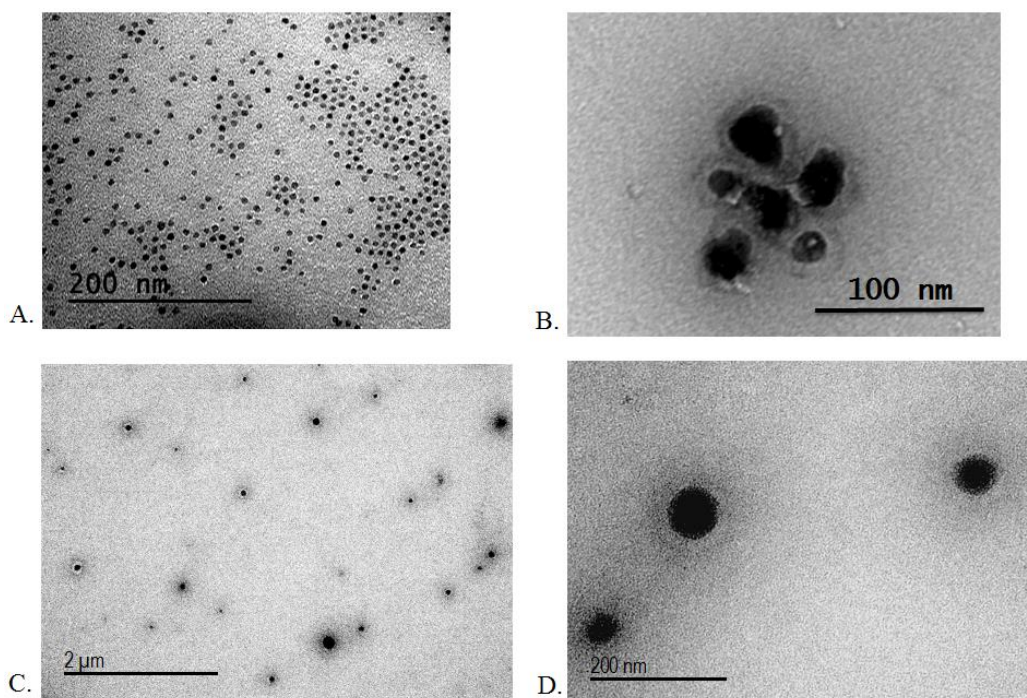


Figure 7.3. TEM of upconverting nanoparticles: A.) Er/Yb doped NaYF_4 core. B.) Er/Yb doped NaYF_4 core with glass spacer. C.) and D.) UCNP@Au nanoshell.

The Au nanoshell design serves two purposes: to provide a gold surface for the urea groups in the polymers to interact with, and to attempt to enhance the $\text{NaYF}_4\text{:Er,Yb}$ upconversion through MEF. If the metal shell is too thick the upconversion will be blocked, making a thin Au layer desirable. A poly-L-histidine templated method achieved Au nanoshell

deposition onto the glass surface of UCNP@SiO₂. In this approach, the positively charged poly-L-histidine hydrochloride adsorbed onto the negatively charged silica surface through electrostatic interactions. After isolation of the polymer-coated nanoparticles to any remove excess polymer, incubation with Au³⁺ ions which interact strongly with the imidazole rings in poly-L-histidine leads to Au³⁺ localization on the particle surface.¹⁸ Subsequent rapid reduction of the Au³⁺ ions with hydroxylamine forms Au nanoshells on the surface of the UCNP@SiO₂, forming UCNP@Au (**Figure 7.3C-D**). The final nanoparticles display diameters around 40-60 nm with high polydispersity, indicating Au nanoshells of 10-15 nm in thickness and greater. Neither the polydispersity nor the thickness of these Au shells are ideal for MEF applications and require further optimization.

Optical Properties of UCNPs and Upconverting Composites

Figure 7.4 shows the optical upconverted emission properties of the nanoparticles when excited with 980 nm laser light, focusing on the relevant emission range showing the red and green emissions. UCNPs and UCNP@SiO₂ display strong upconversion signals and visible emission. Even though the UCNP@SiO₂ particle dispersion had a longer exposure time, it exhibits a lower emission intensity. The difference in solvent environment and amount of upconverting material present in the sample likely account for this decreased intensity. Since the silica shell adds weight and the particles are measured at the same wt % versus solvents, there is more upconverting material in the UCNP sample dispersed in cyclohexane. There is no significant signal from UCNP@Au, as the gold shell's thickness likely attenuated the upconverted emission. A thinner gold shell is required for a proper application of MEF in this system.

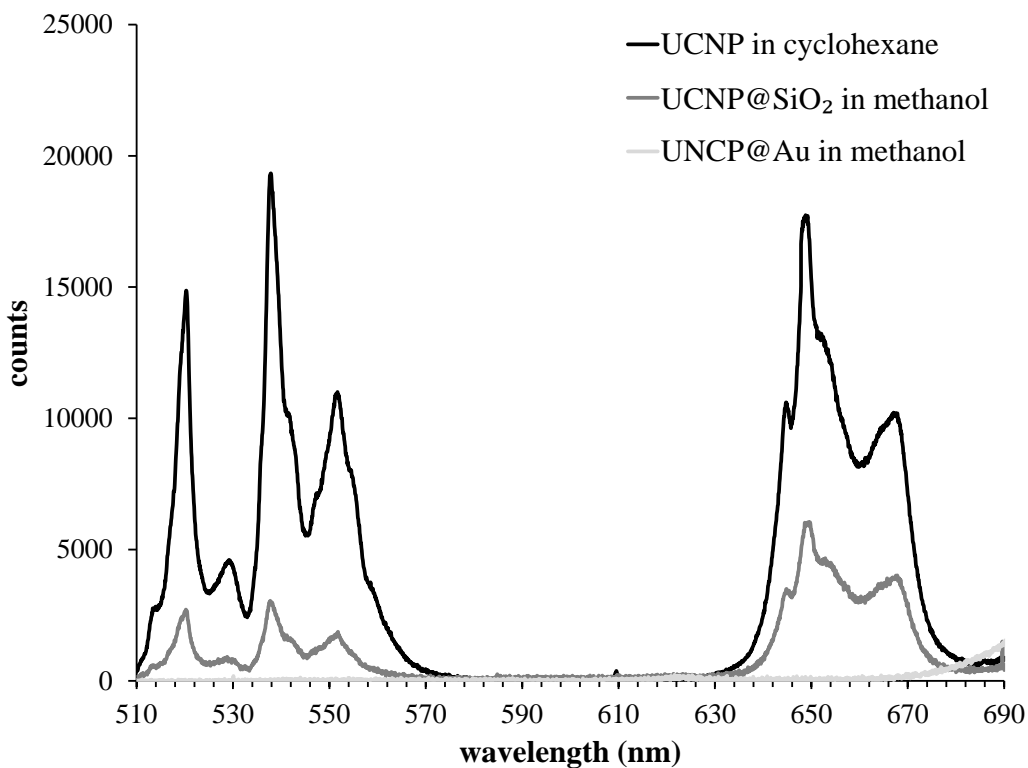


Figure 7.4. Optical emission properties of UCNPs in solution.

Due to the attenuation of the upconverted emission in the UCNP@Au nanoparticles, UCNP@SiO₂ nanoparticles were selected for the formation of nanocomposites with poly(HUrMA). Sonication achieved macroscopic dispersion of UCNP@SiO₂ in the polymer, and the formed composite was slightly opaque due to the high loading of nanoparticles (25 wt%). The composite was very brittle, similar to the homopolymer film. DSC did not show a change in the T_g, however more investigation is required to probe the effect of UCNP@SiO₂ incorporation on polymer physical properties and to determine the state of the UCNP@SiO₂ dispersion in the polymer. Urea groups likely facilitate thorough dispersion of the UCNP@SiO₂ nanoparticles in the polymer matrix through hydrogen bonding. Excitation of the composite film with 980 nm laser light produces a strong upconverted emission signal accompanied by visible emission as

shown in **Figure 7.5**. Excitation with the small laser source causes the whole composite sample to glow with upconverted light, likely due to refraction of the upconverted light throughout the film. The measured properties are very similar between the UCNP@SiO₂ nanoparticles in methanol versus in the film composite. Increased local concentration of the nanoparticles in the film compared to the solution and the enhanced ability to focus the laser precisely on the film sample account for the increased signal in the composite film. These results demonstrate that the UCNP@SiO₂ upconvert light effectively in the polymer matrix. Also, this polymer has no significant absorption in the critical range for this upconversion process.

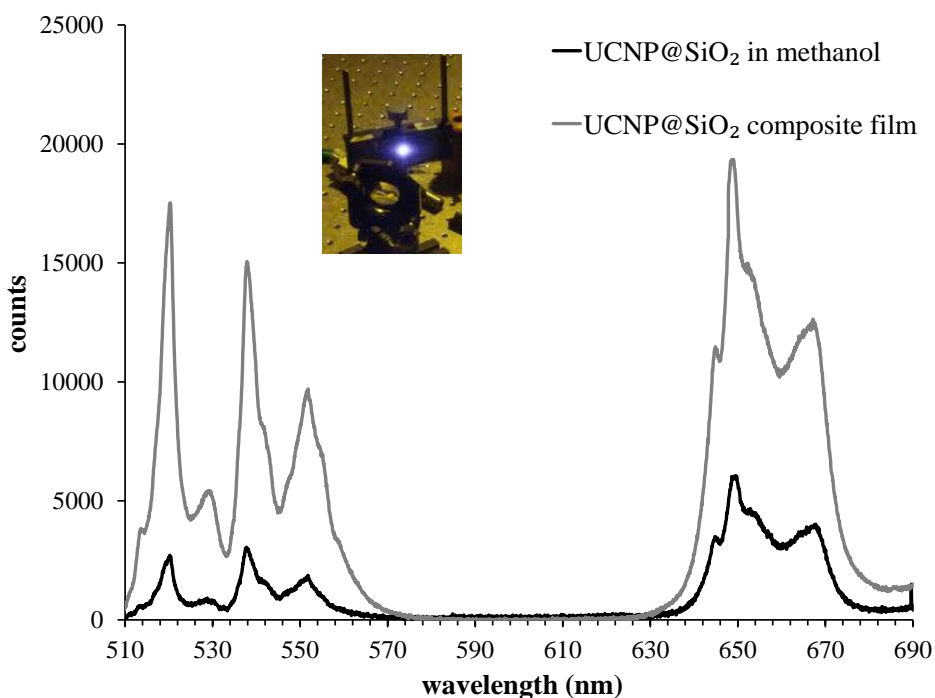


Figure 7.5. Optical emission properties of UCNP@SiO₂ polymer composites. Inset shows visible upconversion emission from UCNP@SiO₂ composite film.

7.5 Conclusions

High temperature degradation of trifluoroacetate salts afforded upconverting Yb/Er doped NaYF₄ nanoparticles. Base-catalyzed hydrolysis of TEOS in the presence of Yb/Er doped NaYF₄ nanoparticles yielded silica coated UCNPs. Both bare and silica coated core nanoparticles displayed desirable and expected upconversion properties upon excitation with 980 nm laser light. Addition of a gold nanoshell attenuated the upconverted emission due to the thickness of the gold nanoshell. Silica coated upconverting nanoparticles were successfully incorporated into a urea-containing methacrylic polymer to form upconverting nanocomposites. Urea-containing methacrylic polymers are promising candidates for polymer matrices in nanocomposites utilizing silica or gold coated upconverting nanoparticles due to the favorable polymer-nanoparticles interactions.

Acknowledgements. The authors would like to thank Kathy Lowe for assistance with TEM performed at the Virginia-Maryland Regional College of Veterinary Medicine morphology lab at Virginia Tech. This work was supported by the Institute for Critical Technology and Applied Science (ICTAS). This work was supported in part by NSF-Career Award DMR-0846834.

7.6 References

1. Hilderbrand, S. A.; Shao, F.; Salthouse, C.; Mahmood, U.; Weissleder, R. *Chem. Commun.* **2009**, 4188.
2. Mader, H. S.; Kele, P.; Saleh, S. M.; Wolfbeis, O. S. *Curr. Opin. Chem. Biol.* **2010**, *14*, 582.
3. Henke, B.; Ahrens, B.; Johnson, J. A.; Miclea, P. T.; Schweizer, S.; International Society for Optics and Photonics, p 74110E.
4. Johnson, C. M.; Reece, P. J.; Conibeer, G. J. *Opt. Lett.* **2011**, *36*, 3990.
5. Auzel, F. *Chem. Rev.* **2004**, *104*, 139.
6. Wang, F.; Liu, X. *Chem. Soc. Rev.* **2009**, *38*, 976.
7. Dong, H.; Sun, L.-D.; Yan, C.-H. *Nanoscale* **2013**, *5*, 5703.
8. Wang, F.; Liu, X. *J. Am. Chem. Soc.* **2008**, *130*, 5642.

9. Ye, X.; Collins, J. E.; Kang, Y.; Chen, J.; Chen, D. T. N.; Yodh, A. G.; Murray, C. B. *Proceedings of the National Academy of Sciences* **2010**, *107*, 22430.
10. Ruiz-Morales, J. C.; Mendez-Ramos, J.; Acosta-Mora, P.; Borges, M. E.; Esparza, P. *Journal of Materials Chemistry C* **2014**, *2*, 2944.
11. Xie, D.; Peng, H.; Huang, S.; You, F. *Journal of Nanomaterials* **2013**, 2013.
12. Zhang, F.; Braun, G. B.; Shi, Y.; Zhang, Y.; Sun, X.; Reich, N. O.; Zhao, D.; Stucky, G. J. *Am. Chem. Soc.* **2010**, *132*, 2850.
13. Schietinger, S.; Aichele, T.; Wang, H.-Q.; Nann, T.; Benson, O. *Nano Lett.* **2009**, *10*, 134.
14. Saboktakin, M.; Ye, X.; Oh, S. J.; Hong, S.-H.; Fafarman, A. T.; Chettiar, U. K.; Engheta, N.; Murray, C. B.; Kagan, C. R. *ACS nano* **2012**, *6*, 8758.
15. Aslan, K.; Leonenko, Z.; Lakowicz, J. R.; Geddes, C. D. *Journal of fluorescence* **2005**, *15*, 643.
16. Li, Z. Q.; Chen, S.; Li, J. J.; Liu, Q. Q.; Sun, Z.; Wang, Z. B.; Huang, S. M. *J. Appl. Phys.* **2012**, *111*, 014310.
17. Zhang, J.; Fu, Y.; Lakowicz, J. R. *The Journal of Physical Chemistry C* **2009**, *113*, 19404.
18. Priyam, A.; Idris, N. M.; Zhang, Y. *J. Mater. Chem.* **2012**, *22*, 960.
19. Yuan, P.; Lee, Y. H.; Gnanasammandhan, M. K.; Guan, Z.; Zhang, Y.; Xu, Q.-H. *Nanoscale* **2012**, *4*, 5132.
20. Stepuk, A.; Mohn, D.; Grass, R. N.; Zehnder, M.; Krämer, K. W.; Pellé, F.; Ferrier, A.; Stark, W. J. *Dent. Mater.* **2012**, *28*, 304.
21. Na, H.; Jeong, J. S.; Chang, H. J.; Kim, H.; Woo, K.; Lim, K.; Mkhoyan, K. A.; Jang, H. S. *Nanoscale* **2014**.
22. Boyer, J. C.; Johnson, N. J. J.; van Veggel, F. C. J. M. *Chem. Mater.* **2009**, *21*, 2010.
23. Seeni Meera, K. M.; Murali Sankar, R.; Paul, J.; Jaisankar, S. N.; Mandal, A. B. *PCCP* **2014**.
24. Chen, C.-J.; Tsai, M.-H.; Tseng, I. H.; Hsu, A.-W.; Liu, T.-C.; Huang, S.-L. *RSC Advances* **2013**, *3*, 9729.
25. Sadeek, S. A.; Refat, M. S. *J. Coord. Chem.* **2005**, *58*, 1727.
26. Nishat, N.; Ahmad, S.; Tansir Ahamad, R. *J. Appl. Polym. Sci.* **2006**, *100*, 928.
27. Penland, R. B.; Mizushima, S.; Curran, C.; Quagliano, J. V. *J. Am. Chem. Soc.* **1957**, *79*, 1575.

Chapter 8: Synthesis and Characterization of Oxalamide Ammonium Ionenes

David L. Inglefield Jr.^a, Chainika Jangu^b, Gregory Fahs^a, Robert B. Moore^{ab}, and Timothy E. Long^{ab}

*^aDepartment of Chemistry, ^bMacromolecules and Interfaces Institute
Virginia Tech, Blacksburg, VA 24061*

8.1 Abstract

A novel oxalamide ionene monomer, N1,N2-bis(3-(dimethylamino)propyl)oxalamide, enabled the synthesis of novel oxalamide-containing ionenes. Exchanging bromide counteranions with bis(trifluoromethane)sulfonimide counteranions probed the effect of counter anion on ionene properties. Thermogravimetric analysis, differential scanning calorimetry, dynamic mechanical analysis, and tensile analysis characterized the thermal and mechanical properties of the resulting ionenes compared to all alkyl ionenes with similar charge density. Exchange to bis(trifluoromethane)sulfonimide counteranions lowered the glass transition temperature in all cases, and the incorporation of the oxalamide group into the ionene structure increased the glass transition temperature. The polymer structure influenced water uptake determined using sorption analysis. Ionic conductivity measured using impedance spectroscopy and small-angle X-ray scattering evidence of ionic aggregation correlated to the polymer structure and physical properties. The hydrogen bonding oxalamide ionenes displayed excellent mechanical properties and relatively high glass transition temperatures in both counter anion forms, and the introduction of the oxalamide groups into the ionene structure affected ionic aggregation and ionic conductivity.

8.2 Introduction

Ammonium ionenes are polyelectrolytes that contain quaternary nitrogen atoms in the polymer backbone. Gibbs *et al.* first synthesized ammonium ionenes in 1933 using AB type dimethylamino-n-alkyl halide monomers.¹ Ammonium ionene synthesis is also achieved through the Menschutkin reaction polymerizing dihalides with ditertiary amines.² Ionenenes are conventionally named by the number of methylene units in the ditertiary amine and dihalide monomers (x,y-ionene).³ The change in charge density and counter anion affects the material properties and solubility of ammonium ionenes.⁴ Molecular weight also influences the properties of ammonium ionenes, and critical molecular weight ranges are required to achieve desirable properties.⁵ Most of the explored applications of ionenes are biomedical including gene delivery vectors and anti-microbials due to their water solubility and easily tuned charged density.⁶⁻⁹ Ammonium ionenes typically display poor mechanical properties with high glass transition temperatures (T_g s) and charge densities contributing to their brittle nature. Also, ammonium ionenes with halide counteranions are very hydrophilic at ambient conditions and tend to absorb large amounts of water, further limiting their mechanical applications. Ammonium ionenes possess limited base and thermal stability due to degradation through Hofmann elimination in basic conditions and at temperatures around 250 °C.¹⁰

The synthesis of ionenes containing imidazolium and phosphonium cations in the polymer backbone is achieved using similar reactions of alkyl dihalides with bis-imidazole and ditertiary phosphine monomers, respectively. Imidazolium and phosphonium cations broaden the monomer selection and material properties of ionenes. Hemp *et al.* recently demonstrated the synthesis of phosphonium ionenes from 1,4-bis(diphenylphosphino) butane and 1,12-dibromododecane.¹¹ The resulting phosphonium ionenes possess superior thermal and base

stability compared to their ammonium counterparts, with degradation temperatures above 300 °C and no observable molecular weight change after exposure to basic conditions. Melt rheology master curves showed two primary relaxations, one attributed to the onset of long-range segmental motion (T_g) and a second relaxation due to electrostatic interactions (ionic dissociation).

Segmented systems further expand the material applications of ionenes by reducing charge density and providing the possibility for phase separation. These segmented ionenes are typically synthesized using halide or tertiary amine end capped low T_g oligomers. Wilkes *et al.* investigated the structure-property relationships of polytetramethylene oxide (PTMO)-based segmented ionenes prepared through the reaction of dimethylamino-terminated PTMO oligomers with 1,4-dibromo-*p*-xylene.¹² These segmented ionenes displayed microphase separation between ionic aggregates and PTMO soft segments indicated through transmission electron microscopy (TEM) showing rod-like ionic domains, and multiple peaks observed in small-angle X-ray scattering (SAXS). The microphase separated morphology led to elastomeric material properties. Williams *et al.* prepared segmented imidazolium ionenes with PTMO soft segments and investigated the morphology and mechanical properties as a function of hard segment content.¹⁰ The mechanical properties and morphology varied with the hard segment content, with compositions of 20 and 38 wt% hard segment displaying lamellar morphologies in SAXS along with soft and hard segment T_g s in dynamic mechanical analysis (DMA). Tamami *et al.* demonstrated the synthesis of segmented polypropylene glycol (PPG)-based ammonium ionenes with varying hard segment content.¹³ DMA showed the dependence of mechanical properties on the hard segment content, and atomic force microscopy (AFM) imaged the phase separated morphology.

Although many polyurethane ionomers have been investigated, few investigations focus on ionenes synthesized through the Menshutkin reaction with significant levels of hydrogen bonding.¹⁴⁻¹⁹ Tamami *et al.* investigated the intermolecular interactions in nucleobase-containing polyethylene glycol (PEG)-based segmented ammonium ionenes functionalized with adenine and thymine.²⁰ Complementary nucleobase guest molecules were successfully incorporated into the polymer matrix and association constants were measured. SAXS analysis revealed a phase separated morphology. Furthermore, AFM imaged a phase separated morphology of PEG soft segments with nucleobase and ionic aggregate rich hard segments. The addition of the complementary nucleobase guest molecules disrupted the phase-separated morphology as evidenced through SAXS and AFM.

Herein we investigate the synthesis of oxalamide ammonium ionenes using a novel oxalamide-containing ditertiary amine monomer. A facile synthesis yields high purity difunctional monomer in quantitative yield with limited purification. High molecular weight oxalamide ionenes were synthesized with varying charge density, named 3ox3,y-ionenes, along with 6,12-alkyl ammonium ionene analogues for comparison. Anion exchange of bromide with bis(trifluoromethane)sulfonimide (Tf₂N) counteranions resulted in lower T_gs and reduced water uptake. Oxalamide ionenes displayed relatively high T_gs and good mechanical properties in both anion forms due to their multi-dentate hydrogen bonding as evidenced in dynamic mechanical analysis (DMA) and tensile testing. Impedance spectroscopy probed the conductivity of these ionenes, and X-ray scattering revealed the effect of counter anion and hydrogen bonding incorporation on ionic aggregation in these ionenes.

8.3 Experimental

Materials and Instrumentation

Ethanol was obtained from Decon Laboratories and used as received. Dimethyl sulfoxide was obtained from Fischer Scientific and used as received. Methanol was obtained from Fischer Scientific and was distilled over molecular sieves before use. All reagents were obtained from Sigma Aldrich. Diethyl oxalate ($\geq 99\%$), dimethylaminopropylamine (99%), and bis(trifluoromethane)sulfonimide lithium salt were used as received without further purification. 1,4-dibromobutane (99%), 1,12-dibromododecane (98%), and N,N,N',N'-tetramethyl-1,6-hexanediamine (99%) were obtained from Sigma Aldrich and distilled before use. Spectra/Por regenerated cellulose dialysis membranes were purchased from Spectrum Laboratories, Inc. with a molecular weight cutoff of 3,500 g/mol.

Differential scanning calorimetry (DSC) was performed using a TA instruments DSC2000 differential scanning calorimeter with a heating rate of 10 °C/min. Thermogravimetric analysis (TGA) was performed using a TA Instruments Q500 thermogravimetric analyzer with a heating rate of 10 °C/min under a nitrogen atmosphere. Dynamic mechanical analysis (DMA) was performed on a TA Instruments Q800 dynamic mechanical analyzer in tension mode using a heating rate of 3 °C/min and an amplitude of 15 μm . Tensile analysis was performed on an Instron 5500 R using a ramp rate of 10 mm/min. All tensile samples were cut using a Pioneer Dietec dog bone cutter (ASTM D-638-V) and 6 trials were performed for each sample. XPS was performed using a PHI Quantera SXM scanning photoelectron spectrometer microprobe. Molecular weights and polydispersity indices (PDIs) of polymers was determined using size exclusion chromatography (SEC) performed using an aqueous solvent of 54/23/23 (v/v/v %) water/methanol/acetic acid with 0.1 M sodium acetate at a flow rate of 0.8 mL/min with a Waters

1515 isocratic HPLC pump, a Waters 717plus autosampler, two Waters Ultrahydrogel linear columns, one Waters Ultrahydrogel 250 column, a Wyatt MiniDAWN, and a Waters 2414 refractive index detector. Offline dn/dc measurements were determined using an Optilab T-rEX refractometer ($\lambda = 658$ nm) to provide absolute molecular weights in SEC analysis. ^1H nuclear magnetic resonance (NMR) spectroscopy was performed on a Varian Unity 400 MHz NMR spectrometer using 64 scans. Liquid chromatography/mass spectrometry analysis was performed using reversed phase liquid chromatographic separations with a LUNA C₁₈ (150 x 2.0mm, 5.0mm dp) column from Waters. High performance liquid chromatography separations were obtained using an Agilent HPLC 1100 series equipped with a diode array detector (DAD), column heater set at 40°C, and a Thermo Survey auto-sampler. For MS analysis, the HPLC column effluent was pumped directly into the Thermo Instrument TSQ triple quadrupole mass spectrometer equipped with an ESI source, operating in scan mode with range of 100-1500 amu. A TA Instruments Q5000 sorption analyzer (TGA-SA) measured water uptake of polymer samples (relative humidity (RH) 0 – 95%, 5% increments) at 25 °C. Electrochemical impedance spectroscopy (EIS) was performed using an Autolab PGSTAT 302N potentiostat and a four-point electrode sample cell purchased from BakkTeck, Inc. An applied alternating sine-wave potential was applied at 0.2 V with frequencies ranging from 0.1 Hz to 1 MHz. The temperature and relative humidity (RH) was controlled using an ESPEC BTL- 433 environmental chamber which controlled the temperature to ± 0.1 °C and 10% RH to $\pm 0.1\%$. An alternating current was applied to the outer electrodes and the real impedance or resistance, R, was measured between the two inner reference electrodes. The resistance was determined from a high x-intercept of the semicircle regression of the Nyquist plot. The ionic conductivity was determined by $\sigma = L/AR$, where L and A are the distance between the two inner electrodes and the cross-sectional area of

the polymer film, respectively. The cross-sectional area is defined as $A = Wl$, where W is the film width and l is the film thickness. Samples were allowed to equilibrate for 1 h at each measurement condition followed by at least five measurements at that condition. The values reported are an average of these steady-state measurements. SAXS experiments were performed using a Rigaku S-Max 3000 3 pinhole SAXS system, equipped with a rotating anode emitting X-ray with a wavelength of 0.154 nm (Cu $K\alpha$). The sample-to-detector distance was 1603 mm, and q -range was calibrated using a silver behenate standard. Two-dimensional SAXS patterns were obtained using a fully integrated 2D multiwire, proportional counting, gas-filled detector, with an exposure time of 2 hours. The SAXS data have been corrected for sample thickness, sample transmission and background scattering. All the SAXS data were analyzed using the SAXSGUI software package to obtain radially integrated SAXS intensity versus scattering vector q , where $q=(4\pi/\lambda)\sin(\theta)$, θ is one half of the scattering angle and λ is the wavelength of X-ray. The profiles were vertically shifted to facilitate a comparison of the peak positions.

Synthesis of N1,N2-bis(3-(dimethylamino)propyl)oxalamide

A 250-mL, round-bottomed, flask equipped with magnetic stirrer and addition funnel was charged with dimethylaminopropylamine (392 mmol, 40 g) in ethanol (70 mL) over an ice bath. Diethyl oxalate (196 mmol, 28.62 g) was added dropwise under magnetic stirring and the reaction proceeded for 4 h at 0 °C, then 20 h at 25 °C. Ethanol was removed under reduced pressure, then the product was removed from the round-bottomed flask and dried at 60 °C *in vacuo* for 12 h yielding a white solid. N1,N2-bis(3-(dimethylamino)propyl)oxalamide was obtained in quantitative yield. The structure and purity were confirmed using ^1H NMR and LC-MS. ^1H NMR (400 MHz, DMSO- d_6): δ 1.54 (m, 4H), 2.06 (s, 12H), 2.15 (t, 4H), 3.10 (m, 4H), 8.72 (t, 2H), 2.47 (DMSO), 3.29 (H $_2$ O).

Synthesis of 3ox3,4-Br Oxalamide Ionenenes

For a typical synthesis: A 100-mL, round-bottomed, flask equipped with a magnetic stirrer and water jacketed condenser was charged with N1,N2-bis(3-(dimethylamino)propyl)oxalamide (11.6 mmol, 3 g) and 1,4-dibromobutane (11.6 mmol, 2.51 g) dissolved at 25 wt% in methanol (20.89 mL). The mixture was reacted under reflux with magnetic stirring at 65 °C for 24 h. Methanol was removed under reduced pressure and the polymer was dried at 65 °C *in vacuo* for 12 h yielding 3ox3,4-Br oxalamide ionene in quantitative yield. All ionenes were stored under vacuum in a desiccator.

Synthesis of 3ox3,12-Br Oxalamide Ionenenes

For a typical synthesis: A 100-mL, round-bottomed, flask equipped with a magnetic stirrer and water jacketed condenser was charged with N1,N2-bis(3-(dimethylamino)propyl)oxalamide (11.6 mmol, 3 g) and 1,12-dibromododecane (11.6 mmol, 3.81 g) dissolved at 25 wt% in methanol (26 mL). The mixture was reacted under reflux with magnetic stirring at 65 °C for 24 h. Methanol was removed under reduced pressure and the polymer was dried at 65 °C *in vacuo* for 12 h yielding 3ox3,12-Br oxalamide ionene in quantitative yield. All ionenes were stored under vacuum in a desiccator.

Synthesis of 6,12-Br Alkyl Ionenenes

For a typical synthesis: A 100-mL, round-bottomed, flask equipped with a magnetic stirrer and water jacketed condenser was charged with N,N,N',N'-tetramethyl-1,6-hexanediamine (11.2 mmol, 1.94 g) and 1,12-dibromododecane (11.2 mmol, 3.69 g) dissolved at 25 wt% in methanol (21.4 mL). The mixture was reacted under reflux with magnetic stirring at 65 °C for 24 h. Methanol was removed under reduced pressure and the polymer was dried at 65 °C *in*

vacuo for 12 h yielding 6,12-Br alkyl ionene in quantitative yield. All ionenes were stored under vacuum in a desiccator.

Anion Exchange and Film Casting

All ionenes were anion exchanged as follows: A 100 mL, round-bottomed, flask equipped with a magnetic stirrer and addition funnel was charged with a 3 g/mL bis(trifluoromethane)sulfonimide lithium salt solution (amount determined by calculating a 5x molar excess of bis(trifluoromethane)sulfonimide lithium salt relative to bromide ionene in the polymer to be anion exchanged). A 10 wt% solution of the ionene (2g in 20 mL of water) was added drop-wise over 1 h to the bis(trifluoromethane)sulfonimide lithium salt solution. The anion exchanged polymer precipitated out of water forming a white solid. The anion exchanged polymer was dissolved in 20 mL of methanol (3ox3,12 oxalamide ionene and 6,12 alkyl ionene) or 20 mL of dimethyl sulfoxide (3ox3,4 oxalamide ionene) and this solution was dialyzed three times for 12 h against 2 L of methanol (3ox3,12 oxalamide ionene and 6,12 alkyl ionene) or dimethyl sulfoxide (3ox3,4 oxalamide ionene) depending on the anion exchanged polymer solubility. The solvent was removed under reduced pressure and the dialyzed, anion exchanged polymers were dried *in vacuo* to a constant weight yielding 3ox3,4- Tf₂N oxalamide, 3ox3,12- Tf₂N oxalamide, and 6,12- Tf₂N alkyl ionenes in 87%, 89%, and 93% yields, respectively. Complete anionic exchange was confirmed by the absence of Br in XPS analysis.

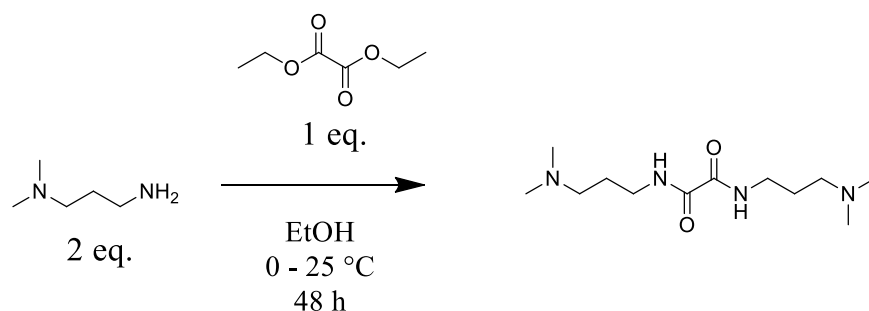
All films were cast identically and had the same thermal history before testing. The polymers were dissolved at 20 wt% in methanol and cast into teflon molds. The films were dried for 48 h at 25 °C, then for 48 h *in vacuo* at 25 °C, then for 48 h *in vacuo* at 70 °C. This method of film casting avoided the formation of bubbles. The films were stored in a desiccator under

vacuum. The 3ox3,4- Tf₂N oxalamide ionene was cast from DMSO with the above drying procedure, but did not form films suitable for mechanical testing.

8.4 Results and Discussion

Oxalamide Ionene Monomer Synthesis

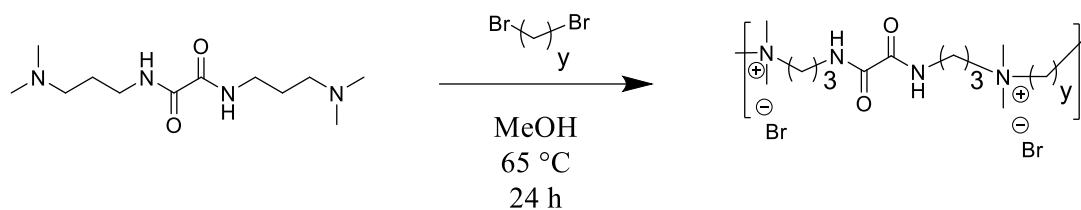
The novel oxalamide ionene monomer N1,N2-bis(3-(dimethylamino)propyl)oxalamide was synthesized in quantitative yield and high purity through a facile synthesis under mild conditions (**Scheme 8.1**). The nucleophilic addition of dimethylaminopropylamine to diethyl oxalate proceeded completely at room temperature in ethanol as a solvent. After ethanol removal under reduced pressure, the product was purified by stripping off any unreacted reagents under high vacuum. After thorough drying, ¹H NMR and LC/MS confirmed the structure and purity of this compound. LC/MS analysis revealed a pure compound with m/z = 259.24 (M+H), compared to a calculated molecular weight 258.38 g/mol. This ionene monomer is exciting due to its facile preparation and low cost of starting materials. The oxalamide group provides added functionality to ionenes synthesized with this monomer through multidentate hydrogen bonding. This low cost, facile synthesis, and added hydrogen bonding makes this ionene monomer attractive when compared to other ditertiary amines.



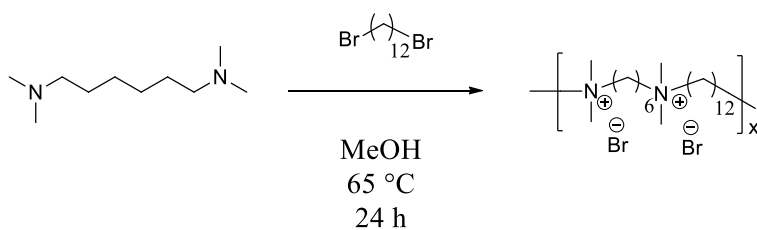
Scheme 8.1. Synthesis of N1,N2-bis (3-(dimethylamino)propyl)oxalamide.

Polymer Synthesis and Molecular Weight Analysis

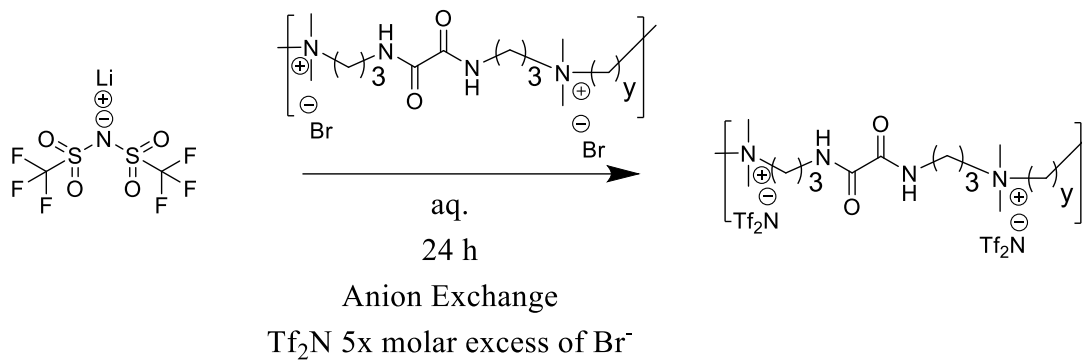
The Menshutkin reaction led to the synthesis of ammonium ionenes from ditertiary amines and dibromides in quantitative yields after isolation by solvent removal. Reaction in refluxing methanol at 65 °C was sufficient to obtain high molecular weight oxalamide (**Scheme 8.2**) and alkyl (**Scheme 8.3**) ionenes as the oxalamide group should have no effect on ditertiary amine reactivity in N1,N2-bis(3-(dimethylamino)propyl)oxalamide. SEC analysis to obtain absolute molecular weights (**Table 8.1**) using dn/dc values determined offline revealed M_w s above 20,000 g/mol, which is in the critical molecular weight range for ionene properties.⁵ Unexpectedly low PDIs are likely the results of limited chromatographic separation on these SEC columns. Anionic exchange with bis(trifluoromethane)sulfonimide lithium salt (**Scheme 8.4**) by a precipitation method and purification by dialysis led to the formation of ionenes with bis(trifluoromethane)sulfonimide (Tf_2N) counteranions. The absence of bromine in XPS analysis confirmed complete anionic exchange with Tf_2N anions.



Scheme 8.2. Synthesis of oxalamide ammonium ionenes.



Scheme 8.3. Synthesis of alkyl ammonium ionenes.



Scheme 8.4. Anionic exchange of oxalamide ionenes.

Thermal and Mechanical Properties of Oxalamide Ionenes

Oxalamide ionenes exhibit interesting and desirable thermal and mechanical properties compared to the alkyl ionene controls. The T_g s and decomposition temperatures at 5 wt% loss ($T_{d5\%}$) are summarized in **Table 8.1**. The 6,12 alkyl ionene is a suitable control for comparison to the 3ox3,4 oxalamide ionene because they possess similar charge densities in the bromide form of 4.0 and 4.2 milli-equivalents charge per gram, respectively, with the 3ox3,12 oxalamide ionene possessing a charge density of 3.4 milli-equivalents/gram. All of the ionenes in the bromide form had similar thermal stability, with $T_{d5\%}$ around 240-250 °C, consistent with ammonium ionenes degrading through Hoffman elimination. Once anion exchanged to the less basic Tf₂N form the ionenes displayed a significant increase in $T_{d5\%}$, which is consistent with literature, as they are less prone to the Hoffman elimination in Tf₂N form. The oxalamide ionenes in the Tf₂N form display a $T_{d5\%}$ around 300 °C, significantly lower than the 6,12-Tf₂N alkyl ionene possessing a $T_{d5\%}$ of 330 °C. This is likely due to the oxalamide group lowering the thermal stability, leading to polymer degradation beginning around 300 °C.

Table 8.1. Ionene molecular weights and thermal properties.

polymer	T_g (°C)	M_n (g/mol)	M_w (g/mol)	PDI	T_{d 5%} (°C)	Anion Exchange Yield (%)
6,12-Br	83	16,500	20,100	1.22	240	-
6,12-Tf₂N	-13	-	-	-	330	93%
3ox3,4-Br	140	23,900	28,100	1.24	252	-
3ox3,4-Tf₂N	67	-	-	-	300	87%
3ox3,12-Br	113	20,000	24,500	1.23	253	-
3ox3,12-Tf₂N	61	-	-	-	305	89%

The T_gs of the ionenes determined using DSC follow logical trends revealing the influence of the oxalamide group on T_g. The T_g of alkyl ammonium ionenes depends on the charge density and counter anion, and the T_gs of the 6,12-Br and 6,12-Tf₂N ionenes are consistent with alkyl ammonium ionenes with this charge density and these counteranions.⁴ The exchange of the bromide anion with Tf₂N⁻ significantly lowers the T_g due to the larger anion introducing a large amount of free volume into the polymer.^{21,22} The 3ox3,4-Br oxalamide ionene displays a significantly higher T_g when compared to the 6,12-Br ionene with a similar charge density. In this case, introduction of the oxalamide group increases the T_g by 57 °C when compared to the all alkyl control due to the presence of multidentate hydrogen bonding. This strong hydrogen bonding is expected to greatly affect the T_g. Again, anion exchange of bromide with Tf₂N anions significantly lowers the T_g, here by 73 °C. The 3ox3,12- Tf₂N ionene also has a significantly lower T_g than the 3ox3,12-Br ionene. In comparison to the 3ox3,4 oxalamide ionene, the 3ox3,12 oxalamide ionene has a lower T_g in both anion forms due to a lower charge density and lower concentration of oxalamide groups along the polymer backbone. In these ammonium ionenes, an increase in charge density or hydrogen bonding increases the T_g. All ionenes formed clear films capable of DMA testing except for the 6,12- Tf₂N ionene that was a

viscous liquid at room temperature due to the low T_g , and the 3ox3,4- Tf₂N ionene that had limited solubility and did not form self-standing films when cast from DMSO. Furthermore, the 3ox3,12 ionenes formed tough, creasable films capable of dogbone cutting of tensile samples and tensile testing.

DMA revealed the temperature dependent viscoelastic behavior of the oxalamide ionenes (**Figure 8.1**). Ionenes in the bromide form displayed two clear transitions evidenced in the storage modulus (**Figure 8.1A**) and tan delta (**Figure 8.1B**) versus temperature plots. The first transition is attributed to the T_g and the second is attributed to rapid temperature-induced ion hopping in relation to the timescale of the experiment which leads to a reduction in modulus.⁵ The closer proximity in temperature makes the two distinct transitions more difficult to observe in the bromide oxalamide ionenes as compared to the 6,12-Br alkyl ionene. The samples flow after these transitions and the failure of chain entanglements evident at higher temperatures in the storage modulus (**Figure 8.1A**). Although they possess similar charge densities, the transitions of the 3ox3,4-Br oxalamide ionene are much higher than in the 6,12-Br alkyl ionene. This indicates that the presence of the oxalamide group affects not only the T_g through hydrogen bonding, but also the polymer backbone ionic mobility at high temperatures. Also, comparing the 6,12-Br alkyl ionene to the 3ox3,12-Br oxalamide ionene which has a lower charge density reveals the effect of the oxalamide group, moving these transitions to higher temperatures. Although it is well established that increases in hydrogen bonding increase the T_g in polymers, the increase in hydrogen bonding in this structure also increases the temperature of the ionic transition.²³⁻²⁶ Although the ionic groups are the same and the charge density is similar between the 6,12-Br alkyl ionene and 3ox3,4-Br oxalamide ionene, the positioning of the strong

hydrogen bonding oxalamide group between the ionic sites likely strengthens the ionic interactions and requires higher temperatures to induce significant ion hopping

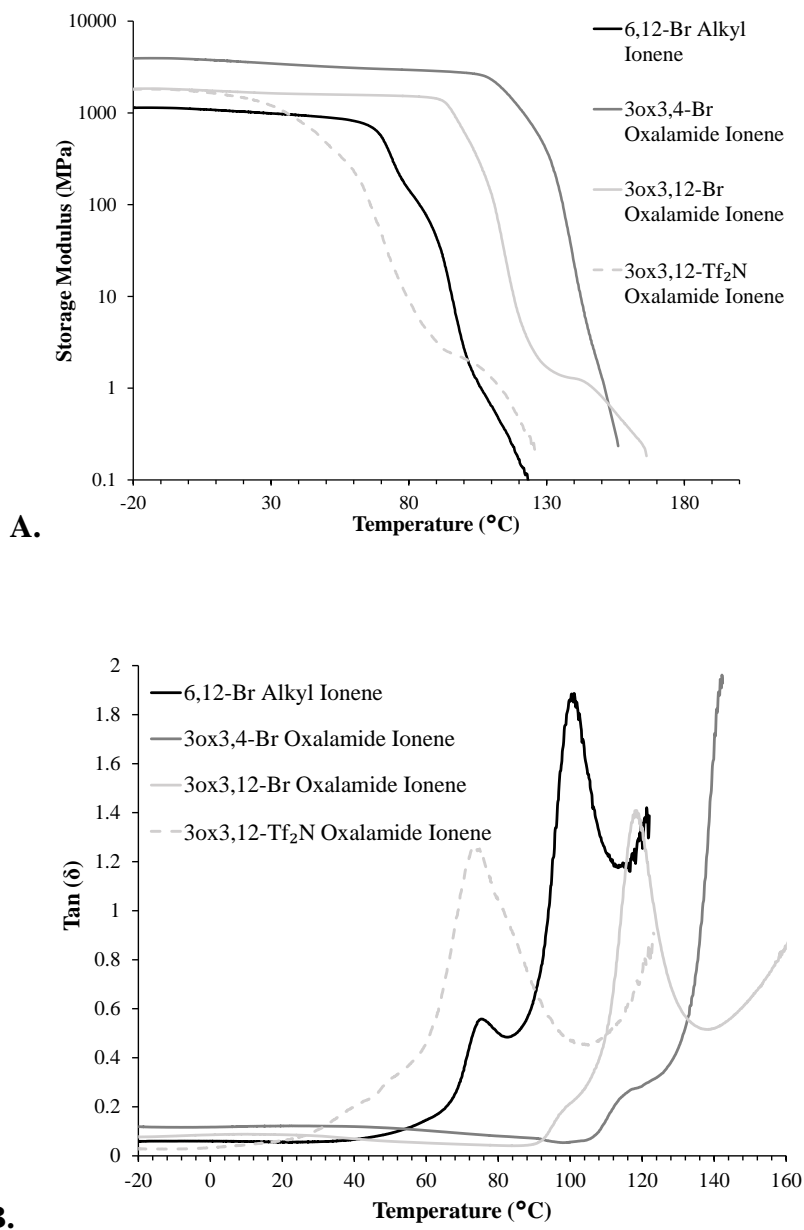


Figure 8.1. Dynamic mechanical analysis of oxalamide ionenes: A.) Storage modulus versus temperature. B.) Tan delta versus temperature.

Alkyl ammonium ionenes with Tf₂N counteranions typically possess low T_gs making them viscous liquids at room temperature unsuitable for DMA, however the 3ox3,12-Tf₂N

oxalamide ionene is a robust film at room temperature. This polymer displays only one broad transition very close to the T_g value obtained using DSC. The large counter anion introduces free volume and reduces the strength of the ionic interactions, effectively plasticizing the polymer and lowering the T_g compared to the bromide form.²⁷⁻²⁹ The ionic transition is either absent or concurrent with the T_g in this experiment. The Tf_2N counter anion's size influences how the ionic sites interact with each other, shielding the charges. The ionic transition may be very broad due to this effect, and concurred with a broad T_g transition.

Tensile testing of the tough, creasable 3ox3,12 ionene films reveal high strength at yield and high Young's modulus (**Table 8.2**). The tensile curves show a rapid yield at low strains, followed by an extension of the samples until break (**Figure 8.2**). The stress at yield, stress at break, and modulus are dependent on the counter anion, with similar strain at break. Stress-induced ion hopping and relaxation of the polymer chains leads to yield of the polymer films, with the larger Tf_2N counteranions leading to a lower yield stress because their size introduces more free volume and weakens the ionic aggregates.⁵ The change in counter anion from bromide to the larger Tf_2N anions also reduces the modulus by the same mechanism. Both counter anion forms have similar strain at break due to identical chain lengths, as the strain at break in ammonium ionenes is dependent on the molecular weight.⁵

Table 8.2. Summary of 3ox3,12 oxalamide ionene tensile properties.

Sample	Stress at Yield (MPa)	Stress at Break (MPa)	Strain at Break (%)	Modulus (MPa)
3ox3,12-Br Oxalamide Ionene	31.9 ± 2.3	16.4 ± 2.4	53.5 ± 2.6	1460 ± 80
3ox3,12- Tf_2N Oxalamide Ionene	17.2 ± 1.8	9.4 ± 1.2	48.6 ± 2.2	988 ± 15

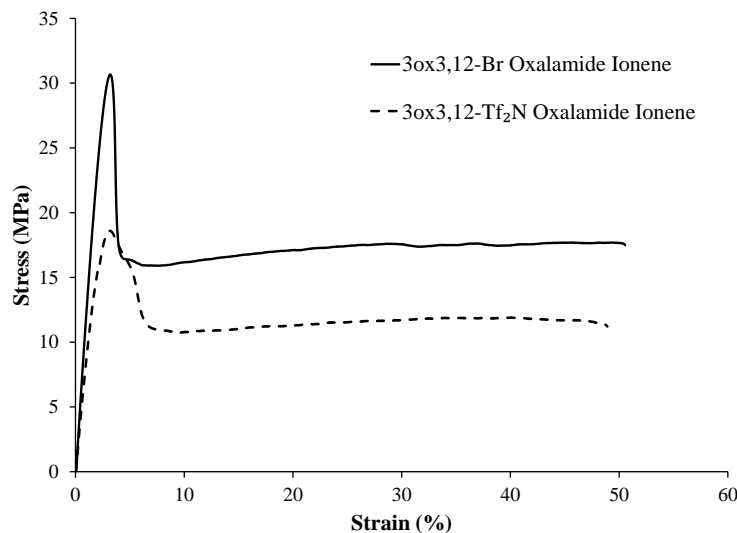


Figure 8.2. Representative tensile curves of 3ox3,12 oxalamide ionenes.

Water Sorption and Conductivity of Oxalamide Ionenes

Water sorption analysis revealed the water uptake behavior of alkyl and oxalamide ionenes (**Figure 8.3**). The water uptake depends on the charge density, concentration of polar oxalamide groups, and counter anion. All ionenes with bromide counteranions are highly hydrophilic, and show significant water uptake at 90% relative humidity (RH). The 3ox3,4-Br ionene has the highest charge density and concentration of oxalamide groups, and therefore absorbs the largest percentage of water with a water sorption of nearly 70% weight increase at 90% RH. The 6,12-Br ionene absorbs the second largest percentage of water due to its charge density, with a water sorption of 48% weight increase at 90% RH. Due to its lower charge density, the 3ox3,12-Br ionene shows the lowest water uptake of the bromide counter anion ionenes, with a water sorption of nearly 30% weight increase at 90% RH.

Anion exchange of bromide to the Tf₂N counteranions drastically reduces the water uptake, with the amount of water sorption dependent on the concentration of the polar oxalamide

groups. The Tf₂N counter anion ionenes are still charged and uptake water, however the organic counter anion is hydrophobic and significantly impacts the hydrophilicity of the ionenes influencing water solubility and reducing water sorption. The 6,12-Tf₂N ionene has the lowest water uptake, with only 2% weight increase at 90% RH. The Tf₂N counter anion oxalamide ionenes display greater water uptake due to the presence of the polar oxalamide groups. The charge density and concentration of oxalamide groups control the water uptake, with the 3ox3,4-Tf₂N and 3ox3,12-Tf₂N ionenes possessing 7% and 16% weight increase at 90% RH, respectively. Overall, the charge density and the concentration of oxalamide groups logically affected the water sorption of these ionenes.

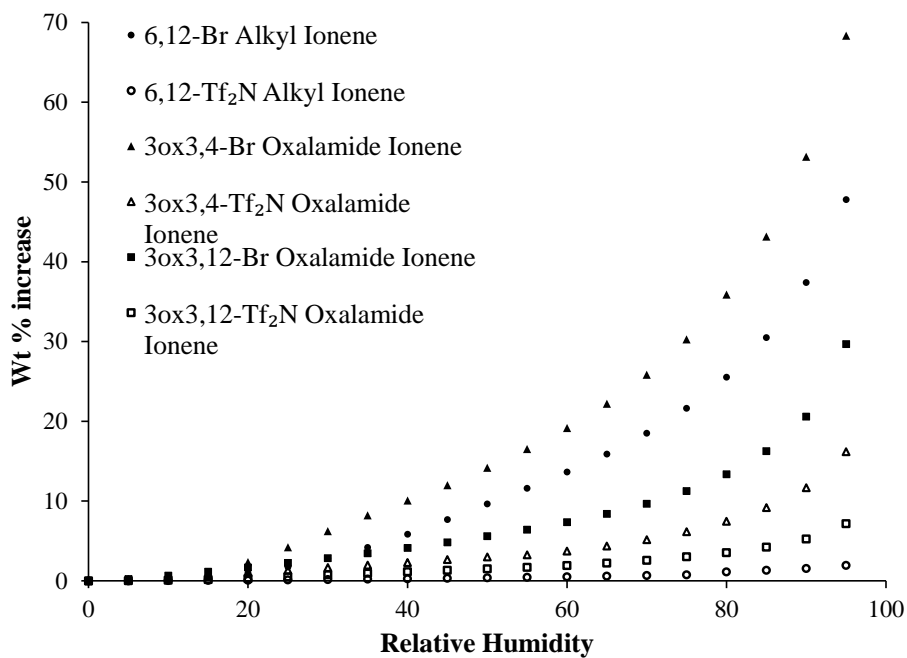
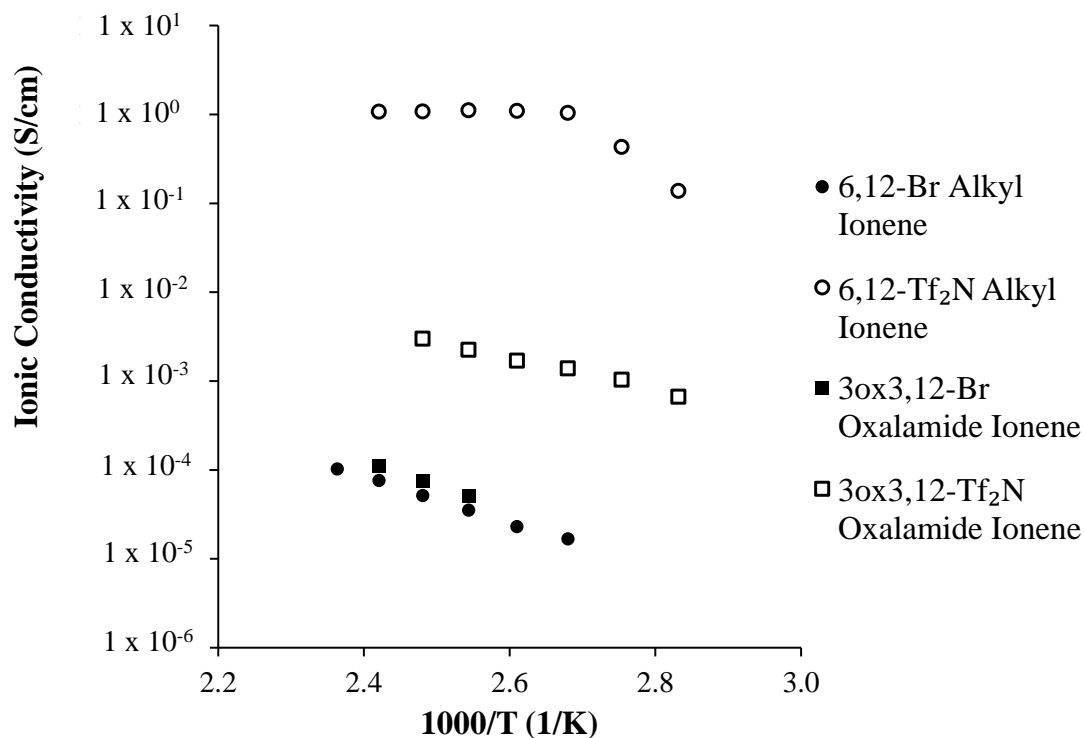
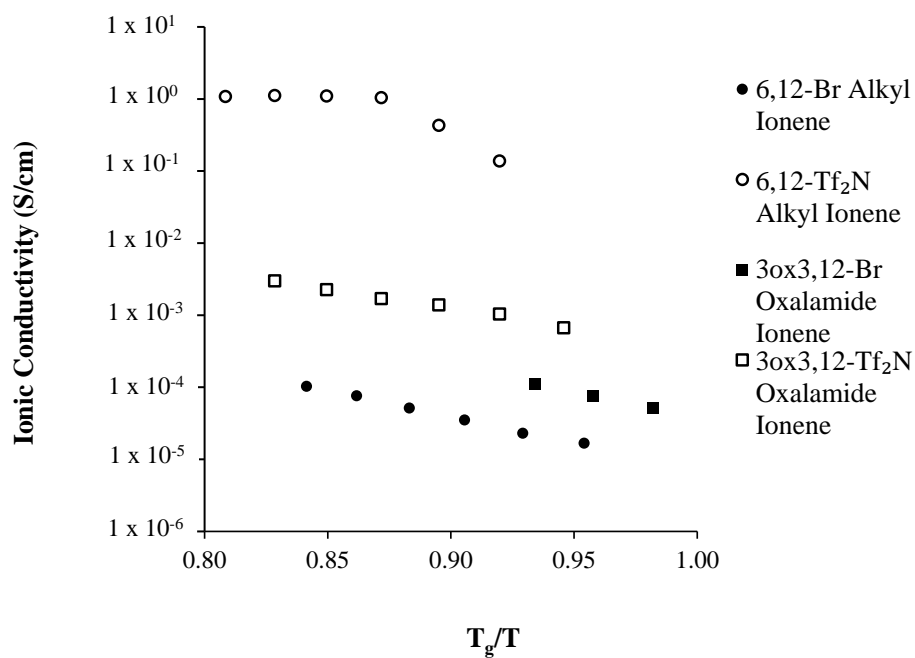


Figure 8.3. Water sorption analysis of ionenes.

The temperature-dependent ionic conductivity of ionenes with different counter-anions is shown in **Figure 8.4A**. Experimental constraints limited the sample selection to polymers with T_g 's below 150 °C, which was the maximum temperature for the environmental chamber. Similar to previous literature reports, the exchange from the hydrophilic bromide anion to relatively more hydrophobic, bulkier fluorine-containing anions such as Tf_2N^- , increased the relative hydrophobicity and resulted in water-insoluble polymers. The ionic conductivity results show that T_g is a dominant, but not exclusive, parameter in determining ion transport as shown in **Figure 8.4B**. The ionic conductivity increased when counter-anion changed from bromide to Tf_2N^- due to low T_g increasing the free volume in Tf_2N^- coupled with segmental motion. Ionic conductivity in our case is also influenced by hydrogen bonding interactions and morphology. The ionic conductivity changes with the introduction of oxalamide groups, decreasing in case of 3ox3,12- Tf_2N ionene as compared to 6,12- Tf_2N ionene.



A.



B.

Figure 8.4. Conductivity analysis of ionenes: A.) Impedance spectroscopy. B.) Impedance spectroscopy normalized by T_g.

SAXS Analysis of Oxalamide Ionenes

SAXS of film forming ionenes shows the effect of structure and counter anion on ionic aggregation in these polymers (**Figure 8.5**). There is a substantial amount of X-ray scattering data in the literature of ionenes in the bromide form, but very little information on ionenes in other counter anion forms. As shown in **Figure 8.5**, all of the ionenes except the 6,12-Tf₂N and 3ox3,4-Br oxalamide ionenes displayed an observable characteristic ionic aggregate peak. The scattering range shown in **Figure 8.5** was the only scattering range with relevant features. This peak position and appearance correlates well with the literature, roughly corresponding to the distance between ionic aggregates which is controlled by the dodecyl alkyl chain length in an all-*trans* conformation.⁴ WAXD only revealed an amorphous halo, and in the case of Tf₂N⁻ anion ionenes a second WAXD peaks appeared corresponding to the spacing between the Tf₂N⁻ anions and the polymer backbone.³⁰

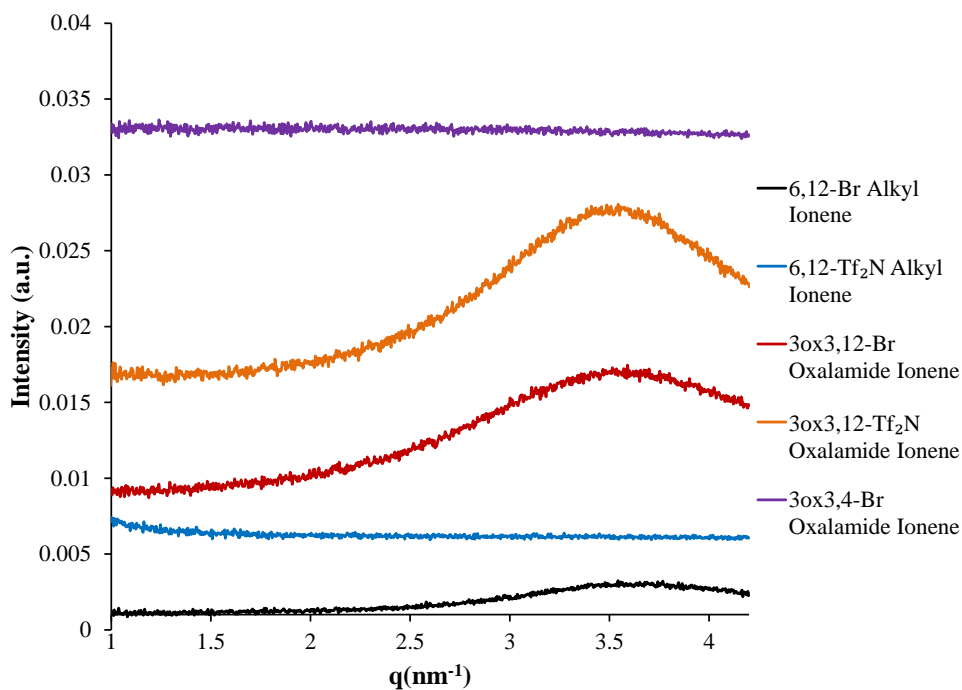


Figure 8.5. SAXS analysis of ionenes.

The 6,12-Tf₂N ionene's lack of an ionic aggregate peak indicates the exchange to the Tf₂N⁻ form prevented the formation of ionic aggregates observable by SAXS. This observation is in agreement with similar ionic polymers, where the introduction of Tf₂N⁻ counteranions disrupt order and leads to an amorphous structure lacking ionic aggregates.^{27,30,31} The 3ox3,12-Tf₂N ionene however, retained the ionic aggregate peak, which suggests the oxalamide groups preserved the formation of the ionic aggregates in this structure through hydrogen bonding. This difference in morphology can be related to the ionic conductivity, where the 6,12-Tf₂N ionene shows a much higher conductivity than the 3ox3,12-Tf₂N ionene. It would be expected that disruption of ionic aggregation would lead to higher conductivity in the sample due to higher ion mobility.³² In this case, both the morphology and T_g effected the 6,12-Tf₂N ionene's conductivity.²⁷ This ionic aggregation can also be related to the ionene's physical properties where the ionic aggregates serve as physical crosslinks contributing to the mechanical properties of the films. The 3ox3,12-Tf₂N ionene which retained ionic aggregation showed a much higher T_g and is a mechanically useful solid at room temperature, in contrast with the 6,12-Tf₂N ionene that is a viscous liquid at room temperature with a relatively low T_g. In the case of the 3ox3,4-Br oxalamide ionene, the lack of an ionic aggregate peak is likely due to the reduced distance between ionic sites. In this polymer structure a short butyl spacer results in significantly less alkyl content than the ionenes with a dodecyl spacer, and the more uniform charge density eliminates ionic aggregation. The 3ox3,4-Br oxalamide ionene does not possess a significant volume fraction per repeat unit of non-polar alkyl content to cause aggregation of polar ionic sites. Unfortunately, instrumental limitations prevented conductivity analysis of this polymer which could further confirm the state of ionic aggregation. In addition, the DMA of this polymer

closely resembles the other ionenes with bromide counteranions, and the presence of ionic aggregation cannot be inferred directly from the DMA.

8.5 *Conclusions*

A facile room temperature reaction yielded the pure novel ionene monomer N1,N2-bis(3-(dimethylamino)propyl)oxalamide that incorporates oxalamide multidentate hydrogen bonding. This monomer allowed for the synthesis of a new class of hydrogen bonding ionenes that displayed excellent mechanical properties. DSC and DMA showed that the introduction of hydrogen bonding increased the T_g of the ionenes compared to all alkyl control ionenes in both bromide and Tf_2N^- counter anion forms. Water sorption analysis showed that water uptake was dependent on charge density, counter anion, and concentration of polar oxalamide groups. Conductivity analysis revealed that ionenes in the Tf_2N^- counter anion form had increased ionic conductivity. SAXS revealed the effect of counter anion and oxalamide groups on ionic aggregation, which correlates to ionic conductivity and ionene physical properties. The novel oxalamide ionenes expand the materials library of ionenes to access more mechanically useful conductive polymers.

Acknowledgements. The authors would like to thank Andrew Giordani for assistance with XPS, which was performed at the Nanoscale Characterization and Fabrication Laboratory (NCFL) operated by the Institute for Critical Technology and Applied Science (ICTAS) at Virginia Tech. We acknowledge Mehdi Ashraf for performing LC-MS analysis. This material is partially based upon work supported by the National Science Foundation under Grant No. DMR-0923107.

8.6 References

1. Gibbs, C. F.; Littmann, E. R.; Marvel, C. S. *J. Am. Chem. Soc.* **1933**, *55*, 753.
2. Abboud, J.-u. M.; Notario, R.; Bertrán, J.; Solà, M. In *Progress in Physical Organic Chemistry*; John Wiley & Sons, Inc.: 1993, p 1.
3. Rembaum, A.; Noguchi, H. *Macromolecules* **1972**, *5*, 261.
4. Tamami, M.; Salas-de la Cruz, D.; Winey, K. I.; Long, T. E. *Macromol. Chem. Phys.* **2012**, *213*, 965.
5. Williams, S. R.; Borgerding, E. M.; Layman, J. M.; Wang, W.; Winey, K. I.; Long, T. E. *Macromolecules* **2008**, *41*, 5216.
6. Zelikin, A. N.; Putnam, D.; Shastri, P.; Langer, R.; Izumrudov, V. A. *Bioconjugate Chem.* **2002**, *13*, 548.
7. Ramirez, S. M.; Layman, J. M.; Long, T. E. *Macromolecular bioscience* **2009**, *9*, 1127.
8. Zheng, A.; Xu, X.; Xiao, H.; Guan, Y.; Li, S.; Wei, D. *Journal of Materials Science* **2012**, *47*, 7201.
9. Xu, X.; Xiao, H.; Ziaee, Z.; Wang, H.; Guan, Y.; Zheng, A. *Journal of Materials Science* **2013**, *48*, 1162.
10. Williams, S. R.; Long, T. E. *Prog. Polym. Sci.* **2009**, *34*, 762.
11. Hemp, S. T.; Zhang, M.; Tamami, M.; Long, T. E. *Polymer Chemistry* **2013**, *4*, 3582.
12. Feng, D.; Wilkes, G. L.; Leir, C. M.; Stark, J. E. *Journal of Macromolecular Science: Part A - Chemistry* **1989**, *26*, 1151.
13. Tamami, M.; Williams, S. R.; Park, J. K.; Moore, R. B.; Long, T. E. *J. Polym. Sci., Part A: Polym. Chem.* **2010**, *48*, 4159.
14. Williams, S. R.; Wang, W.; Winey, K. I.; Long, T. E. *Macromolecules* **2008**, *41*, 9072.
15. Hsu, S. L.; Xiao, H. X.; Szmant, H. H.; Frisch, K. C. *J. Appl. Polym. Sci.* **1984**, *29*, 2467.
16. Dieterich, D.; Keberle, W.; Witt, H. *Angewandte Chemie International Edition in English* **1970**, *9*, 40.
17. Kim, B. K.; Lee, S. Y.; Lee, J. S.; Baek, S. H.; Choi, Y. J.; Lee, J. O.; Xu, M. *Polymer* **1998**, *39*, 2803.
18. Gao, R.; Zhang, M.; Wang, S. W.; Moore, R. B.; Colby, R. H.; Long, T. E. *Macromol. Chem. Phys.* **2013**, *214*, 1027.
19. Gao, R.; Zhang, M.; Dixit, N.; Moore, R. B.; Long, T. E. *Polymer* **2012**, *53*, 1203.
20. Tamami, M.; Hemp, S. T.; Zhang, K.; Zhang, M.; Moore, R. B.; Long, T. E. *Polymer* **2013**, *54*, 1588.
21. Hunley, M. T.; England, J. P.; Long, T. E. *Macromolecules* **2010**, *43*, 9998.
22. Nakamura, K.; Fukao, K.; Inoue, T. *Macromolecules* **2012**, *45*, 3850.
23. Kuo, S.-W.; Tsai, H.-T. *Macromolecules* **2009**, *42*, 4701.
24. Xu, H.; Kuo, S.-W.; Chang, F.-C. *Polym. Bull.* **2002**, *48*, 469.
25. Kuo, S. W.; Xu, H.; Huang, C. F.; Chang, F. C. *J. Polym. Sci., Part B: Polym. Phys.* **2002**, *40*, 2313.
26. Lewis, C. L.; Stewart, K.; Anthamatten, M. *Macromolecules* **2014**, *47*, 729.
27. Chen, H.; Choi, J.-H.; Salas-de la Cruz, D.; Winey, K. I.; Elabd, Y. A. *Macromolecules* **2009**, *42*, 4809.
28. Nakajima, H.; Ohno, H. *Polymer* **2005**, *46*, 11499.
29. Lee, M.; Choi, U. H.; Colby, R. H.; Gibson, H. W. *Chem. Mater.* **2010**, *22*, 5814.

30. Nakamura, K.; Saiwaki, T.; Fukao, K.; Inoue, T. *Macromolecules* **2011**, *44*, 7719.
31. Lee, M.; Choi, U. H.; Salas-de la Cruz, D.; Mittal, A.; Winey, K. I.; Colby, R. H.; Gibson, H. W. *Adv. Funct. Mater.* **2011**, *21*, 708.
32. Choi, U. H.; Lee, M.; Wang, S.; Liu, W.; Winey, K. I.; Gibson, H. W.; Colby, R. H. *Macromolecules* **2012**, *45*, 3974.

Chapter 9: Multi-walled Carbon Nanotubes Decorated with Inorganic Nanoparticles

David L. Inglefield Jr.^a, Erin B. Murphy^a, and Timothy E. Long^{ab}*

^aDepartment of Chemistry, ^bMacromolecules and Interfaces Institute

Virginia Tech, Blacksburg, VA 24061

9.1 *Abstract*

Inorganic nanoparticles offer exciting possibilities to alter the physical properties of multi-walled carbon nanotubes and increase their utility for a number of applications. High temperature degradation of metal or metal oxide precursors and chemical conjugation enable introduction of inorganic nanoparticles into the multi-walled carbon nanotube structure. The facile high temperature decomposition of $\text{Fe}(\text{acac})_3$ facilitated decoration of multi-walled carbon nanotubes with magnetic magnetite nanoparticles, imparting magnetic properties to the multi-walled carbon nanotubes. Acid oxidation introduced carboxylic acid sites onto the multi-walled carbon nanotubes, permitting further functionalization to form thiol functionalized multi-walled carbon nanotubes. The strong thiol-gold interaction enabled conjugation of gold nanoparticles onto the thiol-functionalized multi-walled carbon nanotube surface, which facilitated imaging of functional sites. AuCl_3 loaded into the inner channel of the multi-walled carbon nanotubes through capillary action was subsequently reduced under high temperature to form endohedral gold nanoparticles. Combination of endohedral metal nanoparticle formation and magnetite nanoparticle decoration successfully yielded multi-walled carbon nanotubes containing endohedral gold nanoparticles decorated with magnetite nanoparticles.

9.2 Introduction

Carbon nanotubes (CNTs) represent promising materials for a variety of applications, ranging from medicine to material science.¹⁻⁵ The broad applicability of CNTs to various fields and the intense research interest relating to CNTs results from their unique material properties. CNTs possess excellent mechanical properties, electrical conductivity, and their graphene sidewall structure allows for numerous functionalization strategies, leading to a plethora of functionalized CNTs.⁶⁻⁹ The size, relatively inexpensive methods of production, and inner walls that retain mechanical and electrical properties after extensive functionalization render multi-walled carbon nanotubes (MWCNTs) particularly promising for composite applications. Decoration or functionalization of MWCNTs with inorganic nanoparticles such as gold and magnetite nanoparticles alter the material properties of MWCNTs and expand their utility, particularly in composite applications.¹⁰

High temperature degradation of iron precursors yields superparamagnetic magnetic magnetite (Fe_3O_4) nanoparticles for possible applications in many fields.¹¹⁻¹³ MWCNTs possess the ability to serve as templates for the formation of these magnetic nanoparticles during synthesis, which yields magnetic magnetite nanoparticle decorated MWCNTs.¹⁴ Magnetic nanoparticle decorated MWCNTs will align parallel to sufficiently strong magnetic fields.¹⁵ Alignment of MWCNTs in composites imparts anisotropic mechanical and electrical properties, with applications in composite technologies that benefit from anisotropic properties.¹⁶ However, introduction of magnetite reduces the inherent conductivity of MWCNTs, as magnetite is resistive.

Thiol groups strongly coordinate metallic gold, and the thiol-gold linkage successfully conjugates gold nanoparticles to a variety of functionalized surfaces.^{17,18} Thiol functionalized

MWCNTs readily serve as a template for gold nanoparticle assembly using thiol-gold conjugation.^{19,20} Acid oxidation which introduces carboxylic acid sites onto MWCNT sidewalls and subsequent functionalization of carboxylic acid groups with thiol containing compounds represents a facile and common technique for thiol functionalization.²¹⁻²³ Carbodiimide coupling enables reaction of amine-containing thiol onto carboxylic acid sites in MWCNTs under mild conditions. Imaging of gold nanoparticles under electron microscopy reveals the location of thiol groups (and original carboxylic acid functionality) along the length of the MWCNT structure and helps elucidate the nature of different acid oxidation procedures.²⁴

Capillary action facilitates loading of salt or water-soluble drug solutions into MWCNT structures when the MWCNT ends are open.²⁵ Loading of metal salt solutions leaves behind metal salt solute molecules inside the inner channel of MWCNTs after water evaporation. Subsequent reduction of precursor molecules forms metal nanoparticles inside the MWCNT inner channel. Several investigations demonstrated high temperature reduction of metal salt precursors to form gold, silver, or platinum nanoparticles inside MWCNTs.²⁶ Introduction of endohedral metal nanoparticles into MWCNTs increases the MWCNT conductivity, and also imparts catalytic activity.²⁷ The constrained environment of the MWCNT inner channel influences the catalytic activity of the endohedral metal nanoparticles, increasing their efficiency.²⁸ These unique properties make MWCNT containing endohedral metal nanoparticles promising materials for catalytic and electronic applications.

Herein, we describe the synthesis of various inorganic nanoparticle functionalized MWCNTs. High temperature degradation of $\text{Fe}(\text{acac})_3$ enabled the synthesis of magnetic nanoparticle decorated MWCNTs (mnp-MWCNTs). The relative amount of iron precursor and MWCNTs determined the nanoparticle coverage of the MWCNTs. Acid oxidation and

subsequent carbodiimide coupling of aminoethanethiol enabled the synthesis of thiol-functionalized MWCNTs (SH-MWCNTs). The SH-MWCNTs efficiently templated assembly of gold nanoparticles onto the MWCNT surface, enabling TEM imaging of the distribution of functional sites along the MWCNT structure. Finally, capillary action facilitated loading of AuCl_3 into oxidized MWCNTs (AO-MWCNTs), and subsequent high temperature reduction formed endohedral gold nanoparticles in the MWCNT inner channel. This technique was successfully combined with the magnetic nanoparticle decoration procedure, yielding MWCNTs with endohedral gold nanoparticles and exohedral magnetite nanoparticles (Au@mnp-MWCNTs).

9.3 Experimental

Materials and Instrumentation

All reagents were purchased from Sigma Aldrich and used without further purification unless otherwise noted. All solvents were obtained from Fisher Scientific. Dimethylformamide (DMF) was passed through an Innovative Technology, Inc. PureSolv solvent purification system to remove impurities and water. Concentrated nitric acid (ACS Reagent Plus) and concentrated hydrochloric acid (ACS Reagent Plus) were obtained from Fischer Scientific and used as received. Mesogold colloidal gold nanoparticle solution was obtained from PurestColloids Inc. and used as received. Pristine multi-walled carbon nanotubes (Baytubes®, C70P, carbon purity > 95%, outer diameter: 10-30 nm, catalyst: cobalt metal nanoparticle) was supplied through Bayer and used as received. All MWCNTs were gently powderized before sonication. All dry MWCNTs were handled with care and the proper protective equipment, including respirators. TGA was performed using a TA Instruments HiRes 2950 thermogravimetric analyzer using a

ramp rate of 10 °C/min under an argon atmosphere. SEM was performed using a Zeiss LEO 1550 using the in lens detector with a target voltage of 5 kV. TEM images were generated using a Phillips EM 420 transmission electron microscope operating at 100 kV accelerating voltage. Sonication was performed with a Branson 2510R-MTH sonicator bath.

Synthesis of Magnetic Nanoparticle Decorated MWCNTs

Pristine MWCNTs (150 mg) were dispersed in triethylene glycol (45 mL) by sonication for 50 min in a 250 mL two necked, round-bottomed flask fitted with a water-jacketed condenser. An amount of Fe(acac)₃ determined by the various weight ratios relative to the weight of MWCNTs charged was added to the mixture, and the mixture was reacted at 280 °C for 30 min with rigorous mechanical stirring. After 30 min the reaction mixture was cooled to room temperature, and the mnp-MWCNTs were magnetically separated using a strong rare earth magnet and rinsed with ethanol twice. The mnp-MWCNTs were dried to constant weight *in vacuo* at 60 °C until a constant weight was achieved.

Synthesis of Thiol Functionalized MWCNTs and Conjugation with Gold Nanoparticles

To synthesize thiol functionalized MWCNTs, first an acid oxidation procedure was used to introduce carboxylic acid sites onto the MWCNT sidewall. In a typical procedure, a 2-L, round-bottomed, flask equipped with a magnetic stirrer, was charged with pristine Baytubes (12 g, C70P dispersed at 1 wt% in 8 M HNO₃ (1200 mL) using the sonicator probe and magnetic stirring for 1.5 h. This mixture was refluxed at 110 °C for 24 h. The reaction mixture was diluted with deionized (DI) water and decanted several times, then filtered and washed with DI water until the filtrate reached a neutral pH. Subsequently, to ensure protonation of the carboxylic acid sites, in a 2-L, round-bottomed, flask equipped with magnetic stir bar, the resulting MWCNTs were dispersed in 1 M HCl (1200 mL) through sonication and stirred for 1 h

at 110 °C reflux for 16 h. The MWCNTs were rinsed with DI water and decanted several times, then washed with DI water until the filtrate reached a neutral pH. Finally, the MWCNTs were rinsed with isopropyl alcohol (200 mL) to aid in the drying process. The resulting AO-MWCNTs were then dried *in vacuo* at 60 °C until they achieved a constant weight. Purified MWCNTs, which are an important control, only receive the second 1 M HCl acid reflux step to remove metal catalyst particles without introducing carboxylic acid sites.

Carbodiimide coupling was performed to react aminoethanethiol onto the carboxyl acid sites of AO-MWCNTs. In a typical procedure, 300 mg of AO-MWCNTs were dispersed in 35 mL of DMF by sonication for 1 h in a 100 mL, round-bottomed flask. After sonication, N,N'-dicyclohexylcarbodiimide (DCC, 570 mg) and 2-aminoethanethiol (300 mg) were added and the reaction mixture was stirred for 48 h at 25 °C. After reacting, dichloromethane (DCM, 15 mL) was added to dissolve the formed dicyclohexylurea and the mixture was filtered, then rinsed with 100 mL of DMF twice and 100 mL of DCM. The resulting thiol functionalized MWCNTs (SH-MWCNTs) were dried at 60 °C until achieving a constant weight.

To couple gold nanoparticles to thiol sites, the following procedure was used. SH-MWCNTs (10 mg) was dispersed in 20 mL of DI water for 30 min. Then 1 mL of this SH-MWCNT dispersion was added to 3 mL of Mesogold colloidal gold solution diluted with 6 mL of DI water. This mixture was stirred for 24 h, filtered and rinsed with 100 mL of DI water, and dried at 60 °C until achieving a constant weight. The same procedure was performed with AO-MWCNTs to serve as a control.

Formation of Endohedral Gold Nanoparticles (Au@MWCNTs) and Subsequent Decoration with Magnetic Nanoparticles

To form gold nanoparticles inside AO-MWCNTs, a gold salt precursor was loaded into the AO-MWCNTs using capillary action.²⁶ AO-MWCNTs (150 mg) were sonicated in 5 mL of DI water for 2 h. AuCl₃ (150 mg) dissolved in 2 mL DI water was added and the mixture was stirred for 3 days in air to allow the water to evaporate. The resulting AO-MWCNTs loaded with AuCl₃ were dried at 25 °C until achieving a constant weight to ensure complete removal of water. To reduce the gold salt, the AO-MWCNTs loaded with AuCl₃ were heated in a 250 mL, round-bottomed flask at 400 °C for 4 hours.

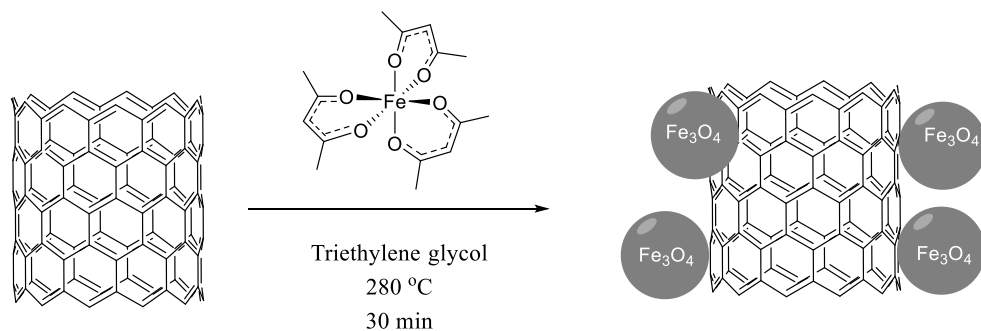
To decorate the resulting Au@AO-MWCNTs with magnetic nanoparticles, Au@AO-MWCNTs (110 mg) were dispersed in triethylene glycol (33 mL) by sonication for 50 min in a 250 mL, two necked, round-bottomed flask fitted with a water-jacketed condenser. Fe(acac)₃ (176 mg) was added to the mixture, and the mixture was reacted at 280 °C for 30 min with rigorous mechanical stirring. After 30 min the reaction mixture was cooled to room temperature, and the Au@mnp-MWCNTs were magnetically separated using a strong magnet and rinsed with ethanol twice. The mnp-MWCNTs were dried *in vacuo* at 60 °C until a constant weight was achieved.

9.4 Results and Discussion

Magnetic Nanoparticle Decorated MWCNTs

The facile high-temperature decomposition of Fe(acac)₃ forms magnetic magnetite nanoparticles in triethylene glycol.¹¹ When MWCNTs are present in the reaction mixture, the magnetite nanoparticles form on the surface of the MWCNTs due to favorable hydrophobic interactions and nucleation of the nanoparticles (**Scheme 9.1**).¹⁴ The amount of Fe(acac)₃

precursor relative to the MWCNTs determined the level of magnetic nanoparticle coverage. **Figure 9.1** shows the magnetic properties of the mnp-MWCNTs, which also allowed for their facile purification. TEM imaged the level of magnetic nanoparticle coverage of the MWCNTs (**Figure 9.2**). The level of coverage varied from no apparent magnetic nanoparticle formation in the 0.2:1 Fe(acac)₃:MWCNT weight ratio reaction to near complete coverage in the 10:1 Fe(acac)₃:MWCNT weight ratio reaction.



Scheme 9.1. Synthesis of mnp-MWCNTs.

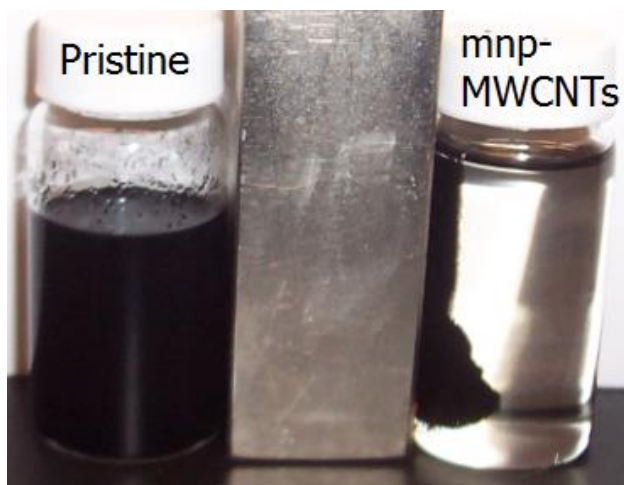


Figure 9.1. Observation of magnetic behavior of mnp-MWCNTs.

TGA further confirmed the amount of magnetic nanoparticle decoration of the mnp-MWCNTs. The rapid combustion of magnetite near 700 °C lead to an abrupt one step degradation in TGA of these samples, summarized in **Table 9.1**. Increase in the $\text{Fe}(\text{acac})_3$:MWCNT weight ratio of the reaction lead to an increase in the weight loss near 700 °C, which correlated with the increase in coverage seen in TEM. **Figure 9.3** shows the alignment of mnp-MWCNTs aggregates after drying under a 1 T magnetic field, further indicating the presence of magnetic nanoparticles and the ability to align mnp-MWCNTs under magnetic fields. The ability to align mnp-MWCNTs in magnetic field allows for anisotropic electrical and mechanical properties in MWCNT composites.¹⁶ However, the magnetite nanoparticles further alter the electrical properties of composites due to the resistivity of magnetite.

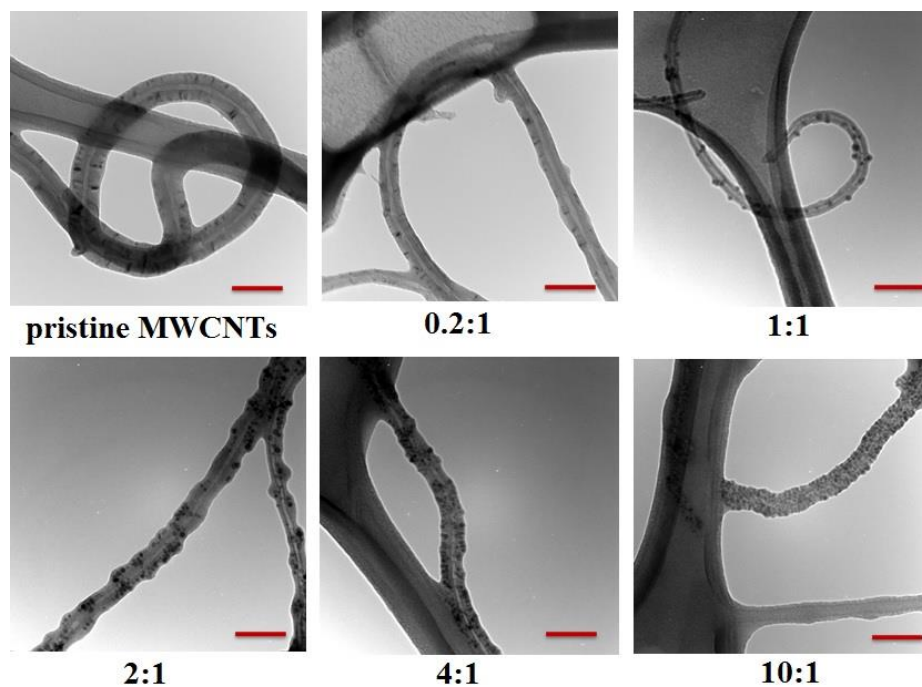


Figure 9.2. TEM imaging of mnp-MWCNTs at various weight ratios of $\text{Fe}(\text{acac})_3$:MWCNTs in the synthesis procedure. Red scale bars are 100 nm.

Table 9.1. Weight loss at magnetite degradation (~700 °C) of different mnp-MWCNTs.

$\text{Fe}(\text{acac})_3$:MWCNTs	%Wt. Loss
Control	none
0.2 : 1	none
1 : 1	1.0
2 : 1	11.6
4 : 1	17.0
10 : 1	21.4

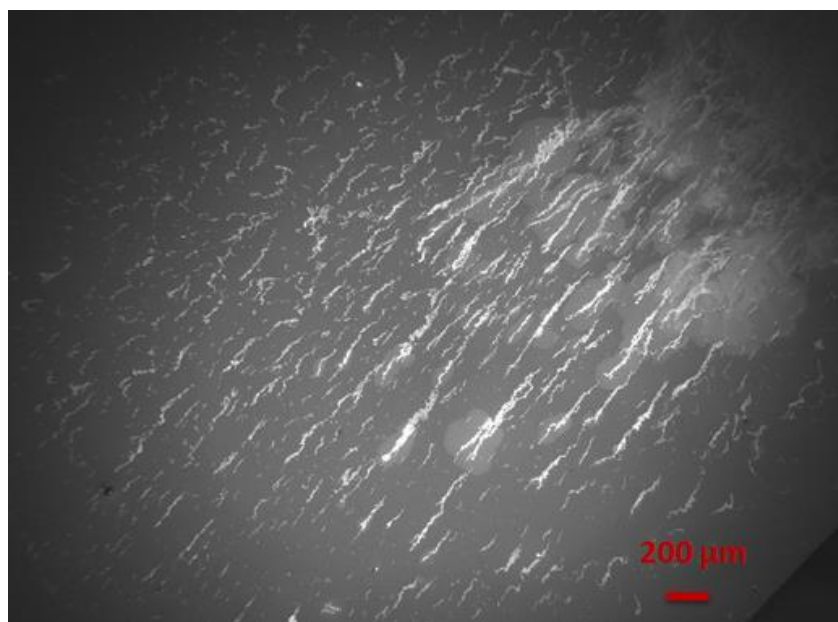
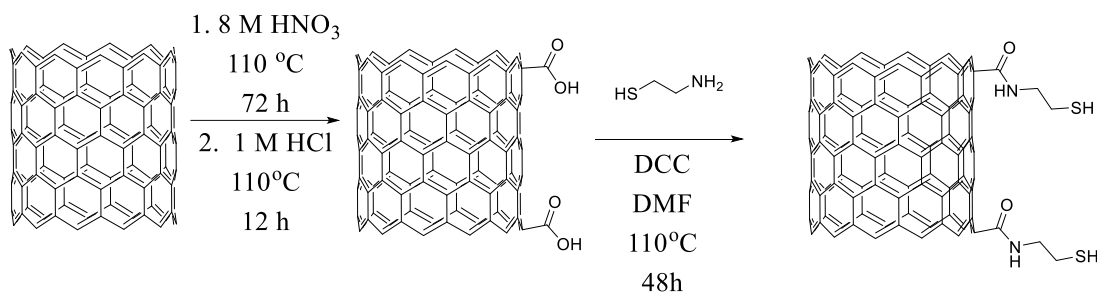


Figure 9.3. Alignment of mnp-MWCNTs in a magnetic field. mnp-MWCNTs (4:1 weight ratio of $\text{Fe}(\text{acac})_3$:MWCNT in initial reaction) were dropped at 7.5×10^{-4} wt % in water on a silicon wafer and dried in a 1 T magnetic field.

Thiol Functionalized MWCNTs and Conjugation with Gold Nanoparticles

The strong thiol-gold interaction enables conjugation of gold nanoparticles to thiol functionalized surfaces, including thiol functionalized MWCNTs.^{19,20} Acid oxidation introduced carboxylic acid sites and enabled further functionalization of the carboxylic acid sites using traditional carboxylic acid chemistry.⁶ Carbodiimide coupling functionalized the carboxylic acid

sites with amino ethane thiol and formed an amide linkage (**Scheme 9.2**). TGA supported successful functionalization according to this functionalization scheme (**Figure 9.4**), using purified MWCNTs to represent a non-functionalized control. Each successive functionalization lead to an increase in weight loss in the critical range of 200-500 °C where organic functionality degrades, supporting successful functionalization.²⁹



Scheme 9.2. Synthesis of thiol functionalized MWCNTs.

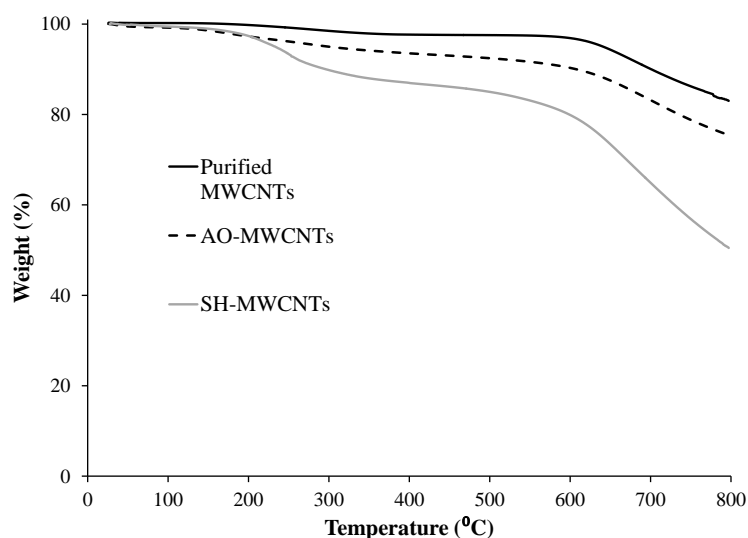
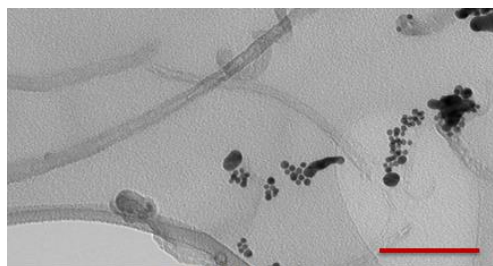


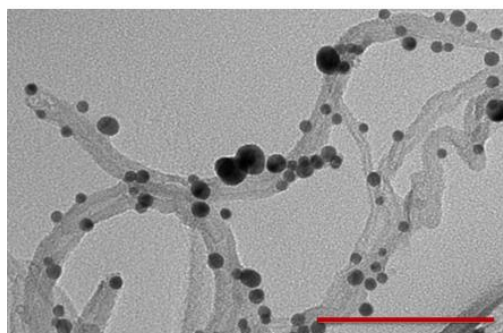
Figure 9.4. TGA analysis of thiol functionalized MWCNTs.

Simple mixing with a gold nanoparticle solution enabled conjugation of Au nanoparticles to the SH-MWCNT surface (Scheme 2). TEM imaged the conjugation of Au nanoparticles to

SH-MWCNTs (**Figure 9.5**). AO-MWCNTs showed no evidence of Au nanoparticle conjugation when utilized in the conjugation procedure, and TEM only observed free Au nanoparticles. However, TEM imaging of the SH-MWCNTs subjected to the conjugation procedure revealed Au nanoparticle conjugation along the whole length of the MWCNTs. This indicated that acid oxidation introduced carboxylic acid functionality all along the MWCNTs.



AO-MWCNTs



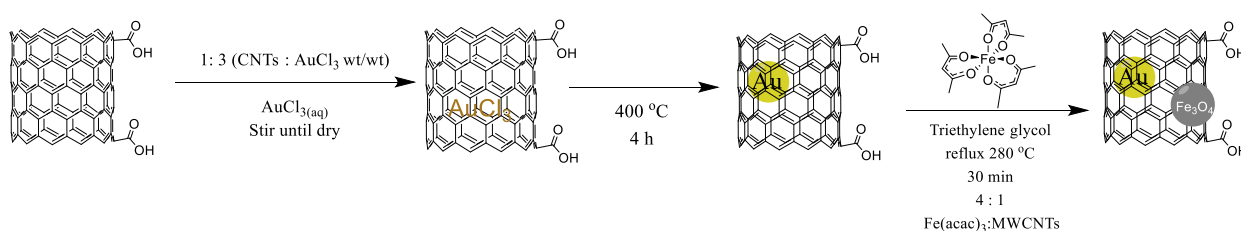
SH-MWCNTs

Figure 9.5. TEM imaging of thiol functionalized MWCNTs decorated with gold nanoparticles and control (AO-MWCNTs) showing no conjugation of gold nanoparticles. Red scale bars are 100 nm.

MWCNTs with Endohedral Gold Nanoparticles (Au@MWCNTs) Decorated with Magnetic Nanoparticles

Capillary action facilitated loading of AuCl₃ into AO-MWCNTs (**Scheme 9.3**). The acid oxidation ensured open ends of the AO-MWCNTs to allow for capillary loading of the AuCl₃ solution.²⁶ After evaporation of water, high temperature reduction of AuCl₃ enabled formation

of endohedral Au nanoparticles (Au@AO-MWCNTs). TEM imaged the Au@AO-MWCNTs (**Figure 9.6A**), showing high contrast Au nanoparticles in the inner channel of the MWCNT structure. Each MWCNT only contained a small number of Au nanoparticles (about one or two) under these conditions. Introduction of Au nanoparticles to MWCNTs increases their conductivity which offers applications in MWCNT composites.³⁰ Also, this high temperature treatment likely degrades organic functionality on the MWCNT sidewall. Furthermore, formation of endohedral Au nanoparticles successfully combined with the magnetic nanoparticle decoration previously described. The high temperature degradation of Fe(acac)₃ led to formation of magnetic nanoparticles on the surface of Au@AO-MWCNTs similar to the pristine MWCNTs shown before, yielding Au@mnp-MWCNTs (**Figure 9.6B**). TEM imaging shows magnetic nanoparticles on the surface of the AO-MWCNTs, with Au nanoparticles visible in the inner channel, indicating the magnetic nanoparticle functionalization procedure does not damage the endohedral Au nanoparticles and that this procedure is applicable to AO-MWCNTs. Energy-dispersive X-ray spectroscopy is required to further confirm the identity of the imaged nanoparticles.



Scheme 9.3. Formation of endohedral gold nanoparticles and subsequent formation of exohedral magnetic nanoparticles.

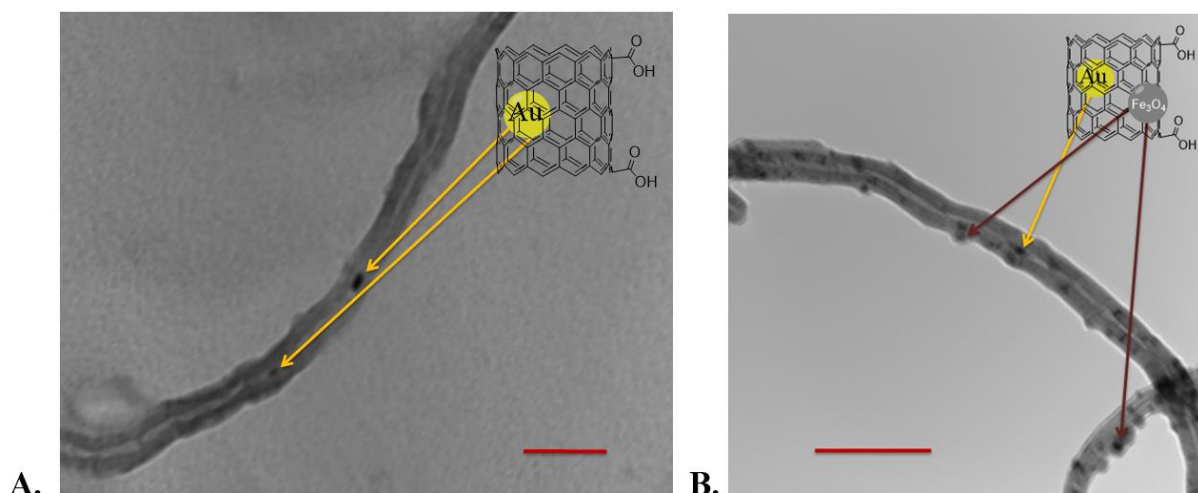


Figure 9.6. TEM imaging of A.) endohedral gold nanoparticles (Au@AO-MWCNTs) and B.) Au@mnp-MWCNTs. Red scale bars are 100 nm.

9.5 Conclusions

Functionalization of MWCNTs with inorganic nanoparticles increases their utility, especially in possible composite applications. High temperature degradation of $\text{Fe}(\text{acac})_3$ enabled formation of magnetic magnetite nanoparticles on the surface of MWCNTs. The decoration of MWCNTs with magnetic nanoparticles allowed for manipulation using magnetic fields. Acid oxidation and subsequent thiol functionalization enabled Au nanoparticle conjugation to thiol sites. This conjugation facilitated TEM imaging of the location of functional sites, which spanned the length of the MWCNT structure. Finally, capillary loading of AuCl_3 solution enabled the formation of endohedral Au nanoparticles which reside inside the inner channel of the MWCNT structure. Furthermore, this procedure was successfully coupled with magnetic nanoparticle decoration to yield Au@mnp-MWCNTs.

Acknowledgements. This work was supported by collaboration with Bayer MaterialScience.

The authors would like to thank Karl Haider and Tao Yu for their guidance on the project. TEM

was performed at the Nanoscale Characterization and Fabrication Laboratory (NCFL) operated by the Institute for Critical Technology and Applied Science (ICTAS) at Virginia Tech. The authors would like to acknowledge the technical expertise of Steve McCartney at the NCFL.

9.6 References

1. Andrews, R.; Weisenberger, M. C. *Curr. Opin. Solid State Mater. Sci.* **2004**, *8*, 31.
2. Dillon, A. C.; Jones, K. M.; Bekkedahl, T. A.; Kiang, C. H.; Bethune, D. S.; Heben, M. J. *Nature* **1997**, *386*, 377.
3. Liu, C.; Chen, Y.; Wu, C.-Z.; Xu, S.-T.; Cheng, H.-M. *Carbon* **2010**, *48*, 452.
4. Niu, C.; Sichel, E. K.; Hoch, R.; Moy, D.; Tennent, H. *Appl. Phys. Lett.* **1997**, *70*, 1480.
5. Spitalsky, Z.; Tasis, D.; Papagelis, K.; Galiotis, C. *Prog. Polym. Sci.* **2010**, *35*, 357.
6. Balasubramanian, K.; Burghard, M. *Small* **2005**, *1*, 180.
7. Ebbesen, T.; Lezec, H.; Hiura, H.; Bennett, J.; Ghaemi, H.; Thio, T. **1996**.
8. Ruoff, R. S.; Lorents, D. C. *Carbon* **1995**, *33*, 925.
9. Salvétat, J. P.; Bonard, J. M.; Thomson, N. H.; Kulik, A. J.; Forro, L.; Benoit, W.; Zuppiroli, L. *Appl. Phys. A* **1999**, *69*, 255.
10. Ventura, D. N.; Stone, R. A.; Chen, K.-S.; Hariri, H. H.; Riddle, K. A.; Fellers, T. J.; Yun, C. S.; Strouse, G. F.; Kroto, H. W.; Acquah, S. F. A. *Carbon* **2010**, *48*, 987.
11. Cai, W.; Wan, J. *J. Colloid Interface Sci.* **2007**, *305*, 366.
12. Lu, A. H.; Salabas, E. e. L.; Schüth, F. *Angew. Chem. Int. Ed.* **2007**, *46*, 1222.
13. Pankhurst, Q. A.; Connolly, J.; Jones, S. K.; Dobson, J. *J. Phys. D: Appl. Phys.* **2003**, *36*, R167.
14. Wan, J.; Cai, W.; Feng, J.; Meng, X.; Liu, E. *J. Mater. Chem.* **2007**, *17*, 1188.
15. Feng, J.; Cai, W.; Sui, J.; Li, Z.; Wan, J.; Chakoli, A. N. *Polymer* **2008**, *49*, 4989.
16. Kim, I. T.; Tannenbaum, A.; Tannenbaum, R. *Carbon* **2011**, *49*, 54.
17. Daniel, M.-C.; Astruc, D. *Chem. Rev.* **2004**, *104*, 293.
18. Westcott, S. L.; Oldenburg, S. J.; Lee, T. R.; Halas, N. J. *Langmuir* **1998**, *14*, 5396.
19. Zanella, R.; Basiuk, E. V.; Santiago, P.; Basiuk, V. A.; Mireles, E.; Puente-Lee, I.; Saniger, J. M. *The Journal of Physical Chemistry B* **2005**, *109*, 16290.
20. Sainsbury, T.; Stolarczyk, J.; Fitzmaurice, D. *The Journal of Physical Chemistry B* **2005**, *109*, 16310.
21. Aviles, F.; Cauich-Rodriguez, J. V.; Moo-Tah, L.; May-Pat, A.; Vargas-Coronado, R. *Carbon* **2009**, *47*, 2970.
22. Datsyuk, V.; Kalyva, M.; Papagelis, K.; Parthenios, J.; Tasis, D.; Siokou, A.; Kallitsis, I.; Galiotis, C. *Carbon* **2008**, *46*, 833.
23. Rosca, I. D.; Watari, F.; Uo, M.; Akasaka, T. *Carbon* **2005**, *43*, 3124.
24. Chopra, N.; Majumder, M.; Hinds, B. J. *Adv. Funct. Mater.* **2005**, *15*, 858.
25. Kim, B. M.; Qian, S.; Bau, H. H. *Nano Lett.* **2005**, *5*, 873.
26. Chu, A.; Cook, J.; Heesom, R. J. R.; Hutchison, J. L.; Green, M. L. H.; Sloan, J. *Chem. Mater.* **1996**, *8*, 2751.

27. Tessonnier, J.-P.; Pesant, L.; Ehret, G.; Ledoux, M. J.; Pham-Huu, C. *Applied Catalysis A: General* **2005**, *288*, 203.
28. Chen, Z.; Guan, Z.; Li, M.; Yang, Q.; Li, C. *Angew. Chem. Int. Ed.* **2011**, *50*, 4913.
29. Ranjan, S.; Jue, Z.-F.; Chen, F. L. *J. Compos. Mater.* **2010**, *44*, 1305.
30. Ma, P.-C.; Siddiqui, N. A.; Marom, G.; Kim, J.-K. *Composites Part A: Applied Science and Manufacturing* **2010**, *41*, 1345.

Chapter 10: Overall Conclusions

The nanoparticle dispersion and complexation methods described in this dissertation rely on effective polymer-nanoparticle interactions enabled through intelligent polymer design incorporating functionalities capable of efficient intermolecular interactions with nanoparticles. Optimal polymer-matrix composite properties typically arise from efficient polymer-nanoparticle interactions, which promote thorough dispersion and enhance interfacial adhesion in composites. Continued development of polymer-nanoparticle interaction strategies will offer new opportunities in the exciting area of nanocomposite materials, which promises numerous revolutionary technologies ranging from energy production and storage to biomedical applications. The realization of these potentially transformative nanocomposite technologies will hinge on interdisciplinary advancement in the areas of polymer synthesis, nanoparticle design, and composite engineering. Applications in biomedical engineering and energy technologies require interdisciplinary synergy between nanocomposite scientists, biologists, and physicists. Attainment of commercially or medically relevant polymer-nanoparticle composites represents a clear example of the increasing importance of interdisciplinary collaboration in modern materials research. Further expanding the utility of polymer-nanoparticle composite materials will rely on novel polymer design that optimizes polymer properties and intermolecular interaction with nanoparticles, combined with nanoparticle surface functionalization strategies which enable enthalpic compatibilization with polymers.

Chapter 11: Suggested Future Work

The work presented in this dissertation offers many insights into nanocomposite systems and raises important questions about the systems presented here. Elucidation of the effect of nanofillers on hydrogen bonding in polyurethane nanocomposites requires further investigation. Investigating the effects of similar nanofillers functionalized with hydrogen bonding groups, such as carboxylic acid functionalized silica nanoparticles, and hydrogen bonding polymers such as poly(acrylic acid) will further reveal how composite formation alters hydrogen bonding in polyurethanes. An important question facing polyurethane-MWCNT composites that still requires a convincing answer is how MWCNT incorporation affects the segmented polyurethane matrix morphology. The size of MWCNTs relative to typical phase-separated polyurethane domains along with preliminary data uncovered in the course of this research and some literature evidence indicate that MWCNTs likely significantly impact the phase-separated morphology of segmented polyurethane matrices. Because desirable segmented polyurethane mechanical properties largely arise from phase separation, this is a critical issue to address in polyurethane-MWCNT composites. This work also provides many possibilities for future nanocomposite design. For example, the ternary carbon nanohorn-quantum dot-diblock copolymer nanocomplexes described here offer many opportunities for further functionalization. Incorporation of targeting ligands onto polymer chain ends and loading of anti-cancer drugs into these nanocomplexes represent possible future improvements on the nanocomplex design.

Phase-separated urea-containing block copolymers provide a platform for possible gold nanoparticle self-assembly. In this work we demonstrated phase separation of urea-containing

methacrylic copolymers leading to urea rich phases, and showed that urea-containing copolymers efficiently complex gold nanoparticles through urea-gold interactions. We also explored the synthesis of gold-coated upconverting nanoparticles. Addition of gold-coated upconverting nanoparticles that exhibit metal-enhanced fluorescence to phase-separated urea-containing block copolymers with controlled morphologies offers an opportunity for self-assembly of these upconverting nanoparticles into nanoscale arrays (**Figure 10.1**). Mechanically useful upconverting nanocomposites able to increase the efficiency of organic photovoltaic cells offer possible applications in solar energy technology. Ordering upconverting nanoparticles into specific nanoscale geometries opens up possibilities for incorporation of other components, such as down-converting materials, into a hierarchical design.

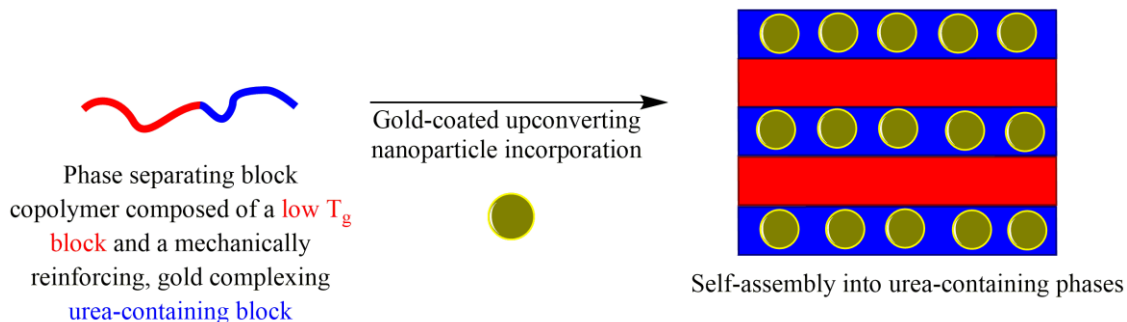
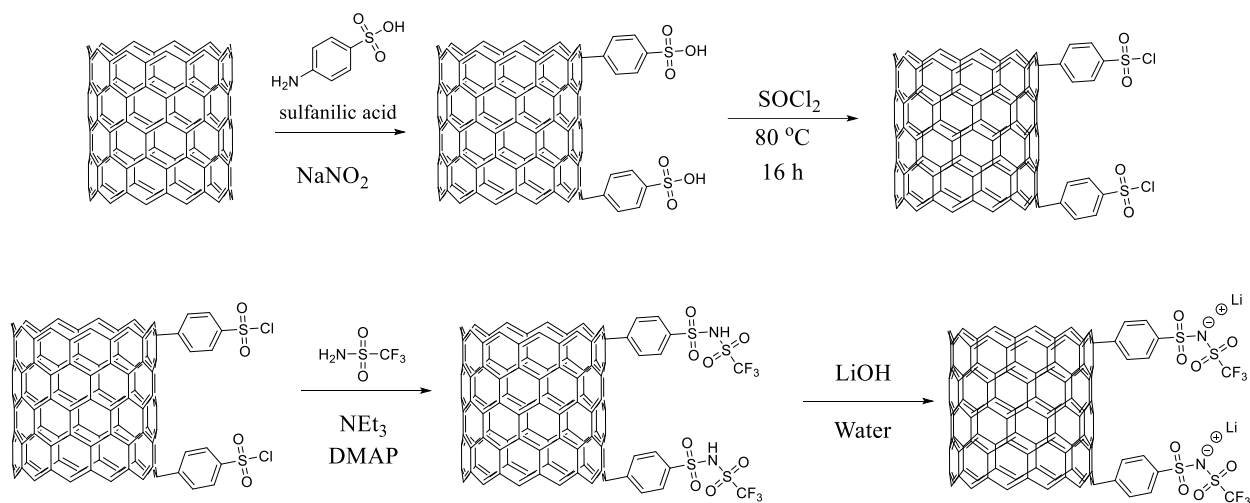


Figure 11.1. Proposed gold-coated upconverting nanoparticle self-assembly in urea-containing block copolymers.

The oxalamide ammonium ionenes described in this dissertation represent exciting polyelectrolytes due to their ionic conductivity and desirable mechanical properties compared to typical ammonium ionenes. Their high levels of hydrogen bonding and charge density render them potentially promising matrix polymers for nanocomposites. Combining oxalamide ammonium ionenes with functionalized carbon nanomaterials may provide mechanically useful materials capable of laser-mediated self-healing. The hydrogen bonds and ionic groups in

oxalamide ammonium ionenes provide labile intermolecular interactions conducive to self-healing properties. These labile, temperature-dependent interactions may be further manipulated through selective heating using laser light that is efficiently absorbed by carbon nanomaterials that then liberated heat to their local environment. This could allow for laser-mediated healing of defects in high performance materials. A promising functionalization of carbon nanomaterials for composite formation with positively charged polymers which also has potential application in battery technology is presented in **Scheme 10.1**. Surface functionalization with the lithium salt of trifluoromethylsulfonyl benzenesulfonamide groups would afford MWCNTs capable of ionic and electronic conductivity with high levels of ionic groups. This functionalization could promote interactions with positively charged polymers and provides possible opportunities in battery technology.



Scheme 11.1. Proposed functionalization for the synthesis of highly charged carbon nanotubes capable of ionic and electronic conductivity.